

---

---

*Alma Mater Studiorum - Università di Bologna*

---

---

DOTTORATO DI RICERCA IN

**SCIENZE CHIMICHE**

Ciclo XXIV

Settore Concorsuale di Afferenza: **03/A2**

Settore Scientifico Disciplinare: **CHIM/02**

**STRUCTURE-PROPERTY RELATIONSHIPS AND  
CHARGE TRANSPORT MODELING OF  
ORGANIC MOLECULAR MATERIALS**

Presentata dal Dott. **Simone Di Motta**

Coordinatore Dottorato  
Prof. **Adriana Bigi**

Relatore  
Prof. **Fabrizia Negri**

---

---

*Esame Finale Anno 2012*

---

---



## ACKNOWLEDGEMENTS

I am indebted to such a great number of people these pages could extend even longer than my pretty verbose dissertation.

I would first like to acknowledge my supervisor Prof. Fabrizia Negri for all the care and time she liked to spend in my Ph.D. education. She is the best teacher I could ever have, an inspiring example of excellent professional attitude, honesty, and objectivity, which are qualities every good scientist should never lack. I thank her for helping me become a better person, then a better researcher. I thank her for believing in my skills, even beyond what I have ever done. I thank her for being always willing to explain and research.

I would like to thank the whole staff of theoretical physical-chemists, for all the knowledge they liked to share with me. In particular, I thank Prof. Giorgio Orlandi, for many useful and enlightening discussions, Prof. Francesco Zerbetto, who has always asked me questions by far smarter than my answers, and Prof. Luca Dore, for his great patience and reliability.

I would like to thank the professors who taught me during my entire education at the Department of Chemistry "G. Ciamician" for their passion for Chemistry and their invaluable contribution to my training. In particular, I thank teachers like Prof. Vincenzo Balzani, who taught me to get down to essentials, Prof. Margherita Venturi, who envisaged in me a gift that I am still looking for, and Prof. Mauro Maestri, who taught me that if one is right, he has to go on his own way no matter what. My special thanks go to Prof. Paola Ceroni, Prof. Alberto Credi, and Dr. Massimo Marcaccio, for involving me in their always intriguing research.

I would like to thank Prof. Magda Monari, for assistance with the access to the Cambridge Crystallographic Data Center along with several clarifying conversations, and Dr. Marianna Fanti, for technical assistance with "the machines" of the computing center.

I would like to thank every person who has collaborated to establishing an enjoyable atmosphere in the computational laboratory. I thank all of them for making these past four years (Master's degree included) amusing and memorable. In particular, my special thanks go to Dr. Tommaso Gallo and Dr. Siegfried Höfner, always willing to be bothered regarding software and hardware trouble, and to Dr. Angela Acocella, Dr. Irene Conti, Dr. Francesca Lugli, Dr. Francesca Toschi, and Dr. Nadja Sändig, for their proficiency, joviality, and fondness. My special thanks go also to Ph.D. students Lorenzo Moro, Marco Dallavalle, and Micaela Matta for being my best colleagues ever.

In addition, I would like to thank the people who have spent with me these past eight years at the Department of Chemistry "G. Ciamician", with particular regard to Ph.D. students Simone Monaco and Massimo Sgarzi, for being a sort of brothers in arms for me.

I am indebted to Dr. Eugenio Di Donato, without whom Pandora Suite would not exist. I also thank him for the fundamental role he played in my Master's degree and the first year of my Ph.D. course.

Because of the nature of the work with which I have been involved, I am also indebted to a great number of people for their experimental collaborations. I thank Prof. Chiara Castiglioni and her group at the Department of Chemistry, Materials, and Chemical Engineering, Politecnico di Milano "G. Natta", also for providing an invaluable contribution regarding theoretical and computational issues. In particular, I thank Dr. Daniele Fazzi for sharing precious ideas and advice. I acknowledge Prof. Zhaohui Wang and his group at the Beijing National Laboratory for Molecular Science, Institute of Chemistry, Chinese Academy of Sciences, for giving me the opportunity to study some of the most interesting organic semiconductors recently synthesized. I thank Prof. Amlan Pal, Indian Association for the Cultivation of Science, Department of Solid State Physics, Jadavpur, Kolkata, for useful discussions. Finally, I acknowledge for recent collaborations Prof. Rainer Friedlein and his group at the School of Materials Science, Japan Advanced Institute of Science and Technology, Nomi, Ishikawa; Prof. Christoph Lambert, Prof. Frank Würthner, and their groups at the Institut für Organische Chemie, Universität Würzburg; Prof. Seth Marder and his group at the School of Chemistry and Biochemistry and Center for Organic Photonics and Electronics, Georgia Institute of Technology.

I would like to acknowledge Prof. Jean-Luc Brédas for giving me the opportunity to visit his group at the School of Chemistry and Biochemistry and Center for Computational Molecular Science and Technology, Georgia Institute of Technology. I first thank Prof. Brédas and his group, the "Brédators", for their unparalleled welcome and friendliness. I am indebted to them for a huge part of my knowledge about charge transport. In particular, for many stimulating conversations, I thank Dr. Veaceslav Coropceanu, Dr. Hong Li, Dr. John Sears, Dr. Chad Risko, Dr. Paul Winget, and Dr. Massimo Malagoli. The time spent in Atlanta was one of the most significant experiences in my life thanks to many people, Brédators and not. Herein, I thank all of them.

Finally, my deepest thanks go to my family and friends whose unwavering love and irreplaceable presence have guided me throughout.

# TABLE OF CONTENTS

ACKNOWLEDGMENTS	i
LIST OF TABLES	vii
LIST OF FIGURES	ix
LIST OF SYMBOLS AND ABBREVIATIONS	xxiii
<b>SUMMARY</b>	<b>1</b>
<b>CHAPTER 1 - INTRODUCTION</b>	<b>2</b>
<b>CHAPTER 2 - ORGANIC TECHNOLOGY</b>	<b>6</b>
2.1 Organic Semiconductors	6
2.2 Organic-Based Devices	9
2.2.1 Organic field-effect transistors	10
2.2.2 Organic photovoltaics	11
2.2.3 Organic light-emitting diodes	12
2.3 Requirements for Functional Organic Layers	14
2.4 Families of Organic Compounds	16
2.5 Structure-Property Relationships	21
2.6 References	25
<b>CHAPTER 3 - THEORETICAL METHODS FOR THE STUDY OF STRUCTURAL, ELECTRONIC, OPTICAL, AND CHARGE TRANSPORT PROPERTIES OF ORGANIC SEMICONDUCTORS</b>	<b>33</b>
3.1 Quantum Mechanics	33
3.1.1 The Schrödinger equation	33
3.1.2 The Hartree-Fock method	35

3.1.3 Post-Hartree-Fock and related methods	39
3.1.4 Semi-empirical methods	43
3.1.5 Density Functional Theory	44
3.1.6 Basis set	49
3.2 Molecular Dynamics	51
3.2.1 Molecular Mechanics	51
3.2.2 Molecular dynamics simulations	53
3.3 Kinetic Monte Carlo	56
3.3.1 Monte Carlo methods	56
3.3.2 Kinetic Monte Carlo simulations	58
3.4 Software	59
3.5 References	60
<b>CHAPTER 4 - INJECTION AND CHARGE TRANSPORT MODELING</b>	<b>64</b>
4.1 Charge Injection - Theoretical model	64
4.2 Charge Injection - Computational approach	66
4.3 Charge Transport - Theoretical models	67
4.3.1 Hopping - Kinetic constants from Marcus and Jortner models	70
4.4 Charge Transport - Adopted theoretical model	73
4.5 Charge Transport - Computational approach	73
4.5.1 Electronic couplings	74
4.5.2 Reorganization energies	76
4.5.3 Thermal fluctuations and molecular dynamics	79
4.5.4 Charge mobility and kinetic Monte Carlo	80

4.6 References	81
<b>CHAPTER 5 - PANDORA SUITE</b>	<b>84</b>
5.1 Crystal Building	85
5.2 Dimers Analysis	85
5.3 Dimers Extraction	86
5.4 $V_{ij}$ Calculation	87
5.5 Thermal Effects Evaluation	87
5.6 $\lambda_i$ Calculation	89
5.7 Charge Mobility	89
5.8 References	91
<b>CHAPTER 6 - RESULTS AND DISCUSSION</b>	<b>93</b>
6.1 BAY-LINKED PERYLENE BISIMIDES	94
6.1.1 Background	94
6.1.2 Computational details	98
6.1.3 Chiral nanoribbons	100
6.1.4 Bowl-shaped diPBIs	102
6.1.5 $\pi$ -conjugation effects and mixed-valence features in diPBIs	109
6.2 N-ANNULATED RYLENES	121
6.2.1 Background	121
6.2.2 Computational details	122
6.2.3 GNRs featuring large dipoles and $H$ aggregation	124
6.3 TETRACENE DIIMIDES	131
6.3.1 Background	131

6.3.2 Computational details	132
6.3.3 NIR dyes TDIs	133
6.4 QUINOIDAL OLIGOTHIOPHENES	142
6.4.1 Background	142
6.4.2 Computational details	144
6.4.3 Biradicaloid and polyenic character in QOTs	146
6.5 OXYGEN DOPED PICENE	160
6.5.1 Background	160
6.5.2 Computational details	161
6.5.3 Effect of O <sub>2</sub> to the electronic structure of highly crystalline picene thin films	162
6.6 RESISTIVE MEMORIES BASED ON BENZOQUINONES AND PENTACENE	171
6.6.1 Background	171
6.6.2 Computational details	173
6.6.3 DDQ as a resistive molecular memory	177
6.7 FLUOROALKYLATED AND CHLORINATED PERYLENE BISIMIDES	195
6.7.1 Background	195
6.7.2 Computational details	198
6.7.3 Charge transport phenomena in fluorinated PBIs	199
6.7.4 Structural and thermal effects on the charge transport of chlorinated PBIs	215
6.8 References	238
<b>CHAPTER 7 - CONCLUDING REMARKS</b>	<b>252</b>

## LIST OF TABLES

- Table 6.1** B3LYP/3-21G\* absolute energies, relative energies, MO energies, HOMO-LUMO gaps and optical gaps ( $\Delta E_{S_0-S_1}$ ) of *cis* and *trans* conformers of **3**, **6**, and **7**. First reduction potentials measured as half-wave potentials *vs.* Fc/Fc<sup>+</sup> in CH<sub>2</sub>Cl<sub>2</sub> solution, with scan rate of 0.1 V s<sup>-1</sup> and TBAPF<sub>6</sub> (0.1 M) as electrolyte.<sup>24</sup> (105)
- Table 6.2** Optical and electrochemical properties of bay-linked oligo-PBIs versus those of PBI **8**.<sup>13</sup> (111)
- Table 6.3** Relative energies of different spin states for the neutral and anionic forms of **1**, **2**, and **3**. From CAM-B3LYP/6-31G\* calculations.<sup>13</sup> (117)
- Table 6.4** Franck-Condon activity parameters computed for the lowest energy intense transition of the three N-annulated rylenes investigated.<sup>45</sup> (127)
- Table 6.5** TD-B3LYP/3-21G computed vertical excitation energies, oscillator strengths, wavefunction analysis, frontier orbital energies and transport gap of **NP**, **BNQ**, **TNH**, and **TNH** dimer and trimer.<sup>45</sup> (129)
- Table 6.6** B3LYP/6-31G\* absolute energies, relative energies, optical gaps (lowest allowed electronic transitions from TDDFT B3LYP/6-31G\* calculations), and the second most important electronic transition in absorption spectra.<sup>53</sup> (137)
- Table 6.7** MO energies (*eV*) of  $\pi$  orbitals and HOMO-LUMO gaps of **NDI**, tetracene, and TDIs **12** and **14**. From B3LYP/6-31G\* calculations at optimized geometries.<sup>53</sup> (137)
- Table 6.8** Orbital nature of the low-lying electronic states of TDI derivatives.<sup>53</sup> (138)
- Table 6.9** Opto-electronic properties of TDIs and energy levels of representative compounds.<sup>53</sup> (141)
- Table 6.10** TD-B3LYP/6-31G\* computed vertical excitation energies, oscillator strengths and wavefunction analysis of **2P-0T**, **2P-1T**, and **2P-2T** at their CS equilibrium structures.<sup>29</sup> (148)
- Table 6.11** Comparison between CASPT2-corrected S<sub>0</sub>→S<sub>1</sub> adiabatic excitation energies (*eV*) and observed weak features in the absorption spectra.<sup>29</sup> (153)
- Table 6.12** Intramolecular reorganization energies (*eV*) computed for **DDQ**, **TCQ**, **TCN** (B3LYP/6-31G\*), and **PNT** (B3LYP/6-31G\*\*).<sup>101</sup> (185)
- Table 6.13** Effective frequency  $\omega_{eff}$  and associated HR factor  $S_{eff}$  employed in the evaluation of charge transfer rate constants of **DDQ**, **TCQ**, **TCN** (B3LYP/6-31G\*), and **PNT** (B3LYP/6-31G\*\*).<sup>101</sup> (185)
- Table 6.14** Electronic coupling integrals  $V_{ij}$  (*cm*<sup>-1</sup>) of **DDQ**, **TCQ**, **TCN**, and **PNT**, computed for the most relevant dimers extracted from the crystal structures.<sup>101</sup> (185)

**Table 6.15** Selection of the largest computed MLJ charge transfer rate constants  $k_{eT}$  (at 300 K) of **DDQ**, **TCQ**, and **TCN**.<sup>101</sup> (192)

**Table 6.16** Frontier orbital energies and transport gap (at the optimized structures of the neutral species), *VEAs*, *AEAs*, AP intramolecular reorganization energies of **1a-model**, **1a**, **2b-2c-model**, **2b**, and **2c**, computed at the B3LYP/3-21G and B3LYP/6-31G\* levels. All values are given in eV.<sup>42</sup> (199)

**Table 6.17** Effective frequency  $\omega_{eff}$  and associated HR factor  $S_{eff}$  employed in the evaluation of charge transfer rate constants of the three PBI derivatives **1a**, **2b**, and **2c**.<sup>42</sup> (202)

**Table 6.18** *n*-type electronic coupling integrals  $V_{ij}^{LUMO}$  (B3LYP/3-21G) and charge transfer rate constant  $k_{eT}$  (at 300 K) for the most relevant dimers of **1a**, **2b**, and **2c** extracted from the crystal structures.<sup>42</sup> (207)

**Table 6.19** Computed electron mobilities  $\mu$  ( $cm^2 V^{-1} s^{-1} \cdot 10^2$ ) for the crystals of **1a**, **2b**, and **2c**; data averaged over 15 groups of 2000 trajectories.<sup>42</sup> (210)

**Table 6.20** Frontier orbital energies of **8Cl**, **2d**, **1d**, and **1a** computed at the B3LYP/3-21G\* optimized structures of the neutral species along with the transport gaps computed at the optimized structures of the neutral and anionic species. All values are given in eV.<sup>43</sup> (216)

**Table 6.21** *VEAs*, *AEAs*, and AP intramolecular reorganization energies  $\lambda_i$  for **8Cl**, **2d**, **1d**, and **1b** computed at the B3LYP/3-21G\*. All values are given in eV.<sup>43</sup> (217)

**Table 6.22** Effective frequency  $\omega_{eff}$  and associated Huang-Rhys factor  $S_{eff}$  employed in the evaluation of charge transfer rate constants.<sup>43</sup> (218)

**Table 6.23** Electronic couplings  $V_{ij}$  (computed at the static crystal structure) and charge transfer rate constants  $k_{eT}$  computed for the systems investigated at the B3LYP/3-21G\* level of theory.<sup>43</sup> (223)

**Table 6.24** Computed electron mobilities  $\mu$  for the crystals of PBI derivatives **1a**, **1b**, **1d**, **2d**, and **8Cl**, and comparison with experimental data.<sup>43</sup> (226)

## LIST OF FIGURES

**Figure 2.1** Schematic representation of polaron, bipolaron, and singlet exciton energy levels in a non-degenerate ground-state polymer. Luminescence from the singlet exciton is also shown. Note that new sub-gap optical transition arise from such intra-gap energy levels. (8)

**Figure 2.2** Schematic representation of the differences between inorganic (left) and polymer (right) semiconductors in terms of doping, charge carriers, and intra-gap energy levels. (8)

**Figure 2.3** Four architectures of OFETs. (a) Bottom gate/bottom contact, (b) bottom gate/top contact, (c) top gate/top contact, and (d) top gate/bottom contact. It was found that devices of the type **b** and **d** always give better performance than that of devices **a** and **c**.<sup>19</sup> Figure adapted from <sup>19</sup>. (11)

**Figure 2.4** (a) Schematic representation of the operation processes of bilayer *pn*-heterojunction OPVs. (b) A bulk heterojunction OPV cell is sketched. Figure adapted from <sup>1,85</sup>. (12)

**Figure 2.5** Schematic representation of the operation processes of single layer (a) and multilayer (b) OLEDs. Figure adapted from <sup>1</sup>. (13)

**Figure 2.6** Structural formula of *p*-type naphthalene (a), anthracene (b), tetracene (c), pentacene (d), picene (e), pyrene (f), perylene (g), coronene (h), and hexabenzocoronene (i). (18)

**Figure 2.7** Structural formula of *n*-type NDI (a), PBI (b), and TDI (c), another diimide derivative. (19)

**Figure 2.8** Oligo-PBIs (a) and oligo(*peri*-N-annulated perylene)s (b) as model compounds of functionalized graphene nanoribbons. Figure adapted from <sup>62b</sup>. (20)

**Figure 2.9** Structural formula of polythiophene (a) and quinoidal oligothiophene (b). (21)

**Figure 2.10** Molecular packing motifs in crystals.<sup>19</sup> (a) Herringbone packing (face-to-edge) without  $\pi$ - $\pi$  overlap (face-to-face) between adjacent molecules (*e.g.*, pentacene); (b) herringbone packing with  $\pi$ - $\pi$  overlap between adjacent molecules (*e.g.*, rubrene); (c) lamellar motif, 1-D  $\pi$ -stacking (*e.g.*, hexyl substituted naphthalene diimide); (d) lamellar motif, 2-D  $\pi$ -stacking (*e.g.*, octachlorinated perylene bisimide<sup>78</sup>). Figure adapted from <sup>19</sup>. (22)

**Figure 3.1** Schematization of the HF self-consistent field method. (39)

**Figure 3.2** Excited determinants  $|\Phi_a^p\rangle$ ,  $|\Phi_{ab}^{pr}\rangle$ , and  $|\Phi_{abc}^{pqr}\rangle$  represent the promotion of one, two, or three electrons from occupied molecular orbital levels, *i.e.*, a, b, and c, into unoccupied molecular orbital levels, *i.e.*, p, q, and r, in comparison with the reference HF Slater determinant  $|\Phi_0\rangle$ . (40)

**Figure 3.3** Considering to study the thermodynamics properties of a gas confined by a piston in a cylinder, a MD simulation is focused on the time evolution of the system, whereas a MC simulation collects every possible

replica, so to say, as scattered snapshots; however, for the ergodic hypothesis, the results of both the techniques must converge. (57)

**Figure 3.4** The Metropolis criterion relies on a Boltzmann distribution. (57)

**Figure 3.5** Choice of the final state. Being  $0 < r \leq 1$  and  $P_{i-1} < r \leq P_i$ , the probability that the system jumps into the  $i$ -th state is proportional to  $P_i$ .<sup>39</sup> Figure adapted from <sup>39</sup>. (59)

**Figure 4.1** Schematization of the band structure at the two metal/organic heterojunctions. (65)

**Figure 4.2** Temperature dependence of the charge mobility shown by molecular crystals of (a) peylene<sup>8</sup> and (b) ultrapure naphthalene.<sup>9</sup> Figure adapted from <sup>27</sup>. (68)

**Figure 4.3** Schematic representation of the diabatic limit (a), non-adiabatic regime (b), and adiabatic regime (c), for a self-exchange charge transfer and within the validity of the harmonic approximation for normal modes. (72)

**Figure 4.4** Energetic trends denoting a typical inconvenience of ESD methods.<sup>10a,19b</sup>  $\epsilon_{1,2}$  are the site energies (*vide infra*),  $t$  the charge transfer integral. The more the ethylene monomers move away from the face-to-face configuration toward a face-to-edge one, the more  $t$  decreases; the problem is that the ESD evaluation, based on  $\Delta E_{12}$ , does not deliver such a trend.<sup>19b</sup> Figure adapted from <sup>19b</sup>. (75)

**Figure 4.5** Schematic representation of the potential energy profiles of neutral and charged species involved in the charge transfer process and indication of the two contributions of the total internal reorganization energy. The scheme, applied to a reduction process, also shows the relation between  $VEA_n$  and  $VEA_a$  and the  $\lambda_i$ .  $E_y^{geo-x}$  represents the energy of the  $y$  state computed at the geometry of the  $x$  state ( $x,y=\{n,a\}$ ). (77)

**Figure 5.1** Scheme of the operating procedure adopted by Pandora Suite. (84)

**Figure 6.1** Schematic representation of diabatic (blue dashed lines) and adiabatic (solid black lines) PESs of Robin-Day class II-III systems with degenerate MV systems; the different colors illustrate the different redox states of the redox centers (circles), while the different sizes illustrate the geometrical differences of charged *vs.* neutral redox centers.<sup>6</sup> Figure adapted from <sup>6</sup>. (95)

**Figure 6.2** Chemical structures of the three bay-linked PBI-based arrays,  $n = 0, \dots, x$ . Figure adapted from <sup>13</sup>. (96)

**Figure 6.3** Chemical structures of the three diPBIs featuring different linkage in the bay regions. They are referred to as **1** the singly, **2** the doubly, and **3** the triply bay-linked. Figure adapted from <sup>13</sup>. (97)

**Figure 6.4** Chiral "ladder-type" doubly-linked PBI dimer (**4**) and trimer (**5**). Figure adapted from <sup>18</sup>. (97)

**Figure 6.5** Chemical structures of the bowl-shaped heterocyclic annelated S-diPBI (**6**) and N-diPBI (**7**), where "R" is a 2,6-diisopropylphenyl. Figure adapted from <sup>24</sup>. (98)

**Figure 6.6** B3LYP/3-21G\* computed structures for the two enantiomers of **4** (top) and the three isomers of **5** (bottom). Hydrogen atoms are omitted for clarity. Figure adapted from <sup>18</sup>. (101)

**Figure 6.7** (a) CD spectra of **4** before HPLC (dashed line) and the first (solid line) and the second (dotted line) fraction after HPLC, (b) CD spectra of the first (solid line), the second (dashed line), and the third (dotted line) fraction of **5** after HPLC in chloroform. (c) TD-CAM-B3LYP/3-21G\* computed CD spectra of the *M,M*-enantiomer (dotted line) and *P,P*-enantiomer (solid line) of **4**. (d) TD-CAM-B3LYP/3-21G\* computed CD spectra of the *M,M,M*-enantiomer (dotted line), *P,P,P*-enantiomer (solid line), and mesomer (dashed line) of **5**. To facilitate comparison, the computed spectra (vibronic structure not included) were red shifted to match the first observed transition. Figure adapted from <sup>18</sup>. (102)

**Figure 6.8** Chemical structures of a perylene bisimide monomer (**8**) and synthesized heterocyclic annelated monoPBIs (**9**, **10**, and **11**). Figure adapted from <sup>24</sup>. (103)

**Figure 6.9** Equilibrium structures of *trans* (a) and *cis* (b) conformers of **3**, **6**, and **7** computed at the B3LYP/3-21G\* level. Figure adapted from <sup>24</sup>. (104)

**Figure 6.10** ORTEP drawing of the molecular structures of (a) **6** and (b) **7** with 30% probability ellipsoids. POAV1 pyramidalization angles ( $\theta_{\sigma\pi} - 90$ ) of one PBI unit based on the crystal structures of **6** and **7** are given: (top) top view and (bottom) side view. Figure adapted from <sup>24</sup>. (106)

**Figure 6.11** Intermolecular interactions in the crystal structure of **6**. Figure adapted from <sup>24</sup>. (106)

**Figure 6.12** (top) The TD-B3LYP/3-21G\* calculated absorption spectra (vibronic structure not included) of **3** (black), **6** (blue), and **7** (red) at the optimized *cis* structures. (bottom) Absorption spectra of **3** (black), **6** (blue), and **7** (red) in CHCl<sub>3</sub>. Figure adapted from <sup>24</sup>. (107)

**Figure 6.13** Comparison between computed frontier orbitals (left) HOMO and (right) LUMO of *trans* **3**, *cis* **6**, and *cis* **7** showing the dominant orbital parentage across diPBI derivatives. Figure adapted from <sup>24</sup>. (108)

**Figure 6.14** UV-Vis absorption spectra: PBI **8** (black), singly-linked **1** (red), doubly-linked **2** (orange), and triply-linked **3** (violet) in chloroform. Figure adapted from <sup>13</sup>. (110)

**Figure 6.15** Reductive cyclic voltammograms of **1** (red), **2** (orange), and **3** (violet) in CH<sub>2</sub>Cl<sub>2</sub> with a scan rate of 100 mVs<sup>-1</sup> vs. Fc/Fc<sup>+</sup> and Bu<sub>4</sub>NPF<sub>6</sub> (0.1 M) as electrolyte. Figure adapted from <sup>13</sup>. (112)

**Figure 6.16** Comparison between observed and computed electronic spectra of (a,d) **1**, (b,e) **2**, and (c,f) **3**. (top) Spectroelectrochemistry in CH<sub>2</sub>Cl<sub>2</sub>/Bu<sub>4</sub>NPF<sub>6</sub> (0.2 M), potentials at which the spectra are measured are given vs. Fc/Fc<sup>+</sup>. (bottom) TD-CAM-B3LYP/6-31G\* computed spectra rigidly shifted to the red by 2500 cm<sup>-1</sup>. Figure adapted from <sup>13</sup>. (113)

**Figure 6.17** CAM-B3LYP/6-31G\* optimized geometries of the neutral ground states of diPBIs **1**, **2**, and **3**; frontal and side views are shown. Figure adapted from <sup>13</sup>. (114)

**Figure 6.18** CAM-B3LYP/6-31G\* frontier molecular orbitals of neutral **1**, **2**, and **3**. The large electronic communication of **3** compared to **1** and **2** results in a large energy split of LUMO/LUMO+1 and HOMO/HOMO-1 pairs of orbitals. Figure adapted from <sup>13</sup>. (115)

**Figure 6.19** CAM-B3LYP/6-31G\* equilibrium bond lengths for the neutral and anionic species of **2**. Figure adapted from <sup>13</sup>. (116)

**Figure 6.20** (a) The localized nature of UCAM-B3LYP/6-31G\* SOMO and LUMO ( $\alpha$  and  $\beta$ ) orbitals of the BS biradical structure of the di-anion of **1**. The two electronic excitations responsible for the low energy (*ca.* 7500  $cm^{-1}$  computed value, *ca.* 5000  $cm^{-1}$  observed value) quasi-CT transition are indicated by dashed red arrows. (b,c) The localized nature of (b) the SOMO and LUMO ( $\alpha$ ) orbitals of the mono-anion of **1** and (c) the SOMO and LUMO ( $\beta$ ) orbitals of the tri-anion of **1**. These orbitals are involved in the electronic excitation responsible for the low energy (*ca.* 1000  $cm^{-1}$  computed value) CT transition indicated by the dashed red arrow. From UCAM-B3LYP/6-31G\* calculations. A schematic representation of electron localization on the singly linked diPBI is shown in the top left corner of each graph. Figure adapted from <sup>13</sup>. (119)

**Figure 6.21** Chemical structures of the synthesized N-annulated perylene (**NP**), bis-N-annulated quaterrylene (**BNQ**), and tri-N-annulated hexarylene (**TNH**); depending on the end group **a**, **b**, or **c**, **TNH<sub>a</sub>**, **TNH<sub>b</sub>**, or **TNH<sub>c</sub>** is obtained, respectively. Figure adapted from <sup>45</sup>. (122)

**Figure 6.22** B3LYP/3-21G equilibrium geometries of the neutral ground states of (a) **NP**, (b) **BNQ**, and (c) **TNH** models. The red arrow indicates the permanent dipole moment of the molecule. Figure adapted from <sup>45</sup>. (124)

**Figure 6.23** B3LYP/3-21G frontier molecular orbitals of (a) **NP**, (b) **BNQ**, and (c) **TNH**. Figure adapted from <sup>45</sup>. (125)

**Figure 6.24** UV-Vis absorption spectra of **NP** (cyan), **BNQ** (magenta), **TNH<sub>a</sub>** (black), **TNH<sub>b</sub>** (red), and **TNH<sub>c</sub>** (blue) in THF ( $1 \cdot 10^{-6}$  M). The apparent reduction of absorbivity for **TNH<sub>a-c</sub>** is due to the fact that only a fraction of the monomer is present, while the remaining **TNH** is present in the form of aggregate. Figure adapted from <sup>45</sup>. (125)

**Figure 6.25** Comparison between observed (dashed) and computed (solid) spectra (including computed vibronic structure) for **NP** in black and **BNQ** in red. The fine structure shown under the broad computed spectra represents the FC activity contributions to each broad band. The origins of the computed spectra were translated to the origins of the respective experimental spectra. Figure adapted from <sup>45</sup>. (126)

**Figure 6.26** Normal coordinates associated with the largest computed FC activity in the spectrum of **TNH**. The vibrational frequency and the associated  $\gamma_i$  value are indicated for each normal mode. Figure adapted from <sup>45</sup>. (127)

**Figure 6.27** Dimer (top) and trimer (bottom) of **TNH** as examples of *H* aggregates. Cyan arrows represent the directions of dipole moments. Red arrows represent the directions of the  $S_0 \rightarrow S_1$  transition dipole moments of each molecule. Figure adapted from <sup>45</sup>. (128)

**Figure 6.28** Comparison between observed (bottom) and simulated (top) absorption spectra of **TNH**. The computed spectra were obtained by superimposing, in different proportions, the spectra of the monomeric and trimeric species with their associated FC structures. Figure adapted from <sup>45</sup>. (129)

**Figure 6.29** Chemical structures of the recently synthesized<sup>53</sup> tetracene diimides **12a**, **13**, and **14**. Derivative **12c** is analogous to **12a** but featuring  $-\text{CH}_2(\text{CF}_2)_2\text{CF}_3$  instead of  $-\text{CH}_2(\text{CH}_2)_6\text{CH}_3$ . Figure adapted from <sup>53</sup>. (132)

**Figure 6.30** Molecular structure of **12c**, the X-ray structure along the crystallographic *b* axis (right), the X-ray structure along the crystallographic *c* axis (left). Figure adapted from <sup>53</sup>. (133)

**Figure 6.31** UV-Vis-NIR absorption spectra of **12a** (black), **13** (red), and **14** (blue) in chloroform. Figure adapted from <sup>53</sup>. (134)

**Figure 6.32** Energies and shapes of B3LYP/6-31G\* frontier orbitals (HOMO and LUMO) of tetracene, **NDI**, and a planar model of **12**. Figure adapted from <sup>53</sup>. (135)

**Figure 6.33** Comparison between computed and observed UV-Vis-NIR absorption spectra. (bottom) TD-B3LYP/6-31G\* calculated absorption spectra of **12** (red) and **14** (blue) in their more stable heliciform structure. (top) Absorption spectra of **12a** (red) and **14** (blue) in  $\text{CHCl}_3$ . Figure adapted from <sup>53</sup>. (136)

**Figure 6.34** Comparison between computed and observed UV-Vis-NIR absorption spectra. (bottom) TD-B3LYP/6-31G\* calculated absorption spectra of **12** (red), **12p** (green), and tetracene (blue). (top) Absorption spectra of **12a** (red) and tetracene (blue) in  $\text{CHCl}_3$ . Figure adapted from <sup>53</sup>. (136)

**Figure 6.35** Energies and shapes of B3LYP/6-31G\* frontier orbitals (HOMO and LUMO) of tetracene, **NDI**, **12p**, **12**, and **14** showing the dominant orbital parentage across TDI derivatives. The orbital shapes of the non-heliciform structures of **12** and **14** are very similar to those of the heliciform species. Figure adapted from <sup>53</sup>. (139)

**Figure 6.36** Energies and shapes of B3LYP/6-31G\* occupied orbitals (HOMO, HOMO-2 (tetracene, **12p**, **12**) and HOMO-1 (for **14**)) involved in the low-lying excitations of the investigated compounds. The comparison shows the dominant orbital parentage with tetracene across TDI derivatives. Figure adapted from <sup>53</sup>. (140)

**Figure 6.37** Structural formula of the quinoid molecules **2P-nT** experimentally investigated ( $R=\text{tert-butyl}$ ) and the model systems considered for computations ( $R=\text{H}$ ), where  $n=0,1,2$ . Figure adapted from <sup>29</sup>. (143)

**Figure 6.38** Comparison between the optimized structures of  $S_0$  (B3LYP/6-31G\*)(black) and of the bright state  $S_2$  (TD-B3LYP/6-31G\*)(red) for (left) **2P-0T** and (right) **2P-1T**. Only selected bond lengths are reported, according to the bond numbering in the inset. Figure adapted from <sup>29</sup>. (147)

**Figure 6.39** Comparison between the optimized structures of  $S_0$  and of the bright state  $S_2$  (TD-B3LYP/6-31G\*)(red) for **2P-2T**. Only selected bond lengths are reported, according to the bond numbering in the inset. For the ground state, the unstable B3LYP/6-31G\* CS quinoid structure (black), the stable UB3LYP/6-31G\* BS biradicaloid structure (green) and the intermediate structure employed to simulate the  $S_0 \rightarrow S_2$  absorption spectrum in Figure 6.41 (blue), are reported. Figure adapted from <sup>29</sup>. (147)

**Figure 6.40** B3LYP/6-31G\* frontier molecular orbital shapes and energy levels of **2P-0T**, **2P-1T**, and **2P-2T** at their equilibrium structures. Figure adapted from <sup>29</sup>. (148)

**Figure 6.41** Comparison between observed (top) absorption spectra in *n*-hexane and TDDFT/6-31G\* computed (bottom) FC structure associated with the  $S_0 \rightarrow S_2$  strongly allowed electronic transition of **2P-2T** (black), **2P-1T** (blue), and **2P-0T** (red). The origins of the computed spectra were translated to the origins of the respective experimental spectra. The arrows indicate features in the experimental spectra assigned to the double-exciton state. Figure adapted from <sup>29</sup>. (149)

**Figure 6.42** Excited state normal coordinates and frequencies (TD-B3LYP/6-31G\*, scaled by 0.97) associated with the largest computed FC activity ( $\gamma_i$  parameters) in the  $S_0 \rightarrow S_2$  absorption spectrum of **2P-0T** (up), **2P-1T** (bottom, left), and **2P-2T** (bottom, right). The scaled vibrational frequency and the associated  $\gamma_i$  value are indicated for each normal mode. Only modes with  $\gamma_i > 0.1$  are reported. Figure adapted from <sup>29</sup>. (150)

**Figure 6.43 2P-2T:** Comparison between the experimental absorption spectrum (top, black) and the computed FC structure (bottom) employing: the quinoid CS ground-state structure (red), the strongly biradicaloid BS ground-state structure (blue), and the intermediate biradicaloid structure between the two (black). Figure adapted from <sup>29</sup>. (151)

**Figure 6.44** Comparison between the ground state equilibrium structures of **2P-1T** computed at CASSCF(12,12)/6-31G\* (red) and B3LYP/6-31G\* (green) levels. Figure adapted from <sup>29</sup>. (153)

**Figure 6.45** Comparison of **2P-2T** ground-state equilibrium structures computed at CASSCF(12,12)/6-31G\* (red), B3LYP/6-31G\* (CS structure) (blue), UB3LYP/6-31G\* (BS structure) (green, and CASPT2 (black) levels. The black structure was determined as the  $\mathcal{A}$ -displaced structure corresponding to the CASSCF(12,12)/6-31G\* + CASPT2 minimum energy. Figure adapted from <sup>29</sup>. (154)

**Figure 6.46** Comparison between the equilibrium structures of  $S_0$  (red) and of the double-exciton state  $S_1$  (black) computed at CASSCF(12,12)/6-31G\* level for (left) **2P-1T** and (right) **2P-2T**. Only selected bond lengths are reported, according to the bond numbering in the inset. Figure adapted from <sup>29</sup>. (154)

**Figure 6.47 2P-2T:** Bond length changes upon excitation to the double-exciton  $S_1$  state from CASSCF(12,12)/6-31G\* calculations (black) and upon moving from the ground-state quinoid CS to the biradicaloid BS structure obtained at the B3LYP/6-31G\* level (red). The bond length changes overlap closely with the displacements (cyan) of the Raman active out-of-phase CC stretching mode (the  $\mathcal{A}$  mode, B3LYP/6-31G\* level) which is mainly localized on the thiophenic molecular region. Figure adapted from <sup>29</sup>. (155)

**Figure 6.48** Potential energy profiles of  $S_0$  and  $S_1$  along the  $\mathcal{A}$  coordinate at CASSCF level and including CASPT2 corrections. The red and black arrows indicate the minima on the CASSCF and CASPT2 profiles. The  $S_0$  minimum is located at a more biradicaloid structure at the CASSCF//CASPT2 level. Figure adapted from <sup>29</sup>. (156)

**Figure 6.49** Projection of the  $S_1$ - $S_0$  geometry change (CASSCF(12,12)/6-31G\* level) over ground state normal modes (dimensionless  $B$  parameter). Contributions for **2P-1T** (black) and **2P-2T** (red). Vibrational frequencies,

scaled by 0.97, were computed at B3LYP/6-31G\* level. The largest contribution in the high frequency region is due, for both molecules, to the mode dominated by the  $\mathcal{A}$  character. Figure adapted from <sup>29</sup>. (158)

**Figure 6.50** Projection of the CASSCF(12,12)/6-31G\* computed derivative coupling between S0 and S1 over ground-state normal modes. Vibrational frequencies, scaled by 0.97, were computed at B3LYP/6-31G\* level. The largest contribution in the high frequency region is due to the mode dominated by the  $\mathcal{A}$  character. Figure adapted from <sup>29</sup>. (158)

**Figure 6.51 2P-2T:** Reorganization energies ( $\lambda_{gr}$  and  $\lambda_{exc}$ ) associated with the S<sub>0</sub>→S<sub>1</sub> excitation from CASSCF(8,8)/6-31G\* + CASPT2 calculations. The largest value of  $\lambda_{exc}$  compared to  $\lambda_{gr}$  suggests a frequency increase in the S<sub>1</sub> state of the mode dominated by the  $\mathcal{A}$  character, as it is well known for polyenes. Figure adapted from <sup>29</sup>. (159)

**Figure 6.52 (a)** UPS spectrum of the picene/Ag(110) multilayer film measured with respect to  $E_F$  and **(b)** a simulated spectrum derived from calculated molecular orbital energies, shown at the bottom. H, H-1, and H-2 denote the three highest occupied molecular orbitals, HOMO, HOMO-1, and HOMO-2, respectively. Feature "X" is attributed to trapping states (*vide infra*). The molecular structure of picene is shown in the inset. Figure adapted from <sup>87</sup>. (161)

**Figure 6.53** Evolution of the valence band photoelectron spectra of picene/Ag(110) as a function of the nominal film thickness, in a wider **(a)** and a narrower range **(b)**. The corresponding spectra of the clean Ag(110) surface are included for comparison. Figure adapted from <sup>87</sup>. (163)

**Figure 6.54** Topographic TM-AFM image of a multilayer picene film on Ag(110), after exposure to air.<sup>87</sup> The image shows an island-like multilayer film with a profile containing protrusions up to 10 nm deep. Within the islands, small grains are visible. The formation of these small grains could have been caused by the exposure to oxygen or air and do not necessarily exist in the pristine films. Figure adapted from <sup>87</sup>. (163)

**Figure 6.55** RHEED pattern of **(a)** the Ag(110) surface and **(b)** picene ML film on Ag(110), with the electron beam directed along the Ag[001] direction and of **(c)** a picene ML film on Ag(110), with the electron beam directed along the Ag[-110] direction. **(d)** Schematic representation of the picene ML unit cell with respect to the underlying Ag(110) lattice. Figure adapted from <sup>87</sup>. (164)

**Figure 6.56** Evolution of the valence band photoelectron spectra of the picene/Ag(110) multilayer film as a function of the oxygen exposure time and pressure, in a wider **(a)** and narrower **(b)** range. The corresponding spectra of the pristine picene film are included for comparison. Figure adapted from <sup>87</sup>. (166)

**Figure 6.57** Qualitative orbital interaction scheme for both orientations ( $\parallel$  and  $\perp$ ) of O<sub>2</sub> in benzene-O<sub>2</sub> complexes. To simplify the scheme, only one of the two singly occupied orbitals of O<sub>2</sub> is shown. Figure adapted from <sup>87</sup>. (168)

**Figure 6.58 (a)** Qualitative orbital interaction scheme for a picene-O<sub>2</sub> complex maximizing the interaction between oxygen and the HOMO orbital of picene. To simplify the scheme only one of the two singly occupied

orbitals of O<sub>2</sub> is shown. Quantum-chemically optimized structures determined for several complexes of oxygen with picene: (b) picene+O<sub>2</sub> ( $\parallel$  and  $\perp$  complexes); (c) picene + three O<sub>2</sub> ( $\parallel$  and  $\perp$  complexes, with the  $\perp$  complex featuring the three oxygens on the same side being the most stable structure); and (d) three  $\perp$  O<sub>2</sub> sandwiched between two picenes. Figure adapted from <sup>87</sup>. (170)

**Figure 6.59** Structural formula of the four molecules considered in this Section. Figure adapted from <sup>101</sup>. (173)

**Figure 6.60** Molecular dimers of **PNT** extracted from the crystal supercell (3x2x2) and considered in the simulation of hopping events. Distances from centers of mass are in Å. Figure adapted from <sup>101</sup>. (175)

**Figure 6.61** Molecular dimers of **DDQ** extracted from the crystal supercell (2x2x4) and considered in the simulation of hopping events. Distances from centers of mass are in Å. Figure adapted from <sup>101</sup>. (176)

**Figure 6.62** Molecular dimers of **TCQ** extracted from the crystal supercell (3x3x3) and considered in the simulation of hopping events. Distances from centers of mass are in Å. Figure adapted from <sup>101</sup>. (176)

**Figure 6.63** Molecular dimers of **TCN** extracted from the crystal supercell (3x3x3) and considered in the simulation of hopping events. Distances from centers of mass are in Å. Figure adapted from <sup>101</sup>. (177)

**Figure 6.64** B3LYP/6-31G\* computed (*eV*, dashed lines) *VEAs* at the equilibrium structures of (a) neutral (*VEA<sub>n</sub>*) and (b) negatively charged (*VEA<sub>a</sub>*) species along with their difference corresponding to  $\lambda_i$ . **DDQ** (left), **TCQ** (center), and **TCN** (right). Comparison with the work function of ITO and Al electrodes (*eV*).<sup>110a</sup> Solid lines below dashed lines represent schematically the stabilizing effect of polarization energy in the organic crystal.<sup>124</sup> Red arrows show the electron injection process from the electrode. Figure adapted from <sup>101</sup>. (179)

**Figure 6.65** B3LYP/6-31G\*\* HOMO energies (*eV*) of **PNT** at the equilibrium structure of (a) neutral and (b) positively charged species along with their difference corresponding to  $\lambda_i$ . Comparison with the work function of ITO and Al electrodes (*eV*).<sup>110a</sup> Red arrows show schematically the hole injection process from the electrode. Figure adapted from <sup>101</sup>. (179)

**Figure 6.66** Bond numbering (bold) and B3LYP/6-31G\* computed equilibrium bond lengths of **DDQ** (left), **TCQ** (center), and **TCN** (right) in the neutral (black) and negatively charged (red) state. Figure adapted from <sup>101</sup>. (181)

**Figure 6.67** Comparison between bond length changes in **DDQ** (blue), **TCN** (green) and **TCQ** (red) upon electron reduction (bond lengths of the charged molecule – bond lengths of the neutral molecule). Bond numbering is defined in Figure 6.66. Figure adapted from <sup>101</sup>. (181)

**Figure 6.68** CC bond numbering (bold) and B3LYP/6-31G\*\* computed equilibrium CC bond lengths of **PNT** in its neutral (black) and positively charged (red) state. Figure adapted from <sup>101</sup>. (182)

**Figure 6.69** Comparison between bond length changes in **PNT** upon electron oxidation (bond lengths of the charged molecule – bond lengths of the neutral molecule). Bond numbering is defined in Figure 6.68. Figure adapted from <sup>101</sup>. (182)

**Figure 6.70** Schematic macroscopic representation of the electric bistability of a memory device based on an  $n$ -type molecular semiconductor wafered between electrodes  $E1$  and  $E2$ . Device levels (top); schematic current-voltage ( $I$ - $V$ ) curve as a function of the voltage scan (bottom). The most relevant processes at the interface are indicated. (a) Initially the device is in its OFF state, and the transport gap is that of the pristine semiconductor. (b) As the applied voltage reaches the threshold value, the improved work function/ $VEA$  alignment favors electron injection. When charged species are at the interface, energy levels associated with the charged species have to be considered, further improving the electron injection. The system switches to the ON state. (c) As long as charge carriers are sustained in the device, the system stays in the ON state also for reverse applied voltages. (d) When the second (reverse) threshold voltage is reached, hole injection becomes competitive and neutralization of the charged species becomes significant, leading to a switch of the system back to the OFF state. (e) The transport gap reverts to that of the neutral species, and the system retains the OFF state. Figure adapted from <sup>101</sup>. (183)

**Figure 6.71** Pictorial representation of the largest FC (HR) parameters associated with vibrational frequencies of the neutral and charged species of (from the top) DDQ, TCQ, TCN, and PNT. From B3LYP/6-31G\*\* calculations. Figure adapted from <sup>101</sup>. (186)

**Figure 6.72** B3LYP/6-31G\*\* normal modes and vibrational frequencies associated with the largest HR parameters of PNT. Figure adapted from <sup>101</sup>. (187)

**Figure 6.73** UB3LYP/6-31G\*\* normal modes and vibrational frequencies associated with the largest HR parameters of PNT<sup>1+</sup>. Figure adapted from <sup>101</sup>. (187)

**Figure 6.74** B3LYP/6-31G\* normal modes and vibrational frequencies associated with the largest HR parameters of DDQ. Figure adapted from <sup>101</sup>. (188)

**Figure 6.75** UB3LYP/6-31G\* normal modes and vibrational frequencies associated with the largest HR parameters of DDQ<sup>1-</sup>. Figure adapted from <sup>101</sup>. (188)

**Figure 6.76** (U)B3LYP/6-31G\* normal modes and vibrational frequencies associated with the largest HR parameters of TCQ (a) and TCQ<sup>1-</sup> (b). Figure adapted from <sup>101</sup>. (189)

**Figure 6.77** B3LYP/6-31G\* normal modes and vibrational frequencies associated with the largest HR parameters of TCN. Figure adapted from <sup>101</sup>. (189)

**Figure 6.78** UB3LYP/6-31G\* normal modes and vibrational frequencies associated with the largest HR parameters of TCN<sup>1-</sup>. Figure adapted from <sup>101</sup>. (190)

**Figure 6.79** (left) The LUMOs of BQs involved in the calculations of  $V_{ij}$ , computed at semiempirical and B3LYP levels of theory. (right) The HOMO of PNT involved in the calculations of  $V_{ij}$ , computed at semiempirical and B3LYP levels of theory. Figure adapted from <sup>101</sup>. (190)

**Figure 6.80** Computed charge mobilities of DDQ (top, left), TCQ (top, right), and TCN (bottom) as a function of the temperature. Figure adapted from <sup>101</sup>. (191)

**Figure 6.81** Thermal disorder effects on the distribution of the largest computed charge transfer integrals of DDQ (left) evaluated at two temperatures (100 and 300 K) and Fourier transforms of the autocorrelation function of the transfer integrals computed at 300 K (right) underscoring the low frequency active modes responsible for the modulation of the charge transfer integrals. Figure adapted from <sup>101</sup>. (193)

**Figure 6.82** Fluctuations of the computed charge transfer integrals of DDQ (due to thermal motions,  $T = 300$  K) as a function of the simulation time (overall 90 ps after equilibration). Integrals corresponding to dimers A, B and C of DDQ are shown. Figure adapted from <sup>101</sup>. (193)

**Figure 6.83** Structural formula of the three fluoroalkylated PBIs. Figure adapted from <sup>42</sup>. (196)

**Figure 6.84** Structural formula of the tetrachloro-substituted (**1b**, **1d**, and **2d**), and octachloro-substituted (**8Cl**) PBI derivatives. Figure adapted from <sup>43</sup>. (197)

**Figure 6.85** Structural formula of the two model PBI derivatives. Figure adapted from <sup>42</sup>. (201)

**Figure 6.86** The frontier molecular orbitals of **1a** (left) and **1a-model** (right). The LUMO orbitals were involved in the calculations of  $V_{ij}$  charge transfer integrals, computed at B3LYP/3-21G level of theory. Figure adapted from <sup>42</sup>. (201)

**Figure 6.87** The frontier molecular orbitals of **2b** (left), **2c** (middle), and **2b-2c-model** (right). The LUMO orbitals were involved in the calculations of  $V_{ij}$ , computed at B3LYP/3-21G level of theory. Figure adapted from <sup>42</sup>. (202)

**Figure 6.88** The vibrational frequencies contributions to the computed  $\lambda_i^{HR}$  of **1a** (top) and **1a-model** (bottom) neutral (left) and charged (right) species. From B3LYP/3-21G calculations. It is seen that the contributions are very similar. Figure adapted from <sup>42</sup>. (203)

**Figure 6.89** The vibrational frequencies contributions to the computed  $\lambda_i^{HR}$  of **2b** (top), **2c** (middle), and **2b-2c-model** (bottom) neutral (left) and charged (right) species. From B3LYP/3-21G calculations. It is seen that the contributions are very similar. Figure adapted from <sup>42</sup>. (203)

**Figure 6.90** Molecular crystals of **1a**, **2b**, and **2c** side and top views showing the presence of columns of  $\pi$ -stacked PBI molecules. The white spheres centered on each molecule represent the centers of mass; H and F atoms are omitted. Figure adapted from <sup>42</sup>. (204)

**Figure 6.91** Crystal of **1a**. (top) The possible intra- (magenta molecules) and *intercolumn* (green and blue molecules) paths taking as reference the red central molecule. The capital letters indicate the jumps that are active because of non-negligible charge transfer integrals. (bottom) Schematic indication of (left) the *intercolumn* paths C and D and (right) the *intracolumn* path A. The sequence of red arrows underscores that the jumps along the column are identical. The white spheres centered on each molecule represent the centers of mass, and hydrogen and fluorine atoms are omitted. Figure adapted from <sup>42</sup>. (205)

**Figure 6.92** Crystal of **2b**. (top) The possible intra- (magenta molecules) and *intercolumn* (green and blue molecules) paths taking as reference the red central molecule. The capital letters indicate the jumps that are active because of non-negligible charge transfer integrals. (bottom) Schematic indication of (left) the *intercolumn* paths C and D and (right) the *intracolumn* paths A (red arrows) and B (blue arrows). The sequence of red and blue arrows underscores that two different jumps (fast and slow) alternate along the column. The absence of the counterpart of jumps C and D in opposite directions, starting from the same red molecule, underscores the asymmetry that also characterizes *intercolumnar* jumps. The two different orientations of the rectangles reflect the presence of two different molecular sites in the crystal. Figure adapted from <sup>42</sup>. (206)

**Figure 6.93** Crystal of **2c**. (top) The possible intra- (magenta molecules) and *intercolumn* (green and blue molecules) paths taking as reference the red central molecule. The capital letters indicate the jumps that are active because of non-negligible charge transfer integrals. (bottom) Schematic indication of (left) the *intercolumn* paths C, D, and E and (right) the *intracolumn* paths A (red arrows) and B (blue arrows). The sequence of red and blue arrows underscores that two different jumps alternate along the column. The counterpart of jump D, in opposite direction starting from the same red molecule, is path E. The counterpart of jump C, in opposite direction starting from the same red molecule, is still path C since the molecular sites involved in the jump are of the same type. The white spheres centered on each molecule represent the centers of mass, and hydrogen and fluorine atoms are omitted. The two different orientations of the rectangles reflect the presence of two different molecular sites in the crystal. Figure adapted from <sup>42</sup>. (207)

**Figure 6.94** Dependence of the charge transfer integral  $V_{ij}$  associated to the A jump of **1a**, as a function of the sliding along the short axis for selected values of the sliding along the long molecular axis, keeping the intermolecular distance fixed to the value observed in the crystal. The red curve corresponds to translation along the short axis, starting from a face to face dimer. The blue curve corresponds to translation along the short axis starting from the dimer configuration in the crystal of **1a**, which is represented by the black square in the figure. Figure adapted from <sup>42</sup>. (208)

**Figure 6.95** (top) First 1000 steps of a KMC trajectory of a charge carrier propagating along a crystal of **2b** (red) and **2c** (green). The trajectory of **2b** shows frequent oscillations (some of which are enclosed in black rectangles) induced by the presence of markedly alternating fast and slow paths ABABAB along the column. These oscillations do not advance the charge carrier and induce a "dimer-trapping retardation effect". The charge is trapped several times and keeps oscillating back and forth in a dimer before it finds its way along the column. The retardation effect is less marked in **2c** because of the similar probability associated with paths A and B. (bottom) For comparison, the first 1000 steps of a carrier propagating in **1a** (blue), for which a single path A is repeated along the column, show no evidence of a retardation effect. Figure adapted from <sup>42</sup>. (212)

**Figure 6.96** (left) Representation of a number of KMC trajectories (in the  $x$ - $y$  plane) computed for system **2b** neglecting *intercolumn* jumps in the KMC simulations: The figure shows a perfectly monodimensional conduction of the charge along the  $x$  intra-column direction. (right) *Intercolumn* jumps are now included in the KMC simulations: The Figure shows still an approximately monodimensional conduction of the charge along the  $x$  intra-column direction. Figure adapted from <sup>42</sup>. (213)

**Figure 6.97** (left) Representation of a number of KMC trajectories (in the  $x$ - $y$  plane) computed for system **2c** neglecting *intercolumn* jumps in the KMC simulations: The figure shows a perfectly monodimensional conduction of the charge along the  $x$  intra-column direction. (right) *Intercolumn* jumps are now included in the KMC simulations: The Figure shows still an approximately monodimensional conduction of the charge along the  $x$  intra-column direction. Figure adapted from <sup>42</sup>. (213)

**Figure 6.98** (left) Representation of a number of KMC trajectories (in the  $x$ - $y$  plane) computed for system **1a** including *intercolumn* jumps and the thermalized value for the intra-column jump  $A$ : The figure shows an almost bidimensional conduction of the charge along the  $x$ - $y$  directions. (right) Herein the crystal value for intra-column probabilities are used: The figure shows an approximately monodimensional conduction along the inter-column jump direction. Figure adapted from <sup>42</sup>. (214)

**Figure 6.99** The frontier molecular orbitals of **8Cl**, **2d**, **1b**, and **1d**. The LUMO orbitals were involved in the calculations of  $V_{ij}$  electronic coupling integrals, computed at B3LYP/3-21G\* level of theory. Figure adapted from <sup>43</sup>. (216)

**Figure 6.100** The vibrational frequencies contributions to the computed  $\lambda_i^{HR}$  of: (left) **8Cl** neutral (top) and anionic (bottom) species; (right) **2d** neutral (top) and anionic (bottom) species. From B3LYP/3-21G\* calculations. It is seen that the contributions are very similar for the neutral and charged states. Figure adapted from <sup>43</sup>. (217)

**Figure 6.101** The vibrational frequencies contributions to the computed  $\lambda_i^{HR}$  of: **1d** neutral (top) and anionic (bottom) species. From B3LYP/3-21G\* calculations. It is seen that the contributions are very similar for the neutral and charged states. Figure adapted from <sup>43</sup>. (218)

**Figure 6.102** B3LYP/3-21G\* computed bond length changes upon charging (anion-neutral) for **8Cl** (blue), **2d** (black), **1b** (red), and **1d** (green). Bond numbering as depicted in the inset. Figure adapted from <sup>43</sup>. (219)

**Figure 6.103** Compounds **2d** (left) and **8Cl** (right). (top) Schematic representation of geometry change upon doping: (magenta) bonds whose length increases upon doping, (cyan) bonds whose length decreases upon doping. (bottom) Vibrational modes (neutral species) contributing most to the intramolecular reorganization energy. It can be seen that nuclear motions of the selected vibrations overlap with the computed geometry change. Figure adapted from <sup>43</sup>. (219)

**Figure 6.104** Molecular crystals of **8Cl**, **2d**, **1b**, and **1d** side and top views showing the presence of columns (**2d**, **1b**, and **1d**) or walls (**8Cl**) of  $\pi$ -stacked PBI molecules. From top to bottom: **8Cl** belongs to the orthorhombic  $Pbcn$  space group; **2d** and **1b** belong to the triclinic  $P-1$  space group; **1d** belongs to the monoclinic  $C2$  space group. Figure adapted from <sup>43</sup>. (220)

**Figure 6.105** PBI derivative **1a** comparison between: (red) radial distribution function of intermolecular distances between centers of mass, computed from MD simulations at 300 K; (blue) center of mass distances computed for the crystal structures. Figure adapted from <sup>43</sup>. (221)

**Figure 6.106** PBI derivatives **2d** (left) and **8Cl** (right) comparison between: (red) radial distribution function of intermolecular distances between centers of mass, computed from MD simulations at 300 K; (blue) center of mass distances computed for the crystal structures. Figure adapted from <sup>43</sup>. (221)

**Figure 6.107** PBI derivatives **1b** (left) and **1d** (right): center of mass distances computed at the crystal structure. Figure adapted from <sup>43</sup>. (222)

**Figure 6.108** Thermal disorder effects (300 K) on the distribution of the *intracolumn* electronic coupling associated with path A of **1a**. (top, left) Gaussian fitting of the B3LYP/3-21G\* computed dispersion of electronic couplings. (top, right) Dispersion of computed values as a function of simulation time. (bottom) Fourier transform of the autocorrelation function of the computed electronic couplings. Figure adapted from <sup>43</sup>. (224)

**Figure 6.109** Representative lattice vibrations (top,  $\omega=23\text{ cm}^{-1}$ ; bottom,  $\omega=31\text{ cm}^{-1}$ ) governing the modulation of *intracolumn* charge transfer A of **1a**. Figure adapted from <sup>43</sup>. (225)

**Figure 6.110** Representation of a number of KMC trajectories (in the *a-b* crystallographic plane) computed for system **1a**. The Brownian motion of the charge carrier shows an approximately bidimensional conduction in the *a-b* plane corresponding to sequences of *intracolumn* and *intercolumn* jumps between PBI units. The direction of path C is also indicated. Figure adapted from <sup>43</sup>. (226)

**Figure 6.111** Crystal of **2d**: (top, left) The possible *intracolumn* (blue and red molecules) and *intercolumn* (cyan, yellow, orange, and magenta molecules) paths taking as reference the green central molecule. (top, right) The jumps included in KMC simulations owing to non-negligible charge transfer integrals. (bottom, left) Top view of the *intracolumn* and *intercolumn* charge paths and (bottom, right) the *intracolumn* paths A (red arrows) and B (blue arrows). The sequence of red and blue arrows underscores that two different jumps (fast and slow) alternate along the *intracolumn* path. Figure adapted from <sup>43</sup>. (227)

**Figure 6.112** Representation (in the *x-y* Cartesian or *a-b* crystallographic plane) of 50 randomly selected KMC trajectories computed for system **2d**. The Brownian motion of the charge carrier shows an approximately bidimensional conduction in the *a-b* plane corresponding to sequences of *intracolumn* and *intercolumn* jumps between PBI units. Figure adapted from <sup>43</sup>. (229)

**Figure 6.113** Displacement along the *a* crystallographic axis (corresponding to the *intracolumn* charge transport channel) of a charge carrier propagating along a crystal of **2d**. The first 1000 steps of a KMC trajectory are shown. (top) KMC simulation including only *intracolumn* jumps A and B. (bottom) KMC simulation including *intracolumn* jumps A and B along with the *intercolumn* jump C. The KMC trajectory shows less evidence of trapping along *a*. Figure adapted from <sup>43</sup>. (229)

**Figure 6.114** Thermal disorder effects (300 K) on the distribution of the *intracolumn* electronic couplings associated with jump A and B of system **2d**. (top, left) Gaussian fitting of the B3LYP/3-21G\* computed dispersion for integral A (red) and B (blue). (top, right) Dispersion of computed values as a function of simulation time. (bottom) Fourier transform of the autocorrelation function of computed electronic couplings. Figure adapted from <sup>43</sup>. (230)

**Figure 6.115** Representative lattice vibrations (top,  $\omega=24\text{ cm}^{-1}$ ; bottom,  $\omega=24\text{ cm}^{-1}$ ) governing the modulation of *intracolumn* electronic couplings A and B of **2d**. Figure adapted from <sup>43</sup>. (231)

**Figure 6.116** Crystal of **1b**: (top) The possible *intracolumn* (blue and red molecules) and *intercolumn* (yellow molecule) paths taking as reference the green central molecule. The capital letters indicate the jumps that are active owing to non negligible charge transfer integrals. (bottom, left) Top view of the *intracolumn* and *intercolumn* charge paths and, (bottom, right) the *intracolumn* paths A (blue arrows) and B (red arrows). The sequence of red and blue arrows underscores that two different jumps alternate along the column owing to the presence of two different molecular sites (enantiomers) in the crystal. Figure adapted from <sup>43</sup>. (232)

**Figure 6.117** Crystal of **1d**: Only *intracolumn* charge jump A is active owing to non negligible charge transfer integral. The sequence of black arrows underscores that only one type of jump determines the charge propagation along the column owing to the presence of one molecular site (enantiomer) in the crystal. Figure adapted from <sup>43</sup>. (233)

**Figure 6.118** Crystal of **8Cl**: (top, left) the possible *intra*wall (red and cyan molecules) and *inter*wall (blue, yellow, and purple molecules) paths (labeled with capital letters) taking as reference the green central molecule. (top, right) Paths included in KMC simulations owing to non-negligible electronic couplings. (bottom, right) Top view of the *intra*wall and *inter*wall charge paths and (bottom, right) the *intra*wall path B. Figure adapted from <sup>43</sup>. (233)

**Figure 6.119** Thermal disorder effects (300 K) on the distribution of the *intra*wall electronic coupling associated with the charge path B of **8Cl**. (top, left) Gaussian fitting of the B3LYP/3-21G\* computed dispersion of the electronic couplings. (top, right) Dispersion of computed values as a function of simulation time. (bottom) Fourier transform of the autocorrelation function of the electronic couplings. Figure adapted from <sup>43</sup>. (235)

**Figure 6.120** Representative lattice vibrations of **8Cl** modulating the *intra*wall electronic coupling for path B. The frequencies of the lattice vibrations are  $19\text{ cm}^{-1}$  (top, left),  $29\text{ cm}^{-1}$  (bottom, left),  $42\text{ cm}^{-1}$  (top, right) and  $85\text{ cm}^{-1}$  (bottom, right). Figure adapted from <sup>43</sup>. (236)

## LIST OF SYMBOLS AND ABBREVIATIONS

$V_{ij}$	electronic coupling integral
$\lambda_i$	intramolecular reorganization energy
$k_{eT}$	charge transfer rate constant
$\mu$	charge mobility
$S_0$	singlet ground state
$S_n$	$n$ -th singlet excited state
$T_n$	$n$ -th triplet excited state
1D	one-dimensional
2D	two-dimensional
8Cl	octa-chlorinated perylene tetracarboxylic bisimide
AEA	adiabatic electron affinity
AIP	adiabatic ionization potential
AP	adiabatic potential
BNQ	bis-N-annulated quaterrylene
BQ	benzoquinone
BS	broken symmetry
CASPT2	complete active space with second-order perturbation theory
CASSCF	complete active space self-consistent field
CD	circular dichroism
CI	configuration interaction
CIS	single configuration interaction

CISD	single and double configuration interaction
CNDO	complete neglect of differential overlap
CS	closed-shell
CSF	configuration state function
CT	charge transport
CV	cyclic voltammogram
DDQ	2,3-dichloro-5,6-dicyano-1,4-benzoquinone
DFT	density functional theory
EA	electronic affinity
ES	Einstein-Smoluchowski
ESD	energy-splitting-in-dimer
ET	electron-transport
FC	Franck-Condon
FF	force field
Full CI	full configuration interaction
GCA	generalized corrected approximation
GGA	generalized gradient approximation
GNR	graphene nanoribbon
GTO	Gaussian-type orbital
HF	Hartree-Fock
HOMO	highest occupied molecular orbital
HR	Huang-Rhys
HT	hole-transport

INDO	intermediate neglect of differential overlap
IP	ionization potential
IR	infrared
ITO	indium tin oxide
IV-CT	intervalence charge transfer
KMC	kinetic Monte Carlo
KS	Kohn-Sham
KT	Koopmans' theorem
KT-ESD	Koopman's theorem based energy-splitting-in-dimer
LCAO	linear combination of atomic orbitals
LDA	local density approximation
LJ	Lennard-Jones
LSDA	local spin-density approximation
LUMO	lowest unoccupied molecular orbital
MC	Monte Carlo
MCSCF	multi-configurational self-consistent field
MD	molecular dynamics
ML	monolayer
MLJ	Marcus-Levich-Jortner
MM	molecular mechanics
MP2	second-order Møller-Plesset perturbation
MPPT	Møller-Plesset perturbation theory
MSD	mean square displacement

MV	mixed valence
NDDO	neglect of diatomic differential overlap
NDI	naphtalene tetracarboxylic diimide
NIR	near-infrared
NP	N-annulated perylene
NVT	canonical ensemble
OFET	organic field-effect transistor
OLED	organic light-emitting diode
OPV	organic photovoltaic device
OSC	organic semiconductors
OTFT	organic thin film transistor
OTS	n-octadecyl-triethoxy-silane
PAH	polycyclic aromatic hydrocarbon
PBC	periodic boundary conditions
PBI	perylene tetracarboxylic bisimide
PCM	polarizable continuum model
PES	potential energy surface
PNT	pentacene
PQ	6,13-pentacenequinone
PR-TRMC	pulse radiolysis-time-resolved microwave conductivity
QOT	quinoidal oligothiophene
RHEED	reflection high-energy electron diffraction
RHF	restricted Hartree-Fock

SA	state average
SCF	self-consistent field
SIE	self-interaction energy
SOMO	singly occupied molecular orbital
SS-SR	single state - single reference
STO	Slater-type orbital
TCN	2,3,5,6-tetracyano-benzoquinone
TCQ	2,3,5,6-tetrachloro-benzoquinone
TDDFT	time-dependent density functional theory
TDI	tetracene tetracarboxylic diimide
TM-AFM	tapping-mode atomic force microscopy
TNH	tri-N-annulated hexarylene
TOF	time-of-flight
UHF	unrestricted Hartree-Fock
UPS	ultraviolet photoelectron spectroscopy
UV	ultraviolet
VEA	vertical electron affinity
VIP	vertical ionization potential
Vis	visible
ZDO	zero differential overlap

## SUMMARY

From the perspective of a new-generation opto-electronic technology based on organic semiconductors, a major objective is to achieve a deep and detailed knowledge of the structure-property relationships, in order to optimize the electronic, optical, and charge transport properties by tuning the chemical-physical characteristics of the compounds. The purpose of this dissertation is to contribute to such understanding, through suitable theoretical and computational studies. Precisely, the structural, electronic, optical, and charge transport characteristics of several promising organic materials recently synthesized are investigated by means of an integrated approach encompassing quantum-chemical calculations, molecular dynamics and kinetic Monte Carlo simulations. Particular care is addressed to the rationalization of optical and charge transport properties in terms of both intra- and intermolecular features. Moreover, a considerable part of this project involves the development of a home-made set of procedures and parts of software code required to assist the modeling of charge transport properties in the framework of the non-adiabatic hopping mechanism applied to organic crystalline materials.

As a first part of my investigations, I mainly discuss the optical, electronic, and structural properties of several core-extended rylene derivatives, which can be regarded to as model compounds for graphene nanoribbons. Two families have been studied, consisting in bay-linked perylene bisimide oligomers and N-annulated rylenes. In particular, it is shown that the different connectivity and derivatizations, such as the inclusion of condensed five-membered aromatic heterocycles, modulate opto-electronic properties through the modification of the  $\pi$ -conjugation of the compounds.

Beside rylene derivatives, my studies also concerned electronic and spectroscopic properties of tetracene diimides, quinoidal oligothiophenes, and oxygen doped picene.

As an example of device application, I studied the structural characteristics governing the efficiency of resistive molecular memories based on a derivative of benzoquinone.

Finally, as a second part of my investigations, I concentrate on the charge transport properties of perylene bisimides derivatives. Precisely, a comprehensive study of the structural and thermal effects on the charge transport of several core-twisted chlorinated and fluoro-alkylated perylene bisimide *n*-type semiconductors is presented.

## CHAPTER 1 - INTRODUCTION

Since the discovery of highly conducting polyacetylene in 1977,<sup>1</sup>  $\pi$ -conjugated systems have attracted much attention as futuristic materials for the development and production of the next generation of the so-called organic electronics and opto-electronics.<sup>2-4</sup> Indeed, although organic semiconductors may exhibit comparable or lower electrical performance than traditional inorganic materials such as amorphous or crystalline silicon, they offer unique attractions like low-temperature processing on flexible substrates, large-area coverage, tunable opto-electronic properties, low-cost, high-speed fabrication, and facile synthetic modification.<sup>5</sup> Such features should enable next-generation opto-electronic devices such as low-power consumption flexible displays, inexpensive plastic radio frequency identification tags, volatile and non-volatile memories, smart cards, biomedical systems, electronic skin, printable sensors, electronic paper, printable organic integrated circuits, and plastic solar cells, to name a few.<sup>6-9</sup> The solubility, stability, and rheological properties of organic materials are compatible with high-throughput printing, patterning, and spin-coating of active materials over large areas under ambient conditions, in marked contrast to silicon microelectronics fabrication which requires highly capital-intensive lithographic techniques.<sup>10</sup> In addition, organic semiconductors can be easily modified via chemical synthesis, affording new materials with tunable chemical, optical, and electrical properties.

Organic semiconductor research has traditionally been closely related to applications and is unique in the synergy between device development and fundamental science, which should eventually lead to organic-based devices with pre-designed properties.<sup>11</sup> Unfortunately, such a molecular engineering is still far from a sound and comprehensive mastery which could deliver a design completely exempt from trial-and-error connotation. Moreover, though the ease of chemical tuning allows efficient screening of structural series to define the required criteria for any particular property or application,<sup>4</sup> lack of basic understanding of structure-property relationships in organic solids results in a knowledge gap that hampers rational efforts to design organic semiconductors with further enhancements in optical and electrical performance.<sup>11</sup>

The most challenging issues introduced by organic-based technology have both empirical and theoretical nature. On the one hand, after three decades of intense and enthusiastic research, the perception might be that some insurmountable physical limitations prevent

organic materials from bettering traditional inorganic semiconductors, for instance, in terms of charge mobility within a transistor or energy conversion efficiency of a photovoltaic cell.<sup>12</sup> Nonetheless, it is also envisaged that the performance of organic devices could be sensibly enhanced under certain conditions, such as in ordered, self-assembled structures<sup>13</sup> and in materials featuring an elevated extent of functional interfaces between the active layers.<sup>14</sup> On the other hand, this research field still suffers from the lack of basic knowledge in fundamental mechanisms of the phenomena occurring within the molecular and polymer materials. In particular, although several theoretical models have been formulated to account for the charge transport mechanisms in organic semiconductors, they often provide only a partial description, whose validity needs to be thoroughly ascertained.<sup>15</sup> Therefore, the rationalization of experimental observations in terms of molecular properties often relies on integrated computational studies which aim toward both the realistic simulation of the investigated phenomena and the comprehension of how macroscopic behaviors correlate with intra- and intermolecular features.

At present, several theoretical and computational studies have sensibly contributed to shed light on the factors governing the performance of different organic based devices and on the structural and electronic properties of their constituent molecular systems, demonstrating the fundamental role of modeling for both the rationalization of experimentally observed behaviors and the design of new organic semiconductors with suitable properties.<sup>16</sup>

From this perspective, the purpose of this dissertation is to contribute, through theoretical and computational studies, to the understanding of the structural-property relationships governing the electronic, optical, and charge transport properties experimentally observed in organic molecular semiconductors. To this end, the structural, electronic, optical, and charge transport characteristics of several promising organic materials recently synthesized have been investigated by means of an integrated approach encompassing quantum-chemical calculations, molecular dynamics and kinetic Monte Carlo simulations. More specifically, the charge transport model employed in this work relies on the non-adiabatic hopping model, and is implemented with the Marcus-Levich-Jortner formalism, for the charge transfer within a molecular crystal. A considerable part of this project involved the development of a home-made set of procedures and parts of software code (referred to as the Pandora Suite) that implement the integrated computational approach required to model charge transport in molecular crystals.

- [1] Chiang, C. K.; Fincher, C. R.; Park, Y. W.; Heeger, A. J.; Shirakawa, H.; Louis, E. J.; Gau, S. C.; MacDiarmid, A. G. *Phys. Rev. Lett.* **1977**, *39*, 1098.
- [2] Shirota, Y.; Kageyama, H. *Chem. Rev.* **2007**, *107*, 953-1010.
- [3] Wang, C.; Dong, H.; Hu, W.; Liu, Y.; Zhu, D. *Chem. Rev.* DOI: 10.1021/cr100380z.
- [4] Usta, H.; Facchetti, A.; Marks, T. J. *Acc. Chem. Res.* **2011**, *44*, 501-510.
- [5] Bao, Z. *Adv. Mater.* **2000**, *12*, 227-230.
- [6] (a) Forrest, S. R. *Nature* **2004**, *428*, 911-918. (b) de Ruiter, G.; Tartakovsky, E.; Oded, N.; van der Boom, M. *Angew. Chem., Int. Ed.* **2010**, *49*, 4780.
- [7] (a) Scott, J. C.; Bozano, L. D. *Adv. Mater.* **2007**, *19*, 1452-1463. (b) Welnic, W.; Wuttig, M. *Mater. Today* **2008**, *11*, 20-27. (c) Ling, Q.-D.; Liaw, D.-J.; Zhu, C.; Chan, D. S.-H.; Kang, E.-T.; Neoh, K.-G. *Prog. Polym. Sci.* **2008**, *33*, 917-978.
- [8] (a) Kim, D.-H.; Rogers, J. A. *Adv. Mater.* **2008**, *20*, 4887. (b) Ghezzi, D.; Antognazza, M. R.; Dal Maschio, M.; Lanzarini, E.; Benfenati, F.; Lanzani, G. *Nature Communications* **2011**, *2*, 166. (c) Lipomi, D. J.; Vosgueritchian, M.; Tee, B. C.-K.; Hellstrom, S. L.; Lee, J. A.; Fox, C. H.; Bao, Z. *Nature Nanotechnology* **2011**, *6*, 788-792. (d) Owens, R. M.; Malliaras, G. G. *MRS Bulletin* **2010**, *35*, 453.
- [9] (a) Nelson, T.; Young, T.; Liu, J.; Mishra, S.; Belot, J.; Balliet, C.; Javier, A.; Kowalewski, T.; McCullough, R. *Adv. Mater.* **2010**, *22*, 4617. (b) Drury, C. J.; Mutsaers, C. M. J.; Hart, C. M.; Matters, M.; de Leeuw, D. M. *Appl. Phys. Lett.* **1998**, *73*, 108. (c) Crone, B.; Dodabalapur, A.; Gelperin, A.; Torsi, L.; Katz, H. E.; Lovinger, A. J.; Bao, Z. *Appl. Phys. Lett.* **2001**, *78*, 2229.
- [10] Sirringhaus, H.; Kawase, T.; Friend, R. H.; Shimoda, T.; Inbasekaran, M.; Wu, W.; Woo, E. P. *Science* **2000**, *290*, 2123-2126.
- [11] Burtman, V.; Alexander, Z.; Pakoulev, A. V. *Int. J. Mol. Sci.* **2011**, *12*, 173-225.
- [12] (a) Borchert, H. *Energy Environ. Sci.* **2010**, *3*, 1682-1694. (b) Glatthaar, M.; Riede, M.; Keegan, N.; Sylvester-Hvid, K.; Zimmermann, B.; Niggemann, M.; Hinsch, A.; Gombert, A. *Solar Energy Mater. Solar Cells* **2007**, *91*, 390-393. (c) Forrest, S. R. *MRS Bulletin* **2005**, *30*, 28-32. (d) Nayak, P. K.; Bisquert, J.; Cahen, D. *Adv. Mater.* **2011**, *23*, 2870-2876.

[13] (a) Virkar, A. A.; Mannsfeld, S.; Bao, Z.; Stingelin, N. *Adv. Mater.* **2010**, *22*, 3857. (b) Zhang, H.; Hoeben, F. J. M.; Pouderoijen, M. J.; Schenning A. P. H. L.; Meijer, E. W.; Schryver, F. C.; De Feyter, S. *Chem.-Eur. J.* **2006**, *12*, 9046-9055. (c) Vijayakumar, C.; Praveen, V. K.; Ajayaghosh, A. *Adv. Mater.* **2009**, *21*, 2059-2063. (d) Hirai, Y.; Babu, S. S.; Praveen, V. K.; Yasuda, T.; Ajayaghosh, A.; Kato, T. *Adv. Mater.* **2009**, *21*, 4029. (e) Lee, O. P.; Yiu, A. T.; Beaujuge, P. M.; Woo, C. H.; Holcombe, T. W.; Millstone, J. E.; Douglas, J. D.; Chen, M. S.; Frechet, J. M. J. *Adv. Mater.* **2011**, *23*, 5359. (f) Murphy, A. R.; Chang, P. C.; VanDyke, P.; Liu, J. S.; Frechet, J. M. J.; Subramanian, V.; DeLongchamp, D. M.; Sambasivan, S.; Fischer, D. A.; Lin, E. K. *Chem. Mater.* **2005**, *17*, 6033-6041.

[14] (a) Chang, C.-Y.; Cheng, Y.-J.; Hung, S.-H.; Wu, J.-S.; Kao, W. S.; Lee, C.-H.; Hsu, C.-S. *Adv. Mater.* **2012**, *24*, 549. (b) Reid, O. G.; Malik, J. A. N.; Latini, G.; Dayal, S.; Kopidakis, N.; Silva, C.; Stingelin, N.; Rumbles, G. *J. Polym. Sci. Part B* **2012**, *50*, 27-37. (c) Keivanidis, P. E.; Howard, I. A.; Friend, R. H. *Adv. Funct. Mater.* **2008**, *18*, 3189-3202.

[15] Troisi, A. *Chem. Soc. Rev.* **2011**, *40*, 2347-2358.

[16] (a) Kippelen, B.; Brédas, J.-L. *Energy Environ. Sci.* **2009**, *2*, 251. (b) Brédas, J.-L.; Norton, J.; Cornil, J.; Coropceanu, V. *Acc. Chem. Res.* **2009**, *42*, 1691. (c) Risko, C.; McGehee, M. D.; Brédas, J.-L. *Chem. Sci.* **2011**, *2*, 1200. (d) Beljonne, D.; Cornil, J.; Muccioli, L.; Zannoni, C.; Brédas, J.-L.; Castet, F. *Chem. Mat.* **2011**, *23*, 591. (e) Yi, Y.; Coropceanu, V.; Brédas, J.-L. *J. Mater. Chem.* **2011**, *21*, 1479-1486. (f) Martsinovich, N.; Troisi, A. *Energy Environ. Sci.* **2011**, *4*, 4473-4495. (g) Coropceanu, V.; Cornil, J.; da Silva, D. A.; Olivier, Y.; Silbey, R.; Brédas, J.-L. *Chem. Rev.* **2007**, *107*, 926-952. (h) Brédas, J.-L.; Beljonne, D.; Coropceanu, V.; Cornil, J. *Chem. Rev.* **2004**, *104*, 4971. (i) Brédas, J.-L.; Calbert, J. P.; da Silva, D. A.; Cornil, J. *Proc. Natl. Acad. Sci. USA* **2002**, *99*, 5804. (j) Hales, J. M.; Matichak, J.; Barlow, S.; Ohira, S.; Kada, Y.; Brédas, J.-L.; Perry, J. W.; Marder, S. R. *Science* **2010**, *327*, 1485-1488. (k) Appleton, A. L.; Brombosz, S. M.; Barlow, S.; Sears, J. S.; Brédas, J.-L.; Marder, S. R.; Bunz, U. H. F. *Nature Communications* **2010**, *1*, DOI: 10.1038/ncomms1088. (l) Salman, S.; Ruiz Delgado, M. C.; Coropceanu, V.; Brédas, J.-L. *Chem. Mater.* **2009**, *21*, 3593-3601. (m) Vehoff, T.; Baumeier, B.; Troisi, A.; Andrienko, D. *J. Am. Chem. Soc.* **2010**, *132*, 11702-11708. (n) Cheung, D. L.; McMahon, D. P.; Troisi, A. *J. Am. Chem. Soc.* **2009**, *131*, 11179-11186. (o) Troisi, A.; Cheung, D. L.; Andrienko, D. *Phys. Rev. Lett.* **2009**, *102*, 116602.

## CHAPTER 2 - ORGANIC TECHNOLOGY

In this Chapter, an overview of the fundamental principles of organic based technology is given. First of all, organic semiconductors are introduced through a brief overview of the fundamental characteristics of molecular and polymer semiconductors. Second, the principles and operation processes of the most important electronic and opto-electronic devices are shown, along with the requirements that the organic semiconductor to be employed as the functional material of the device has to fulfill. From this perspective, several families of molecular and polymer semiconductors are reviewed, focusing on the main contributions they can provide for a particular application. Finally, the most intriguing property of organic semiconductors - the ability to be easily tuned at both molecular and electronic structures is discussed, and the intramolecular and intermolecular structure-property relationships that will be deepened within this dissertation are briefly presented.

### 2.1 Organic Semiconductors

Organic semiconductors (OSCs) are  $\pi$ -conjugated molecules or polymer compounds. Precisely, organic charge-transporting materials include both small molecules, that is, molecular materials, and polymers, the latter of which are mainly classified into  $\pi$ -conjugated polymers and non-conjugated polymers containing pendant  $\pi$ -electron systems.<sup>1</sup> Usually, vacuum deposition and spin-coating methods are used for small molecules and polymers, respectively, for the preparation of thin films; recently, printing-like techniques have also been developed for both.<sup>2-4</sup>

OSCs can be classified as hole- or electron-transport (HT or ET) materials according to whether the majority charge carriers, under a given set of conditions, arise from removal of electrons from the manifold of filled  $\pi$  molecular orbitals or from the addition of electrons to empty  $\pi$  orbitals, respectively. Indeed, hole-transporting materials are those that accept hole carriers with a positive charge and transport them. Likewise, electron-transporting materials are those that accept electron carriers with a negative charge and transport them. For this

reason, they are usually referred to as *p*-type (positive charges, HT) and *n*-type (negative charges, ET) organic semiconductors. Materials which have low ionization potentials together with low electron affinities usually function as *p*-type OSCs, whereas materials which have high electron affinities together with high ionization potentials usually function as *n*-type OSCs. In other words, OSCs with electron-donating and electron-accepting properties usually serve as HT and ET materials, respectively. An additional class of materials consists in OSCs exhibiting ambipolar character, namely, materials that can transport both holes and electrons.

Organic HT and ET materials differ from classical inorganic *p*-type and *n*-type semiconductors in many aspects. First, OSCs are generally undoped, so that very few charge carriers are typically present except under an applied field, in which case carriers can be injected from electrodes, from other proximate organic materials, or are generated via photoexcitation. Doping processes include also electrochemical redox reactions in solution and chemical reactions through suitable oxidant reactants like Br<sub>2</sub>, SbF<sub>5</sub>, WF<sub>6</sub>, and H<sub>2</sub>SO<sub>4</sub>, or reductant reactants like alkali metals, but usually to such doping methods the direct charge injection from electrodes is preferred, considering that in most devices the architecture features the functional organic material layers sandwiched between cathode and anode. Hence, another difference with respect to inorganic semiconductors is that no substitutional doping is envisaged.

The mechanisms of charge transport in OSCs are different with respect to inorganic semiconductors as well. While these latter form energy band structures, namely, valence and conduction bands where holes and electrons are fully delocalized, respectively, driven by strong electronic couplings between the constituting moieties, organic materials, in which only weak intermolecular interactions such as van der Waals forces are operative, in most cases do not form energy bands. Thus, a charge carrier for organic materials mainly corresponds to a localized charge associated with a structural distortion; such so-called "polaron" consists in the cation or anion radicals of a molecule in molecular materials, and in a spin- $\frac{1}{2}$  radical coupled with a spin-less positive or negative charge through a local structural reorganization in  $\pi$ -conjugated polymers. In Figure 2.1, the energy levels of positive and negative polarons along with other localized electronic states like bipolarons and excitons are illustrated, whereas a schematic comparison between inorganic and (polymer) organic semiconductors is reported in Figure 2.2.

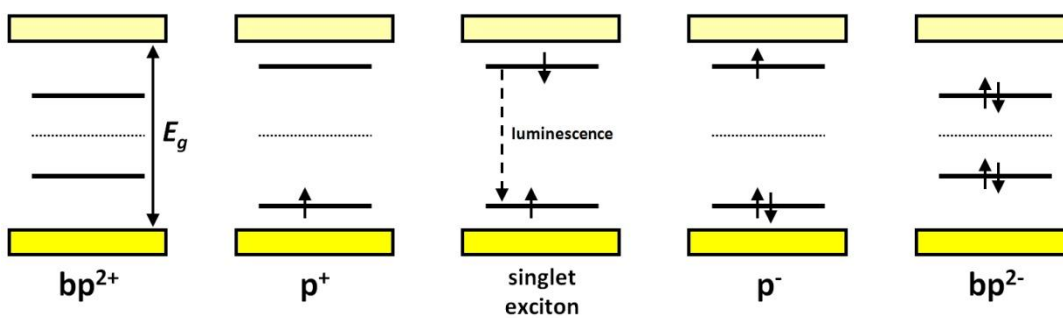


**Figure 2.1** Schematic representation of polaron, bipolaron, and siglet exciton energy levels in a non-degenerate ground-state polymer. Luminescence from the singlet exciton is also shown. Note that new sub-gap optical transition arise from such intra-gap energy levels.

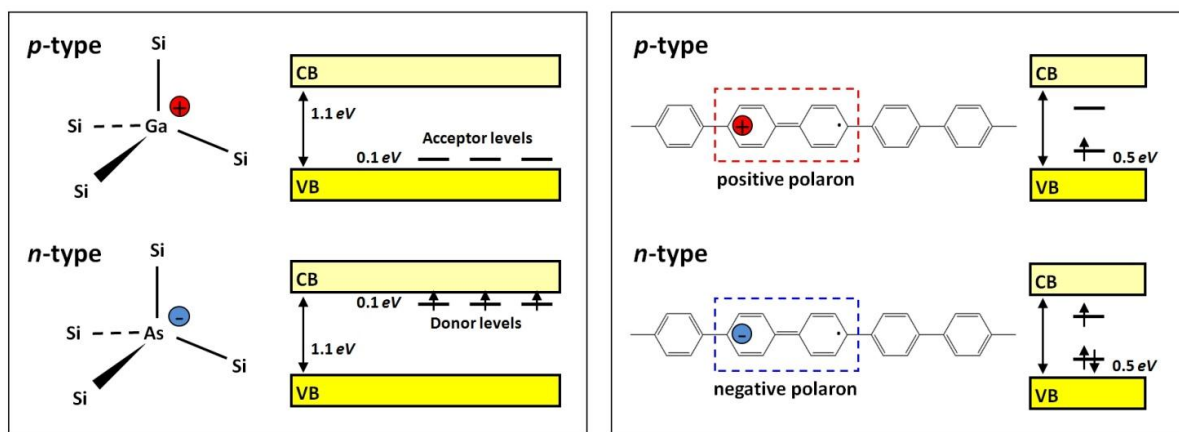


**Figure 2.2** Schematic representation of the differences between inorganic (left) and polymer (right) semiconductors in terms of doping, charge carriers, and intra-gap energy levels.

The tendency of the charge carriers to migrate under the influence of an electric field can be described by the charge mobility  $\mu$  of the material;  $\mu$  has units of velocity per unit field and is, in general, dependent on both the electric field and temperature. Several theoretical models have been formulated in order to correctly reproduce the temperature dependence shown by the charge mobility of OSCs, but none of those developed so far provides a description that can be comprehensively applied to all charge-transporting materials. Band-like transport and hopping transport are the main two charge transport mechanisms one has recourse to, basically depending on the strength and the coherence of the electronic couplings within the organic material. However, it has generally been accepted that charge transport in organic disordered systems and in high-temperature regimes takes place by a

hopping process. Accordingly, charge transport can be described as a series of successive electron-transfer reactions between neutral and charged molecular or polymeric repeat units, that is, between local neutral and polaronic ground states.

$\pi$ -system characterizing organic compounds is also responsible for several properties such as light absorption and emission in the UV-Vis-NIR wavelength region, charge-carrier generation and transport, nonlinear optical properties, and so forth, which make OSCs promising alternative to the more expensive and less versatile inorganic semiconductors for many typologies of electronic and opto-electronic devices.

## 2.2 Organic-Based Devices

Electronic and opto-electronic devices using organic materials as active elements, for example, organic light-emitting diodes (OLEDs), organic photovoltaic devices (OPVs), and organic field-effect transistors (OFETs), have recently received a great deal of attention from the standpoint of potential technological applications as well as fundamental science.<sup>1,5-8</sup> The devices using organic materials are attractive because they can take advantage of organic materials such as light weight, potentially low cost, and capability of thin-film, large-area, flexible device fabrication. If photoreceptors in electrophotography using organic photoconducting materials have already established wide markets of copying and laser printers, OLEDs have also found practical applications in both small displays such as mobile phones, digital camera finders, and car audios, and large-area panels for flat-screen televisions and lighting.<sup>9</sup> Organic field-effect transistors (OFETs) are expected to be a promising technology as well for large-area, low cost, and flexible electronics for applications in displays,<sup>10</sup> sensors,<sup>11</sup> electronic papers,<sup>12</sup> radio frequency identification tags,<sup>13</sup> and memories.<sup>14</sup> Finally, a continuous improvement in OPV performance has been recorded with energy conversion efficiency exceeding 8%,<sup>15-16</sup> with the potential that organic solar cells may one day offer an optimal efficiency/cost ratio, thus better traditional inorganic photovoltaic devices in these terms.

### 2.2.1 Organic field-effect transistors

Organic field-effect transistors (OFETs) are a kind of device consisting of an organic semiconducting layer, a gate insulator layer, and three terminals, namely, source, drain, and gate electrodes. Since their discovery in the 1980s<sup>17</sup> research has involved with enthusiasm in discovery, design, and synthesis of  $\pi$ -conjugated systems for OFETs, device optimization, and development of new applications beside inorganic equivalent devices on the basis of the new possibilities offered by intrinsic characteristics of organic materials such as flexibility and biocompatibility.<sup>18</sup> Nonetheless, OFETs are not only essential building blocks for the next generation of cheap and flexible organic circuits, but they also provide an important insight into the charge transport of  $\pi$ -conjugated systems. Indeed, they act as powerful tools for the exploration of the structure-property relationships of  $\pi$ -conjugated systems, such as parameters of field-effect mobility ( $\mu$ , the drift velocity of carriers under unit electric field), current on/off ratio (the ratio of the maximum on-state current to the minimum off-state current), and threshold voltage (the minimum gate voltage that is required to turn on the transistor).<sup>19</sup>

Several architectures have been proposed for the fabrication of OFETs (Figure 2.3), but the operation process is basically the same. When there is no voltage application to the gate electrode, only small currents flow between the source and drain electrodes; this state is referred to as the off-state of transistor. When negative voltage, for example, is applied to the gate electrode, hole carriers in the organic semiconductor layer become accumulated at the interface with the gate dielectric, and hence, hole transport takes place from the source to the drain electrode; this state corresponds to the on-state of transistor. This type of device is called a *p*-channel device. Likewise, application of positive voltage to the gate electrode causes electron transport in the case of *n*-channel devices. Since OSCs are essentially electrical insulators, charge carriers in these semiconductors are usually supplied by injection from the source electrode into the organic layer. The current flow can be modulated by the magnitude of both the gate voltage and the source/drain voltage.

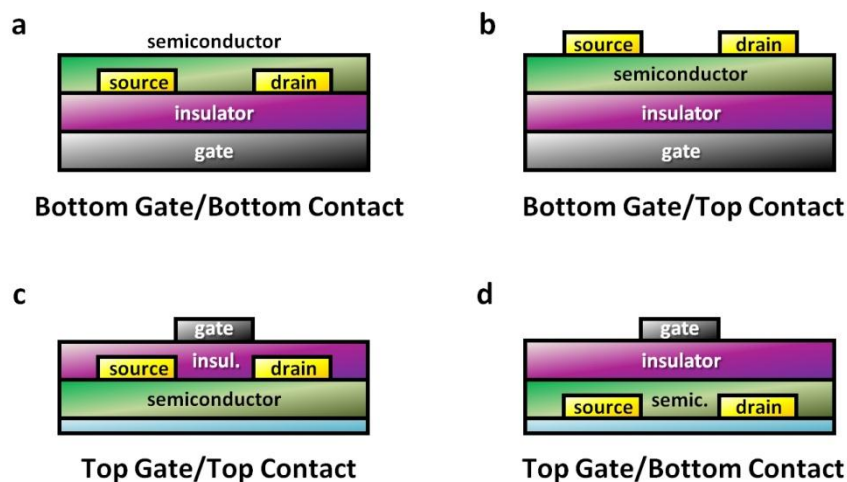


**Figure 2.3** Four architectures of OFETs. (a) Bottom gate/bottom contact, (b) bottom gate/top contact, (c) top gate/top contact, and (d) top gate/bottom contact. It was found that devices of the type **b** and **d** always give better performance than that of devices **a** and **c**.<sup>19</sup> Figure adapted from <sup>19</sup>.

### 2.2.2 Organic photovoltaics

Solar cells are devices that directly convert light energy into electrical energy. OPVs cover a broad range of photovoltaic device architectures that contain at least one organic material in the functional light absorbing layer. These devices include dye sensitized solar cells,<sup>20</sup> hybrid solar cells consisting of inorganic nanoparticles<sup>21</sup> or nanostructured templates,<sup>22</sup> and all-organic solid state donor-acceptor based heterojunction solar cells.<sup>23</sup> Of these, heterojunction solar cells have captured a huge amount of attention in recent twenty years due to the rapid increase in reported efficiencies derived from these cells, in the pursuit of using solar energy as a clean and inexhaustible new energy source.

An organic *pn*-heterojunction solar cell typically consists of a thin active organic layer sandwiched between a high work function anode, typically a transparent indium tin oxide (ITO) layer, and a relatively low work function metal cathode. The active layer is made up of two light-absorbing organic semiconductors, one with an electron-donating character (donor) and the other with an electron-accepting character (acceptor). These semiconductors could either be deposited as two distinct layers where the donor-acceptor interface resides only between the two layers (bilayer, Figure 2.4a), or be blended as an almost homogeneous mix where interfacial interaction between donor and acceptor exists throughout the blended bulk layer (bulk heterojunction, Figure 2.4b).

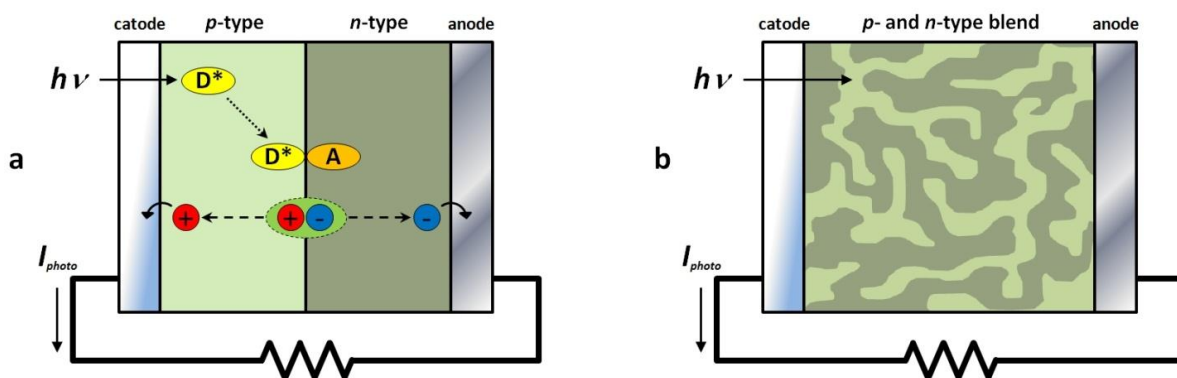


**Figure 2.4** (a) Schematic representation of the operation processes of bilayer *pn*-heterojunction OPVs. (b) A bulk heterojunction OPV cell is sketched. Figure adapted from <sup>1,85</sup>.

Many physical processes are involved in energy conversion, which makes it necessary to consider a huge variety of variables and phenomena (*e.g.*, the electronic structure and the photophysical and photochemical activities of the active organic compounds) in order to improve the efficiency of the device. The basic operation processes of *pn*-heterojunction OPVs are as follows (Figure 2.4): (i) light absorption by organic semiconductors to form excitons, (ii) diffusion of excitons, (iii) charge carrier generation and separation at the organic/organic interface, (iv) charge transport through the organic layers, and (v) charge collection at both electrodes. Nevertheless, several secondary, undesired processes may occur, reducing energy conversion efficiency, such as exciton quenching phenomena and charge recombination.<sup>24</sup>

### 2.2.3 Organic light-emitting diodes

Electroluminescence in organics was first reported using single crystals of anthracene in the 1960s,<sup>25</sup> with an extremely high voltage of 400 V required to obtain blue emission resulting from anthracene. Since then, an extensive research has led to the development of low drive voltage, high brightness, full-color emission, rapid response, and easy fabrication of large-area, thin-film OLEDs.<sup>26-27</sup>

OLEDs are current-driven devices that utilize emissions from the electronically excited states of molecules. The operation of OLEDs involves (i) charge injection from the anode and the cathode into the adjacent organic layers, (ii) transport of injected charge carriers through the

organic layers, (iii) exothermic recombination of holes and electrons to generate excitons, (iv) exciton deactivation by emission of either fluorescence or phosphorescence, (v) light extraction out of the device (Figure 2.5, where both single layer and multilayer architectures are reported).

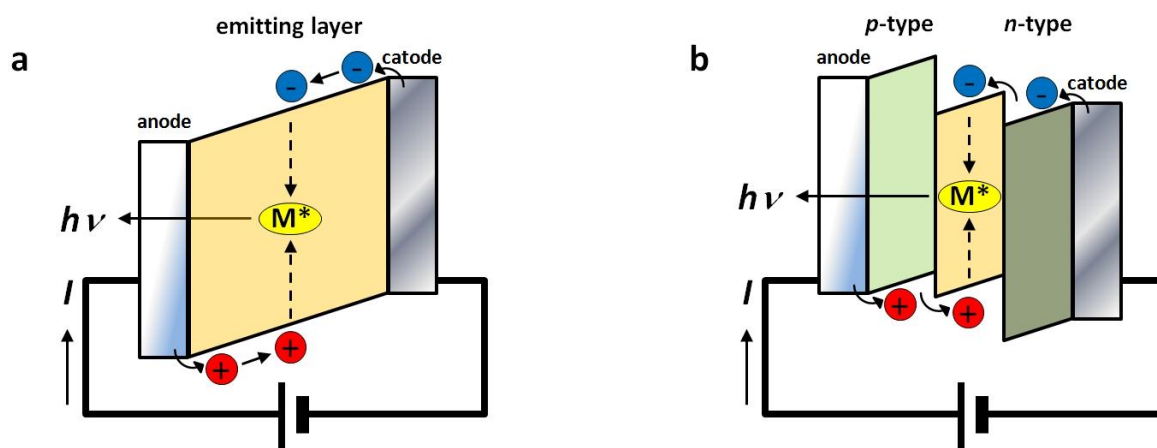


**Figure 2.5** Schematic representation of the operation processes of single layer (a) and multilayer (b) OLEDs. Figure adapted from <sup>1</sup>.

Note that these processes are just the opposite of those of OPVs; accordingly, a phenomenon like charge recombination, which is detrimental for solar cells, is fundamental for the proper functioning of OLEDs. In particular, the factors determining the efficiency of OLED devices are the efficiency of charge carrier injection from the anode and the cathode at low drive voltage, charge balance, spin multiplicity of the luminescent state (consider that the generation probability of either excited singlet or triplet state is 0.25 and 0.75, respectively), photoluminescence quantum yield, and extraction of the emission out of the device. When fluorescent emitters are employed, only 25% of the generated excitons are utilized. However, when phosphorescent emitters are used, an internal quantum efficiency up to 100% can be virtually achieved since the phosphorescent emitters, which are usually doped in a host material, can capture both singlet and triplet excitons generated by the recombination of injected holes and electrons.<sup>26,28</sup>

To attain optimal performance from OLEDs, it is necessary a good confinement of the injected charge carriers within the emitting layer to increase the probability of the desired emissive recombination. To this end, hole-transport and electron-transport layers are inserted between the electrodes and the emitting layer, reducing the energy barriers for the

injection of charge carriers from the electrodes into the emitting layer by a stepwise process, thus resulting in efficient charge injection and charge balance. Precisely, charge carriers injected from the electrodes into the adjacent charge-transport layers are transported through the charge-transport layers and then injected into the emitting layer. The hole- and electron-transport layers can also act as electron- and hole-blocking layers, respectively, thus, confining the electrons and holes within the emitting layer and preventing them from escaping to the adjacent carrier-transport layers. A structure of multilayer OLEDs consisting of the emitting and hole- and electron-transport layers sandwiched between the ITO anode and the metal cathode is shown in Figure 2.5b.

### 2.3 Requirements for Functional Organic Layers

It is undoubted that the performance of an organic-based device tightly relies on the structural, electronic, and charge transport properties of the functional molecular or polymer semiconductor employed.

First of all, the device efficiency is highly dependent on the morphology of the material. According to their morphology, molecular OSCs are classified into single crystals, polycrystals, liquid crystals, and amorphous glasses. Electroluminescent devices and OFETs using organic single crystals have been reported;<sup>25,29</sup> however, the single-crystal growth on the plane of a large-area substrate for device applications is not easy, as organic compounds tend to yield single-crystals that are not only usually very fragile but also very small.<sup>30</sup> Polycrystalline materials have been used mostly in OFETs and OPVs. The grain size, grain boundaries, and molecular orientations affect the device performance. Amorphous materials have advantages over crystalline materials in device fabrication because of their good processability, transparency, and isotropic and homogeneous properties. Amorphous molecular materials have recently constituted a new class of organic materials for use in various applications, in particular, OLEDs.<sup>5b,d</sup> Liquid crystalline materials have also been studied for emitters or a host matrix for emitters in OLEDs to obtain polarized emission from the devices.<sup>31</sup> Therefore, several factors have to be taken into account, ranging from the extension of the active interface where the specific phenomena take place (*e.g.*, charge

recombination at the *p-n* heterojunction) to the order degree and presence of defects, along with specific functional requirements (*i.e.*, the ability of liquid crystals to reorganize their arrangement under certain stimuli), and the right balance between number of contacts, ease of fabrication, and functional packing must be reached.

Second, among the difficulties to overcome in the design of suitable OSCs, solution-processability and ambient-stability are often the most challenging. Regarding processability, the strong  $\pi$ -interactions and rigid conjugated backbones, which are usually required to improve charge transport efficiency, would seem to contradict those factors which enhance solubility in common organic solvents - lipophilic substituents and segmental mobility. This requirement of balancing solid-state packing and solubility introduces significant synthetic challenges indeed.<sup>32</sup> As for ambient stability, such issue is particularly weighty for *n*-type OSCs<sup>32</sup> and was first addressed by de Leeuw in 1997; accordingly, degradation was attributed to reaction of the charge-carrying organic  $\pi$ -radical anions (negative polarons) with O<sub>2</sub> and H<sub>2</sub>O.<sup>33</sup> Although several different strategies, such as lowering frontier molecular orbital energies or introducing kinetic O<sub>2</sub>/H<sub>2</sub>O barriers (*e.g.*, steric hindrance given by long and flexible secondary chains or substituents), have been pursued to enhance device durability, the number of materials with desired properties has been inadequate until recently, and the fundamental limitations not well-established.<sup>34</sup>

Third, as active organic layers are supposed to be interfaced with metal electrodes, one of the most necessary aspects to be taken into account consists in the alignment of energy levels. Precisely, a proper matching must be ensured between the work functions of the metal electrodes and the electron affinities and ionic potentials of the OSC materials, as well as between the energy levels of two different adjacent organic layers, in order to facilitate processes like charge carrier injection from contacting electrodes into the organic material, exciton separation or charge recombination at the *pn*-heterojunction, and so forth.

Finally, OSCs should meet further specialized needs according to the roles that they play in devices, for example, hole transport, electron transport, charge blocking, electrical bistability, and light absorption and emission.

From this perspective, on the one hand, several families of organic compounds have been synthesized, looking for new intrinsic characteristics directly given by the peculiar connectivity and the consequent electronic structure featured by the molecule. On the other hand, an extensive research has been performed to suitably tailor the  $\pi$ -conjugated system,

along with other modifications to the  $\sigma$ -backbone of the given compound, to modulate the related optical and charge transport properties, pursuing a control at both intramolecular and intermolecular levels.

## 2.4 Families of Organic Compounds

To date, a huge number of  $\pi$ -conjugated semiconducting materials have either been discovered or synthesized. Polymer OSCs were the first being recorded in 1977;<sup>35</sup> since then, a great interest has been dedicated to development of new and high-performance polymers, such as polythiophene and its many and promising co-polymers and derivatives.<sup>36,19</sup> Although the important role played by polymer materials in organic technology, this dissertation focuses on the equally relevant contribution given by small molecule OSCs. Small molecule semiconductors have been widely studied because they are easy to purify and easily form crystalline films for the fabrication of the desired high performance devices. Indeed, up until now, the  $\pi$ -conjugated systems that are reported to have the highest mobility are small molecules such as pentacene, rubrene, alkylated benzothieno[3,2-*b*]benzothiophene, and titanyl phthalocyanine.<sup>19</sup>

Oligoacenes (Figure 2.6) are certainly of great importance in this research field, and are among the most studied *p*-type OSC families indeed.<sup>19</sup> Naphthalene and anthracene can be considered as less extended acenes. Single crystals of naphthalene have been studied by using the time-of-flight (TOF)<sup>37</sup> method, but few reports have actually addressed the use of naphthalene in OFETs. Anthracene has also been examined in OFETs and its single crystal devices may eventually exhibit hole mobilities approaching  $3 \text{ cm}^2 \text{ V}^{-1} \text{ s}^{-1}$ , according to the results of room temperature TOF.<sup>38</sup> Normally, with the expansion of the  $\pi$ -conjugated system, the intermolecular electronic couplings are likely to increase while the intramolecular reorganization energy tends to decrease (see Chapter 4); as a consequence, enhanced charge transport performance is expected for longer acenes. Indeed, pentacene demonstrated hole mobilities of up to  $1.5 \text{ cm}^2 \text{ V}^{-1} \text{ s}^{-1}$  in thin film transistors,<sup>39</sup> and  $5.0 \text{ cm}^2 \text{ V}^{-1} \text{ s}^{-1}$  when polycrystalline films are used in OFETs.<sup>40</sup>

One disadvantage of using higher acenes in OFETs is not only their high sensitivity to light because of their narrow energy gaps (from anthracene,<sup>41</sup> tetracene,<sup>42</sup> to pentacene:<sup>43</sup> 4.0, 2.6, 1.8 eV) leading to easy molecular excitation by light but also their high HOMO energy levels (from anthracene,<sup>41</sup> tetracene,<sup>42</sup> to pentacene:<sup>43</sup> -5.7, -5.2, -5.0 eV) which results in high oxidation sensitivity to oxygen. For example, pentacene easily forms dimers and trimers in ambient conditions or can be oxidized into 6,13-pentacenequinone (PQ). Moreover, the solubility of pentacene is also very poor in common organic solvents.<sup>44</sup> The result is that the purification of pentacene is highly challenging (ultrapure pentacene is almost impossible to obtain due to the existence of PQ). However, when utilizing this PQ as the gate dielectric to fabricate single crystal field-effect transistors of pentacene, Palstra *et al.*<sup>45</sup> achieved a mobility as high as 15-40  $\text{cm}^2 \text{V}^{-1} \text{s}^{-1}$ , with a current on/off ratio of up to 106. This was attributed to the fact that PQ has a structure similar to pentacene and this provides an intimate contact between the semiconductor and the dielectric layer. With a further increase in the number of benzene rings for extension of the  $\pi$ -conjugated systems, the stability and solubility of the larger acenes become even poorer so that OFETs based on hexacene<sup>46</sup> and heptacene<sup>47</sup> have never been addressed.

Picene<sup>48</sup> is an isomeric compound of pentacene (Figure 2.6) but shows higher stability because its energy band gap is larger ( $E_g = 3.3 \text{ eV}$ ) and its ionization potential is higher ( $IP = 5.5 \text{ eV}$ ) than those of pentacene ( $E_g = 1.8 \text{ eV}$ ,  $IP = 5.0 \text{ eV}$ ). The OFET performance of picene exhibited typical *p*-channel characteristics with a mobility of 1.1  $\text{cm}^2 \text{V}^{-1} \text{s}^{-1}$  and an on/off ratio of 105 under atmospheric conditions. The mobility was found to approach 3.2  $\text{cm}^2 \text{V}^{-1} \text{s}^{-1}$  if the device was exposed to O<sub>2</sub> for oxygen doping.<sup>49</sup>

It has been shown<sup>50</sup> that introducing polar groups is an efficient way to change the molecular packing and obtain  $\pi$ - $\pi$  stacking acenes, along with new optical and charge transport features. As a result, acene derivatives have been widely studied.<sup>19</sup>

On going from oligoacenes to fused ring aromatics, it is envisaged that (i) the extension of  $\pi$ -conjugated system may increase the transfer integrals and lower the reorganization energies, (ii) the increased C/H ratio may lead to a  $\pi$ - $\pi$  stacking which is eventually advantageous for high mobility. Certainly, the solubility, stability,<sup>51</sup> planar conjugation,<sup>52</sup> and molecular packing all need further consideration in order to extend the practical applications of polycyclic aromatic hydrocarbons (PAHs) and their derivatives. It is interesting to compare the linear acenes such as tetracene and pentacene, which have the herringbone packing

motif, with pyrene and perylene, which, although they have the same number of benzene rings as that of tetracene and pentacene, exhibit  $\pi$ - $\pi$  stacking motif in crystals. Triphenylenes and coronenes (Figure 2.6) are extensively studied as organic liquid crystal materials because of their unique tendency to aggregate into one- or two-dimensional (1D or 2D) columnar arrays.<sup>53</sup> For instance, by applying a high magnetic field, a high mesoscopic order<sup>54</sup> was obtained in thin films of hexabenzocoronene derivatives with a discotic liquid crystal phase.

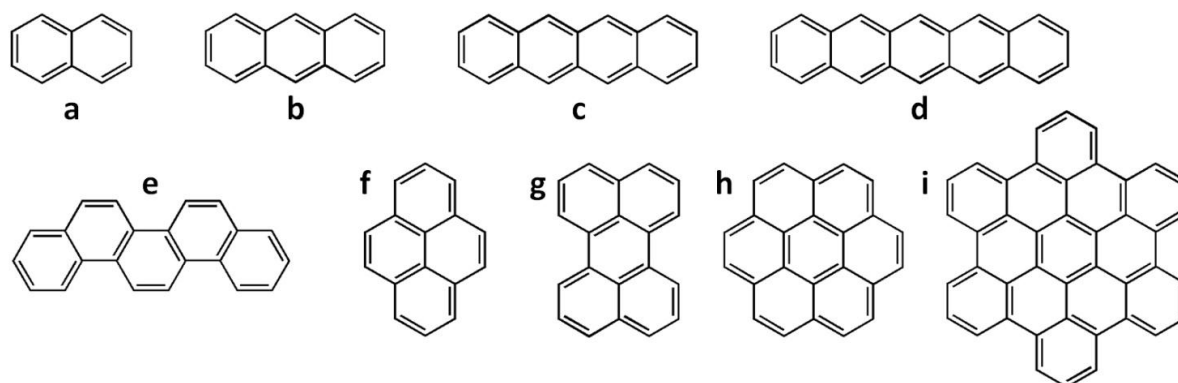


**Figure 2.6** Structural formula of *p*-type naphthalene (a), anthracene (b), tetracene (c), pentacene (d), picene (e), pyrene (f), perylene (g), coronene (h), and hexabenzocoronene (i).

Another extensively studied OSCs family, which is of great importance in this dissertation, is that of rylene tetracarboxylic diimides.<sup>55</sup> Rylenes are hydrocarbon families that can be regarded as naphthalene oligomers, with bonds between the 1 and 1' positions and between the 8 and 8' positions of adjacent naphthalene units, *i.e.*, they are oligo(*peri*-naphthalene)s. The rylene tetracarboxylic diimides considered herein all bear two six-membered dicarboxylic imide rings fused to the terminal naphthalene units; the two simplest rylene diimide systems, naphthalene-1,8:4,5-tetracarboxylic diimides (NDIs) and perylene-3,4:9,10-tetracarboxylic bisimides (PBIs), are shown in Figure 2.7. Interest in rylene diimides and other aromatic diimides, such as those based on tetracene (Figure 2.7), stems from early observations of *n*-type character and the ability to tune molecular electronic properties by well-established organic chemistry, through either variation of substituents on the imide nitrogen atoms or on the rylene skeleton.<sup>55</sup> Rylene diimides can exhibit relatively high electron affinities, high electron mobilities, and excellent chemical, thermal, and photochemical stabilities.<sup>55</sup> These molecules and their derivatives have been used not only as building blocks for electronic and opto-electronic devices such as organic light-emitting diodes,<sup>56</sup> dye lasers,<sup>57</sup> optical switches,<sup>58</sup> and photodetectors,<sup>59</sup> but also as electron acceptors

for studying photoinduced energy- and electron-transfer processes.<sup>60</sup> Several accounts have summarized the synthesis and organization for various applications of NDI and PBI materials.<sup>61</sup>

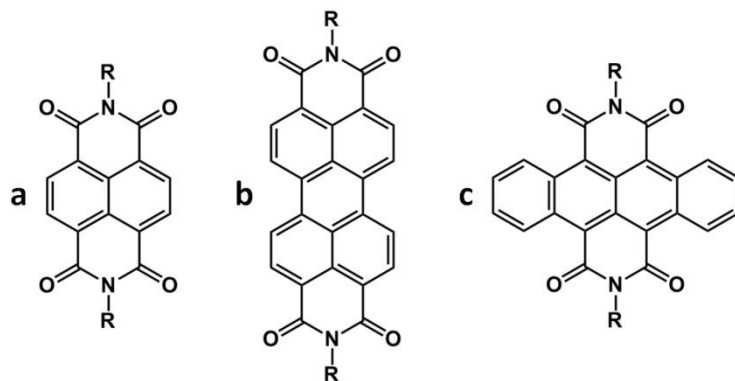


**Figure 2.7** Structural formula of *n*-type NDI (a), PBI (b), and TDI (c), another diimide derivative.

Another recently synthesized OSC family consists in N-annulated rylenes (Figure 2.8).<sup>62-63</sup> Beside promising optical and electronic properties,<sup>62-63</sup> the most fascinating aspect of such compounds lies in that, along with oligomers of PBIs (Figure 2.8), they can be regarded to as model compounds of functionalized graphene nanoribbons.<sup>62</sup> Therefore, they offer a bottom-up approach to obtain such interesting graphene-like nanostructures for which the width of the  $\pi$ -conjugated sheet is confined to a finite size, while the length is considered infinitely long. It is such lateral quantum confinements to open an electronic gap that controls several optical and charge transport properties.<sup>64</sup> Note that, contrary to graphene<sup>65</sup> (to date, the aromatic compound with the highest mobility and which recently won its discoverers the 2010 Nobel Prize in Physics), graphene nanoribbons can show a remarkable on/off ratio, thus they can be successfully used in devices relying on diodes.<sup>64</sup> Derivatization through insertion of electron-withdrawing or electro-donating groups, as well as inclusion of five-membered rings and other functional moieties, further enhance the versatility of such model compounds by suitably tuning both optical and charge transport features.<sup>62-63</sup>

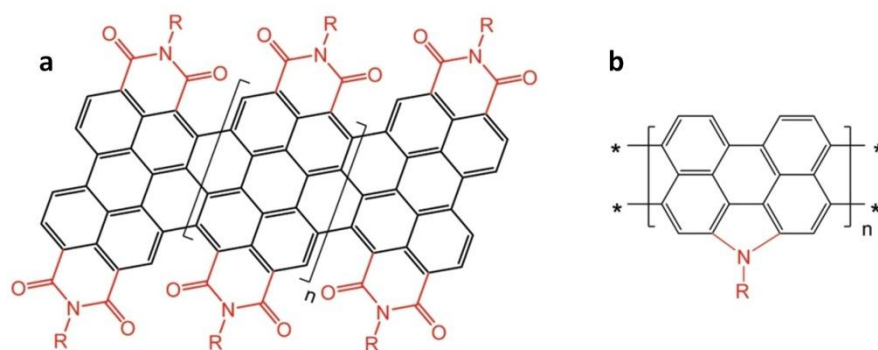


**Figure 2.8** Oligo-PBIs (a) and oligo(*peri*-N-annulated perylene)s (b) as model compounds of functionalized graphene nanoribbons. Figure adapted from <sup>62b</sup>.

Polythiophene (Figure 2.9a) was the first material used in organic field-effect transistors.<sup>66</sup> Since then, polymers, oligomers, and fused ring aromatic materials containing thiophene units have all been thoroughly examined.<sup>19</sup> The rapid development of chalcogen-containing heterocyclic semiconductors can be explained by the following reasons. First, because of its similarity to the benzene ring, the thiophene ring also has six  $\pi$  electrons and hence aromaticity ( $4n + 2$ ). Second, compared to the corresponding benzene-ring-based materials, those containing thiophene units benefit from the fact that the molecules can pack in planar structures (*e.g.*, polythiophenes or oligothiophenes).<sup>67</sup> Third, fused-thiophene-ring materials exhibit a much higher ability for anti-oxidation due to the absence of a Diels-Alder cyclization active center.<sup>68</sup> With the introduction of heteroatoms, even higher thienoacenes with six or seven fused aromatic rings exhibit excellent OFET performance and high stability. Finally, S atoms are able to introduce  $S \cdots S$ ,  $S \cdots H$ , and  $S \cdots \pi$  intermolecular interactions which enhance intermolecular interactions, namely, both charge transport performance and self-assembly capability. As a result, sulfur-containing materials have become one of the most important semiconductors, in particular for OFET applications.

Recently, a great deal of attention has been attracted by quinoidal oligothiophenes (Figure 2.9b), as they show, beside interesting features like biradicaloid character<sup>69</sup> and amphoteric properties,<sup>70</sup> narrow optical gaps making such compounds promising NIR dyes for solar cell.<sup>71</sup> Indeed, in order to improve the energy conversion efficiency of photovoltaic devices, one strategy lies in exploiting as much as possible the conspicuous infrared portion of solar emission.<sup>72</sup>

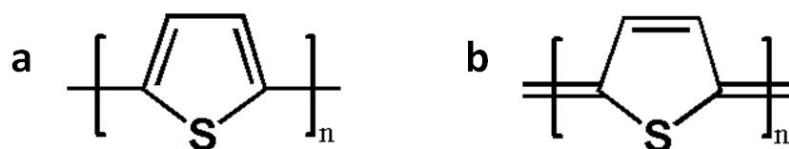


**Figure 2.9** Structural formula of polythiophene (a) and quinoidal oligothiophene (b).

Finally, although they are not discussed within this dissertation, some other OSCs deserve at least a brief mention for their importance in organic opto-electronics: fullerenes, whose optimal application seems to be as ET materials in OPVs; phthalocyanines, porphyrins, and organometallic complexes, mainly for their promising performance in OLEDs and OPVs; fluorene and carbazole derivatives, usually as polymers and co-polymers, also with perylene and thiophene moieties, or featuring condensed aromatic rings, for their comprehensive versatility.<sup>19</sup>

## 2.5 Structure-Property Relationships

Incorporation of functionality by molecular design is undoubtedly the most appealing capability offered by organic technology. However, to take advantage of the easily tunable optical and charge transport properties of organic molecular materials, it is necessary to obtain a comprehensive and detailed knowledge of the structure-property relationships. To this end, not only intramolecular, but also intermolecular properties must be considered and investigated. Indeed, although a huge variety of single-molecule opto-electronic devices have been extensively produced,<sup>73</sup> such systems, which certainly maintain a relevant role for the research providing an insight into charge transport mechanisms, are far from being suitable for massive industrial production. As a consequence, in order to understand the phenomena occurring within common organic-based devices, thin-film, bulk, and interface systems have to be considered, thus taking into account intermolecular arrangements and interactions.

Principally, the charge mobility of the organic semiconductor should be as high as possible, which is achieved when efficient charge transport from one molecule to another is attainable. This in turn is intimately related to the electronic couplings between two neighboring molecules, linearly proportional to  $\pi$ - $\pi$  orbital overlap,<sup>74</sup> and the energy required by the transfer and localization of the charge, as neutral and charged species have usually different equilibrium structures and also in the surrounding medium reorganization processes (*e.g.*, polarization effects) take place. Thus, it is clear how these parameters are both extremely dependent on the packing of the organic molecules.<sup>75</sup> Accordingly, the packing mode of the OSCs becomes very important for the analysis of the charge transport between molecules. There are four different kinds of packing motifs, as shown in Figure 2.10:<sup>19</sup> (i) herringbone packing (face-to-edge) without  $\pi$ - $\pi$  overlap (face-to-face) between adjacent molecules; (ii) herringbone packing with  $\pi$ - $\pi$  overlap between adjacent molecules, also called slipped  $\pi$ -stacking in some literature reports;<sup>76</sup> (iii) lamellar packing, one-dimension (1D)  $\pi$ -stacking, and (iv) lamellar packing, two-dimension (2D)  $\pi$ -stacking, also called slipped brick-stone arrangement.<sup>77</sup>

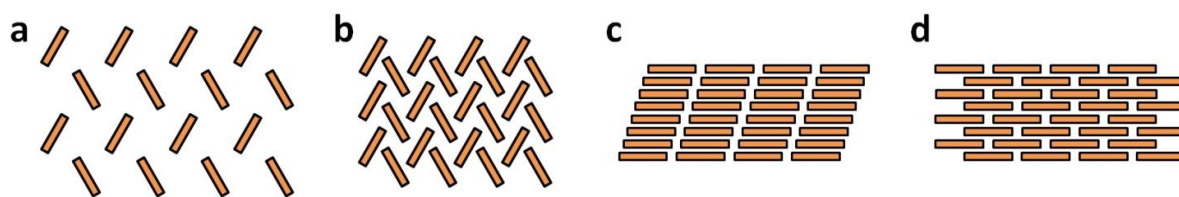


**Figure 2.10** Molecular packing motifs in crystals.<sup>19</sup> (a) Herringbone packing (face-to-edge) without  $\pi$ - $\pi$  overlap (face-to-face) between adjacent molecules (*e.g.*, pentacene); (b) herringbone packing with  $\pi$ - $\pi$  overlap between adjacent molecules (*e.g.*, rubrene); (c) lamellar motif, 1D  $\pi$ -stacking (*e.g.*, hexyl substituted naphthalene diimide); (d) lamellar motif, 2D  $\pi$ -stacking (*e.g.*, octachlorinated perylene bisimide<sup>78</sup>). Figure adapted from <sup>19</sup>.

Although  $\pi$ -stacking is believed to lead to higher mobilities, such a generalization is mostly unreliable.<sup>79</sup> In fact, there are cases of molecules that have effective overlap without extensive  $\pi$ -stacking and likewise there are cases of molecules with strong  $\pi$ -stacking but which lack effective wave function overlap. In other words, one must not only consider the spatial overlap of orbitals to determine coupling but also the phase relationships between the orbitals of each molecule.<sup>74</sup>

In addition, several factors may contribute to complicate the effective charge transfer process.<sup>80-81</sup> For instance, it has been recently shown<sup>80</sup> the undeniable importance of thermally induced disorder effects, that is,  $\pi$ - $\pi$  overlap variations and consequent electronic coupling fluctuations due to thermally induced vibrations. Hence, such dynamic effects may dramatically change the charge conduction preferential paths with respect to a static description where the packing optimizes intermolecular interactions but disadvantages the electronic coupling between two adjacent molecules.<sup>80</sup>

Note that suitable reciprocal orientations of the molecules in an organic material not only impact the charge conduction but also determine relevant optical phenomena such as the formation of *J*- or *H*-aggregates and other excitonic effects.<sup>82-83, 62b</sup>

The way molecules arrange, namely, molecular packing depends upon many processing factors,<sup>84</sup> but in a relevant extent it is the molecular structure itself to determine the possible arrangements.<sup>19</sup> From this point of view, research has been putting a lot of effort to achieve the control on a predictable packing by the modulation of the structural features of the organic compound,<sup>19</sup> keeping in mind that strategies favorable to the desired arrangement may reduce solubility, whereas a balance between solid-state packing and solution-processability is often required.<sup>32</sup> To this purpose, self-assembly capability shown by some molecules clears the way for easily controlled, pre-designed arrangements.<sup>84</sup>

Another challenge that organic technology has to face is rationalization of those structural and electronic molecular properties ensuring efficient *p*-type and *n*-type organic semiconductors. Actually, such issue is more pressing for these latter, as relatively fewer *n*-type materials have been reported so far.<sup>32,55,85</sup> In particular, the development of high-performance *n*-type OSCs has been hampered by intrinsic limitations like a more remarked ambient instability than *p*-type materials.<sup>32,55,86</sup> To this end, a strategy relies on appending strong electron-withdrawing substituents, such as fluoro, cyano, or acyl, to  $\pi$ -conjugated cores such as acenes and oligothiophenes, which, in the absence of these substituents, exhibit *p*-type character.<sup>55</sup>

Fundamental requirements such as ambient stability, as well as suitable matching between the energy levels of both organic materials and metal electrodes, are satisfied by tailoring the electronic structure of the organic compounds. Indeed, several operating definitions can be considered based upon both oxidation or ionization potentials, both related to the energy of

the highest occupied molecular orbital (HOMO) in a one electron picture, or the reduction potentials or electron affinities, both related to the energy of the lowest unoccupied molecular orbital (LUMO). In general, the linear extension of  $\pi$ -systems tends to both raise the HOMO and lower the LUMO making the molecule both easier to oxidize and easier to reduce. Such strategies have been employed to make so-called ambipolar materials into which both hole and electrons can be injected and in some cases can show reasonable mobilities for both. If one desires to preferentially lower the energy of the LUMO and have a smaller impact on the HOMO, the substitution of the  $\pi$ -system with  $\pi$ -acceptors (such as cyano, carbonyls, and the like) is a reasonable strategy. This approach increases both the conjugation length (thereby impacting both the energy of the HOMO and LUMO), but in addition, because the  $\pi^*$  energy of the acceptor is often relatively close to that of the LUMO of the conjugated  $\pi$ -system, these orbitals can mix efficiently leading to stabilization of the LUMO.<sup>79</sup> Another approach to making a system more electron deficient is by attachment of groups that are inductively electron withdrawing, *e.g.*, by replacement of an alkyl group with a perfluoroalkyl group. Such substitution directly impacts the energy of the  $\sigma$ -orbitals and effectively lowers the electron density at the nuclei of the atoms in the  $\pi$ -systems. As a consequence the  $p$ -orbitals that comprise the  $\pi$ -system are less effectively screened and therefore both the occupied and unoccupied orbitals will tend to be lowered.<sup>79</sup>

Basically, tuning of molecular orbitals through extension of the  $\pi$ -conjugated system, as well as derivatization with electron-withdrawing or electron-donating groups, impacts both transport and optical gaps; hence, both charge transport and optical properties of the organic material can be tailored by suitably modifying structural features of the molecule.

From this perspective, my investigations, carried out by means of suitable theoretical and computational studies, along with the development of software tools, mainly focus on such determination of the relationships between intra- and intermolecular structure of organic materials and their electronic, optical, and charge transport properties, aiming to contribute to both the rationale of experimentally observed behaviors and the improvement of the design of new organic semiconductors with properties suitable for particular devices.

## 2.6 References

- [1] Shirota, Y.; Kageyama, H. *Chem. Rev.* **2007**, *107*, 953-1010.
- [2] Sirringhaus, H.; Kawase, T.; Friend, R. H.; Shimoda, T.; Inbasekaran, M.; Wu, W.; Woo, E. *P. Science* **2000**, *290*, 2123-2126.
- [3] Wen, Y.; Liu, Y.; Guo, Y.; Yu, G.; Hu, W. *Chem. Rev.* **2011**, *111*, 3358-3406.
- [4] (a) Lussem, B.; Karipidou, Z.; Scheriber, A.; Yasuda, A.; Wessels, J. M.; Nelles, G. *Microelec. Eng.* **2010**, *87*, 614-619. (b) Jang, Y.; Park, Y. D.; Lim, J. A.; Lee, H. S.; Lee, W. H.; Cho, K. *App. Phys. Lett.* **2006**, *89*, 183501. (c) Ai, Y. M.; Liu, Y.; Cui, T. H.; Varshneyan, K. *Thin Solid Films* **2004**, *450*, 312-315.
- [5] (a) Friend, R. H.; Gymer, R. W.; Holmes, A. B.; Burroughes, J. H.; Marks, R. N.; Taliani, C.; Bradley, D. D. C.; Dos Santos, D. A.; Brédas, J. L.; Lögdlund, M.; Salaneck, W. R. *Nature* **1999**, *397*, 121. (b) Shirota, Y. *J. Mater. Chem.* **2000**, *10*, 1. (c) Forrest, S. R. *Nature* **2004**, *428*, 911. (d) Shirota, Y. *J. Mater. Chem.* **2005**, *15*, 75.
- [6] (a) *Organic Electroluminescent Materials and DeVices*; Miyata, S., Nalwa, H. S., Eds.; Gordon and Breach: New York, 1997. (b) Kraft, A.; Grimsdale, A. C.; Holmes, A. B. *Angew. Chem., Int. Ed. Engl.* **1998**, *37*, 402. (c) Mitschke, U.; Bäuerle, P. *J. Mater. Chem.* **2000**, *10*, 1471. (d) *Organic Electroluminescence*; Kafafi, Z. H., Ed; Taylor & Francis: New York, 2005. (e) *Organic Light-Emitting Devices, Synthesis, Properties, and Applications*; Müllen, K, Scherf, U., Eds.; Wiley-VCH: Weinheim, Germany, 2006.
- [7] (a) Spanggaard, H.; Krebs, F. C. *Solar Energy Mater. Solar Cells* **2004**, *83*, 125. (b) *Organic PhotoVoltaics, Mechanisms, Materials and Devices*; Sun, S. S., Sariciftci, N. S., Eds.; CRC Press: New York, 2005.
- [8] (a) Horowitz, G. *Adv. Mater.* **1998**, *10*, 365. (b) Katz, H. E.; Bao, Z.; Gilat, S. L. *Acc. Chem. Res.* **2001**, *34*, 359. (c) Dimitrakopoulos, C. D.; Malenfant, P. R. L. *Adv. Mater.* **2002**, *14*, 99. (d) Katz, H. E. *Chem. Mater.* **2004**, *16*, 4748. (e) Sun, Y., Liu, Y., Zhu, D. *J. Mater. Chem.* **2005**, *15*, 53. (f) Mas-Torrent, M.; Rovira, C. *J. Mater. Chem.* **2006**, *16*, 433.
- [9] (a) Forrest, S. R. *Nature* **2004**, *428*, 911-918. (a) Kim, S.; Choi, W.; Rim, W.; Chun, Y.; Shim, H.; Kwon, H.; Kim, J.; Kee, I., Kim, S.; Lee, S.; Park, J. *IEEE Trans. Electr. Dev.* **2011**, *58*, 3609-3615. (b) He, G. F.; Rothe, C.; Murano, S.; Werner, A.; Zeika, O.; Birnstock, J. *J. Soc. Inf. Display* **2009**, *17*, 159-165. (c) Shinar, J.; Shinar, R. *J. Phys. D* **2008**, *41*, 133001.

[10] (a) Gelinck, G. H.; Huitema, H. E. A.; Van Veenendaal, E.; Cantatore, E.; Schrijnemakers, L.; Van der Putten, J.; Geuns, T. C. T.; Beenhakkers, M.; Giesbers, J. B.; Huisman, B. H.; Meijer, E. J.; Benito, E. M.; Touwslager, F. J.; Marsman, A. W.; Van Rens, B. J. E.; De Leeuw, D. M. *Nat. Mater.* **2004**, *3*, 106. (b) Huitema, H. E. A.; Gelinck, G. H.; van der Putten, J. B. P. H.; Kuijk, K. E.; Hart, C. M.; Cantatore, E.; Herwig, P. T.; van Breemen, A. J. J. M.; de Leeuw, D. M. *Nature* **2001**, *414*, 599.

[11] Sokolov, A. N.; Roberts, M. E.; Bao, Z. *Mater. Today* **2009**, *12*, 12.

[12] (a) Bollström, R.; Määttä, A.; Tobjörk, D.; Ihalainen, P.; Kaihoviirta, N.; Österbacka, R.; Peltronen, J.; Toivakka, M. *Org. Electron.* **2009**, *10*, 1020-1030. (b) Tobjörk, D.; Österbacka, R. *Adv. Mater.* **2011**, *23*, 1935-1961. (c) Rogers, J. A.; Bao, Z.; Baldwin, K.; Dodabalapur, A.; Crone, B.; Raju, V. R.; Kuck, V.; Katz, H.; Amundson, K.; Ewing, J.; Drzaic, P. *Proc. Natl. Acad. Sci. U. S. A.* **2001**, *98*, 4835. (d) Comiskey, B.; Albert, J. D.; Yoshizawa, H.; Jacobson, J. *Nature* **1998**, *394*, 253.

[13] (a) Myny, K.; Steudel, S.; Smout, S.; Vicca, P.; Furthner, F.; van der Putten, B.; Tripathi, A. K.; Gelinck, G. H.; Genoe, J.; Dehaene, W.; Heremans, P. *Org. Electr.* **2010**, *11*, 1176-1179; (b) Cantatore, E.; Geuns, T. C. T.; Gelinck, G. H.; van Veenendaal, E.; Gruijthuisen, A. F. A.; Schrijnemakers, L.; Drews, S.; de Leeuw, D. M. *IEEE J. Solid-State Circuits* **2007**, *42*, 84-92; (c) Subramanian, V.; Chang, P. C.; Lee, J. B.; Molesa, S. E.; Volkman, S. K. *IEEE Trans. Comp. Pack. Tech.* **2005**, *28*, 742-747.

[14] (a) Scott, J. C.; Bozano, L. D. *Adv. Mater.* **2007**, *19*, 1452-1463. (b) Welnic, W.; Wuttig, M. *Mater. Today* **2008**, *11*, 20-27. (c) Ling, Q.-D.; Liaw, D.-J.; Zhu, C.; Chan, D. S.-H.; Kang, E.-T.; Neoh, K.-G. *Prog. Polym. Sci.* **2008**, *33*, 917-978.

[15] (a) O'Regan, B.; Grätzel, M. *Nature* **1991**, *353*, 737. (b) Nazeeruddin, M. K.; Kay, A.; Rodicio, I.; Humphry-Baker, R.; Müller, E.; Liska, P.; Vlachopoulos, N.; Grätzel, M. *J. Am. Chem. Soc.* **1993**, *115*, 6382. (c) Scharber, M. C.; Mühlbacher, D.; Koppe, M.; Denk, P.; Waldauf, C.; Heeger, A. J.; Brabec, C. J. *Adv. Mater.* **2006**, *18*, 789.

[16] (a) <http://www.forbes.com/feeds/businesswire/2010/07/27/businesswire142993163.html>. (b) <http://www.heliatek.com/news-19>.

[17] Tsumura, A.; Koezuka, H.; Ando, T. *Appl. Phys. Lett.* **1986**, *49*, 1210.

- [18] (a) Duarte, A.; Pu, K. Y.; Liu, B.; Bazan, G. C. *Chem. Mater.* **2011**, *23*, 501-505. (b) Feili, D.; Schuettler, M.; Doerge, T.; Kammer, S.; Hoffmann, K. P.; Stieglitz, T. *J. Micromech. Microeng.* **2006**, *16*, 1555-1561. (c) Peterson, S. L.; McDonald, A.; Gourley, P. L.; Sasaki, D. Y. *J. Biomed. Mater. Res. Part A* **2005**, *72A*, 10-18.
- [19] Wang, C.; Dong, H.; Hu, W.; Liu, Y.; Zhu, D. *Chem. Rev.* DOI: 10.1021/cr100380z.
- [20] (a) Grätzel, M. *Nature* **2010**, *414*, 338. (b) Grätzel, M. *Acc. Chem. Res.* **2009**, *42*, 1788. (c) Hagfeldt, A.; Boschloo, G.; Sun, L.; Kloo, L.; Pettersson, H. *Chem. Rev.* **2010**, *110*, 6595.
- [21] Milliron, D. J.; Gur, I.; Alivisatos, A. P. *MRS Bull.* **2010**, *30*, 41.
- [22] (a) Gonzalez-Valls, I.; Lira-Cantu, M. *Energy Environ. Sci.* **2009**, *2*, 19. (b) Coakley, K. M.; Liu, X. Y.; Goh, C.; McGehee, M. D. *MRS Bull.* **2010**, *30*, 37.
- [23] Gunes, S.; Neugebauer, H.; Sariciftci, N. S. *Chem. Rev.* **2007**, *107*, 1324.
- [24] (a) Kippelen, B.; Brédas, J.-L. *Energy Environ. Sci.* **2009**, *2*, 251. (b) Brédas, J.-L.; Norton, J.; Cornil, J.; Coropceanu, V. *Acc. Chem. Res.* **2009**, *42*, 1691. (c) Risko, C.; McGehee, M. D.; Brédas, J.-L. *Chem. Sci.* **2011**, *2*, 1200. (d) Beljonne, D.; Cornil, J.; Muccioli, L.; Zannoni, C.; Brédas, J.-L.; Castet, F. *Chem. Mat.* **2011**, *23*, 591.
- [25] Pope, M.; Kallmann, H. P.; Magnante, P. J. *Chem. Phys.* **1963**, *38*, 2042.
- [26] Baldo, M. A.; O'Brien, D. F.; You, Y.; Shoustikov, A.; Sibley, S.; Thompson, M. E.; Forrest, S. R. *Nature* **1998**, *395*, 151.
- [27] (a) Baldo, M. A.; Lamansky, S.; Thompson, P. E.; Forrest, S. R. *Appl. Phys. Lett.* **1999**, *75*, 4. (b) Lamansky, S.; Djurovich, P.; Murphy, D.; Abdel-Razzaq, F.; Lee, H.-E.; Adachi, C.; Burrows, P. E.; Forrest, S. R.; Thompson, M. E. *J. Am. Chem. Soc.* **2001**, *123*, 4304.
- [28] Cleave, V.; Yahiolu, G.; Le Barny, P.; Friend, R. H.; Tessler, N. *Adv. Mater.* **1999**, *11*, 285.
- [29] (a) Horowitz, G.; Garnier, F.; Yassar, A.; Hajlaoui, R.; Kouki, F. *Adv. Mater.* **1996**, *8*, 52. (b) Podzorov, V.; Pudalov, V. M.; Gershenson, M. E. *Appl. Phys. Lett.* **2003**, *82*, 1739.
- [30] (a) Li, R.; Hu, W.; Liu, Y.; Zhu, D. *Acc. Chem. Res.* **2010**, *43*, 529. (b) Jiang, L.; Dong, H.; Hu, W. *J. Mater. Chem.* **2010**, *20*, 4994.
- [31] (a) Mochizuki, H.; Hasui, T.; Shiono, T.; Ikeda, T.; Adachi, C.; Taniguchi, Y.; Shirota, Y. *Appl. Phys. Lett.* **2000**, *77*, 1587. (b) Mochizuki, H.; Hasui, T.; Kawamoto, M.; Shiono, T.; Ikeda,

- T.; Adachi, C.; Taniguchi, Y.; Shirota, Y. *Chem. Commun.* **2000**, 1923. (c) Mochizuki, H.; Hasui, T.; Kawamoto, M.; Ikeda, T.; Adachi, C.; Taniguchi, Y.; Shirota, Y. *Macromolecules* **2003**, *36*, 3457.
- [32] Usta, H.; Facchetti, A.; Marks, T. J. *Acc. Chem. Res.* **2011**, *44*, 501-510.
- [33] de Leeuw, D. M.; Simenon, M. M. J.; Brown, A. R.; Einerhand, R. E. F. *Synth. Met.* **1997**, *87*, 53-59.
- [34] Weitz, R. T.; Amsharov, K.; Zschieschang, U.; Villas, E. B.; Goswami, D. K.; Burghard, M.; Dosch, H.; Jansen, M.; Kern, K.; Klauk, H. *J. Am. Chem. Soc.* **2008**, *130*, 4637-4645.
- [35] Chiang, C. K.; Fincher, C. R.; Park, Y. W.; Heeger, A. J.; Shirakawa, H.; Louis, E. J.; Gau, S. C.; MacDiarmid, A. G. *Phys. Rev. Lett.* **1977**, *39*, 1098.
- [36] Tsumura, A.; Koezuka, H.; Ando, T. *Appl. Phys. Lett.* **1986**, *49*, 1210.
- [37] Warta, W.; Karl, N. *Phys. Rev. B* **1985**, *32*, 1172.
- [38] (a) Karl, N.; Marktanner, J. *Mol. Cryst. Liq. Cryst.* **2001**, *355*, 149. (b) Ito, K.; Suzuki, T.; Sakamoto, Y.; Kubota, D.; Inoue, Y.; Sato, F.; Tokito, S. *Angew. Chem., Int. Ed.* **2003**, *42*, 1159.
- [39] Lin, Y. Y.; Gundlach, D. J.; Nelson, S. F.; Jackson, T. N. *IEEE Electron Device Lett.* **1997**, *18*, 606.
- [40] Kelley, T. W.; Muires, D. V.; Baude, P. F.; Smith, T. P.; Jones, T. D. *Mater. Res. Soc. Symp. Proc.* **2003**, *771*, 169.
- [41] Nayak, P. K.; Periasamy, N. *Org. Electron.* **2009**, *10*, 1396.
- [42] Chen, Z.; Muller, P.; Swager, T. M. *Org. Lett.* **2006**, *8*, 273.
- [43] Klauk, H.; Zschieschang, U.; Weitz, R. T.; Meng, H.; Sun, F.; Nunes, G.; Keys, D. E.; Fincher, C. R.; Xiang, Z. *Adv. Mater.* **2007**, *19*, 3882.
- [44] Ito, K.; Suzuki, T.; Sakamoto, Y.; Kubota, D.; Inoue, Y.; Sato, F.; Tokito, S. *Angew. Chem., Int. Ed.* **2003**, *42*, 1159.
- [45] Jurchescu, O. D.; Popinciuc, M.; Wees, B. J. v.; Palstra, T. T. M. *Adv. Mater.* **2007**, *19*, 688.
- [46] Mondal, R.; Adhikari, R. M.; Shah, B. K.; Neckers, D. C. *Org. Lett.* **2007**, *9*, 2505.

- [47] Mondal, R.; Shah, B. K.; Neckers, D. C. *J. Am. Chem. Soc.* **2006**, *128*, 9612.
- [48] Okamoto, H.; Kawasaki, N.; Kaji, Y.; Kubozono, Y.; Fujiwara, A.; Yamaji, M. *J. Am. Chem. Soc.* **2008**, *130*, 10470.
- [49] Kawasaki, N.; Kubozono, Y.; Okamoto, H.; Fujiwara, A.; Yamaji, M. *Appl. Phys. Lett.* **2009**, *94*, 043310.
- [50] Wang, C.; Dong, H.; Li, H.; Zhao, H.; Meng, Q.; Hu, W. *Cryst. Growth Des.* **2010**, *10*, 4155.
- [51] Mativetsky, J. M.; Kastler, M.; Savage, R. C.; Gentilini, D.; Palma, M.; Pisula, W.; Mullen, K.; Samori, P. *Adv. Funct. Mater.* **2009**, *19*, 2486.
- [52] Xiao, S. X.; Myers, M.; Miao, Q.; Sanaur, S.; Pang, K. L.; Steigerwald, M. L.; Nuckolls, C. *Angew. Chem., Int. Ed.* **2005**, *44*, 7390.
- [53] Funahashi, M. *Polym. J.* **2009**, *41*, 459.
- [54] Shklyarevskiy, I. O.; Jonkheijm, P.; Stutzmann, N.; Wasserberg, D.; Wondergem, H. J.; Christianen, P. C. M.; Schenning, A.; de Leeuw, D. M.; Tomovic, Z.; Wu, J. S.; Mullen, K.; Maan, J. C. *J. Am. Chem. Soc.* **2005**, *127*, 16233.
- [55] Zhan, X.; Facchetti, A.; Barlow, S.; Marks, T. J.; Ratner, M. A.; Wasielewski, M. R.; Marder, S. R. *Adv. Mater.* **2011**, *23*, 268-284.
- [56] Ego, C.; Marsitzky, D.; Becker, S.; Zhang, J.; Grimsdale, A. C.; Müllen, K.; MacKenzie, J. D.; Silva, C.; Friend, R. H. *J. Am. Chem. Soc.* **2003**, *125*, 437.
- [57] Sadrai, M.; Hadel, L.; Sauers, R. R.; Husain, S.; Krogh-Jespersen, K.; Westbrook, J. D.; Bird, G. R. *J. Phys. Chem.* **1992**, *96*, 7988.
- [58] O'Neil, M. P.; Niemczyk, M. P.; Svec, W. A.; Gosztola, D.; Gaines III, G. L.; Wasielewski, M. R. *Science* **1992**, *257*, 63.
- [59] Law, K.-Y. *Chem. Rev.* **1993**, *93*, 449.
- [60] Schenning, A. P. H. J.; Herrikhuyzen, J. v.; Jonkheijm, P.; Chen, Z.; Würthner, F.; Meijer, E. W. *J. Am. Chem. Soc.* **2002**, *124*, 10252.
- [61] (a) Würthner, F. *Chem. Commun.* **2004**, 1564. (b) Elemans, J. A. A. W.; van Hameren, R.; Nolte, R. J. M.; Rowan, A. E. *Adv. Mater.* **2006**, *18*, 1251. (c) Zang, L.; Che, Y.; Moore, J. S. *Acc.*

- Chem. Res.* **2008**, *41*, 1596. (d) Bhosale, S. V.; Jani, C. H.; Langford, S. J. *Chem. Soc. Rev.* **2008**, *37*, 331. (e) Chen, Z.; Lohr, A.; Saha-Möller, C. R.; Würthner, F. *Chem. Soc. Rev.* **2009**, *38*, 564.
- [62] (a) Li, Y.; Wang, Z. *Org. Lett.* **2009**, *11*, 1385-1387. (b) Li, Y.; Gao, J.; Di Motta, S.; Negri, F.; Wang, Z. *J. Am. Chem. Soc.* **2010**, *132*, 4208-4213.
- [63] (a) Jiao, C.; Huang, K.-W.; Luo, J.; Zhang, K.; Chi, C.; Wu, J. *Org. Lett.* **2009**, *11*, 4508-4511. (b) Li, Y.; Hao, L.; Fu, H.; Pisula, W.; Feng, X.; Wang, Z. *Chem. Comm.* **2011**, *47*, 10088-10090. (c) Zhu, L.; Jiao, C.; Xia, D.; Wu, J. *Tetrah. Lett.* **2011**, *52*, 6411-6414. (d) Liu, X.-T.; Guo, J.-F.; Ren, A.-M.; Huang, S.; Feng, J.-K. *J. Org. Chem.* **2012**, *77*, 585-597.
- [64] (a) Han, M. Y.; Özyilmaz, B.; Zhang, Y.; Kim, P. *Phys. Rev. Lett.* **2007**, *98*, 206805. (b) Wang, X.; Ouyang, Y.; Li, X.; Wang, H.; Guo, J.; Dai, H. *Phys. Rev. Lett.* **2008**, *100*, 206803. (c) Yan, Q.; Huang, B.; Yu, J.; Zheng, F.; Zang, J.; Wu, J.; Gu, B.-L.; Liu, F.; Duan, W. *Nano Lett.* **2007**, *7*, 1469-1473.
- [65] (a) Geim, A. K.; Novoselov, K. S. *Nature Materials* **2007**, *6*, 183-191. (b) Novoselov, K. S.; Jiang, D.; Schedin, F.; Booth, T. J.; Khotkevich, V. V.; Morozov, S. V.; Geim, A. K. *Proc. Natl Acad. Sci. USA* **2005**, *102*, 10451-10453. (c) Novoselov, K. S.; Geim, A. K.; Morozov, S. V.; Jiang, D.; Katsnelson, M. I.; Grigorieva, I. V.; Dubonos, S. V.; Firsov, A. A. *Nature* **2005**, *438*, 197-200. (d) Zhang, Y., Tan, J. W., Stormer, H. L., Kim, P. *Nature* **2005**, *438*, 201-204.
- [66] Murphy, A. R.; Frechet, J. M. J. *Chem. Rev.* **2007**, *107*, 1066.
- [67] Garnier, F.; Yassar, A.; Hajlaoui, R.; Horowitz, G.; Deloffre, F.; Servet, B.; Ries, S.; Alnot, P. *J. Am. Chem. Soc.* **1993**, *115*, 8716.
- [68] Laquindanum, J. G.; Katz, H. E.; Lovinger, A. J. *J. Am. Chem. Soc.* **1998**, *120*, 664.
- [69] (a) Ortiz, R. P.; Casado, J.; Gonzalez, S. R.; Hernandez, V.; Navarrete, J. T. L.; Viruela, P. M.; Orti, E.; Takimiya, K.; Otsubo, T. *Chem.-Eur. J.* **2010**, *16*, 470-484. (b) Ortiz, R. P.; Casado, J.; Hernandez, V.; Navarrete, J. T. L.; Viruela, P. M.; Orti, E.; Takimiya, K.; Otsubo, T. *Angew. Chem., Int. Ed.* **2007**, *46*, 9057-9061. (c) Fazzi, D.; Canesi, E. V.; Negri, F.; Bertarelli, C.; Castiglioni, C. *ChemPhysChem* **2010**, *11*, 3685-3695.
- [70] (a) Takahashi, T.; Matsuoka, K. I.; Takimiya, K.; Otsubo, T.; Aso, Y. *J. Am. Chem. Soc.* **2005**, *127*, 8928-8929. (b) Ribierre, J. C.; Fujihara, T.; Watanabe, S.; Matsumoto, M.; Muto, T.; Nakao, A.; Aoyama, T. *Adv. Mater.* **2010**, *22*, 1722-1726. (c) Ribierre, J. C.; Watanabe, S.; Matsumoto, M.; Muto, T.; Nakao, A.; Aoyama, T. *Adv. Mater.* **2010**, *22*, 4044-4048.

- [71] (a) Agostinelli, T., Caironi, M., Natali, D., Sampietro, M., Dassa, G., Canesi, E. V., Bertarelli, C., Zerbi, G., Cabanillas-Gonzalez, J., De Silvestri, S.; Lanzani, G. *J. Appl. Phys.* **2008**, *104*, 114508. (b) Yao, Y.; Liang, Y. Y.; Shrotriya, V.; Xiao, S. Q.; Yu, L. P.; Yang, Y. *Adv. Mater.* **2007**, *19*, 3979–3983.
- [72] (a) Zhang, F. L.; Mammo, W.; Andersson, L. M.; Admassie, S.; Andersson, M. R.; Inganas, O. *Adv. Mater.* **2006**, *18*, 2169–2173. (b) Zimmerman, J. D.; Diev, V. V.; Hanson, K.; Lunt, R. R.; Yu, E. K.; Thompson, M. E.; Forrest, S. R. *Adv. Mater.* **2010**, *22*, 2780–2783.
- [73] (a) Zimbovskaya, N. A.; Pederson, M. R. *Physics Reports* **2011**, *509*, 1-87. (b) Del Nero, J.; de Souza, F. M.; Capaz, R. B. *J. Comp. Theor. Nanoscience* **2010**, *7*, 503-516. (c) Moth-Poulsen, K.; Bjornholm, T. *Nature Nanotechnology* **2009**, *4*, 551-556. (d) Choi, H.; Mody, C. C. M. *Social Studies Science* **2009**, *39*, 11-50. (e) Heath, J. R. *Ann. Rev. Mater. Res.* **2009**, *39*, 1-23.
- [74] (a) Coropceanu, V.; Cornil, J.; da Silva, D. A.; Olivier, Y.; Silbey, R.; Brédas, J.-L. *Chem. Rev.* **2007**, *107*, 926–952. (b) Brédas, J.-L.; Beljonne, D.; Coropceanu, V.; Cornil, J. *Chem. Rev.* **2004**, *104*, 4971.
- [75] Brédas, J.-L.; Calbert, J. P.; da Silva, D. A.; Cornil, J. *Proc. Natl. Acad. Sci. USA* **2002**, *99*, 5804.
- [76] Moon, H.; Zeis, R.; Borkent, E. J.; Besnard, C.; Lovinger, A. J.; Siegrist, T.; Kloc, C.; Bao, Z. *J. Am. Chem. Soc.* **2004**, *126*, 15322.
- [77] (a) Chen, J. H.; Subramanian, S.; Parkin, S. R.; Siegler, M.; Gallup, K.; Haughn, C.; Martin, D. C.; Anthony, J. E. *J. Mater. Chem.* **2008**, *18*, 1961–1969. (b) Park, S. K.; Jackson, T. N.; Anthony, J. E.; Mourey, D. A. *Appl. Phys. Lett.* **2007**, *91*, 063514. (c) Anthony, J. E. *Chem. Rev.* **2006**, *106*, 5028–5048. (d) Anthony, J. E.; Brooks, J. S.; Eaton, D. L.; Parkin, S. R. *J. Am. Chem. Soc.* **2001**, *123*, 9482–9483.
- [78] Gsanger, M.; Oh, J. H.; Konemann, M.; Hoffken, W.; Krause, A. M.; Bao, Z.; Wurthner, F. *Angew. Chem., Int. Ed. Engl.* **2010**, *49*, 740–743.
- [79] Anthony, J. E.; Facchetti, A.; Heeney, M.; Marder, S. R.; Zhan, X. *Adv. Mater.* **2010**, *22*, 3876-3892.
- [80] (a) Sleigh, J. P.; McMahon, D. P.; Troisi, A. *Appl. Phys. A* **2009**, *95*, 147-152. (b) Martinelli, N. G.; Olivier, Y.; Athanasopoulos, S.; Delgado, M. C. R.; Pigg, K. R.; da Silva, D. A.; Sanchez-Carrera, R. S.; Venuti, E.; Della Valle, R. G.; Brédas, J.-L.; Beljonne, D.; Cornil, J.

*ChemPhysChem* **2009**, *10*, 2265–2273. (c) Troisi, A. *Mol. Simul.* **2006**, *32*, 707–716. (d) Cheung, D. L.; Troisi, A. *Phys. Chem. Chem. Phys.* **2008**, *10*, 5941–5952. (e) Troisi, A.; Orlandi, G. *J. Phys. Chem. A* **2006**, *110*, 4065–4070. (f) Troisi, A. *Chem. Soc. Rev.* **2011**, *40*, 2347–2358.

[81] Troisi, A.; Orlandi, G. *Chem. Phys. Lett.* **2001**, *344*, 509–518.

[82] McRae, E. G.; Kasha, M. J. *Chem. Phys.* **1958**, *28*, 721.

[83] Ambrosek, D.; Marciniak, H.; Lochbrunner, S.; Tatchen, J.; Li, X.-Q.; Würthner, F.; Kühn, O. *Phys. Chem. Chem. Phys.* **2011**, *13*, 17649–17657.

[84] (a) Virkar, A. A.; Mannsfeld, S.; Bao, Z.; Stingelin, N. *Adv. Mater.* **2010**, *22*, 3857. (b) Baklar, M. A.; Koch, F.; Kumar, A.; Domingo, E. B.; Campoy-Quiles, M.; Feldman, K.; Yu, L.; Wobkenberg, P.; Ball, J.; Wilson, R. M.; McCulloch, I.; Kreouzis, T.; Heeney, M.; Anthopoulos, T.; Smith, P.; Stingelin, N. *Adv. Mater.* **2010**, *22*, 3942.

[85] Sonar, P.; Lim, J. P. F.; Chan, K. L. *Energy Environ. Sci.* **2011**, *4*, 1558.

[86] Burtman, V.; Alexander, Z.; Pakoulev, A. V. *Int. J. Mol. Sci.* **2011**, *12*, 173–225.

# CHAPTER 3 - THEORETICAL METHODS FOR THE STUDY OF STRUCTURAL, ELECTRONIC, OPTICAL AND CHARGE TRANSPORT PROPERTIES OF ORGANIC SEMICONDUCTORS

In this Chapter, we introduce the basic principles of the Modern Computational Chemistry methods adopted to study the structural, electronic, and charge transport properties of the organic semiconductors considered in this text. In particular, a fundamental description of the employed Quantum-Chemical methods is first provided in Section 3.1; then, the principles of Molecular Mechanics and Molecular Dynamics are dealt with in Section 3.2; finally, the basics of a Kinetic Monte Carlo simulation are described in Section 3.3.

## 3.1 Quantum Mechanics

Quantum-Chemical methods have been mainly used in this work to obtain an accurate and realistic description of those properties and interactions which are closely linked to the electronic structure of the molecular materials. The following overview encompasses several theories, ranging from Hartree-Fock and Post-Hartree-Fock methods to Semi-empirical methods and Density Functional Theory, employed to find a suitable representation of the electronic wavefunction.

The notation and terminology presented herein are primarily taken from the following texts: Levine,<sup>1</sup> Cohen-Tannoudji,<sup>2</sup> Szabo and Ostlund,<sup>3</sup> Jensen,<sup>4</sup> Cramer,<sup>5</sup> and Koch and Holstein.<sup>6</sup>

### 3.1.1 The Schrödinger equation

To describe the electronic structure of a stationary organic molecular system, the principal quantum-mechanical tool is the non-relativistic, time-independent Schrödinger equation:

$$\mathcal{H}|\Psi_i(\bar{r}_1, \bar{r}_2, \bar{r}_3, \dots, \bar{r}_N; \bar{R}_1, \bar{R}_2, \bar{R}_3, \dots, \bar{R}_M)\rangle = E_i|\Psi_i(\bar{r}_1, \bar{r}_2, \bar{r}_3, \dots, \bar{r}_N; \bar{R}_1, \bar{R}_2, \bar{R}_3, \dots, \bar{R}_M)\rangle \quad (3.1)$$

where  $\mathcal{H}$  is the Hamiltonian operator for any system with  $N$  electrons and  $M$  nuclei, described by position vectors  $\bar{r}_i$  and  $\bar{R}_A$ , respectively. In atomic units, the Hamiltonian operator in differential form is:

$$\mathcal{H} = -\frac{1}{2} \sum_{i=1}^N \nabla_i^2 - \frac{1}{2} \sum_{A=1}^M \frac{1}{M_A} \nabla_A^2 - \sum_{i=1}^N \sum_{A=1}^M \frac{Z_A}{r_{iA}} + \sum_{i=1}^N \sum_{j>i}^N \frac{1}{r_{ij}} + \sum_{A=1}^M \sum_{B>A}^M \frac{Z_A Z_B}{R_{AB}} \quad (3.2)$$

where  $r_{iA} = |r_i - R_A|$  is the distance between the  $i$ -th electron and  $A$ -th nucleus,  $r_{ij} = |r_i - r_j|$  is the distance between the  $i$ -th electron and  $j$ -th electron,  $R_{AB} = |R_A - R_B|$  is the distance between the  $A$ -th nucleus and  $B$ -th nucleus,  $M_A$  is the ratio of the mass of nucleus  $A$  to the mass of an electron,  $Z_A$  is the atomic number of nucleus  $A$ , and the Laplacian operators  $\nabla_i^2$  and  $\nabla_A^2$  involve differentiation with respect to the coordinates of the  $i$ -th electron and  $A$ -th nucleus, respectively. In the Hamiltonian operator, the first two terms represent the kinetic energies of the electrons and nuclei, respectively; the third term represents the electrostatic interactions (Coulombic attraction) between the electrons and nuclei; and the fourth and fifth terms represent Coulombic electron-electron and nuclear-nuclear repulsions, respectively.

As electrons are much lighter than nuclei, one can approximate that the electrons move within a stationary field of fixed nuclei. This assumption, which is known as the Born-Oppenheimer approximation, allows to consider the nuclear and electronic motions separately, so that in Eq. (3.2) the nuclear kinetic term can be neglected while the nuclear repulsion term can be considered a constant. The remaining terms define the electronic Hamiltonian:

$$\mathcal{H}_{el} = -\frac{1}{2} \sum_{i=1}^N \nabla_i^2 - \sum_{i=1}^N \sum_{A=1}^M \frac{Z_A}{r_{iA}} + \sum_{i=1}^N \sum_{j>i}^N \frac{1}{r_{ij}} \quad (3.3)$$

The eigenfunction associated with  $\mathcal{H}_{el}$  is the electronic wavefunction  $\Psi_{el} = \Psi_{el}(\bar{r}_i; \bar{R}_A)$ , which explicitly depends on the electronic coordinates and only parametrically on the nuclear coordinates, leading to the electronic Schrödinger equation:

$$\mathcal{H}_{el} |\Psi_{el}(\bar{r}_i; \bar{R}_A)\rangle = E_{el}(\bar{R}_A) |\Psi_{el}(\bar{r}_i; \bar{R}_A)\rangle \quad (3.4)$$

Note that  $\Psi_{el}$  is not observable; the only physical interpretation comes from the probability to find an electron within a defined volume, as given by  $|\Psi_{el}(\bar{r}_1, \bar{r}_2, \bar{r}_3, \dots, \bar{r}_N)|^2 d\bar{r}_1, d\bar{r}_2, d\bar{r}_3, \dots, d\bar{r}_N$ . By the inclusion of the nuclear repulsion, the total energy for a system of fixed nuclei is obtained as:

$$E_{total}(\bar{R}_A) = E_{el}(\bar{R}_A) + \sum_{A=1}^M \sum_{B>A}^M \frac{Z_A Z_B}{R_{AB}} \quad (3.5)$$

This total energy function provides a potential energy surface for nuclear motion.

As the Hamiltonian for the motion of nuclei in the average field of the fast-moving electrons is:

$$\mathcal{H}_n = -\frac{1}{2} \sum_{A=1}^M \frac{1}{M_A} \nabla_A^2 + E_{total}(\bar{R}_A) \quad (3.6)$$

the corresponding nuclear Schrödinger equation

$$\mathcal{H}_n |\Psi_n(\bar{R}_A)\rangle = E_n |\Psi_n(\bar{R}_A)\rangle \quad (3.7)$$

describes the vibrational, translational, and rotational modes of the molecular system.

In addition to the spatial wavefunction  $\Psi_{el}(\bar{r}_i; \bar{R}_A)$ , spin wavefunctions  $\alpha(\omega)$  and  $\beta(\omega)$  representing the non-classical term for spin must be introduced to completely describe an electron in the nonrelativistic theory. An electronic wavefunction that describes both the spatial and spin components is defined as a spin orbital  $\chi(\bar{x})$ , where  $\bar{x}$  indicates both the spatial and spin components. As electrons are fermions, it must be satisfied the antisymmetry principle, which states that a many-electron wavefunction must be antisymmetric with respect to interchange of  $\bar{x}_i$  for any two electrons:

$$\Psi(\bar{x}_1, \dots, \bar{x}_i, \dots, \bar{x}_j, \dots, \bar{x}_N) = -\Psi(\bar{x}_1, \dots, \bar{x}_j, \dots, \bar{x}_i, \dots, \bar{x}_N) \quad (3.8)$$

### 3.1.2 The Hartree-Fock method

The impossibility of treating exactly the many-body electronic repulsion term in the electronic Schrödinger equation leads to the next approximation in which each electron is considered to move in the mean field due to all other electrons. By introducing the concept of molecular orbitals through the Hartree, or independent-particle, approximation, the total wavefunction can be expressed as a product of orthonormal wavefunctions:

$$\Psi_{HP}(\bar{x}_1, \bar{x}_2, \dots, \bar{x}_N) = \chi_1(\bar{x}_1) \chi_2(\bar{x}_2) \dots \chi_N(\bar{x}_N) \quad (3.9)$$

Such an expression, which is known as the Hartree product, does not satisfy the indistinguishability requirement of the antisymmetry principle unfortunately. Instead, the most correct and convenient way to express the wavefunction of an  $N$ -electron system is by means of Slater determinants. According to the Hartree-Fock (HF) approximation, the ground state  $N$ -electron wavefunction can be described by a single Slater determinant of the form:

$$\Psi_{HF}(\bar{x}_1, \bar{x}_2, \dots, \bar{x}_N) = \frac{1}{\sqrt{N!}} \begin{vmatrix} \chi_1(\bar{x}_1) & \chi_2(\bar{x}_1) & \cdots & \chi_N(\bar{x}_1) \\ \chi_1(\bar{x}_2) & \chi_2(\bar{x}_2) & \cdots & \chi_N(\bar{x}_2) \\ \vdots & \vdots & \ddots & \vdots \\ \chi_1(\bar{x}_N) & \chi_2(\bar{x}_N) & \cdots & \chi_N(\bar{x}_N) \end{vmatrix} \equiv |\chi_1 \chi_2 \dots \chi_N| \quad (3.10)$$

Indeed, such a mathematical form completely fulfills the Pauli principle (*e.g.*, the interchange of any two coordinates  $\bar{x}_i$  exchanges two rows of the determinant bringing forth a change in sign of the wavefunction). The Slater determinant introduces both exchange (due to the requirement for the probability to be invariant to the exchange of space and spin coordinates of any two electrons) and correlation (the motion of two electrons with parallel spins is correlated) effects. However, since the motion of electrons with opposite spins is uncorrelated in single-determinant wavefunctions, the HF approach is said not to account for the correlation.

The Variational theorem imparts that, for any trial wavefunction  $\Psi$ , the expectation value of the Hamiltonian is always

$$\frac{\langle \Psi | \mathcal{H} | \Psi \rangle}{\langle \Psi | \Psi \rangle} \geq E_0 \quad (3.11)$$

with the equality occurring if and only if  $\Psi$  is an eigenvector of  $\mathcal{H}$  with eigenvalue  $E_0$ .

Within the HF method, which obeys the variational principle, the HF energy can be written in terms of one- and two-electron integrals and the nuclear repulsions, as:

$$E_{HF} = \sum_{i=1}^N I_i + \frac{1}{2} \sum_{i=1, j>1}^N (J_{ij} - K_{ij}) + \sum_{A=1, B>A}^M V_{AB} \quad (3.12)$$

where the first summation corresponds to the one-electron core integrals

$$I_i = \langle \chi_i(\bar{x}_i) | \hat{h}(i) | \chi_i(\bar{x}_i) \rangle = \int \chi_i^*(\bar{x}_i) \left( -\frac{1}{2} \nabla_i^2 - \sum_{A=1}^M \frac{Z_A}{r_{iA}} \right) \chi_i(\bar{x}_i) d\bar{x}_i \quad (3.13)$$

representing the contribution for a single electron in a field of nuclei, while the second summation is composed of the two-electron Coulomb  $J_{ij}$  and exchange  $K_{ij}$  integrals:

$$J_{ij} = \left\langle \chi_i(\bar{x}_1) \chi_j(\bar{x}_2) \left| \frac{1}{r_{12}} \right| \chi_i(\bar{x}_1) \chi_j(\bar{x}_2) \right\rangle = \iint \chi_i^*(\bar{x}_1) \chi_j^*(\bar{x}_2) \frac{1}{r_{12}} \chi_i(\bar{x}_1) \chi_j(\bar{x}_2) d\bar{x}_1 d\bar{x}_2 \quad (3.14)$$

$$K_{ij} = \left\langle \chi_i(\bar{x}_1) \chi_j(\bar{x}_2) \left| \frac{1}{r_{12}} \right| \chi_j(\bar{x}_1) \chi_i(\bar{x}_2) \right\rangle = \iint \chi_i^*(\bar{x}_1) \chi_j^*(\bar{x}_2) \frac{1}{r_{12}} \chi_j(\bar{x}_1) \chi_i(\bar{x}_2) d\bar{x}_1 d\bar{x}_2 \quad (3.15)$$

While the Coulomb term can be interpreted in a classical view as the electrostatic interaction of an electron in a spatially-averaged one-electron potential of all other electrons, the exchange term, arising directly from the asymmetric nature of the determinantal wavefunction, has fully quantum-mechanical nature.

In the ground state, the  $N$  electrons of a closed-shell neutral system are paired such that there are  $N/2$  occupied orbitals. As a consequence, according to the so-called restricted Hartree-Fock (RHF) formalism, spin can be eliminated from the orbital picture and the resulting closed-shell restricted ground state is:

$$\Psi_0 = |\chi_1 \chi_2 \dots \chi_{N-1} \chi_N| = |\psi_1 \bar{\psi}_1 \dots \psi_{N/2} \bar{\psi}_{N/2}| \quad (3.16)$$

having the restricted set of spin orbitals, written in terms of their spatial and spin parts, the form:

$$\chi_i(\bar{x}_i) = \begin{cases} \psi_j(\bar{r}_i) \alpha(\omega) \\ \psi_j(\bar{r}_i) \beta(\omega) \end{cases} = \begin{cases} \psi_j(\bar{r}_i) \\ \bar{\psi}_j(\bar{r}_i) \end{cases} \quad (3.17)$$

For a closed-shell and restricted set of orbitals, the spatial HF equation can be written:

$$\hat{f}(\bar{r}_1) |\psi_i(\bar{r}_1)\rangle = \varepsilon_i |\psi_i(\bar{r}_1)\rangle \quad (3.18)$$

where the Fock operator is defined as:

$$\hat{f}(\bar{r}_1) = \hat{h}(\bar{r}_1) + \sum_{j=1}^{N/2} 2J_j(\bar{r}_1) - \mathcal{K}_j(\bar{r}_1) \quad (3.19)$$

The closed-shell Coulomb and exchange operators are now defined in terms of spatial orbitals as:

$$\mathcal{J}_j(\bar{r}_1)\psi_i(\bar{r}_1) = \left[ \int d\bar{r}_2 \psi_j^*(\bar{r}_2) \frac{1}{r_{12}} \psi_j(\bar{r}_2) \right] \psi_i(\bar{r}_1) \quad (3.20a)$$

$$\mathcal{K}_j(\bar{r}_1)\psi_i(\bar{r}_1) = \left[ \int d\bar{r}_2 \psi_j^*(\bar{r}_2) \frac{1}{r_{12}} \psi_i(\bar{r}_2) \right] \psi_j(\bar{r}_1) \quad (3.20b)$$

To solve the spatial HF equation, it is usually performed a change of basis from molecular orbitals to atomic orbitals by means of the linear combination of atomic orbitals (LCAO) approximation, which allows to expand the  $K$  unknown molecular orbitals in the  $K$  basis functions chosen to represent the atomic orbitals (see Section 3.1.5):

$$\psi_i = \sum_{\mu=1}^K c_{i\mu} \varphi_{\mu} \quad i = 1, 2, \dots, K \quad (3.21)$$

where  $c_{i\mu}$  are a set of unknown expansion coefficients. Substituting  $\psi_i$  into the spatial HF equation yields a set of  $K$  equations known as the Roothaan equations, which can be written into matrix form as:

$$\mathbb{F}\mathbb{C} = \mathbb{S}\mathbb{C}\mathbb{E} \quad (3.22)$$

where  $\mathbb{F}$ , the Fock matrix, is a Hermitian  $K \times K$  matrix with the elements:

$$F_{\mu\nu} = \int d\bar{r}_1 \varphi_{\mu}^*(\bar{r}_1) \mathcal{H}(\bar{r}_1) \varphi_{\nu}(\bar{r}_1) \quad (3.23)$$

$\mathbb{C}$ , the coefficient matrix, is a Hermitian  $K \times K$  matrix;  $\mathbb{S}$ , the overlap matrix, is also a Hermitian  $K \times K$  matrix with elements:

$$S_{\mu\nu} = \int d\bar{r}_1 \varphi_{\mu}^*(\bar{r}_1) \varphi_{\nu}(\bar{r}_1) \quad (3.24)$$

and  $\mathbb{E}$  is a  $K \times K$  diagonal matrix consisting of one-electron spin orbital energies. The solution to the Roothaan equations is performed through an iterative procedure meant to obtain, by diagonalization, the optimal coefficients  $c_{i\mu}$  (the variational parameters), with respect to selected convergence criteria (e.g.,  $\varepsilon_i^{(\text{final})} \approx \varepsilon_i^{(\text{final}-1)}$ ). The so-called self-consistent field (SCF) procedure is sketched in Figure 3.1.

Note that if all the integrals appearing in Eq. (3.22) in the expression of the Fock and overlap matrices are evaluated, the method is referred to as Hartree-Fock *ab initio*.

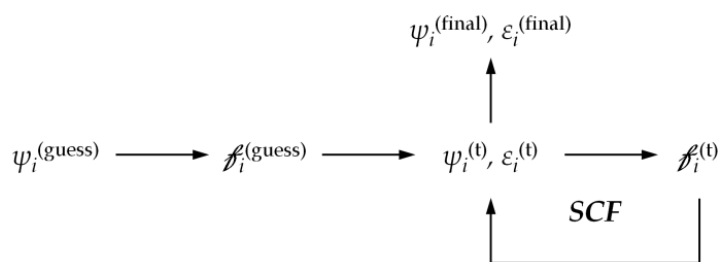


**Figure 3.1** Schematization of the HF self-consistent field method.

With RHF spin orbitals and determinants, the spatial orbitals are constrained to be identical for both  $\alpha$  and  $\beta$  spins. In order to allow for spin polarization effects derived from the interaction of electrons with like spins, it is necessary to permit the spins to occupy different regions of space and treat them individually in the construction of the molecular orbitals. The separation of the two spins into two different determinants leads to the unrestricted Hartree-Fock (UHF) formalism. Note that unrestricted wavefunctions are generally not eigenfunctions of the spin operator  $S^2$ . Additionally, because the spatial relaxation of the spins brings forth different spin contributions which do not cancel each other within a same orbital like the RHF case, the final wavefunction can be contaminated by the inclusion of higher spin states (*e.g.*, triplet, pentet, *etc.* states for singlet wavefunctions and quartet, sextet, *etc.* states for doublet wavefunctions).

In general, the unrestricted formalism is typically a good approximation for doublets and triplets because unrestricted wavefunctions have lower energies than their restricted counterparts. Moreover, it is an adequate method to account for the correlation in the description of the biradicaloid character eventually shown by a singlet wavefunction, whereas for closed-shell singlets unrestricted wavefunctions frequently collapse to the corresponding restricted singlets.

### 3.1.3 Post-Hartree-Fock and related methods

Within Hartree-Fock theory, the fundamental assumption is made that each electron moves in a static field that is created by all other electrons. Thus, instantaneous electron-electron repulsion processes, or the correlated motions of electrons, are not taken into account. Among the post-Hartree-Fock methods that have been formulated to address these issues

can be found the formalisms based on Configuration Interaction and the Møller-Plesset Perturbation Theory.

In Configuration Interaction (CI), the exact wavefunction is represented as a linear combination of  $N$ -electron trial functions:

$$\Psi \approx C_0|\Phi_0\rangle + \sum_{a,p} C_a^p|\Phi_a^p\rangle + \sum_{a<b,p<q} C_{ab}^{pq}|\Phi_{ab}^{pq}\rangle + \sum_{a<b<c,p<q<r} C_{abc}^{pqr}|\Phi_{abc}^{pqr}\rangle + \dots \quad (3.25)$$

Each trial function is the Slater determinant that is obtained, in a given basis set, as a consequence of a singly, doubly, *etc.* excitation, as depicted in Figure 3.2, hence Eq. (3.25) can be expressed more simply as:

$$\Psi \approx C_0|\Phi_0\rangle + \sum C_S|S\rangle + \sum C_D|D\rangle + \sum C_T|T\rangle + \dots \quad (3.26)$$

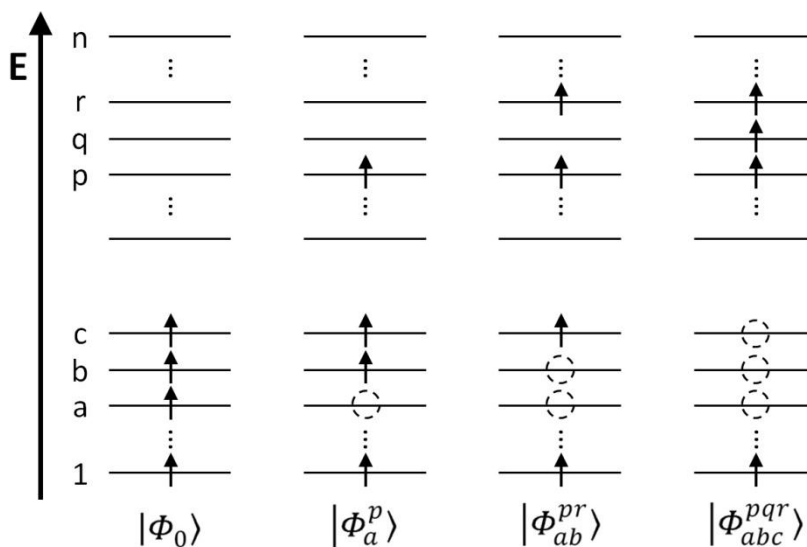


**Figure 3.2** Excited determinants  $|\Phi_a^p\rangle$ ,  $|\Phi_{ab}^{pq}\rangle$ , and  $|\Phi_{abc}^{pqr}\rangle$  represent the promotion of one, two, or three electrons from occupied molecular orbital levels, *i.e.*,  $a$ ,  $b$ , and  $c$ , into unoccupied molecular orbital levels, *i.e.*,  $p$ ,  $q$ , and  $r$ , in comparison with the reference HF Slater determinant  $|\Phi_0\rangle$ .

Eq. (3.26) is the form of the Full Configuration Interaction (Full CI) wavefunction, which represents the exact solution within the Born-Oppenheimer approximation. In practice, the expansion has to be truncated at a certain point, *e.g.*, the second term leading to Single

Configuration Interaction (CI), the third term leading to Single and Double Configuration Interaction (CISD), *etc.*, resulting in an improved, but not exact, solution to the Schrödinger equation.

Brillouin's theorem states that: (i) all matrix elements  $\langle \Phi_0 | \mathcal{H} | S \rangle$  are zero; (ii) all matrix elements of the Hamiltonian between determinants that differ by more than two spin orbitals are zero. Point (i) means that there is no interaction between the HF reference ground state and single excitations. However, they still can indirectly mix since there is coupling between  $\Phi_0$  and double excitations that interact with single excitations.

Multi-Configurational Self-Consistent Field (MCSCF) is a method which uses a linear combination of Configuration State Functions (CSFs) to approximate the exact electronic wavefunction. In a MCSCF calculation, the set of coefficients of both the configuration determinants ( $C_i$ , Eq. (3.26)) and the basis functions in the molecular orbitals ( $c_{i\mu}$ , Eq. (3.21)) are varied to obtain the total electronic wavefunction with the lowest possible energy. This method can be considered a combination between CI (where the molecular orbitals are not varied but the expansion of the wavefunction) and HF (where there is only one determinant but the molecular orbitals are varied).

A particular MCSCF approach is the Complete Active Space SCF (CASSCF) method, where the linear combination of CSFs includes all those arising from a selected number of electrons in a selected number of orbitals. For example, the definition of a CAS(12,8) implies that 12 valence electrons are distributed between all configurations that can be constructed from 8 chosen molecular orbitals.

MCSCF wavefunctions are often used as reference states for multi-reference perturbation theories like complete active space perturbation theory (*vide infra*).

Perturbation Theory is applicable when the Hamiltonian of a system can be written as:

$$\mathcal{H}(\lambda) = \mathcal{H}_0 + \lambda \mathcal{H}' \quad (3.27)$$

where the eigenstates and eigenvalues of  $\mathcal{H}_0$  are known and  $\mathcal{H}'$  is the perturbation; by definition,  $\mathcal{H}'$  is much smaller than  $\mathcal{H}_0$ .  $\lambda$  is a parameter ranging from zero to one. The

eigenvalues and eigenfunctions of  $\mathcal{H}$  are expanded in a Taylor series in  $\lambda$  of nth-order correction terms:

$$E_i \cong E_i^{(0)} + \lambda E_i^{(1)} + \lambda^2 E_i^{(2)} + \dots \quad (3.28a)$$

$$\Psi_i \cong \Psi_i^{(0)} + \lambda \Psi_i^{(1)} + \lambda^2 \Psi_i^{(2)} + \dots \quad (3.28b)$$

In Møller-Plesset Perturbation Theory (MPPT), the unperturbed electronic Hamiltonian is defined as the sum of one-electron Fock operators:

$$\mathcal{H}_0 = \sum_{i=1}^N f(\bar{x}_i) \quad (3.29)$$

The zeroth-order energy is given by:

$$E^{(0)} = \langle \Psi_{el} | \mathcal{H}_0 | \Psi_{el} \rangle \quad (3.30)$$

while the first-order energy correction is given by:

$$E^{(1)} = \langle \Psi_{el} | \mathcal{H}' | \Psi_{el} \rangle \quad (3.31)$$

where the perturbation is given by the difference between the real electronic Hamiltonian and the sum of the Fock operators, thus representing the correlation potential that in HF is treated as a mean field:

$$\mathcal{H}' = \mathcal{H} - \mathcal{H}_0 = \mathcal{H} - \sum_{i=1}^N f(\bar{x}_i) \quad (3.32)$$

Summation of the zeroth-energy and first-order energy correction gives:

$$E^{(0)} + E^{(1)} = \langle \Psi_{el} | \mathcal{H}_0 | \Psi_{el} \rangle + \langle \Psi_{el} | \mathcal{H}' | \Psi_{el} \rangle = \langle \Psi_{el} | \mathcal{H}_0 + \mathcal{H}' | \Psi_{el} \rangle = \langle \Psi_{el} | \mathcal{H} | \Psi_{el} \rangle \quad (3.33)$$

which is simply the HF energy.

In order to improve upon the perturbation, a second-order energy correction is made. Application of Brillouin's theorem and Condon-Slater rules reveals that only doubly-excited determinants contribute to the second-order Møller-Plesset correction. The second-order energy correction takes the form:

$$E^{(2)} = \frac{1}{4} \sum_{i>j}^{occ} \sum_{a>b}^{virt} \frac{[\langle \chi_i \chi_j | \chi_a \chi_b \rangle - \langle \chi_i \chi_j | \chi_b \chi_a \rangle]^2}{(\varepsilon_i + \varepsilon_j) - (\varepsilon_a + \varepsilon_b)} \quad (3.34)$$

where:

$$\langle \chi_i \chi_j | \chi_a \chi_b \rangle = \int \chi_i^*(\bar{x}_1) \chi_j^*(\bar{x}_2) \frac{1}{r_{12}} \chi_a(\bar{x}_1) \chi_b(\bar{x}_2) d\bar{x}_1 d\bar{x}_2 \quad (3.35a)$$

$$\langle \chi_i \chi_j | \chi_b \chi_a \rangle = \int \chi_i^*(\bar{x}_1) \chi_j^*(\bar{x}_2) \frac{1}{r_{12}} \chi_b(\bar{x}_1) \chi_a(\bar{x}_2) d\bar{x}_1 d\bar{x}_2 \quad (3.35b)$$

In these equations,  $\chi_i$  and  $\chi_j$  are occupied spin orbitals,  $\chi_a$  and  $\chi_b$  are virtual spin orbitals, and  $\varepsilon_i$ ,  $\varepsilon_j$ ,  $\varepsilon_a$ , and  $\varepsilon_b$  are the energies of the respective spin orbitals.

Single-reference second-order Møller-Plesset perturbation (MP2) theory is widely considered one of the simplest methods to compute the electron (dynamical) correlation. However, its use is limited to systems whose electronic ground state is non-degenerate and accurately represented by a single configuration of closed-shell or open-shell type. Problems might appear when the highest occupied and the lowest unoccupied orbitals in the reference wavefunction become nearly degenerate, leading to poor convergence or even divergence of the Møller-Plesset expansion (note that MPPT does not obey the variational principle). To account for these strong non-dynamical correlation effects, a multireference wavefunction is needed. A Complete Active Space Perturbation Theory such as CASPT2 is a multireference perturbation method that address dynamical correlation after a separate treatment of the non-dynamical correlation ensured by its CASSCF aspect.<sup>5,7</sup>

### 3.1.4 Semi-empirical methods

Due to the fact that Hartree-Fock calculations scale formally to the fourth power of the number of basis functions, semi-empirical methods have been introduced early on to reduce the number of integrals and allow for the study of large molecular systems. Semi-empirical methods reduce the computational cost by considering only valence electrons explicitly, and utilizing only minimal basis sets (see Section 3.1.5). The central assumption of semi-empirical methods is the Zero Differential Overlap (ZDO) approximation, which neglects all basis functions depending on the same electron coordinates when located on different atoms:

$$S = \langle \varphi_\mu^A | \varphi_\nu^B \rangle = \delta_{AB} \delta_{\mu\nu} \quad (3.36)$$

where  $S$  is the overlap integral between the basis functions  $\varphi_\mu$  and  $\varphi_\nu$  located on atoms (the so-called "centers" within semi-empirical methods)  $A$  and  $B$ , respectively;  $\delta_{ij}$  is the Kronecker delta:

$$\delta_{ij} = \begin{cases} 1, & \text{if } i = j \\ 0, & \text{if } i \neq j \end{cases} \quad (3.37)$$

Under the ZDO approximation, the overlap matrix  $S$  is reduced to a unit matrix, all one-electron integrals involving three centers (two from the basis function and one from the operator) are set to zero, and all three- and four-center two-electron integrals are neglected. The remaining integrals are parameterized based upon assignment on the basis of calculation or experiment to compensate for the approximations, hence the name "semi-empirical".

Several semi-empirical methods have been formulated according to a differently strict application of the ZDO approximation. In the Neglect of Diatomic Differential Overlap (NDDO) method, ZDO is applied exclusively between atomic orbitals centered on distinct atoms, such as:

$$S = \langle \varphi_\mu^A | \varphi_\nu^B \rangle = \delta_{AB} \quad (3.38)$$

In the Intermediate Neglect of Differential Overlap (INDO)<sup>8</sup> model, all two-center two-electron integrals that are not of the Coulomb type are neglected; in addition, to preserve rotational invariance, some of the integrals are made independent of the orbital type. Finally, in the Complete Neglect of Differential Overlap (CNDO)<sup>9</sup> approximation, only the Coulomb one-center and two-center two-electron integrals remain. Thus, the main difference between NDDO, INDO, and CNDO methods is the treatment of the two-electron integrals; while all one- and two-center integrals are kept in the NDDO approximation, INDO and CNDO reduce these to just two semi-empirical parameters.

### 3.1.5 Density Functional Theory

An alternative method to those based upon the Hartree-Fock formalism is found within Density Functional Theory (DFT), which moves from a totally different theoretical approach and yet delivers equations outwardly analogous.

The basis for DFT is the proof by Hohenberg and Kohn<sup>10a</sup> that the ground-state electronic energy of a molecular system is determined completely by the electron density, which, unlike a wavefunction, is observable. The electron density is defined as a multiple integral over the spin coordinates of all electrons and over all but one of the spatial variables:

$$\rho(\bar{r}_i) = N \int \dots \int |\Psi(\bar{x}_1, \bar{x}_2, \dots, \bar{x}_N)|^2 ds_1 d\bar{x}_2 \dots d\bar{x}_N \quad (3.39)$$

where  $\rho(\bar{r}_i)$  determines the probability of finding any of the  $N$  electrons within a volume element  $d\bar{r}_i$ , but with arbitrary spin while the other  $N - 1$  electrons have arbitrary positions and spin.

The First Hohenberg-Kohn theorem implies that, since  $\rho(\bar{r}_i)$  uniquely determines the Hamiltonian operator, the average value of any observable can be written as its functional:

$$\langle A \rangle = A[\rho(\bar{r}_i)] \quad (3.40)$$

Therefore, the total energy of the electronic system can be expressed as a functional of the electron density:

$$E = E[\rho] = T[\rho] + E_{eN}[\rho] + E_{ee}[\rho] \quad (3.41)$$

where  $T[\rho]$  represents the kinetic energy of the system, and  $E_{eN}[\rho]$  and  $E_{ee}[\rho]$  are the nuclear-electron and electron-electron interactions, respectively. The sum of  $T[\rho]$  and  $E_{ee}[\rho]$  is called the universal functional of Hohenberg and Kohn  $F_{HK}[\rho]$ ; if  $F_{HK}[\rho]$  were known exactly, the Schrödinger equation could be solved exactly. By extracting from  $E_{ee}[\rho]$  the Coulomb integral  $J[\rho]$ , it is given:

$$F_{HK}[\rho] = T[\rho] + J[\rho] + E_{ncl}[\rho] \quad (3.42)$$

where  $E_{ncl}[\rho]$  incorporates the non-classically defined electron-electron interactions of self-interaction, exchange, and electron correlation effects.

The Second Hohenberg-Kohn theorem, stating that  $F_{HK}[\rho]$  delivers the lowest energy if and only if the input density is the true ground-state density, is basically a restatement of the variational principle for DFT.

Kohn and Sham<sup>10b</sup> hypothesized that the Hamiltonian would be simpler if it were one for a system of non-interacting electrons that has the same density of some system where electrons

do interact. For such a system of non-interacting electrons, the kinetic energy is the sum of the individual electronic kinetic energies:

$$T_S = -\frac{1}{2} \sum_{i=1}^N \langle \phi_i(\bar{x}_i) | \nabla^2 | \phi_i(\bar{x}_i) \rangle \quad (3.43)$$

where  $\phi_i(\bar{x}_i)$  are Kohn-Sham (KS) orbitals (in complete analogy to HF orbitals) that are components of a Slater determinant that represents the ground-state wavefunction:

$$\theta_{KS}(\bar{x}_1, \bar{x}_2, \dots, \bar{x}_N) = \frac{1}{\sqrt{N!}} \begin{vmatrix} \phi_1(\bar{x}_1) & \phi_2(\bar{x}_1) & \cdots & \phi_N(\bar{x}_1) \\ \phi_1(\bar{x}_2) & \phi_2(\bar{x}_2) & \cdots & \phi_N(\bar{x}_2) \\ \vdots & \vdots & \ddots & \vdots \\ \phi_1(\bar{x}_N) & \phi_2(\bar{x}_N) & \cdots & \phi_N(\bar{x}_N) \end{vmatrix} \equiv |\phi_1 \phi_2 \dots \phi_N| \quad (3.44)$$

Note that the KS orbitals and their eigenvalues, in the strictest sense, have no physical significance being an abstract construct used to solve the many-body problem. Though, the interpretative power of these orbitals is commonly used in rationalising chemical phenomena; this is justified by noting that KS orbitals return the exact ground-state density and fully incorporate all non-classical effects.

Since  $T_S$  does not equal  $T[\rho]$ , by defining the exchange-correlation energy term  $E_{XC}[\rho]$ , which incorporates both the residual part of the true kinetic energy and the non-classical interactions as:

$$E_{XC}[\rho] \equiv (T[\rho] - T_S[\rho]) + (E_{ee}[\rho] - J[\rho]) = T_S[\rho] + E_{ncl}[\rho] \quad (3.45)$$

it is possible to express the total energy for the system as:

$$E[\rho] = T_S[\rho] + J[\rho] + E_{eN}[\rho] + E_{XC}[\rho] \quad (3.46)$$

With the introduction of orbitals, the minimized energy can be found through solving the pseudo-eigenvalue equation:

$$\mathcal{H}_i^{KS} \phi_i = \epsilon_i \phi_i \quad (3.47)$$

where the one-electron KS operator is defined as:

$$\mathcal{H}_i^{KS} = -\frac{1}{2} \nabla_i^2 - \sum_{A=1}^M \frac{Z_A}{r_{iA}} + \int \frac{\rho(\bar{r}_j)}{r_{ij}} d\bar{r}_j + V_{XC}(\bar{r}_i) \quad (3.48)$$

with

$$V_{XC} = \frac{\delta E_{XC}}{\delta \rho} \quad (3.49)$$

$V_{XC}$  is the exchange-correlation potential which is best described as the one-electron operator for which the expectation value of the KS Slater determinant is  $E_{XC}$ ; as it is not known how to express  $E_{XC}[\rho]$ , there is no explicit form for  $V_{XC}$  and reasonable approximations need to be made. To date, the three most commonly adopted approximations are the localized density approximation, the generalized gradient approximations, and the formation of hybrid functionals through the incorporation of part of the exact HF exchange in the DFT functionals.

By assuming that electrons move on a positive background charge distribution like a uniform electron gas, the Local Density Approximation (LDA) defines the  $E_{XC}[\rho]$  as:

$$E_{XC}^{LDA}[\rho] = \int \rho(\vec{r}) \varepsilon_{XC}[\rho(\vec{r})] d\vec{r} \quad (3.50)$$

where  $\varepsilon_{XC}[\rho(\vec{r})]$  is the exchange-correlation energy per particle of a uniform electron gas of density  $\rho(\vec{r})$ . Through the introduction of spin into Eq. (3.50), the Local Spin-Density Approximation (LSDA) is obtained, which allow to handle the unrestricted case. The term  $\varepsilon_{XC}[\rho(\vec{r})]$  can be segmented into exchange and correlation contributions:

$$\varepsilon_{XC}[\rho(\vec{r})] = \varepsilon_X[\rho(\vec{r})] + \varepsilon_C[\rho(\vec{r})] \quad (3.51)$$

The exchange portion is generally expressed as:

$$\varepsilon_X[\rho(\vec{r})] = -\frac{3}{4} \sqrt{\frac{\rho(\vec{r})}{\pi}} \quad (3.52)$$

As for the correlation contribution, no such explicit expression is known, with analytical expressions typically derived from highly accurate simulations of a homogeneous electron gas.

In a molecular system, the electron density is typically not spatially uniform. To improve upon this limitation in the LDA/LSDA approach, information pertaining to the gradient of the charge density  $\nabla\rho(\vec{r})$  is supplemented to the density  $\rho(\vec{r})$  at a particular point  $\vec{r}$ . Such an approximation is known as either Gradient Corrected (GCA) or Generalized Gradient

Approximation (GGA). In general, GGA functionals are constructed with a correction added to the original LDA/LSDA term:

$$\varepsilon_{X/C}^{GGA}[\rho(\vec{r})] = \varepsilon_{X/C}^{LDA/LSDA}[\rho(\vec{r})] + \Delta\varepsilon \left[ \frac{\nabla\rho(\vec{r})}{\rho^{4/3}(\vec{r})} \right] \quad (3.53)$$

where the subscript  $X/C$  indicates that the same functional form holds for either exchange or correlation. In principle, any exchange and correlation functionals developed under the GGA formalism can be added together to form the full exchange-correlation functional. The most popular GGA exchange functional was developed by Becke (often denoted B).<sup>11</sup> Popular correlation functionals include those developed by Perdew (P86),<sup>12</sup> Perdew and Wang (PW91),<sup>13</sup> and Lee, Yang, and Parr (LYP).<sup>14</sup>

In general, exchange contributions are significantly larger than correlation effects; thus, an accurate expression for the exchange energy is a requirement for a meaningful exchange-correlation functional. For this purpose, an exact Hartree-Fock exchange contribution can be incorporated into the DFT functional, obtaining a so-called hybrid functional. One of the most popular exchange-correlation hybrid functionals in current use, and one that is used predominately throughout the remainder of this text, is the three-parameter B3LYP functional:<sup>14-17</sup>

$$E_{XC}^{B3LYP} = (1 - a)E_X^S + aE_X^{HF} + b\Delta E_X^B + (1 - c)E_C^{VWN} + cE_C^{LYP} \quad (3.54)$$

which incorporates the exact HF exchange, exchange (Slater, S) and correlation (Vosko-Wilk-Nusair, VWN) terms derived from LSDA, and the Becke exchange and LYP correlation terms. The values optimized for  $a$ ,  $b$ , and  $c$  are 0.20, 0.72, and 0.81, respectively, as derived from atomization and ionization energies and proton and electron affinities within 1 kcal/mol of experimental results for 125 reference molecules containing main group elements.<sup>15</sup> Hence, it is clear the semi-empirical nature in hybrid functionals.

One of the most known issue of DFT methods, no matter what the approximation, is the so-called self-interaction energy error (SIE). The classical electrostatic repulsion term

$$J[\rho] = \iint \frac{\rho(\vec{r}_i)\rho(\vec{r}_j)}{r_{ij}} d\vec{r}_i d\vec{r}_j \quad (3.55)$$

does not completely vanish for a one-electron system because the density interacts with itself. As  $E_{XC}[\rho]$  is never exact and independent of  $J[\rho]$ , there is generally a residual energy due to self-interaction effects. As a consequence, DFT methods tend to reproduce an over-delocalized electron density (*i.e.*,  $\pi$ -conjugated system might feature exceeding charge delocalization). Because of these shortcomings, the use of non-corrected DFT methods may be questionable in dealing with charge-transfer states and systems featuring electrons weakly tied to the molecule.

In recent years, several functionals have been formulated to counteract SIE. Two examples are readily given by the long-range interaction corrected CAM<sup>18</sup> and M06<sup>19</sup> functionals. Though the systematic application of a computational method to a given system cannot be established *a priori*, broadly speaking, CAM seems to be suitable for charge-transfer states, while M06 seems to perform adequately in dealing with non-covalent interactions.<sup>18-20</sup>

Excited states within the DFT methodology are investigated through Time-Dependent DFT (TDDFT).<sup>21</sup> The formal foundation of TDDFT is the Runge-Gross theorem - the time-dependent analogue of the Hohenberg-Kohn theorem.<sup>21</sup> TDDFT employs the fact that the frequency-dependent linear response of a finite system with respect to a time-dependent perturbation has discrete poles at the exact, correlated excitation energies of the unperturbed system. In the Kohn-Sham formalism, the orbital eigenvalue differences of the ground state act as a first approximation to the excitation energies. TDDFT is usually most successful for low-energy excitations, because the high-lying KS virtual orbitals are typically poor.

### 3.1.6 Basis set

A linear combination of different basis functions is used to represent the different molecular orbitals. Thus, the quality of a calculation depends upon the number of basis functions used, keeping in mind that an infinite number of functions to be used is impossible in actual calculations.

Two types of orbitals are typically used in electronic-structure calculations. The first, Slater-Type Orbitals (STOs), have the form:

$$\chi_{\zeta,n,l,m}(r, \theta, \varphi) = NY_{l,m}(\theta, \varphi)r^{(n-1)}e^{-\zeta r} \quad (3.56)$$

where  $N$  is a normalization constant,  $Y_{l,m}(\theta, \varphi)$  is a spherical harmonic function, and  $\zeta$  the Slater orbital exponent. Gaussian-Type Orbitals (GTOs) can be written in terms of both polar and Cartesian coordinates:

$$\chi_{\zeta,n,l,m}(r, \theta, \varphi) = NY_{l,m}(\theta, \varphi)r^{(2n-2-l)}e^{-\alpha r^2} \quad (3.57a)$$

$$\chi_{\zeta,l_x,l_y,l_z}(x, y, z) = Nx^{l_x}y^{l_y}z^{l_z}e^{-\alpha r^2} \quad (3.57b)$$

where the sum of  $l_x$ ,  $l_y$ , and  $l_z$  determine the type of orbital, and  $\alpha$  is the Gaussian orbital exponent. Versus their STO counterparts, GTOs have two complicating factors due to their  $r^2$ -dependence. First, at the nucleus, GTOs have zero slope versus the "cusp" of the STO, thus GTOs have difficulty representing the behavior of the wavefunction near the nucleus and consequentially the energetics of the system. Second, GTOs fall off too rapidly at distances far from the nucleus, which obviously penalize the description of chemical bonds as well as non-covalent interactions. In order to overcome these issues, additional GTOs are necessary to achieve the same level of accuracy as STOs; to be more precise, several GTOs are combined to form contracted GTOs. However, the ease by which the GTOs can be integrated (the product of two Gaussians being a Gaussian) compensates for the addition of functions to improve the accuracy.

The simplest form for a contracted GTO is:

$$\phi^\mu = \sum_{i=1}^L d_{i\mu} \varphi_i^\mu(\alpha_{i\mu}) \quad (3.58)$$

where  $\varphi_i^\mu(\alpha_{i\mu})$  is the  $i$ -th GTO constituting the basis function  $\phi^\mu$ ,  $L$  is the contraction length, and  $d_{i\mu}$  is a contraction coefficient.

A minimal basis set is one that uses one basis function per atomic orbital of the electronic shells occupied in the free atom. Improvement upon this rather simplistic model is made through a double-zeta basis set; the term "zeta" arises from the Greek notation traditionally used for the Slater orbital exponent (denoted  $\zeta$ ). A double-zeta basis set employs two basis functions per atomic orbital. Further extension of the basis sets is done through triple-zeta, quadruple-zeta, *etc.* basis sets. In addition to the incorporation of more functions per atomic orbital, split-valence basis sets employ extra functions for each valence orbital, *e.g.*, the split-

valence double-zeta basis sets, which are now routinely used, employ one contraction per core atomic orbital and two contractions per valence orbital.

Basis sets can also be extended through the addition of polarization and diffuse functions. Atomic orbitals often become distorted (polarized) under the influence of other atoms within a molecular system. To account for these effects, polarization functions (often denoted \*) with higher angular momentum terms are added to the basis sets. Diffuse functions, *i.e.*, basis functions with small exponents  $\alpha$  (often denoted +), are added to account for properties that extend far away from the atomic nucleus, *e.g.*, for the proper description of loosely bound electrons in radical anions and molecular polarizability (dependent on the wavefunction tail). Thus, variations in the combination of these functions provide the ability to create the diverse assortment of basis sets utilized throughout the literature, including such examples as 3-21G, 6-31G\*, 6-31+G\*, and 6-311G\*\*.

## 3.2 Molecular Dynamics

Molecular Dynamics simulations have been performed in this work to evaluate thermally induced disorder effects on the charge transport of the molecular materials. In this Section, the principles of Molecular Mechanics and Molecular Dynamics are overviewed.

### 3.2.1 Molecular Mechanics

By ignoring electron motions and focusing only on nuclear coordinates, Molecular Mechanics (MM) uses Newtonian mechanics to model molecular systems. Due to its rather moderate computational cost, MM can readily handle even material assemblies with many thousands of atoms.

MM is strongly based on the definition of the so-called "force fields".<sup>22</sup> A Force Field (FF) is a coherent set of parametrical potential functions and parametrical values adopted to describe the potential energy of the system, which is given as a sum of individual energy terms:

$$\begin{aligned}
E &= E_{\text{covalent}} + E_{\text{non-covalent}} \\
&= (E_{\text{stretching}} + E_{\text{bending}} + E_{\text{torsion}}) + (E_{\text{electrostatic}} + E_{\text{vdW}})
\end{aligned} \tag{3.59}$$

There is not a correct form for each energy term; the empirical nature of a FF lies in the choice of those options providing the best compromise between accuracy and efficiency. Thus, many FFs have been developed, each of them featuring different formulations for the energy terms. For the sake of clarity, the formal structure of a FF may look as:<sup>22</sup>

$$\begin{aligned}
E(Q) &= \sum_{\text{bonds}} \frac{k_i^l}{2} (l_i - l_{i,0})^2 \\
&+ \sum_{\text{angles}} \frac{k_i^\theta}{2} (\theta_i - \theta_{i,0})^2 + \sum_{\text{dihedrals}} \frac{V_n}{2} (1 + \cos(n\omega - \gamma)) \\
&+ \sum_{A=1, B>A}^M \left( 4\varepsilon_{AB} \left[ \left( \frac{\sigma_{AB}}{R_{AB}} \right)^{12} - \left( \frac{\sigma_{AB}}{R_{AB}} \right)^6 \right] + \frac{q_A q_B}{4\pi\varepsilon_0 \varepsilon R_{AB}} \right)
\end{aligned} \tag{3.60}$$

where  $E(Q)$  is a function of the nuclear coordinates  $Q$ ; the first term refers to bond stretching, with  $k_i^l$  being Hooke's spring constant for the  $i$ -th bond and  $l_{i,0}$  being the equilibrium bond length; the second term refers to bond bending, with  $k_i^\theta$  being similarly the force constant and  $\theta_{i,0}$  being the equilibrium bond angle; the third term refers to torsions around bonds, with  $n$  describing a rotation that is periodic by  $2\pi/n$  and  $V_n$  determining the height of the barrier; the fourth term is a Lennard-Jones (LJ) potential accounting for van der Waals interactions between two atoms at distance  $R_{AB}$ , with  $\varepsilon_{AB}$  being the well depth and  $\sigma_{AB}$  being the collision diameter; the final term is the Coulombic interaction between two partial atomic charges (here assumed one for each atom)  $q_A$  and  $q_B$  at distance  $R_{AB}$ , with  $\varepsilon_0$  being the vacuum permittivity and  $\varepsilon$  the absolute permittivity of the medium.

Actually,  $E_{\text{stretching}}$  and  $E_{\text{bending}}$  are both expanded in a Taylor series that is terminated at a chosen order, in order to improve the approximation. Note that it is quite common to prefer a harmonic Hooke form to a Morse potential, as the former implies simpler calculations, when there is no need to account for bonds far from their equilibrium length and angle.

In addition to the terms in Eq. (3.59), other terms can be included, such as cross terms that reflect coupling between the internal coordinates, *e.g.*, the stretching/bending cross term for an A-B-C sequence of atoms:<sup>22</sup>

$$E_{\text{stretch/bend}} = k^{ABC} (\theta^{ABC} - \theta_0^{ABC}) [(l^{AB} - l_0^{AB}) + (l^{BC} - l_0^{BC})] \tag{3.61}$$

Other added terms are those formulated to represent specific interactions, such as hydrogen bond or  $\pi$ - $\pi$  interaction.

The electrostatics of the system can be described in terms of partial atomic charges or multipole expansion. As for the former, partial atomic charges approximate the quantum-mechanical electrostatic potential (of both nuclei and electrons) at a series of points surrounding the molecule; charge values are obtained by means of several possible methodologies, such as by fitting the electrostatic potential calculated *ab initio* or semi-empirically. As for the latter, a multipole expansion is a mathematical series representing the charge distribution of the system as a linear combination of point charges, dipoles, quadrupoles, *etc.*

Each force field relies on its own definition of atom types. An atom type is basically the set of values assumed by the parameters like those in Eq. (3.60) for a certain type of atom. Note that not only different atom types correspond to different elements, but also an  $sp^2$  carbon can substantially differ from an  $sp^3$  carbon in terms of atom type, or even an  $sp^2$  carbon bonded to a nitrogen rather than an oxygen. The atom types parametric values are determined by means of either experimental data fitting or high-level quantum-chemical, *ab initio* or semi-empirical, calculations.

Because of their empirical and specific nature, force fields must never be mixed, and the choice of a FF must be unambiguous.

### 3.2.2 Molecular dynamics simulations

The essence of a Molecular Dynamics (MD) simulation is to solve Newton's equations of motion for the atoms constituting the molecular system; if it is assumed that atoms interact according to molecular mechanics, the MD simulation is referred to as classical, and only nuclear motions are taken into account. Classical MD simulations are the ones that are dealt with in the remainder of this text.

MD is a deterministic, time-dependent computational method. Given at any time  $t$  for any atom its position  $\bar{q}$ , its linear momentum  $\bar{p}$ , and the force  $\bar{F}$  applied on it, it is always possible to determine  $(\bar{q}, \bar{p}, \bar{F})(t + \Delta t)$ . Hence, by the integration of Newton's equations of motion, a MD simulation delivers the trajectory of the atoms of the system. In addition to this, the results of a MD simulation may be used to determine macroscopic thermodynamic

properties of the system, on the basis of the ergodic hypothesis - the statistical time averages are equal to ensemble averages of the system:

$$\langle A \rangle = \frac{1}{\tau} \int_0^{\tau} A(t) dt = \frac{1}{M} \sum_i^M A_i \quad (3.62)$$

where  $A$  is the observable,  $M$  the number of microstates constituting the ensemble, and  $\tau$  is the total simulation time.<sup>22</sup>

Ergodic hypothesis is satisfied under certain conditions, such as if and only if  $\tau, M \rightarrow +\infty$ , which is obviously impossible in practice in the strictest sense. As an approximation, to be valid and representative, a MD simulation should last  $10^3$  times the simulated phenomena. Also, to correctly explore the  $(\bar{q}, \bar{p})$  phase space, the integration time-step  $\Delta t$  must be chosen small enough to avoid discretization errors (*i.e.*, smaller than the inverse of the fastest vibrational frequency in the system). Thus, typical time-steps are in order of 1 fs. This value may be extended by introducing constraints that fix the vibrations of the fastest atoms (*e.g.*, hydrogens); such a simulation is referred to as constrained MD.<sup>22</sup>

Another requirement is that the modeled system is representative of the macroscopic counterpart. For this purpose, in order to simulate, *i.e.*, the bulk of a molecular crystal, surface effects must be ideally suppressed and bulk interactions must dominate. This is gained by means of Periodic Boundary Conditions (PBC), which allow to overcome the intrinsic limit of the given boundaries of the modeled system by repeating the model as if it were the unit cell for an ideal crystal. Interactions between the original system and its images are managed through suitable cut-offs.<sup>22</sup>

The MD method consists in the numerical, step by step, solution of Newton's equations of motion, which for a simple atomic system can be written as:

$$\frac{d^2 \bar{r}_i(t)}{dt^2} = \frac{\bar{F}_i}{m_i} \quad (3.63a)$$

$$F_i = - \frac{\partial V(\bar{r}_1, \dots, \bar{r}_N)}{\partial \bar{r}_i} \quad (3.63b)$$

where  $m_i$  is the mass of the  $i$ -th atom. Thus, upon the calculation of all the forces, Newton's equations can be integrated. For this purpose, several algorithms have been designed. In Verlet algorithm,<sup>23</sup> the atomic positions  $\bar{r}$  and velocities  $\bar{v}$  are calculated as:

$$\bar{r}(t + \Delta t) = 2\bar{r}(t) - \bar{r}(t - \Delta t) + \frac{\bar{F}(t)}{m} \Delta t^2 \quad (3.64a)$$

$$\bar{v}(t) = \frac{\bar{r}(t + \Delta t) - \bar{r}(t - \Delta t)}{2\Delta t} \quad (3.64b)$$

where  $m$  is the mass of the atom.

In Beeman's algorithm,<sup>24</sup> which yields the same trajectories as the Verlet algorithm, but provides better estimates of the velocity,  $\bar{r}$  and  $\bar{v}$  are given by:

$$\bar{r}(t + \Delta t) = \bar{r}(t) + \bar{v}(t)\Delta t + \frac{4\bar{F}(t) - \bar{F}(t - \Delta t)}{6m} \Delta t^2 \quad (3.65a)$$

$$\bar{v}(t + \Delta t) = \bar{v}(t) + \frac{2\bar{F}(t + \Delta t) + 5\bar{F}(t) - \bar{F}(t - \Delta t)}{6m} \Delta t \quad (3.65b)$$

As a consequence of a more accurate expression for the velocity, the total energy conservation is better described under this approach, in which the kinetic energy is calculated directly from the velocities.

MD simulations can describe the time evolution of different ensembles. In a microcanonical ensemble  $NVE$ , the total energy  $E$  of the macroscopic system is conserved, as well as the composition  $N$  and the volume  $V$ . Instead, in a canonical ensemble, which is the one of interest in the remainder of this text, it is the temperature  $T$  to be conserved, and the ensemble is referred to as  $NVT$ . The temperature of a system is related to the time average of the kinetic energy as:

$$E_{kin}(t) = \frac{3}{2} N k_B T(t) \quad (3.66)$$

where

$$T(t) = \frac{1}{3k_B N} \sum_{i=1}^N m_i v_i^2 \quad (3.67)$$

with  $k_B$  the Boltzmann constant.

Thus, a simple way to control the temperature of the system is to scale the velocities. In particular, the velocities are multiplied at each time step by the factor  $[T_0/T(t)]^{1/2}$  where  $T(t)$  is the temperature calculated from the kinetic energy and  $T_0$  is the desired temperature. An alternative way to maintain the temperature is to couple the system to an external heat bath that is fixed at the desired temperature, like in Berendsen's algorithm.<sup>25</sup> The velocities are scaled at each step, such that the rate of change of temperature is proportional to the difference in temperature between the bath and the system:

$$\frac{dT(t)}{dt} = \frac{1}{\sigma} (T_{bath} - T(t)) \quad (3.68)$$

where  $\sigma$  is a coupling parameter.

### 3.3 Kinetic Monte Carlo

Kinetic Monte Carlo simulations have been performed in this work to investigate the charge transport phenomena occurring in molecular crystals. In this Section, a basic overview of Monte Carlo methods is first provided, followed by an essential description of the Kinetic Monte Carlo typology.

#### 3.3.1 Monte Carlo methods

On the contrary of MD simulations, Monte Carlo (MC) methods are stochastic, time-independent computational algorithms. If MD simulations yield trajectories and time averages, MC simulations deliver ensemble averages acquired by exploring only positions in the phase space. In Figure 3.3, the different approaches of these two computational techniques are sketched.

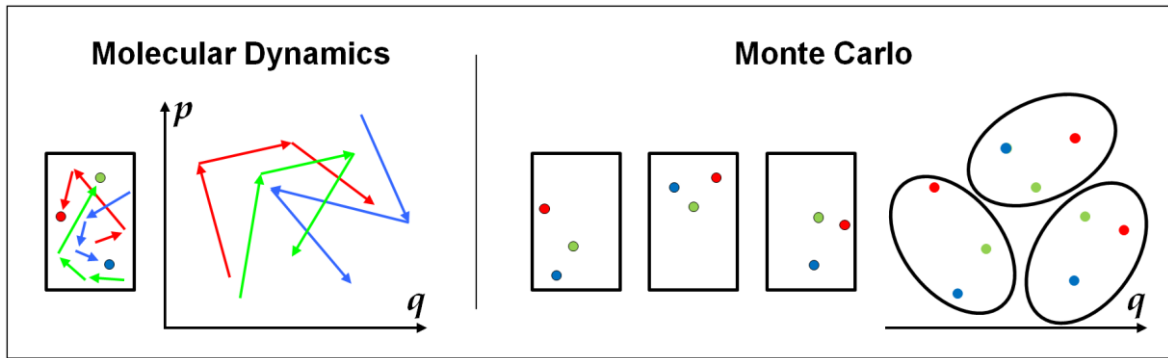


**Figure 3.3** Considering to study the thermodynamics properties of a gas confined by a piston in a cylinder, a MD simulation is focused on the time evolution of the system, whereas a MC simulation collects every possible replica, so to say, as scattered snapshots; however, for the ergodic hypothesis, the results of both the techniques must converge.

In a MC simulation,<sup>26</sup> which is referred to as a Markovian method, each new configuration depends only on the previous one. The new configuration, generated through a random move (*e.g.*, the change of a intra- or intermolecular degree of freedom), is accepted or rejected according to the Metropolis criterion.<sup>27</sup>  $\Delta E = E_{new} - E_{old}$  be the difference between the potential energy of the new ( $E_{new}$ ) and the previous ( $E_{old}$ ) configuration,  $B$  be the Boltzmann distribution:

$$B = e^{-\frac{\Delta E}{k_B T}} \quad (3.69)$$

and  $r \in \mathfrak{R}$ ,  $0 < r < 1$  be a random generated number; if  $\Delta E < 0$ , the new configuration is accepted; if  $\Delta E > 0$ , which means a destabilization, the new configuration is accepted only if  $B > r$ , as depicted in Figure 3.4.

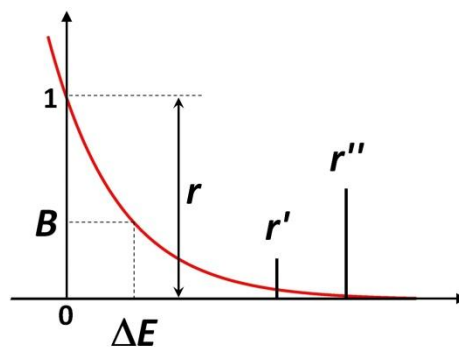


**Figure 3.4** The Metropolis criterion relies on a Boltzmann distribution.

### 3.3.2 Kinetic Monte Carlo simulations

The Kinetic Monte Carlo (KMC) method is a particular MC method intended to simulate the time evolution of some processes, which typically occur with a given known rate.<sup>28-29</sup> Note that these rates (*i.e.*, the charge transfer rates between two molecules) are inputs for the KMC algorithm, since the method cannot predict them for intrinsic theoretical limitations. To introduce the time description into a MC method, the ploy is to define time as the inverse of the selected event probability. Probabilities are determined by the rates of the phenomena involved in the simulation.

The KMC algorithm can be written for instance as follows:<sup>39</sup>

1. Set the time  $t = 0$
2. Form a list of the  $N$  rates  $k_i$  in the system; each rate is correlated to its probability  $p_i = \frac{k_i}{\sum_j^N k_j}$
3. Calculate the cumulative probability  $P_i = \sum_{j=1}^i p_j, i = 1, \dots, N$
4. Get a uniformly distributed random number  $r, 0 < r \leq 1$
5. Find the event to carry out by finding the  $i$ -th event for which  $P_{i-1} < r \leq P_i$  ( $P_{i-1} < rP_N \leq P_i$ )
6. Carry out the  $i$ -th event
7. Get a new uniform random number  $r', 0 < r' \leq 1$
8. Update the time with  $t = t + \frac{1}{k_i}$  (or  $t = t + \frac{\ln(1/r')}{P_N}$ )
9. Recalculate all rates which may have changed due to the transition. If appropriate, remove or add new events, and update  $N$  and the list of events and cumulative probability accordingly.
10. The end of a single KMC cycle is reached. Return to step 4.

By defining cumulative probabilities, the KMC algorithm is efficient in the sense that every iteration is guaranteed to lead to a new configuration, according to the extent of the probability (see Figure 3.5).<sup>39</sup> This choice simplifies the evaluation of the time by avoiding the ambiguous definition of the delay to be associated to a rejected configuration.

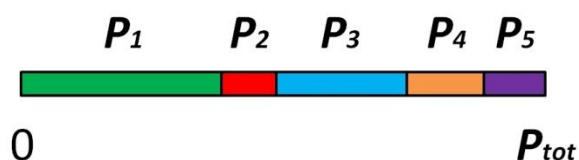


**Figure 3.5** Choice of the final state. Being  $0 < r \leq 1$  and  $P_{i-1} < r \leq P_i$ , the probability that the system jumps into the  $i$ -th state is proportional to  $P_i$ .<sup>39</sup> Figure adapted from <sup>39</sup>.

### 3.4 Software

All the QM methods discussed throughout the remainder of this dissertation are used as implemented in the following commercially-available software packages:

- Gaussian03 <sup>30</sup> [HF, CIS, INDO, CNDO, B3LYP, TD-B3LYP]
- Gaussian09 <sup>31</sup> [HF, CIS, MP2, DFT, B3LYP, CAM, M06, TD-B3LYP, CAM-TD-B3LYP]
- MolPro <sup>32</sup> [HF, CASSCF, CASPT2]

The MD simulations are performed by means of the Tinker 4.2 molecular modeling packages.<sup>33</sup>

The KMC simulations are performed by a home-made Fortran code.

Several visual software packages are used to prepare molecular structure pictures: Molekel 4.3 (also for orbital pictures),<sup>34</sup> Molden 4.7 (mainly used for molecular modeling),<sup>35</sup> Mercury,<sup>36</sup> PyMOL,<sup>37</sup> and VMD.<sup>38</sup>

### 3.5 References

- [1] Levine, I. N. *Quantum Chemistry*, 5th ed.; Prentice Hall: Upper Saddle River, NJ, **2000**.
- [2] Cohen-Tannoudji, C.; Diu, B.; Laloë, F. *Quantum Mechanics*; John Wiley and Sons: New York, **1977**; Vol. 1-2.
- [3] Szabo, A.; Ostlund, N. S. *Modern Quantum Chemistry: Introduction to Advanced Electronic Structure Theory*, 1st ed. revised; Dover Publications: Mineola, NY, **1989**.
- [4] Jensen, F. *Introduction to Computational Chemistry*; John Wiley and Sons: Chichester, UK, **1999**.
- [5] Cramer, C. J. *Essentials of Computational Chemistry: Theories and Models*, 2nd ed.; John Wiley and Sons: Chichester, UK, **2004**.
- [6] Koch, W.; Holthausen, M. C. *A Chemist's Guide to Density Functional Theory*, 2nd ed.; Wiley-VCH: Weinheim, **2001**.
- [7] (a) Werner, H.-J. *Mol. Phys.* **1996**, *89*, 645. (b) Celani, P.; Werner, H.-J. *J. Chem. Phys.* **2000**, *112*, 5546.
- [8] Pople, J. A.; Beveridge, D.; Dobosh, P. *J. Chem. Phys.* **1967**, *47*, 2026–2033.
- [9] Segal, G.; Pople, J. A. *J. Chem. Phys.* **1966**, *44*, 3289–3296.
- [10] (a) Hohenberg, P.; Kohn, W. *Phys. Rev. B* **1964**, *136*, 864. (b) Kohn, W.; Sham, L. J. *Phys. Rev. A* **1965**, *140*, 1133.
- [11] Becke, A. D. *Phys. Rev. A: At., Mol., Opt. Phys.* **1988**, *38*, 3098.
- [12] Perdew, J. P. *Phys. Rev. B: Condens. Matter Mater. Phys.* **1986**, *33*, 8822.
- [13] Burke, K.; Perdew, J. P.; Wang, Y., In *Electronic Density Functional Theory: Recent Progress and New Directions*. Dobson, J. F.; Vignale, G.; Das, M. P., Eds. Plenum: **1998**.
- [14] Lee, C.; Yang, W.; Parr, R. G., *Phys. Rev. B: Condens. Matter Mater. Phys.* **1988**, *37*, 785.
- [15] Becke, A. D. *J. Chem. Phys.* **1993**, *98*, 5648.
- [16] Vosko, S. H.; Wilk, L.; Nusair, M. *Can. J. Phys.* **1980**, *58*, 1200.

- [17] Stephens, P. J.; Devlin, F. J.; Chabalowski, C. F.; Frisch, M. J., *J. Chem. Phys.* **1994**, *98*, 11623.
- [18] Yanai, T.; Tew, D. P.; Handy, N. C. *Chem. Phys. Lett.* **2004**, *393*, 51.
- [19] Zhao, Y.; Truhlar, D. G. *Theor. Chem. Acc.* **2008**, *120*, 215.
- [20] (a) Li, R. F.; Zheng, J. J.; Truhlar, D. G. *Phys. Chem. Chem. Phys.* **2010**, *12*, 12696-12701. (b) Aragó, J.; Sancho-García, J. C.; Ortí, E.; Beljonne, D. *J. Chem. Theory Comput.* **2011**, *7*, 2068-2077.
- [21] Runge, E.; Gross, E. K. U. *Phys. Rev. Lett.* **1984**, *52*, 997-1000.
- [22] Leach, A. R. *Molecular Modelling: Principles and Applications*, 2nd ed.; Prentice Hall: Dorchester, UK, **2001**.
- [23] Verlet, L. *Phys. Rev.* **1967**, *159*, 98.
- [24] Beeman, D. J. *Comp. Phys.* **1976**, *20*, 130.
- [25] Berendsen, H. J. C.; Postma, J. P. M.; Vangunsteren, W. F.; Dinola, A.; Haak, J. R. *J. Chem. Phys.* **1984**, *81*, 3684.
- [26] Fehske, H.; Schneider, R.; Weisse, A. *Computational Many-Particle Physics*, Lect. Notes Phys. 739; Springer: Berlin Heidelberg, **2008**.
- [27] Metropolis, N.; Rosenbluth, A. W.; Rosenbluth, M. N.; Teller, A. H.; Teller, E. *J. Chem. Phys.* **1953**, *21*, 1087-1092.
- [28] Voter, A. F. *Rad. Eff. Sol.* **2007**, *235*, 1568-2609.
- [29] Gillespie, D.T. *J. Phys. Chem.* **1977**, *81*, 2340-2361.
- [30] Frisch, M. J.; Trucks, G. W.; Schlegel, H. B.; Scuseria, G. E.; Robb, M. A.; Cheeseman, J. R.; Montgomery, J. A., Jr.; Vreven, T.; Kudin, K. N.; Burant, J. C.; Millam, J. M.; Iyengar, S. S.; Tomasi, J.; Barone, V.; Mennucci, B.; Cossi, M.; Scalmani, G.; Rega, N.; Petersson, G. A.; Nakatsuji, H.; Hada, M.; Ehara, M.; Toyota, K.; Fukuda, R.; Hasegawa, J.; Ishida, M.; Nakajima, T.; Honda, Y.; Kitao, O.; Nakai, H.; Klene, M.; Li, X.; Knox, J. E.; Hratchian, H. P.; Cross, J. B.; Bakken, V.; Adamo, C.; Jaramillo, J.; Gomperts, R.; Stratmann, R. E.; Yazyev, O.; Austin, A. J.; Cammi, R.; Pomelli, C.; Ochterski, J. W.; Ayala, P. Y.; Morokuma, K.; Voth, G. A.; Salvador, P.; Dannenberg, J. J.; Zakrzewski, V. G.; Dapprich, S.; Daniels, A. D.; Strain, M.

C.; Farkas, O.; Malick, D. K.; Rabuck, A. D.; Raghavachari, K.; Foresman, J. B.; Ortiz, J. V.; Cui, Q.; Baboul, A. G.; Clifford, S.; Cioslowski, J.; Stefanov, B. B.; Liu, G.; Liashenko, A.; Piskorz, P.; Komaromi, I.; Martin, R. L.; Fox, D. J.; Keith, T.; Al-Laham, M. A.; Peng, C. Y.; Nanayakkara, A.; Challacombe, M.; Gill, P. M. W.; Johnson, B.; Chen, W.; Wong, M. W.; Gonzalez, C.; Pople, J. A. *Gaussian 03*, revision C.02; Gaussian, Inc.: Wallingford, CT, **2003**.

[31] Frisch, M. J.; Trucks, G. W.; Schlegel, H. B.; Scuseria, G. E.; Robb, M. A.; Cheeseman, J. R.; Scalmani, G.; Barone, V.; Mennucci, B.; Petersson, G. A.; Nakatsuji, H.; Caricato, M.; Li, X.; Hratchian, H. P.; Izmaylov, A. F.; Bloino, J.; Zheng, G.; Sonnenberg, J. L.; Hada, M.; Ehara, M.; Toyota, K.; Fukuda, R.; Hasegawa, J.; Ishida, M.; Nakajima, T.; Honda, Y.; Kitao, O.; Nakai, H.; Vreven, T.; Montgomery, J. A., Jr.; Peralta, J. E.; Ogliaro, F.; Bearpark, M.; Heyd, J. J.; Brothers, E.; Kudin, K. N.; Staroverov, V. N.; Kobayashi, R.; Normand, J.; Raghavachari, K.; Rendell, A.; Burant, J. C.; Iyengar, S. S.; Tomasi, J.; Cossi, M.; Rega, N.; Millam, N. J.; Klene, M.; Knox, J. E.; Cross, J. B.; Bakken, V.; Adamo, C.; Jaramillo, J.; Gomperts, R.; Stratmann, R. E.; Yazyev, O.; Austin, A. J.; Cammi, R.; Pomelli, C.; Ochterski, J. W.; Martin, R. L.; Morokuma, K.; Zakrzewski, V. G.; Voth, G. A.; Salvador, P.; Dannenberg, J. J.; Dapprich, S.; Daniels, A. D.; Farkas, O.; Foresman, J. B.; Ortiz, J. V.; Cioslowski, J.; Fox, D. J. *Gaussian 09*, revision A.02; Gaussian, Inc.: Wallingford, CT, **2009**.

[32] Werner, H.-J.; Knowles, P. J.; Lindh, R.; Manby, F. R.; Schütz, M.; Celani, P.; Korona, T.; Mitrushenkov, A.; Rauhut, G.; Adler, T. B.; Amos, R. D.; Bernhardsson, A.; Berning, A.; Cooper, D. L.; Deegan, M. J. O.; Dobbyn, A. J.; Eckert, F.; Goll, E.; Hampel, C.; Hetzer, G.; Hrenar, T.; Knizia, G.; Koppl, C.; Liu, Y.; Lloyd, A. W.; Mata, R. A.; May, A. J.; McNicholas, S. J.; Meyer, W.; Mura, M. E.; Nicklass, A.; Palmieri, P.; Pflüger, K.; Pitzer, R.; Reiher, M.; Schumann, U.; Stoll, H.; Stone, A. J.; Tarroni, R.; Thorsteinsson, T.; Wang, M.; Wolf, A. *MOLPRO*, version 2008.1, *A package of ab initio programs*; University College Cardiff Consultants Limited: Wales, U.K., **2008**; see <http://www.molpro.net>.

[33] *TINKER, Software Tools for Molecular Design*, version 4.2; Ponder, J. W.; **2004**. Kundrot, C. E.; Ponder, J. W.; Richards, F. M. J. *Comput. Chem.* **1991**, *12*, 402; Ponder, J. W.; Richards, F. M. J. *Comput. Chem.* **1987**, *8*, 1016. <http://dasher.wustl.edu/ffe/>

[34] *Molekel*, version 4.3; Portmann, S.; Lüthi, H. P. *Chimia* **2000**, *54*, 766. <http://www.cscs.ch/molekel/>

[35] *Molden*, version 4.7; Schaftenaar, G.; Noordik, J. H. J. *Comput. Aided Mol. Design* **2000**, *14*, 123-134. <http://www.cmbi.ru.nl/molden/>

[36] *Mercury CSD 2.0*; Macrae, C. F.; Bruno, I. J.; Chisholm, J. A.; Edgington, P. R.; McCabe, P.; Pidcock, E.; Rodriguez-Monge, L.; Taylor, R.; van de Streek, J.; Wood, P. A. *J. Appl. Cryst.* **2008**, *41*, 466-470. <http://www.ccdc.cam.ac.uk/products/mercury/>

[37] *The PyMOL Molecular Graphics System, Version 1.2r3pre*, Schördinger, LLC. <http://www.pymol.org/>

[38] *VMD - Visual Molecular Dynamics*; Humphrey, W., Dalke, A. and Schulten, K., *J. Molec. Graphics* **1996**, *14*, 33-38. <http://www.ks.uiuc.edu/Research/vmd/>

[39] [http://en.wikipedia.org/wiki/Kinetic\\_Monte\\_Carlo](http://en.wikipedia.org/wiki/Kinetic_Monte_Carlo)

## CHAPTER 4 - INJECTION AND CHARGE TRANSPORT MODELING

Regardless of the typology of the opto-electronic device, the organic semiconductor material must basically satisfy two requirements to assure high efficiency - a favorable level alignment with electrode work functions as well as an elevated charge conduction within the bulk. From this perspective, in this Chapter, we introduce the theoretical models and the computational approaches that we adopted to describe these two fundamental phenomena: the charge injection and the charge transport.

### 4.1 Charge Injection - Theoretical model

A heterojunction is generally the interface that occurs between two layers or regions of dissimilar materials in solid phase. The most common heterojunctions are both those made up by two semiconductors, featuring typically unequal band gaps, and those interfacing a semiconductor with a metal. In particular, our interest lies in metal/organic molecular semiconductor heterojunctions.

In this work, the description of the phenomena occurring at the heterojunction relies on three fundamental parameters: Electron Affinity ( $EA$ ), which is the amount of energy released by the organic material on the acquisition of an electron from the vacuum; Ionization Potential ( $IP$ ), which is the amount of energy needed to extract an electron from the organic material to the vacuum; the electrode work function ( $\Phi_M$ ), which is the amount of energy needed to extract an electron from the metallic surface to the vacuum. These parameters are illustrated in Figure 4.1.

The efficiency of the charge injection, *i.e.*, from the metal electrode to the organic material, can be evaluated considering the reciprocal position of the energetic levels. Note that in Figure 4.1 the assumption is made that the metal and the semiconductor share the same

vacuum level, according to the Schottky-Mott rule.<sup>1</sup> Indeed, this assumption is maintained in the remainder of this text, although we are aware of several cases departing from it, mainly due to surface dipoles occurring at the metal/organic interface.<sup>2</sup>

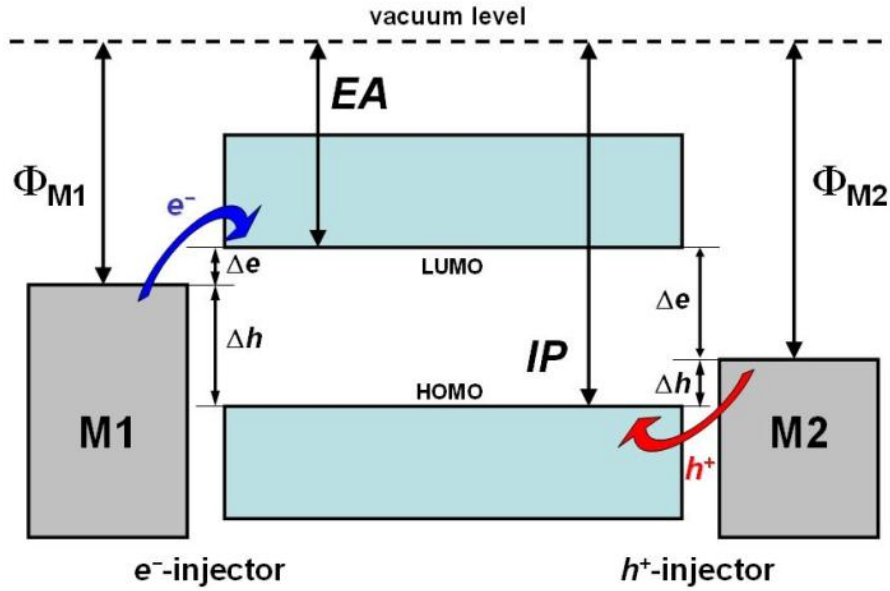


**Figure 4.1** Schematization of the band structure at the two metal/organic heterojunctions.

Within the validity of the Schottky-Mott rule, we define the energetic barriers for the injection of electrons ( $\Delta e$ ) and holes ( $\Delta h$ ) as:

$$\Delta e = \Phi_M - EA \quad (4.1a)$$

$$\Delta h = IP - \Phi_M \quad (4.1b)$$

When:

$$\Phi_M - EA < IP - \Phi_M \quad (4.2)$$

the electron injection barrier is smaller than hole injection barrier, thus the electron injection is the preferred process. Vice versa, the hole injection takes place predominantly when:

$$\Phi_M - EA > IP - \Phi_M \quad (4.3)$$

## 4.2 Charge Injection - Computational approach

From a computational point of view, the analysis is based on the calculation of  $EA$  and  $IP$  of the organic semiconductor and the comparison of these energetic levels with the experimental  $\Phi_M$  of some among the most common electrodes, such as Indium Tin Oxide (ITO) or gold. Though the computational determination of  $\Phi_M$  is known in literature,<sup>3</sup> it was not the purpose of this work; moreover, as calculations and experimental measurements converge,<sup>3</sup> to a first approximation we simply chose experimental values as reference.

Two approaches are available to calculate  $EA$  and  $IP$  - the use of Koopmans' Theorem (KT)<sup>4</sup> and the direct calculation as the energy difference between electronic states.

KT method is based on the relationships:<sup>4,5</sup>

$$IP = -\varepsilon_{HOMO} \quad (4.4a)$$

$$EA = -\varepsilon_{LUMO} \quad (4.4b)$$

Where  $\varepsilon_{HOMO}$  and  $\varepsilon_{LUMO}$  are the eigenvalues of the Highest Occupied Molecular Orbital (HOMO) and the Lower Unoccupied Molecular Orbital (LUMO), respectively. It is possible to calculate  $EA$  and  $IP$  at geometries different from the optimized geometry of the neutral state, though remaining within the wavefunction of the neutral state; we refer to these values as:

$$IP^c = -\varepsilon_{HOMO}^{n/c} \quad (4.5a)$$

$$EA^c = -\varepsilon_{LUMO}^{n/c} \quad (4.5b)$$

where the superscript  $n/c$  indicates that the calculation is performed for the wavefunction of the neutral species at the optimized geometry of the charged (cationic for  $IP^c$ , anionic for  $EA^c$ ) species. The difference between these two sets reported in Equations (4.4,5) reflects the effect of the geometrical relaxation associated to the charge transfer and localization.<sup>6</sup> Note that KT application within DFT methods is known to deliver, for a molecule in gas phase, values that are rather distant from experimental data.<sup>7</sup>

The alternative approach relies on the calculation of the Potential Energy Surface (PES) of both neutral and charged electronic ground states.  $EA$  and  $IP$  can be evaluated as either vertical or adiabatic. The Vertical Electron Affinity ( $VEA$ ) is given by:

$$VEA_n = E_n^{geo-n} - E_a^{geo-n} \quad (4.6a)$$

$$VEA_a = E_n^{geo-a} - E_a^{geo-a} \quad (4.6b)$$

where  $n$  and  $a$  indicate the neutral and anionic species, respectively, and  $E_y^{geo-x}$  represents the energy of the  $y$  state computed at the geometry of the  $x$  state ( $x,y=\{n,a\}$ ). The Vertical Ionization Potential ( $VIP$ ) is similarly defined as:

$$VIP_n = E_c^{geo-n} - E_n^{geo-n} \quad (4.7a)$$

$$VIP_c = E_c^{geo-c} - E_n^{geo-c} \quad (4.7b)$$

where  $c$  indicates the cationic species. As for the Adiabatic Electron Affinity ( $AEA$ ) and Adiabatic Ionization Potential ( $AIP$ ), they are given by:

$$AEA = E_n^{geo-n} - E_a^{geo-a} \quad (4.8a)$$

$$AIP = E_c^{geo-c} - E_n^{geo-n} \quad (4.8b)$$

Independently of the adopted approach, it must be considered that the calculations discussed in this text are performed in gas phase, whereas the system of interest is in solid phase, wherein stabilizing polarization effects take place. Thus, an overestimation of the energy gap calculated between  $EA$  and  $IP$  is expectable.

### 4.3 Charge Transport - Theoretical models

Charge Transport (CT) models are all based on an idealized representation of the system, as well as on a series of approximations apt to simplify, or even allow, the discussion. The aim of such models is to reproduce the behaviors observed experimentally, *e.g.*, the temperature dependence of the charge mobility. In experimental measurements, the charge mobility shows a temperature dependence like those reported in Figure 4.2. Such trends vary

appreciably changing over single crystals to disordered materials. For crystals, the mobility  $\mu$  decreases with temperature  $T$  as:

$$\mu \propto T^{-n}, \quad n > 0 \quad (4.9)$$

Charge mobility can also decrease when the material is cooled down below a threshold temperature (e.g., 30 K for perylene).

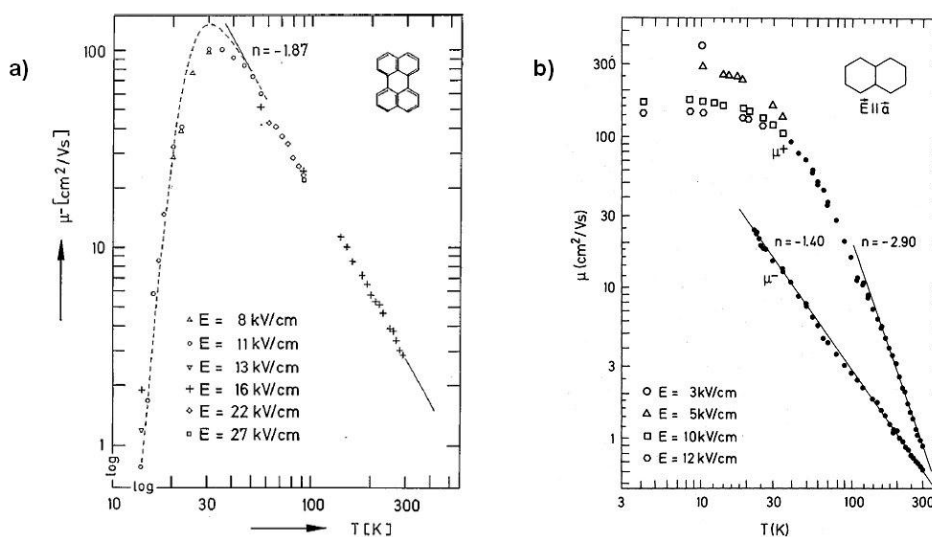


**Figure 4.2** Temperature dependence of the charge mobility shown by molecular crystals of (a) perylene<sup>8</sup> and (b) ultrapure naphthalene.<sup>9</sup> Figure adapted from <sup>27</sup>.

The two main models dealing with charge transport are band theory and hopping.<sup>10</sup>

Band theory is based on an Hamiltonian featuring an intense electronic interaction between adjacent molecules. Because of such strong electronic couplings, the charge carriers are completely delocalized over the solid material, with the formation of a conduction band (electrons) and a valence band (holes), and charge transfer occurs according to a tunneling, coherent mechanism. Generally, an electronic band structure occurs only in those cases where intense electronic couplings come with a certain degree of symmetry and periodicity, as assured by a highly crystalline material.

Band theory is often invoked in those cases satisfying the requisite of intermolecular strong electronic couplings because it can reproduce a temperature dependence of charge mobility like that reported in Eq. (4.9). In particular, the reason why the charge mobility decreases

with temperature is attributed to reticular phonon scattering effects, which limit the free mean path of the delocalized charge carrier.

The problem related to the applicability of a band model lies in the fact that the carrier free mean path experimentally determined for molecular crystals with strong electronic couplings like pentacene or rubrene is comparable to cell unit dimensions, which is in contrast to the delocalization of the charge carrier fundamental for a band-like transport.<sup>11</sup>

If band theory is based on a delocalized description of the electronic states of the crystalline semiconductor, a hopping model is preferred for systems featuring (i) weak electronic couplings and (ii) either static or dynamic disorder, thus either amorphous materials or molecular crystals with strong intermolecular electron-phonon couplings, respectively.<sup>10</sup>

In a hopping model, each molecule is considered rather isolated from the others in terms of electronic coupling; hence, the charge carrier is localized on the single molecule, leading to the formation of a polaron. Basically, charge transfer occurs between the polaron and a neighboring molecule giving a suitable orbital overlap. Moreover, as both molecules are required to modify their geometry upon charge transfer, by means of intramolecular normal modes, the charge transfer occurs through thermal activation. Hence, it is readily understood the fundamental role of intramolecular vibronic coupling for the hopping mechanism. The kinetic constant of the hopping charge transfer can be described by Fermi's golden rule.<sup>10,12</sup>

In a hopping model, the description of the charge transport can be carried out just in terms of the pairs of the molecules giving charge transfer. If the molecules are of the same type, the discussion relies on monomers constituting dimers.

Incidentally, we remind that there are other models describing intermediate situations of those depicted in band theory or hopping models. It is the case of the so-called polaron models, characterized by a purely electronic Hamiltonian derived from band theory enriched with terms accounting for intramolecular electron-phonon coupling.<sup>10b</sup> According to the magnitude of the vibronic coupling, either the band-like or the hopping character may prevail.

### 4.3.1 Hopping - Kinetic constants from Marcus and Jortner models

Hopping kinetic constants can be derived from Fermi's golden rule.<sup>10,12</sup> Within the Franck-Condon (FC) approximation, the charge transfer kinetic constant  $k_{eT}$  is factorized in an electronic term and in a vibrational term:

$$k_{eT} = \frac{2\pi}{\hbar} (V_{eT})^2 (FCWD) \quad (4.10)$$

where  $FCWD$  is the Franck-Condon weighted density of states and  $V_{eT}$  is the electronic coupling, also known in literature as charge transfer integral. In the high-temperature limit, wherein all normal modes can be treated as classical ( $\hbar\omega \ll k_B T$ ),  $FCWD$  is described by the Arrhenius equation:

$$FCWD = \sqrt{\frac{1}{4\pi k_B T \lambda}} e^{\left[-\frac{(\Delta G^\circ + \lambda)^2}{4\lambda k_B T}\right]} \quad (4.11)$$

By substituting Eq. (4.11) in Eq. (4.10), semi-classical Marcus theory is given as:

$$k_{eT} = \frac{2\pi}{\hbar} (V_{eT})^2 \sqrt{\frac{1}{4\pi \lambda k_B T}} e^{\left[-\frac{(\Delta G^\circ + \lambda)^2}{4\lambda k_B T}\right]} \quad (4.12)$$

Indeed, the Marcus Theory of Electron Transfer<sup>13</sup> (proposed by R. A. Marcus in 1956 and awarded with the Nobel Prize in Chemistry in 1992) consists in a kinetic model rather general and applicable, at the given level of approximation, to every system wherein an electronic transfer occurs, encompassing supramolecular triads, biochemical photosystems, electrode reduction-oxidation processes, and hopping transfer in a molecular material.

In Equations (4.11,12), beside  $V_{eT}$  (along with the standard Gibbs free energy  $\Delta G^\circ$ , which will be discussed in the following of this Chapter), another fundamental parameter is present - the reorganization energy  $\lambda$ , which is usually expressed as the sum of two terms:

$$\lambda = \lambda_o + \lambda_i \quad (4.13)$$

$\lambda_o$  is the outer-sphere or intermolecular reorganization energy, which is mainly related to polarization effects occurring around the polaron (be the surroundings either solvation shells or the bulk of an organic semiconductor);  $\lambda_i$  is the inner-sphere or intramolecular reorganization energy, accounting for the structural distortion associated to the transfer and localization of the charge, or, in other words, the intramolecular electron-phonon coupling.

Note that Eq. (4.13) is valid when the molecules constituting the redox couple are weakly interacting, which is generally the case of organic materials, thus  $\lambda_o$  and  $\lambda_i$  can be considered mutually independent.

An alternative method to represent the Arrhenius equation, in the high-temperature limit, which means within the validity of the semi-classical Marcus theory, is given by:<sup>14</sup>

$$k_{eT} \propto \Gamma_N \kappa_e \nu_N e^{(-\Delta G^\ddagger/k_B T)} \quad (4.14)$$

where  $\Gamma_N$  is the nuclear tunneling factor;  $\kappa_e$  is the electronic transmission factor;  $\nu_N$  is the nuclear vibrational frequency effective along the reaction coordinate;  $\Delta G^\ddagger$  is the diabatic free energy of the transition state, namely an estimate of the activation energy of the process determined in the diabatic limit. According to the comparison between  $V_{eT}$  and the pre-exponential terms in Eq. (4.14), it is possible to identify two distinct regimes, referred to as adiabatic and non-adiabatic.<sup>10,14-15</sup>

The non-adiabatic regime is characterized by a moderate electronic coupling  $V_{eT}$ ; thus, the electronic contribution to the charge transfer is the rate-determining step, while the nuclear vibrational activity would be sufficient to induce the overcoming of the energy barrier. The limit case of the non-adiabatic regime is defined by  $V_{eT}, \kappa_e \rightarrow 0$ ; in the so-called diabatic limit, because of the total absence of electronic coupling, no charge transfer happens at all (Figure 4.3a). Within the non-adiabatic regime, Eq. (4.14) can be developed into:

$$k_{eT} \sim \nu_e e^{(-\Delta G^\ddagger/k_B T)} \propto (V_{eT})^2 e^{(-\Delta G^\ddagger/k_B T)} \quad (4.15)$$

Instead, the adiabatic regime is characterized by an elevated electronic coupling  $V_{eT}$ ; accordingly, the electronic states of charge transfer donor and acceptor are delocalized over the whole system, and, as nuclear contribution is now the rate determining step, Eq. (4.14) turns into:

$$k_{eT} \sim \nu_N e^{(-\Delta G^\ddagger/k_B T)} \quad (4.16)$$

Observing the potential energy surfaces, an avoided crossing much remarked than in the non-adiabatic case is present (Figure 4.3c). Indeed, such energetic splitting  $\Delta E_s$  is:

$$\Delta E_s \propto 2V_{eT} \quad (4.17)$$

and only in the case of an self-exchange charge transfer with normal modes described by a harmonic approximation:

$$\Delta E_S = 2V_{eT} \quad (4.18)$$

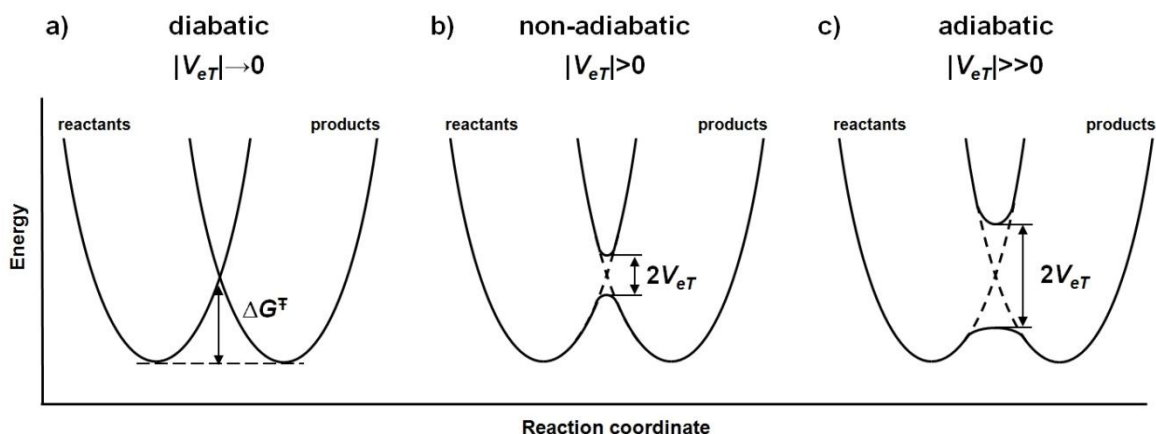


**Figure 4.3** Schematic representation of the diabatic limit (a), non-adiabatic regime (b), and adiabatic regime (c), for a self-exchange charge transfer and within the validity of the harmonic approximation for normal modes.

When contributions to the reorganization energy are given by nuclear motions that cannot be described in classical terms (being  $\hbar\omega \gg k_B T$ ), the semi-classical Marcus Eq. (4.12) must be reformulated. Typically, for the organic molecules of interest, the  $\lambda_o$  contribution falls into a classical description, but this is not true for high frequency intramolecular normal modes. In this case, a more adequate expression for the charge transfer kinetic constant is given by the formalism developed by Jortner<sup>16</sup> and known as the Marcus-Levich-Jortner (MLJ) formalism:

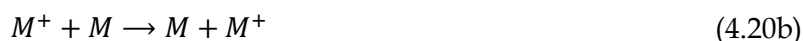
$$k_{eT}^{MLJ} = \frac{2\pi}{\hbar} (V_{ij})^2 \sqrt{\frac{1}{4\pi\lambda_{class}k_B T}} \cdot \sum_{v=0}^{\infty} \left[ e^{(-S_{eff})} \frac{S_{eff}^v}{v!} \cdot \exp \left[ -\frac{(\Delta G^\circ + \lambda_{class} + v\hbar\omega_{eff})^2}{4\lambda k_B T} \right] \right] \quad (4.19)$$

where a single effective mode of frequency  $\omega_{eff}$  and associated Huang-Rhys parameter<sup>12,15</sup>  $S_{eff}$  accounts for all the non-classical normal modes (see Section 4.5, also for the definition of  $V_{ij}$ ,  $\lambda_{class}$ , and  $\Delta G^\circ$ );  $v$  is the vibrational quantum.

#### 4.4 Charge Transport - Adopted theoretical model

For the description of the charge transport in the organic semiconductors studied in this work, we adopted a non-adiabatic hopping model according to the MLJ formalism. The fundamental requirement for the application of a non-adiabatic model is the electronic coupling being smaller than the reorganization energy ( $V_{eT} < \lambda/2$ );<sup>10b</sup> otherwise, an elevated electronic coupling would delocalize the charge carrier over the whole system, hence the charge transfer should be described more conveniently as a band-like transport.

We assumed mono-electronic, self-exchange charge transfer processes for both electron and hole transfer, respectively:



where  $M$  is the neutral molecule of the organic semiconductor.

#### 4.5 Charge Transport - Computational approach

According to the Marcus theory, the most important parameters for a charge transport study based on a non-adiabatic hopping model are the electronic couplings and the reorganization energies, which are obtained through quantum-mechanical calculations. Known the charge transfer kinetic constants, it is possible to propagate the charge and eventually predict the charge mobility for the organic semiconductor by means of kinetic Monte Carlo simulations. Moreover, molecular dynamics simulations can be performed to investigate thermal effects on the charge transport. In this Section, we show how these properties can be evaluated by means of QM, MD, and KMC methods.

### 4.5.1 Electronic couplings

Electronic coupling integrals can be evaluated according to two main models.

The so-called Energy-Splitting-in-Dimer (ESD) method<sup>10a</sup> basically relies on Eq. (4.18). In particular, the fundamental assumption is that at the transition state, wherein the exceeding charge is equally delocalized on both the molecules in a self-exchange charge transfer, the energy separation between the two adiabatic states is exactly twice the electronic coupling. By applying Koopmans' theorem,<sup>4</sup> the single-electron approximation is introduced, which allows to express the electronic coupling as:

$$V_n^{KT-ESD} = \frac{\varepsilon_{\text{LUMO}+1} - \varepsilon_{\text{LUMO}}}{2} \quad (4.21a)$$

$$V_p^{KT-ESD} = \frac{\varepsilon_{\text{HOMO}} - \varepsilon_{\text{HOMO}-1}}{2} \quad (4.21b)$$

where  $V_n^{KT-ESD}$  and  $V_p^{KT-ESD}$  are the Koopmans' Theorem based Energy-Splitting-in-Dimer (KT-ESD) electronic couplings for  $n$ -type and  $p$ -type semiconductors, respectively;  $\varepsilon_i$  are the eigenvalues of the frontier molecular orbitals, *e.g.*, the Highest Occupied Molecular Orbital (HOMO) and the previous one (HOMO-1), obtained from the closed-shell wavefunction of the neutral ground state of the dimer.

For its simplicity, the KT-ESD approach is the most common method for the charge transfer integrals evaluation in organic semiconductors at the moment. Nevertheless, the ESD model is not exempt from inconvenience. In particular, when the two molecules constituting the dimer are not symmetrically equivalent, the monomers, though geometrically and chemically identical, biases each other with polarization effects of different extent. In this case, the ESD approach can drastically overestimate the electronic coupling (Figure 4.4).<sup>19b</sup>

The other method consists in the calculation of the electronic coupling integrals directly from the Hamiltonian of the system, hence it is referred to as Direct Method.<sup>17</sup> Precisely, in a two-state description, the electronic coupling integral is defined as:

$$t_{DA} = \langle \Psi_D | \mathcal{H} | \Psi_A \rangle \quad (4.22)$$

where  $\mathcal{H}$  is the Hamiltonian of the dimer,  $\Psi_D$  and  $\Psi_A$  the ground-state wavefunctions of the charge transfer donor and acceptor states, respectively. Within the single-electron-single-

state approximation, it is possible to express the electronic coupling integral by means of just the wavefunctions of the involved molecular orbitals, calculated for just the ground-state wavefunction of the neutral monomer, such as:

$$t_{ij}^{n\text{-type}} = \langle \psi_i^{\text{LUMO}} | \mathcal{H} | \psi_j^{\text{LUMO}} \rangle \quad (4.23a)$$

$$t_{ij}^{p\text{-type}} = \langle \psi_i^{\text{HOMO}} | \mathcal{H} | \psi_j^{\text{HOMO}} \rangle \quad (4.23b)$$

where the subscripts  $i$  and  $j$  refer to the monomers constituting the dimer.

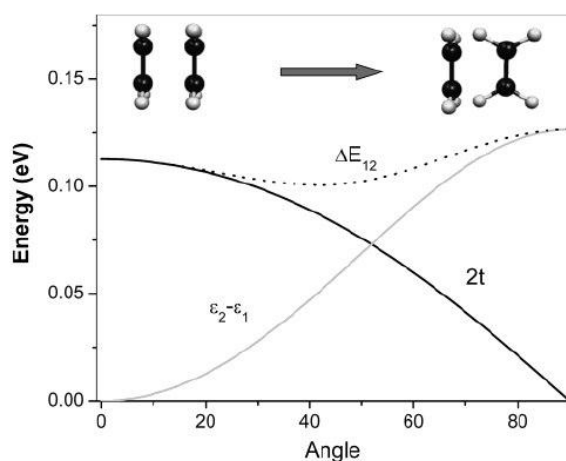


**Figure 4.4** Energetic trends denoting a typical inconvenience of ESD methods.<sup>10a,19b</sup>  $\epsilon_{1,2}$  are the site energies (*vide infra*),  $t$  the charge transfer integral. The more the ethylene monomers move away from the face-to-face configuration toward a face-to-edge one, the more  $t$  decreases; the problem is that the ESD evaluation, based on  $\Delta E_{12}$ , does not deliver such a trend.<sup>19b</sup> Figure adapted from <sup>19b</sup>.

The direct method adopted in this work relies on the formalism described in <sup>18</sup>. Basically,  $t_{ij}$  is an off-diagonal element of the interaction matrix:

$$\mathbb{T} = \mathbb{C}_0^\dagger \mathbb{S}_1 \mathbb{C}_1 \mathbf{e}_1 \mathbb{C}_1^\dagger \mathbb{S}_1 \mathbb{C}_0 \quad (4.24)$$

where  $\mathbb{C}_0$  is the matrix of the coefficient of the dimer molecular orbitals localized on the two non-interacting monomers;  $\mathbb{C}_1$  is the matrix of the coefficient of the dimer molecular orbitals delocalized over the interacting monomers, obtained from the first SCF iteration using  $\mathbb{C}_0$  as guess;  $\mathbf{e}_1$  is the vector of the eigenvalues of the delocalized dimer molecular orbitals with coefficients  $\mathbb{C}_1$ ;  $\mathbb{S}_1$  is the matrix of the overlap integrals between the atomic orbitals corresponding to  $\mathbb{C}_1$ . The diagonal elements of  $\mathbb{T}$  are referred to as the site energies  $e_i$  and

each of them represents the energy of one electron populating a certain orbital (*e.g.*, the LUMO) localized on one of the two monomers.

Eq. (4.24) yields electronic couplings and site energies corresponding to a non-orthogonal basis set. Nevertheless, the MLJ formalism requires parameters defined on the basis of orthogonal molecular orbitals. Löwdin's symmetric transformation<sup>19</sup> allows to orthonormalize direct method electronic coupling integrals  $t_{ij}$  and site energies  $e_i$ , as given by:

$$\epsilon_{i,j} = \frac{1}{2} \frac{(e_i + e_j) - 2t_{ij}S_{ij} \pm (e_i - e_j)\sqrt{1 - (S_{ij})^2}}{1 - (S_{ij})^2} \quad (4.25a)$$

$$V_{ij} = \frac{t_{ij} - \frac{1}{2}(e_i + e_j)S_{ij}}{1 - (S_{ij})^2} \quad (4.25b)$$

where  $\epsilon_{i,j}$  are the orthonormalized, effective site energies, and  $V_{ij}$  are the orthonormalized, effective electronic coupling integrals; the subscripts  $i$  and  $j$  refer to the monomers constituting the dimer.

In principle, the polarization effects related to site energies should be accounted for in the  $\Delta G^\circ$  of the Marcus expression of the charge transfer kinetic constant. However, as demonstrated in <sup>19b</sup>, depending on the topology and symmetry of a crystal, a near-complete cancellation of the polarization effects may occur. Accordingly, in this work, due to the high symmetry featured by most of the crystalline systems studied, we chose to neglect such an energetic disorder.<sup>10a</sup>

#### 4.5.2 Reorganization energies

The intramolecular contribution to the reorganization energy  $\lambda_i$  can be evaluated by two approaches: the first method relies on the calculation of the Huang-Rhys (HR) parameters<sup>12,20</sup>, thus requiring the calculation of the normal modes of both neutral and charged molecules; the second method uses simpler calculations regarding with the potential energy surfaces of both neutral and charged molecules, and it is called Adiabatic Potential (AP) method.<sup>20</sup>

Within the AP method, referring to Figure 4.5, where the potential energy surfaces of the neutral and anionic ground states of the molecule are schematically represented, the contribution  $\lambda_i^{AP,n}$  of the neutral state and the contribution  $\lambda_i^{AP,c}$  of the  $c$  charged state (anionic or cationic) are calculated as:

$$\lambda_i^{AP,n} = |E_n^{geo-n} - E_n^{geo-c}| \quad (4.26a)$$

$$\lambda_i^{AP,c} = |E_c^{geo-c} - E_c^{geo-n}| \quad (4.26b)$$

where  $E_y^{geo-x}$  represents the energy of the  $y$  state computed at the geometry of the  $x$  state.

The total AP intramolecular reorganization energy  $\lambda_i^{AP}$  is defined by:

$$\lambda_i^{AP} = \lambda_i^{AP,n} + \lambda_i^{AP,c} \quad (4.27)$$

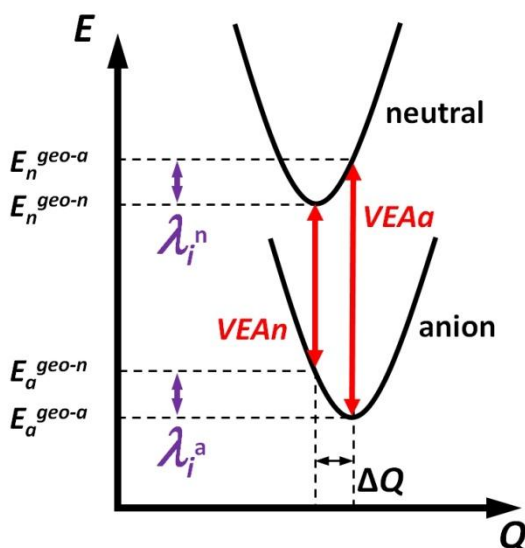


**Figure 4.5** Schematic representation of the potential energy profiles of neutral and charged species involved in the charge transfer process and indication of the two contributions of the total internal reorganization energy. The scheme, applied to a reduction process, also shows the relation between  $VEA_n$  and  $VEA_a$  and the  $\lambda_i$ .  $E_y^{geo-x}$  represents the energy of the  $y$  state computed at the geometry of the  $x$  state ( $x,y=\{n, a\}$ ).

The HR method is also based on a relationship completely analogue to Eq. (4.27), but in this case the contributions are given by:

$$\lambda_i^{HR,n,c} = \sum_m \lambda_m^{HR} = \sum_m \hbar \omega_m S_m \quad (4.28)$$

where the Huang-Rhys parameter  $S_m$  can be obtained from the dimensionless displacement parameter  $B_m$  usually employed in the evaluation of the Franck-Condon (FC) vibronic progressions in electronic spectra as:<sup>21</sup>

$$S_m = \frac{1}{2} (B_m)^2 \quad (4.29)$$

with  $m$  referring to the totalsymmetric normal mode  $Q_m$  with frequency  $\omega_m$ . Assuming the harmonic approximation,  $B_m$  is defined as:

$$B_m = \sqrt{\frac{\omega_m}{\hbar}} \{ \mathbf{x}_n - \mathbf{x}_c \} \mathbb{M}^{1/2} \mathbb{l}_m \quad (4.30)$$

where  $\mathbf{x}_n$  and  $\mathbf{x}_c$  are the  $3N$  dimensional vector of the equilibrium Cartesian coordinates of the neutral and charged molecular states, respectively;  $\mathbb{M}$  is the  $3N \times 3N$  diagonal matrix of the atomic masses;  $\mathbb{l}_m$  is the  $3N$  vector describing the mass-weighted Cartesian coordinates of the normal mode  $Q_m$  of the neutral or charged state, depending on which contribution is considered between  $\lambda_i^{HR,n}$  and  $\lambda_i^{HR,c}$ . Thus, in other words,  $\lambda_i^{HR}$  is determined by considering which normal modes mainly contribute to the geometrical distortion associated to the charge transfer and localization.

The HR method is necessary to determine the effective mode whose frequency  $\omega_{eff}$  and HR parameter  $S_{eff}$  are used in the MLJ formulation reported in Eq. (4.19); these parameters are defined as:

$$\omega_{eff} = \sum_m \omega_m \frac{S_m}{\sum_n S_n} \quad (4.31a)$$

$$S_{eff} = \frac{\lambda_i^{HR}}{\hbar \omega_{eff}} \quad (4.31b)$$

where  $m$  and  $n$  refer to the totalsymmetric normal modes, and  $\lambda_i^{HR} = \lambda_i^{HR,n} + \lambda_i^{HR,c}$  is the total intramolecular reorganization energy calculated by means of the HR parameters. Since the low frequency vibrations can be described, to a good approximation, in classical terms, and because of their possible anharmonicity, the contributions for frequencies below  $250 \text{ cm}^{-1}$  were generally not included in the evaluation of  $\omega_{eff}$ .

The difference between  $\lambda_i^{AP}$  and  $\lambda_i^{HR}$  is mainly due to low frequency, classical degrees of freedom, often associated with long and flexible substituents. Thus, these exceeding classical contributions, if not negligible, are usually summed to the outer-sphere, intermolecular reorganization energy  $\lambda_o$  and included in the classical reorganization energy contribution  $\lambda_{class}$  of the MLJ kinetic constant in Eq. (4.19).

As for  $\lambda_o$ , since it cannot be easily estimated for charge transport phenomena taking place in solid state media,<sup>22-23</sup> it was assumed to be either 0.1 eV, in our earlier investigations, or 0.01 eV, in the later ones, in keeping with more recent studies<sup>24</sup> available in literature, to the best of our knowledge. Note that the absolute values of the charge transfer rate constants (and hence the computed charge mobilities) can be strongly influenced by the value chosen for  $\lambda_o$ .

#### 4.5.3 Thermal fluctuations and molecular dynamics

As organic semiconductors are materials characterized by weak intermolecular interactions, it is reasonable to suppose that the molecules are highly sensitive to thermally induced fluctuations; accordingly, also charge transport properties should be susceptible to thermally induced disorder.

Recently, it was shown<sup>10b,11b,25</sup> that the thermal fluctuations of charge transfer integrals is of the same magnitude of the electronic couplings and that the fluctuations are induced by low frequency vibrational modes, corresponding basically to intermolecular, lattice vibrations. These observations suggest that it is fundamental to estimate the electronic couplings not only from the static perspective of a crystalline structure, but also in a dynamical representation that may reasonably simulate their thermally induced evolution.

The study of the thermally induced disorder effects relies on the execution of classical molecular dynamics simulations. Among the configurations generated by the MD simulation, some are selected for the quantum-mechanical calculation of the electronic coupling integrals. MD simulations can be performed at different temperatures, in order to gain information on temperature dependences.

#### 4.5.4 Charge mobility and kinetic Monte Carlo

To evaluate the charge mobility of the organic semiconductors, we perform kinetic Monte Carlo simulations in both Brownian and time of flight regimes, hence basically either in the absence or presence of an applied voltage. In both cases, we consider a single charge carrier per simulation, which means that there is only one charge propagating in the organic molecular semiconductor. As we neglect energetic disorder,<sup>10a</sup> the standard Gibbs free energy of the mono-electron self-exchange charge transfer  $\Delta G^\circ$  is equal to zero in the Brownian limit of zero field and zero concentration, whereas, within time of flight regime, it is:

$$\Delta G^\circ = -e\bar{F} \cdot \bar{d} \quad (4.32)$$

where  $e$  is the electron charge,  $\bar{F}$  is the applied electric field, and  $\bar{d}$  is the vector connecting the two molecular sites forming the dimer. Once the kinetic constants  $k_{eT}^{MLJ}$  are built as reported in Eq. (4.19), the rate constants are the input for the KMC simulations. Charge mobility is calculated in the Brownian regime according to the Einstein-Smoluchowski (ES) equation:

$$\mu^{ES} = \frac{eD}{k_B T} \quad (4.33)$$

where the diffusion coefficient  $D$  is obtained from the fitted linear dependence of the mean square displacement ( $MSD$ ) employing the Einstein equation:<sup>17,26</sup>

$$D = \lim_{t \rightarrow \infty} \frac{MSD}{6t} \quad (4.34)$$

Instead, the charge mobility in the time of flight (TOF) regime is given by:<sup>26d</sup>

$$\mu^{TOF} = \frac{d}{F\tau} \quad (4.35)$$

where  $d$  is the distance traveled by the charge carrier,  $F$  is the module of the electric field applied along  $\bar{d}$ , and  $\tau$  is the time required to cover the distance  $d$ .

More computational details are provided in the following Chapter.

## 4.6 References

- [1] Schottky, W. *Z. Phys.* **1942**, *118*, 539.
- [2] (a) Hill, I. G.; Rajagopal, A.; Kahn, A.; Hu, Y. *Appl. Phys. Lett.* **1998**, *73*, 662. (b) Kahn, A.; Koch, N.; Gao, W. *J. Polym. Sci. Polym. Phys.* **2003**, *41*, 2529.
- [3] (a) Skriver, H. L.; Rosengard, N. M. *Phys. Rev. B* **1992**, *46*, 7157. (b) Methfessel, M.; Hennig, D.; Scheffler, M. *Phys. Rev. B* **1992**, *46*, 4816. (c) Fall, C. J.; Binggeli, N.; Baldereschi, A. *J. Phys.: Condens. Matter* **1999**, *11*, 2689-2696.
- [4] Koopmans, T. *Physica* **1933**, *1*, 104.
- [5] Szabo, A.; Ostlund, N. S. *Modern Quantum Chemistry: Introduction to Advanced Electronic Structure Theory*, 1st ed. revised; Dover Publications: Mineola, NY, **1989**.
- [6] Brédas, J.-L.; Street, G. B. *Acc. Chem. Res.* **1985**, *18*, 309-315.
- [7] (a) Hohenberg, P.; Kohn, W. *Phys. Rev. B* **1964**, *136*, 864; (b) Kohn, W.; Sham, L. J. *Phys. Rev. A* **1965**, *140*, 1133.
- [8] Karl, N.; Kraft, K.-H.; Marktanner, J.; München, M.; Schatz, F.; Stehle, R.; Uhde, H.-M. *J. Vac. Sci. Technol. A* **1999**, *17*, 2318.
- [9] Warta, W.; Karl, N. *Phys. Rev. B* **1985**, *32*, 1172.
- [10] (a) Coropceanu, V.; Cornil, J.; da Silva Filho, D. A.; Olivier, Y.; Silbey, R.; Brédas, J.-L. *Chem. Rev.* **2007**, *107*, 926-952. (b) Troisi, A. *Chem. Soc. Rev.* **2011**, *40*, 2347-2358.
- [11] (a) Troisi, A. *Adv. Mater.* **2007**, *19*, 2000-2004. (b) Troisi, A.; Orlandi, G. *J. Phys. Chem. A* **2006**, *110*, 4065-4070.
- [12] Cornil, J.; Coropceanu, V.; Beljonne, D.; Brédas, J.-L. *Chem. Rev.* **2004**, *104*, 4971-5003.
- [13] (a) Marcus, R. A. *J. Chem. Phys.* **1956**, *24*, 4966. (b) Marcus, R. A. *Can. J. Chem.* **1959**, *37*, 155. Marcus, R. A. *J. Phys. Chem.* **1963**, *67*, 853.
- [14] Newton, M. D. *Chem. Rev.* **1991**, *91*, 767-792.
- [15] Coropceanu, V.; André, J. M.; Malagoli, M.; Brédas, J.-L. *Theor. Chem. Acc.* **2003**, *110*, 59-69.

- [16] Jortner, J. *J. Chem. Phys.* **1976**, *64*, 4860-4867.
- [17] Yang, X.; Wang, L.; Wang, C.; Long, W.; Shuai, Z. *Chem. Mater.* **2008**, *20*, 3205-3211.
- [18] Orlandi, G.; Troisi, A.; Zerbetto, F. *J. Am. Chem. Soc.* **1999**, *121*, 5392-5395.
- [19] (a) Löwdin, P. O. *J. Chem. Phys.* **1950**, *18*, 365. (b) Valeev, E. F.; Coropceanu, V.; da Silva Filho, D. A.; Salman, S.; Brédas, J.-L. *J. Am. Chem. Soc.* **2006**, *128*, 9882-9886.
- [20] (a) Malagoli, M.; Coropceanu, V.; da Silva Filho, D. A.; Brédas, J.-L. *J. Chem. Phys.* **2004**, *120*, 7490-7496. (b) Sánchez-Carrera, R. S.; Coropceanu, V.; da Silva Filho, D. A.; Friedlein, R.; Osikowicz, W.; Murdey, R.; Suess, C.; Salaneck, W. R.; Brédas, J.-L. *J. Phys. Chem. B* **2006**, *110*, 18904-18911.
- [21] (a) Negri, F.; Orlandi, G. *J. Chem. Phys.* **1995**, *103*, 2412-2419. (b) Negri, F.; Zgierski, M. Z. *J. Chem. Phys.* **1995**, *102*, 5165-5173.
- [22] Koh, S. E.; Risko, C.; da Silva Filho, D. A.; Kwon, O.; Facchetti, A.; Brédas, J.-L.; Marks, T. J.; Ratner, M. A. *Adv. Funct. Mater.* **2008**, *18*, 332-340.
- [23] Lemaure, V.; Steel, M.; Beljonne, D.; Brédas, J.-L.; Cornil, J. *J. Am. Chem. Soc.* **2005**, *127*, 6077-6086.
- [24] McMahon, D. P.; Troisi, A. *J. Phys. Chem. Lett.* **2010**, *1*, 941-946.
- [25] (a) Sleight, J. P.; McMahon, D. P.; Troisi, A. *Appl. Phys. A* **2009**, *95*, 147-152. (b) Martinelli, N. G.; Olivier, Y.; Athanasopoulos, S.; Delgado, M. C. R.; Pigg, K. R.; da Silva, D. A.; Sanchez-Carrera, R. S.; Venuti, E.; Della Valle, R. G.; Brédas, J.-L.; Beljonne, D.; Cornil, J. *ChemPhysChem* **2009**, *10*, 2265-2273. (c) Troisi, A. *Mol. Simul.* **2006**, *32*, 707-716. (d) Cheung, D. L.; Troisi, A. *Phys. Chem. Chem. Phys.* **2008**, *10*, 5941-5952.
- [26] (a) Marcon, V.; Breiby, D. W.; Pisula, W.; Dahl, J.; Kirkpatrick, J.; Patwardhan, S.; Grozema, F.; Andrienko, D. *J. Am. Chem. Soc.* **2009**, *131*, 11426-11432. (b) Martinelli, N. G.; Savini, M.; Muccioli, L.; Olivier, Y.; Castet, F.; Zannoni, C.; Beljonne, D.; Cornil, J. *Adv. Funct. Mater.* **2009**, *19*, 3254-3261. (c) Athanasopoulos, S.; Kirkpatrick, J.; Martinez, D.; Frost, J. M.; Foden, C. M.; Walker, A. B.; Nelson, J. *Nano Lett.* **2007**, *7*, 1785-1788. (d) Olivier, Y.; Lemaure, V.; Brédas, J.-L.; Cornil, J. *J. Phys. Chem. A* **2006**, *110*, 6356-6364. (e) Andrienko, D.; Kirkpatrick, J.; Marcon, V.; Nelson, J.; Kremer, K. *Phys. Status Solidi B* **2008**, *245*, 830-834. (f) Tan, L.; Zhang, L.; Jiang, X.; Yang, X. D.; Wang, L. J.; Wang, Z.; Li, L. Q.; Hu, W. P.; Shuai, Z.

G.; Li, L.; Zhu, D. B. *Adv. Funct. Mater.* **2009**, *19*, 272–276. (g) Nan, G. J.; Yang, X. D.; Wang, L. J.; Shuai, Z. G.; Zhao, Y. *Phys. Rev. B* **2009**, *79*, 115203.

[27] Pope, M.; Swenberg, C. E. *Electronic Processes in Organic Crystals and Polymers*; Oxford University Press, **1999**.

## CHAPTER 5 - PANDORA SUITE

The Pandora Suite is a computational tool that I developed during my thesis project to investigate the charge transport properties of organic molecular semiconductors in their crystalline phase. At present, the tool encompasses a suite of scripts and programs that assist the prediction of the charge mobility of a molecular crystal in a non-adiabatic hopping regime according to the Marcus-Levich-Jortner formalism. The suite makes use of Gaussian09<sup>1</sup> quantum-mechanical calculations to compute intra- and intermolecular properties such as the reorganization energy contributions and the electronic coupling integrals. Thermally induced disorder effects are evaluated by performing Tinker<sup>2</sup> molecular dynamics simulations followed by analyses of the distribution of electronic couplings, eventually also in terms of Fourier transform analysis.<sup>3</sup> Finally, the charge mobility is determined by propagating the charge carrier through kinetic Monte Carlo simulations, in either Brownian or time of flight regimes.<sup>4</sup> In Figure 5.1, the Pandora Suite operating procedure is summarized.

In this Chapter, the description of each step of our procedure is provided along with the necessary computational details.

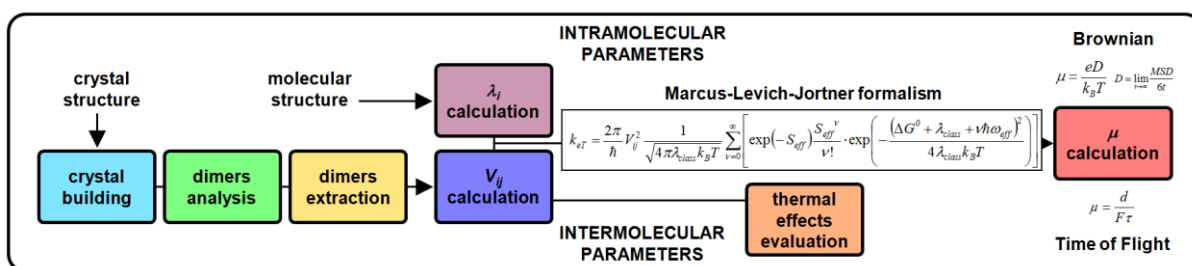


**Figure 5.1** Scheme of the operating procedure adopted by the Pandora Suite.

## 5.1 Crystal Building

To a first approximation, we modeled every organic material as a perfect molecular crystal, without defects or microcrystalline boundaries, keeping in mind that devices usually feature either amorphous or nanocrystalline organic thin films whose exact morphology is often not known. Our choice is motivated by the computational ease of dealing with periodical systems. Another sound advantage lies in the ease of modeling the charge carrier propagation in a periodical pattern of charge transfer jumps within a kinetic Monte Carlo simulation. These limitations were introduced to simplify the approach, but their removal will be the subject of future developments.

The molecular geometry, the spatial group, and the cell parameters of the molecular crystal are extracted from files in the Crystallographic Information File (.cif) format, which are downloaded from the Cambridge Crystallographic Data Centre (CCDC)<sup>5</sup> and Crystallography Open Database (COD)<sup>6</sup> official sites.

The supercell is a multiple of the unit cell, from which it is built through Tinker subprogram *crystal*.<sup>2</sup> The supercell is used as the initial simulation box for MD simulations, and it is also fundamental to perform an exhaustive research of the different types of charge transfer dimer (see Section 5.2).

## 5.2 Dimers Analysis

The first step for the electronic coupling integrals calculation is the identification of the different pairs of molecules wherein the hopping charge transfer may reasonably take place.

A simple, rather accurate method to individuate how many dimer types are present in the supercell consists in determining the radial distribution function  $g(r)$  of the monomer centers of mass at distance  $r$ .  $g(r)$  is obtained by means of Tinker subprogram *radial*,<sup>2</sup> following the transformation of the supercell Cartesian coordinates from a monomer basis to a center of mass basis (*e.g.*, each monomer is represented only by its center of mass). The

same input is used by a home-made code to perform a Gaussian fitting on the output distributions.

Note that the  $g(r)$  calculated for a MD trajectory allows to evaluate, on the basis of the broadening of the peaks, the time evolution of the distances between the centers of mass at a given temperature. Instead, the  $g(r)$  calculated for the original crystal structure is a histogram that simplifies the identification of dimer types. Nevertheless, it must be pointed out that pairs of monomers with the same distance  $r$  may consist in different dimer types because of different reciprocal orientations of the constituting monomers.

### 5.3 Dimers Extraction

The least automated step in the procedure consists in the selection, and consequent extraction of the Cartesian coordinates of the dimers from the supercell structure. Dimers structures must be extracted because they are used as the geometrical guess for the following QM calculations of the electronic coupling integrals.

The choice of the dimers is strongly based on the concept that in a hopping transport the charge carrier jumps from the polaron to a neighboring molecule, which becomes the polaron, and so on. Accordingly, first the different "hopping sites" (as we are used to referring to) are identified; generally, a hopping site is each crystallographically non-equivalent monomer within the unit cell. As a rule of thumb, chiral monomers (*e.g.*, two atropo-enantiomers in the unit cell) lead to different hopping sites. Then, with respect to the center of mass of each hopping site, monomers with centers of mass within a radius of about 15 Å are generally selected. Such a cut-off is due to the direct proportion between electronic couplings and overlap integrals.<sup>7</sup>

## 5.4 $V_{ij}$ Calculation

Electronic coupling integrals are calculated according to the direct method described in Section 4.5.1. The Hamiltonian type for the calculations is chosen depending on the molecular system complexity, the desired level of approximation, and the computational cost. Hence, for instance, both DFT and semi-empirical methods can be used; the latter may be a convenient choice whenever many calculations have to be performed (see Section 5.5), provided that the description obtained through a semi-empirical method is sufficiently representative of the system of interest.

Referring to Section 4.5.1, the procedure for the electronic couplings calculation for each dimer can be summarized as:

1. calculation of the molecular orbitals of the separate monomers A and B
2. construction of the localized dimer molecular orbitals  $\mathbb{C}_0$  (which is the electronic guess for the following point)
3. calculation of the delocalized dimer molecular orbitals  $\mathbb{C}_1$
4. extraction of the overlap integrals matrix  $\mathbb{S}_1$
5. calculation of the non-orthonormal  $t_{ij}$
6. Löwdin's transformation of  $t_{ij}$  into the orthonormal  $V_{ij}$

## 5.5 Thermal Effects Evaluation

The main aim of the thermal effects evaluation is to see the magnitude of the fluctuations of the transfer integrals. Another interesting aspect of the evaluation of thermal effects is to find the reticular vibrations that contribute to the variation of the electronic couplings and what is the extent of such thermally induced fluctuations.

First of all, a MD simulation is performed, using the supercell as the simulation box, with periodic boundary conditions applied. Typically, we run a 100 *ps* MD simulation, with MM3 force field, in the *NVT* ensemble at 300 *K*, using Berendsen's algorithm<sup>8</sup> to simulate the presence of a thermal bath; the integration time-step is set to 1 *fs*. Since recent studies<sup>9</sup> have shown that low frequency intermolecular vibrations can sensibly modulate the magnitude of the electronic couplings, we froze all the intramolecular degrees of freedom and kept each molecule rigid at its crystal structure while allowing intermolecular motions.

Secondly, the transfer integrals between the frontier molecular orbitals (basically, HOMO for *p*-type, LUMO for *n*-type semiconductors) are calculated every 30 *fs* for the selected dimers. This means that the procedure described in Section 5.4 is repeated thousands times; as a consequence, we often adopt the B3LYP/3-21G\* level of theory, or even INDO or CNDO semi-empirical Hamiltonians, which lower the computational cost.

Once the charge transfer integrals are known, to extract the phonon frequencies leading to more effective coupling modulation, we calculate the Fourier transform of the autocorrelation function of the time evolution of each electronic coupling integral as:

$$\langle \delta V_{ij}(0) \delta V_{ij}(t) \rangle = \lim_{\tau \rightarrow \infty} \frac{1}{\tau} \int_{t=0}^{t=\tau} \delta V_{ij}(t) \delta V_{ij}(t + \tau) dt \quad (5.1)$$

where  $\tau$  is the simulation time, and  $\delta V_{ij}(t)$  is the deviation from the mean value defined as:

$$\delta V_{ij}(t) = V_{ij}(t) - \langle V_{ij}(t) \rangle \quad (5.2)$$

As the frequencies of interest are smaller than 100-200 *cm*<sup>-1</sup>, in order to calculate a Fourier transform that covers the frequency range of 0-550 *cm*<sup>-1</sup>, a transfer integral sampling time-step of 30 *fs* is necessary.

Finally, the  $V_{ij}$  distributions are fitted, usually with a Gaussian function, to evaluate, *i.e.*, the standard deviation  $\sigma$ , which expresses in this case the extent of the thermally induced disorder effects.

## 5.6 $\lambda_i$ Calculation

Parallel to the determination of the intermolecular parameters  $V_{ij}$ , which is necessarily based on the knowledge of the whole crystal structure, the intramolecular reorganization energies are calculated from the molecular structure only.

Referring to Sections 4.2 and 4.5.2, the equilibrium structures of the neutral and charged ground states, which are necessary to calculate  $\lambda_i^{AP}$  (along with the electron affinities and ionization potentials), are obtained from DFT geometry optimization calculations. Closed-shell wavefunctions are dealt with through a restricted Hamiltonian, whereas open-shell wavefunctions by means of the unrestricted analogue. The energies referred to as  $E_y^{geo-x}$ , with  $x \neq y$ , are obtained from single point calculations.

The nature of the critical points determined by such QM calculations is assessed by evaluating vibrational frequencies at the optimized geometries. Vibrational frequencies are also employed to estimate the vibrational contributions to  $\lambda_i^{HR}$ , as described in Section 4.5.2.

## 5.7 Charge Mobility

With all the needed intra- and intermolecular computed parameters, MLJ charge transfer kinetic constants can be calculated, as reported in Eq. (4.19), with  $\nu$  set equal to 5. Note that usually not all the dimers extracted from the automated procedure (*e.g.*, those within the 15 Å cut-off) contribute to the rate constants. Because of statistical limitations (*vide infra*), charge jumps featuring electronic couplings smaller than 30  $cm^{-1}$  and without a remarkable standard deviation are generally excluded from the  $k_{eT}^{MLJ}$  evaluation. The rate constants are the input for the KMC simulations.

In each KMC simulation a single charge carrier is let move within the crystal via hopping events occurring between neighboring molecules forming a dimer. The probability  $P_i$  associated with the charge jump to the  $i$ -th neighbor of a given molecule is determined by the corresponding rate constant  $k_{eT}^{MLJ}$  (for simplicity, " $k$ " from here onwards) as:

$$p_i = \left( \frac{k_i}{\sum_j k_j} \right) \quad (5.3)$$

where  $j$  runs over possible paths for a charge localized on a given molecule in the crystal. The time associated with the electron transfer to the  $i$ -th neighbor is:

$$t_i = \frac{1}{k_i} \quad (5.4)$$

and the covered distance is the distance between the centers of mass of the two molecules forming the dimer. The trajectory is propagated by selecting randomly one molecule in the crystal as the starting point. Depending on the dimers that have been selected, a list of possible neighbors is available and the trajectory is advanced by choosing a random number  $r$  uniformly distributed between 0 and 1 and by selecting the  $j$ -th neighbor such that:<sup>10-11</sup>

$$\sum_i^{j-1} p_i < r \leq \sum_i^j p_j \quad (5.5)$$

The position of the charge carrier is saved and accumulated for groups of, *i.e.*, 2000 trajectories. An approximately linear dependence<sup>11</sup> of the mean square displacement

$$MSD = \langle [\bar{r}(t) - \bar{r}(0)]^2 \rangle \quad (5.6)$$

as a function of time  $t$  is obtained by averaging over the subsets of 2000 KMC trajectories. The diffusion coefficient  $D$  is readily obtained from the fitted linear dependence of  $MSD$  employing the Einstein equation, as in Eq. (4.34).

A certain number of subgroups of 2000 trajectories each, *e.g.*, ten subgroups are produced and the final charge mobilities are obtained by averaging over those computed for each subgroup.

Each KMC trajectory consists of typically  $10^6$  moves and the temperature is set to 300 K. Because of the limited number ( $10^6$ ) of charge jumps, a cut-off of 30  $cm^{-1}$  is applied to the electronic couplings contributing to the charge propagation, in order to avoid that small coupling jumps acquire an overestimated statistical weight and suppress the charge mobility for such an artifact.

## 5.8 References

- [1] Frisch, M. J. *Gaussian 09*, revision A.02, Gaussian, Inc., Wallingford CT, **2009**.
- [2] Ponder, J. W. *TINKER, Software Tools for Molecular Design Version 4.2*; **2004**.  
<http://dasher.wustl.edu/ffe/>
- [3] Skourtis, S. S.; Balabin, I. A.; Kawatsu, T.; Beratan, D. N. *Proc. Natl. Acad. Sci. U.S.A.* **2005**, *102*, 3552–3557.
- [4] (a) Marcon, V.; Breiby, D. W.; Pisula, W.; Dahl, J.; Kirkpatrick, J.; Patwardhan, S.; Grozema, F.; Andrienko, D. *J. Am. Chem. Soc.* **2009**, *131*, 11426–11432. (b) Martinelli, N. G.; Savini, M.; Muccioli, L.; Olivier, Y.; Castet, F.; Zannoni, C.; Beljonne, D.; Cornil, J. *Adv. Funct. Mater.* **2009**, *19*, 3254–3261. (c) Athanasopoulos, S.; Kirkpatrick, J.; Martinez, D.; Frost, J. M.; Foden, C. M.; Walker, A. B.; Nelson, J. *Nano Lett.* **2007**, *7*, 1785–1788. (d) Olivier, Y.; Lemaire, V.; Brédas, J.-L.; Cornil, J. *J. Phys. Chem. A* **2006**, *110*, 6356–6364. (e) Andrienko, D.; Kirkpatrick, J.; Marcon, V.; Nelson, J.; Kremer, K. *Phys. Status Solidi B* **2008**, *245*, 830–834. (f) Tan, L.; Zhang, L.; Jiang, X.; Yang, X. D.; Wang, L. J.; Wang, Z.; Li, L. Q.; Hu, W. P.; Shuai, Z. G.; Li, L.; Zhu, D. B. *Adv. Funct. Mater.* **2009**, *19*, 272–276. (g) Nan, G. J.; Yang, X. D.; Wang, L. J.; Shuai, Z. G.; Zhao, Y. *Phys. Rev. B* **2009**, *79*, 115203. (h) Yang, X.; Wang, L.; Wang, C.; Long, W.; Shuai, Z. *Chem. Mater.* **2008**, *20*, 3205–3211.
- [5] *Cambridge Crystallographic Data Centre*. <http://www.ccdc.cam.ac.uk/>
- [6] *Crystallography Open Database*. <http://www.crystallography.net/>
- [7] Coropceanu, V.; Cornil, J.; da Silva Filho, D. A.; Olivier, Y.; Silbey, R.; Brédas, J.-L. *Chem. Rev.* **2007**, *107*, 926–952.
- [8] Berendsen, H. J. C.; Postma, J. P. M.; Vangunsteren, W. F.; Dinola, A.; Haak, J. R. *J. Chem. Phys.* **1984**, *81*, 3684.
- [9] (a) Sleight, J. P.; McMahon, D. P.; Troisi, A. *Appl. Phys. A* **2009**, *95*, 147–152. (b) Martinelli, N. G.; Olivier, Y.; Athanasopoulos, S.; Delgado, M. C. R.; Pigg, K. R.; da Silva, D. A.; Sanchez-Carrera, R. S.; Venuti, E.; Della Valle, R. G.; Brédas, J.-L.; Beljonne, D.; Cornil, J. *ChemPhysChem* **2009**, *10*, 2265–2273. (c) Troisi, A. *Mol. Simul.* **2006**, *32*, 707–716. (d) Cheung, D. L.; Troisi, A. *Phys. Chem. Chem. Phys.* **2008**, *10*, 5941–5952. (e) Troisi, A.; Orlandi, G. *J. Phys. Chem. A* **2006**, *110*, 4065–4070. (f) Troisi, A. *Chem. Soc. Rev.* **2011**, *40*, 2347–2358.

[10] Fichtorn, K. A.; Weinberg, W. H. *J. Chem. Phys.* **1991**, *95*, 1090-1096.

[11] (a) Yang, X. D.; Wang, L. J.; Wang, C. L.; Long, W.; Shuai, Z. G. *Chem. Mater.* **2008**, *20*, 3205-3211. (b) Tan, L.; Zhang, L.; Jiang, X.; Yang, X. D.; Wang, L. J.; Wang, Z.; Li, L. Q.; Hu, W. P.; Shuai, Z. G.; Li, L.; Zhu, D. B. *Adv. Func. Mat.* **2009**, *19*, 272-276. (c) Nan, G. J.; Yang, X. D.; Wang, L. J.; Shuai, Z. G.; Zhao, Y. *Phys. Rev. B* **2009**, *79*, 115203.

## CHAPTER 6 - RESULTS AND DISCUSSION

This Chapter is an overview of my theoretical and computational investigations on organic molecular semiconductors, which were carried out within two main fields of interest.

As a first part of my investigations, I mainly discuss the optical, electronic, and structural properties of several core-extended rylene derivatives, which can be regarded to as model compounds for graphene nanoribbons. Two families have been studied, consisting in bay-linked perylene bisimide oligomers (Section 6.1) and N-annulated rylenes (Section 6.2). In particular, it is shown that the different connectivity and derivatizations, such as the inclusion of condensed five-membered aromatic heterocycles, modulate opto-electronic properties through the modification of the  $\pi$ -conjugation of the compounds.

Beside rylene derivatives, my studies also concerned electronic and spectroscopic properties of tetracene diimides (Section 6.3), quinoidal oligothiophenes (Section 6.4), and oxygen doped picene (Section 6.5).

As an example of device application, I studied the structural characteristics governing the efficiency of resistive molecular memories based on a derivative of benzoquinone (Section 6.6).

Finally, as a second part of my investigations, I concentrated on the charge transport properties of perylene bisimides derivatives. Precisely, a comprehensive study of the structural and thermal effects on the charge transport of several core-twisted chlorinated and fluoro-alkylated perylene bisimide *n*-type semiconductors is presented (Section 6.7).

## 6.1 BAY-LINKED PERYLENE BISIMIDES

The reason for the great interest regarding the synthesis of highly regiocontrolled oligomers of perylene bisimides (PBIs), beside the promising opto-electronic and *n*-type charge transport properties of the compound, lies in the possibility to obtain a fine tuning of such properties by controlling structural features like the atomic connectivity, the substituents, and the chirality of the molecule. From this perspective, singly, doubly, and triply bay-linked oligo-PBIs, comprising bay-region-tetrachlorinated doubly-linked oligomers and bowl-shaped triply-linked PBI dimers featuring condensed thiophene or pyrrole rings in the bay-regions, have been recently synthesized by Prof. Wang and his group at the Beijing National Laboratory for Molecular Science, Institute of Chemistry, Chinese Academy of Sciences, with whom we are collaborating. A further motivation for our computational analysis lies in the collaboration with Prof. Lambert and his group at the Institut für Organische Chemie, Universität Würzburg, who performed the spectroelectrochemical characterization of some of these compounds. In this Section, the structural, optical, and electrochemical properties of oligo-PBIs are discussed.

### 6.1.1 Background

Functional  $\pi$ -systems with well-defined structures have evoked considerable interest in light of their potential applications in molecular electronics in the past decades.<sup>1</sup> "The larger the  $\pi$ -system, the better the delocalization/stabilization of charge" is common belief in organic chemistry. While this is true for very small  $\pi$ -systems (*e.g.*, naphthalene *vs.* benzene), it is not for very large systems where charge localization is frequently observed.<sup>2</sup> In general, the reason for charge localization is a competition between the gain of resonance energy by charge delocalization and gain of energy by structural distortion.<sup>3</sup>

In organic and inorganic molecular chemistry, localization *vs.* delocalization of charge along with possible charge transfer phenomena is frequently explained by the concept of mixed valence (MV) chemistry.<sup>2b</sup> In the simplest case, a two-state model is used to outline the electronic situation: two redox centers in different redox states are connected within one molecular unit. The two diabatic, formally non interacting states in which a charge is localized at either of the two redox centers may then be coupled by an electronic coupling

interaction in order to yield two adiabatic (ground and excited) states that represent the physically observable states. In the adiabatic ground state, the charge may then be localized at one or the other redox center (a so-called Robin-Day class II situation)<sup>4</sup> or be delocalized between both redox centers (a Robin-Day class III situation).

For Robin-Day class II systems, the rate of electron transfer between the two redox centers is determined by the electronic coupling  $V$  and the barrier (and thus the shape of ground-state potential) between the state minima along the reaction coordinate (Figure 6.1).<sup>5</sup> According to R. Marcus, the barrier is associated with a fraction (approximately one quarter) of the reorganization energy  $\lambda$ .<sup>7</sup> The latter energy refers to the structural changes needed for making charge transfer possible. Using these terms and the harmonic approximation for the diabatic states, resonance energy is given by  $V^2/\lambda$ , which leads to delocalization the larger  $V$  and the smaller  $\lambda$  is.

Thus, if complete delocalization of a charge is wanted, one aims at increasing  $V$  and decreasing  $\lambda$ , which is particularly difficult for large  $\pi$ -systems, as for class II systems usually  $V$  gets smaller and  $\lambda$  (here especially the solvent part of  $\lambda$ ) increases the larger the  $\pi$ -system is.<sup>8</sup> Both trends could be counteracted by making stiff  $\pi$ -systems, which led us to use perylene bisimides on this account. Concerning mixed valence chemistry we also note that PBIs have hitherto not been employed as redox centers in this context.

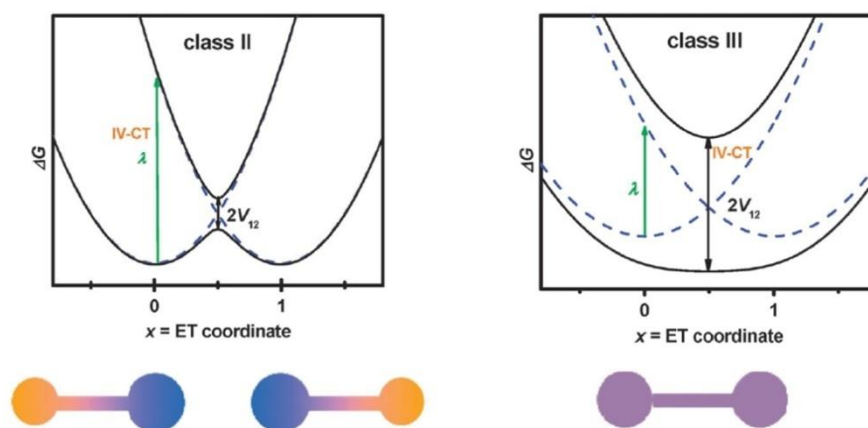


**Figure 6.1** Schematic representation of diabatic (blue dashed lines) and adiabatic (solid black lines) PEs of Robin-Day class II-III systems with degenerate MV systems; the different colors illustrate the different redox states of the redox centers (circles), while the different sizes illustrate the geometrical differences of charged *vs.* neutral redox centers.<sup>6</sup> Figure adapted from <sup>6</sup>.

Recently, synthetic routes have been found for linking in different ways the PBI units and obtaining, in order of increasing stiffness of the  $\pi$ -system, singly, triply, and doubly bay-linked oligo-PBIs.<sup>9</sup> Basically, copper-mediated coupling reactions have been widely employed in the formation of C-N, C-S, C-O, and CC bonds.<sup>10</sup> First of all, doubly-linked PBI chiral nanoribbons have recently been developed from tetrachloro-PBI simply mediated by copper (Figure 6.2).<sup>11-12,24</sup> Furthermore, a series of fully conjugated triply-linked PBI graphene nanoribbons of up to four units with very broad spectra and strong electron-accepting ability have also been synthesized by the combination of copper involved Ulmann coupling and C-H transformation (Figure 6.2).<sup>13</sup> However, there are structural isomers of triply-linked oligo-PBIs ( $n \geq 1$ ) according to the two possible coupling sites, which lead to difficulties in synthesis and separation of regiospecifically higher homologues. Consequently, structurally perfect singly bay-linked PBI arrays may be a fascinating candidate for exploring a novel connectivity and further constructing regiospecifically triply-linked PBI oligomers by ring fusion (Figure 6.2).

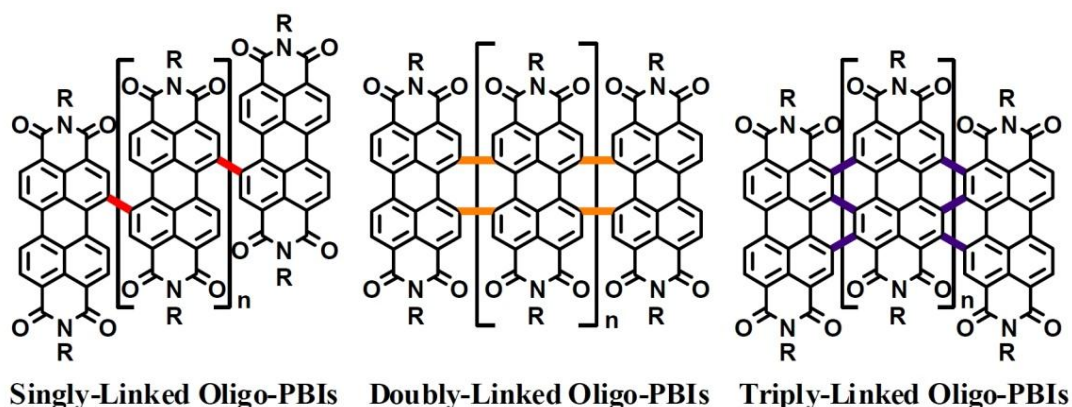


**Figure 6.2** Chemical structures of the three bay-linked PBI-based arrays,  $n = 0, \dots, x$ . Figure adapted from <sup>13</sup>.

In particular, we discuss in this contribution the structural and opto-electronic properties of the three diPBIs reported in Figure 6.3. We also performed a combined UV-Vis-NIR spectroelectrochemical and computational study to characterize their radical anionic states spectroscopically, pointing the MV nature of such compounds out.<sup>13</sup>

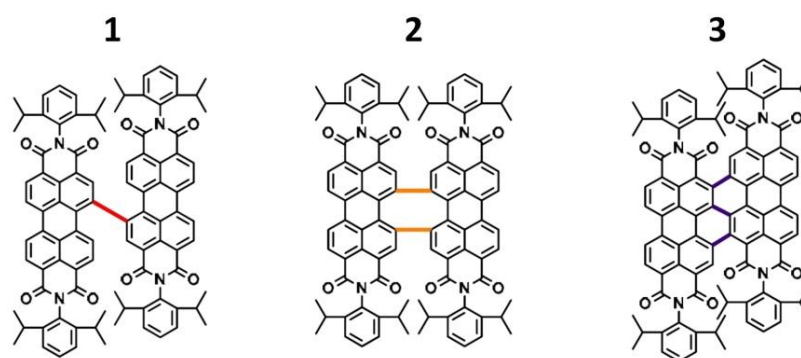


**Figure 6.3** Chemical structures of the three diPBIs featuring different linkage in the bay regions. They are referred to as **1** the singly, **2** the doubly, and **3** the triply bay-linked. Figure adapted from <sup>13</sup>.

The last decades have also witnessed an increasing attention toward the design and construction of chiral  $\pi$ -conjugated molecules and polymers with specific functions.<sup>14</sup> Induction of molecular twisting conformations represents a suitable strategy to achieve chirality for these systems. Although a wide range of chiral  $\pi$ -conjugated systems have been reported,<sup>15</sup> in most cases a dynamic racemization is observed due to relatively low energy inversion barriers.<sup>16</sup> Sterically encumbered substituents in bay regions can result in twisted  $\pi$ -systems of PBIs. However, in general the two twisted enantiomers interconvert easily in solution and coexist in the solid state. Würthner and co-workers<sup>17</sup> demonstrated that the racemization barriers of PBIs depend on the sizes of the bay substituents, and reported tetrabromo-PBI as the first example of enantiomerically pure core-twisted PBI. Then, the first example of conformationally stable chiral oligo-PBIs consist just in the doubly-linked PBI derivatives recently synthesized by Prof. Wang and co-workers.<sup>18</sup> In this Section, we also report the identification of the atropo-enantiomers of the compounds illustrated in Figure 6.4 by the comparison of their measured and simulated circular dichroism (CD) spectra.<sup>18</sup>

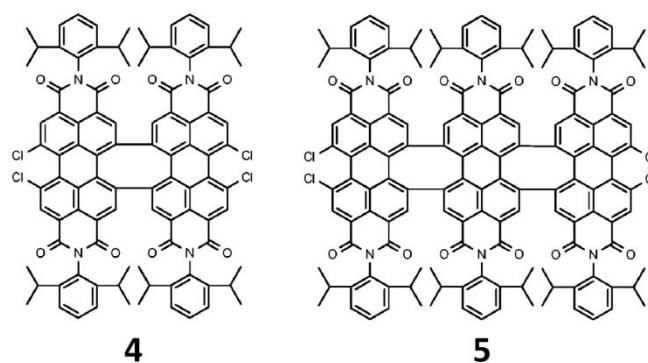


**Figure 6.4** Chiral "ladder-type" doubly-linked PBI dimer (**4**) and trimer (**5**). Figure adapted from <sup>18</sup>.

Finally, the immense interest surrounding fullerenes has directed increasing attention toward bowl-shaped polycyclic aromatic hydrocarbons (PAHs), also called molecular bowls, and these have become attractive targets for design and synthesis.<sup>19</sup> In recent years, various molecular bowls, displaying curved molecular structures and  $\pi$ -surfaces, extraordinary chemical and physical properties, and unique self-assembly behavior, have been prepared by either flash vacuum pyrolysis<sup>20</sup> or fully solution-phase synthetic methods.<sup>21</sup> Incorporation of heteroatoms into curved PAHs has been shown to determine several intriguing properties associated with the modified  $\pi$ -system and the potential applications.<sup>22</sup> However, there have been only few reports on strained aromatic polycycles including heteroatoms such as S and N in their frameworks.<sup>23</sup> From this perspective, the recently synthesized<sup>24</sup> bowl-shaped triply-linked heterocyclic annelated PBI dimers put themselves as an interesting contribution to such research topic. In this text, we discuss our joint experimental characterization and computational study<sup>24</sup> regarding the structural features and the UV-Vis absorption and electrochemical properties of the bowl-shaped diPBIs illustrated in Figure 6.5.

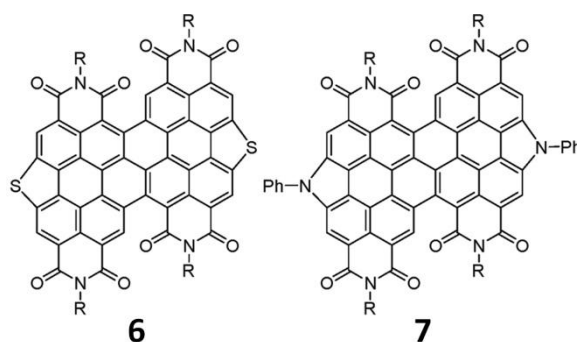


**Figure 6.5** Chemical structures of the bowl-shaped heterocyclic annelated S-diPBI (**6**) and N-diPBI (**7**), where "R" is a 2,6-diisopropylphenyl. Figure adapted from <sup>24</sup>.

### 6.1.2 Computational details

Model structures for bay-linked PBIs featuring methyl substituents instead of isopropyl units on the phenyl rings were optimized with DFT calculations. For compounds **1**, **2**, and **3** it was adopted the CAM-B3LYP long-range corrected functional with the 6-31G\* basis set. Since the problem of poor asymptotic of the exchange-correlation potential is considered to be a consequence of the self-interaction energy error, in turn responsible for the over-delocalization, it is expected that CAM-B3LYP should also provide a more realistic description of the localization of charges in our systems compared to the B3LYP functional.

Note that the B3LYP functional predicts fully delocalized structures for all the systems investigated and localization is not recovered by the inclusion of solvent effects through the use of the polarizable continuum model (PCM) approach.<sup>6,25</sup> As such issues were further the desired analysis, for compounds **4**, **5**, **6**, and **7** the ground states were optimized at the simpler B3LYP/3-21G\* level, also owing to the large dimension of the chromophores and the presence of heavy heteroatoms like sulfur and chlorine.

The tendency of CAM-B3LYP to overestimate the excitation energy (particularly for valence excitations)<sup>26</sup> is well known and thus all the computed spectra were rigidly shifted to the red by 2500  $cm^{-1}$ . It is also true that CAM-B3LYP was recently shown to be preferable to other functionals, and in particular to B3LYP, for TD-DFT calculations of excitation energies and properties, especially involving charge transfer (CT) states, since it can give a balanced description of local, Rydberg, and CT excitations.<sup>27</sup> For this reason, it was used for diPBIs **1**, **2**, and **3**, and to simulate the circular dichroism spectra of the doubly-linked **4** and **5**. Instead, the excitation energies and oscillation strength for the bowl-shaped **6** and **7** were determined by means of TD-B3LYP, since long-range corrected functionals had not been included in the current Gaussian(03) package yet.

Regarding the spectroelectrochemical analysis of the neutral and radical anions of **1**, **2**, and **3**, from a computational point of view, the correct description of a biradical contribution requires one to go beyond the single determinant approximation whose limit is readily established by checking the stability of the wavefunction. An alternative to computationally expensive multi-determinant approaches, is to relax the constraints of identical spatial occupation for  $\alpha$  and  $\beta$  electrons, as done in the unrestricted approach. Spin-restricted closed-shell (CS) calculations for singlet states were performed with the CAM-B3LYP functional. The stability of the singlet state CS wavefunction was tested, for each compound (the Gaussian09 keyword `stable=opt` was used)<sup>28-29</sup> in the di-anion and tetra-anion states; for those molecules showing instability of the CS wavefunction, we determined the stable broken symmetry (BS)<sup>30</sup> wavefunction (open-shell biradicaloid configuration) and we optimized the molecular structure also at the unrestricted UCAM-B3LYP (BS) level. In addition, the lowest-energy triplet states ( $T_1$ ) were optimized at the UCAM-B3LYP level.

Orbital pictures were prepared with Molekel 4.3 visual software; some molecular structure pictures were realized with PyMOL visual software. Electronic excitation energies and oscillation strengths were computed: for the 30 lowest singlet excited electronic states of **1**, **2**, and **3** with time dependent (TD) CAM-B3LYP calculations; for the 140 lowest singlet excited

states of **4** and **5** with TD-CAM-B3LYP; and for the 60 lowest singlet excited electronic states of **6** and **7** with TD-B3LYP. In plotting computed electronic spectra, a Lorentzian line-width of 0.2 (0.1) eV was superimposed to each computed intensity to facilitate the comparison with experimental spectra of **1**, **2**, and **3** (**6** and **7**); whereas, in plotting computed CD spectra of **4** and **5**, a Lorentzian line-width of 0.1 eV was adopted. The computed spectra did not include the vibronic structure associated with electronic bands and as a result they show a reduced number of bands compared with the experimental spectra. All QM calculations were performed with the Gaussian09 (Gaussian03 for bowl-shaped **6** and **7**) package.

While non-covalently linked aggregates of PBIs need more elaborate methods to cover the electronic structure in the excited state,<sup>31</sup> our above outlined protocol appears to be sufficiently reliable to treat the electronic aspects of the covalently linked PBIs of this work.

### 6.1.3 Chiral nanoribbons

The B3LYP/3-21G\* computed structures of doubly-linked dimer **4** and trimer **5** indicate that the two adjacent PBI moieties entangle almost perpendicularly with each other, driven by the intrinsic tendency of the tetraarylene unit to adopt the low-energy  $D_{2d}$  geometry (Figure 6.6). The twisted (*anti*) configuration of each PBI unit combined with the reciprocal orientation of the two PBI units leads to two enantiomeric configurations for dimer **4**. As for trimer **5**, each of the three PBI units (in *anti* configuration) is twisted with respect to the adjacent one. Obviously, the conformational analysis is similar to that of triply linked tri(perylene bisimide)s.<sup>11</sup> The two pairs of adjacent PBI units bend in the same direction forming a helical structure (with two enantiomeric forms), while bending in opposite directions provides a non-helical structure (a *meso*-configuration). Interestingly, the lowest energy computed *meso* configuration features a central PBI unit in its (high energy) *syn* configuration and the two lateral PBIs in their (low energy) *anti* configuration with a resulting energy *ca.* 8.6 kcal mol<sup>-1</sup> above the two enantiomeric forms.<sup>18</sup>

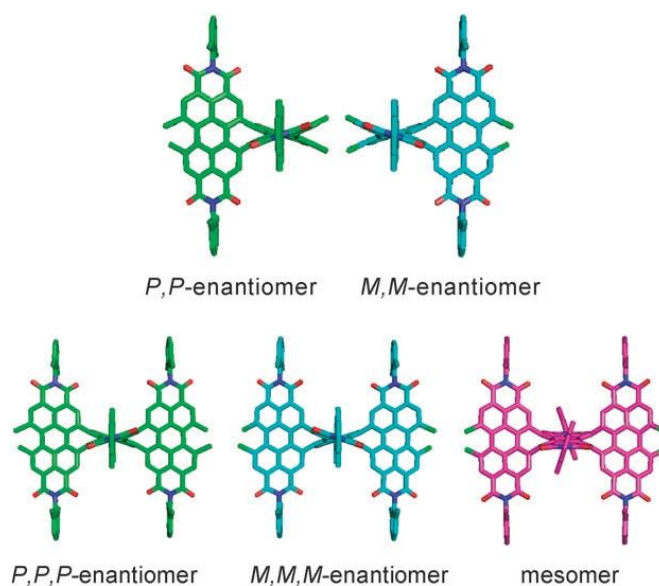


**Figure 6.6** B3LYP/3-21G\* computed structures for the two enantiomers of **4** (top) and the three isomers of **5** (bottom). Hydrogen atoms are omitted for clarity. Figure adapted from <sup>18</sup>.

The absolute configurations of dimer **4** and trimer **5** were deduced by comparing the experimental with the TD-CAM-B3LYP/3-21G\* computed<sup>18</sup> CD spectra as shown in Figure 6.7. The low energy transitions observed in UV-Vis spectra correspond to an overall bisignated CD signal for both **4** and **5**, in agreement with calculations. The computed sequence of positive and negative Cotton effects (or *vice versa*) enabled the unequivocal assignment to specific enantiomers. According to simulations, the first fraction after HPLC for **4** can be assigned to the  $P,P$ -enantiomer, whereas the  $M,M$ -enantiomer is responsible for the CD spectrum of the second fraction. As for **5**, the first and the third fractions are determined to be the  $P,P,P$ - and  $M,M,M$ -enantiomers, respectively, while the second fraction is consistent with the *meso*-configuration due to no observed (or computed) CD signal in the UV-Vis region.

All the enantiomers of **4** and **5** can be kept under argon for 3 h at 150 °C with unchanged features in their CD spectra in chloroform. Notably, the tetraphenylene building block imparts high barrier to such chiral conformers for interconversion that occurs easily in triply linked diPBIs and triPBIs.

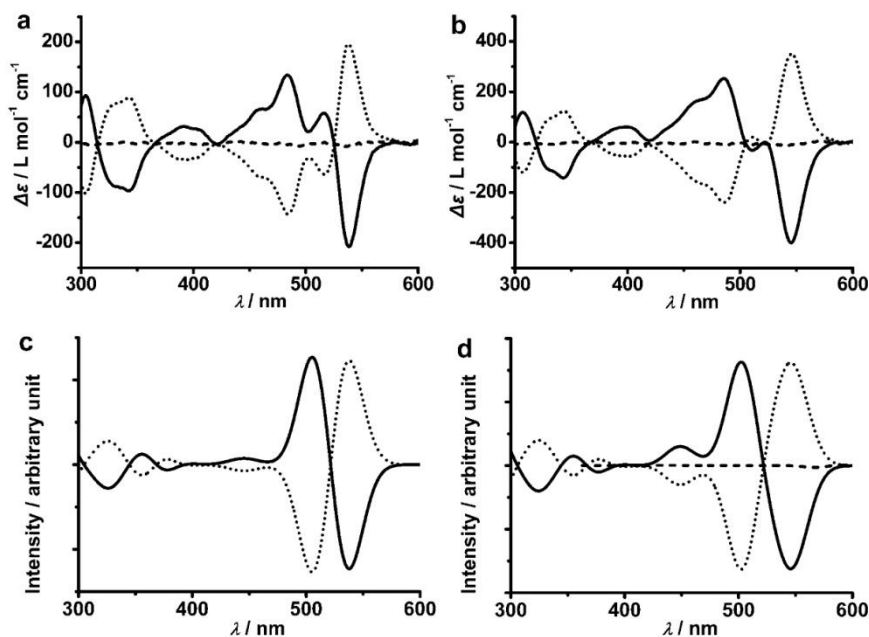


**Figure 6.7** (a) CD spectra of **4** before HPLC (dashed line) and the first (solid line) and the second (dotted line) fraction after HPLC, (b) CD spectra of the first (solid line), the second (dashed line), and the third (dotted line) fraction of **5** after HPLC in chloroform. (c) TD-CAM-B3LYP/3-21G\* computed CD spectra of the *M,M*-enantiomer (dotted line) and *P,P*-enantiomer (solid line) of **4**. (d) TD-CAM-B3LYP/3-21G\* computed CD spectra of the *M,M,M*-enantiomer (dotted line), *P,P,P*-enantiomer (solid line), and mesomer (dashed line) of **5**. To facilitate comparison, the computed spectra (vibronic structure not included) were red shifted to match the first observed transition. Figure adapted from <sup>18</sup>.

In light of their high extinction coefficients in the UV-Vis region, moderate fluorescence quantum yields and electron-accepting ability (that we discussed in <sup>18</sup>), the twisted chiral systems are likely to be promising materials for applications in special opto-electronic devices, enantioselective recognition and for the design of chiral supramolecules.

#### 6.1.4 Bowl-shaped diPBIs

Referring to the compounds reported in Figure 6.8, it was attempted to prepare annelated monoPBIs **9** and **10** by the incorporation of two thiophene and pyrrole rings, respectively.<sup>24</sup> The crystal structure of **9** previously reported in <sup>32</sup> revealed a planar perylene core probably because of the long length of C-S bonds (1.78 Å) and thus the weak ring strain. In contrast with **9**, the DFT optimized structure of **10** showed a deeply bowl-shaped configuration<sup>24</sup> due

to the strong strain resulting from the short length of C-N bonds (1.41 Å). The expected product **10** (by the Buchwald-Hartwig reaction<sup>33</sup> of tetrahalogen-PBIs with an amine) was not obtained, while the only observed product was **11**, indicating the high energy needed for simultaneously forming two strained pyrrole rings in bay regions. These findings demonstrate the difficulty in preparing a PBI bowl by modifying the bay regions, suggesting that an extended aromatic system may be necessary for flexibility and to reduce the energy costs of making the five-membered ring.

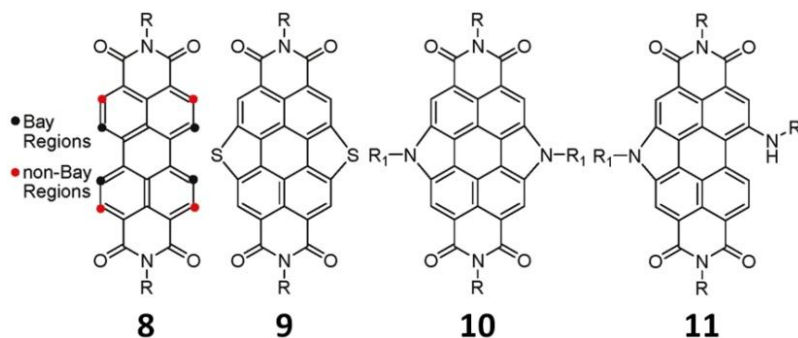


**Figure 6.8** Chemical structures of a perylene bisimide monomer (**8**) and synthesized heterocyclic annelated monoPBIs (**9**, **10**, and **11**). Figure adapted from <sup>24</sup>.

It was demonstrated, by the computed structures of **8** and its extended trimers, that the steric congestion between H atoms in the non-bay region and the adjacent O atoms (blue label in **8** shown in Figure 6.8) twists the aromatic core to an out-of-plane configuration.<sup>11</sup> Accordingly, the synthetic route was modified for the design of PBI bowls, first by introducing the steric congestion in non-bay regions through the synthesis of diPBIs and second by including the strained heterorings in bay regions.

For the triply-linked diPBI series, the steric congestion between oxygen and the neighboring hydrogen atom is expected to result in two possible conformers, namely, the *trans* and *cis* conformer, in which both ends of each PBI unit tilt in different and the same direction, respectively. To investigate the effect of the steric congestion and the heterorings strain on structures, quantum chemical calculations were carried out on models for **6** and **7** as well as **3** for comparison, featuring methyl substituents instead of the isopropyl units on the phenyl rings.

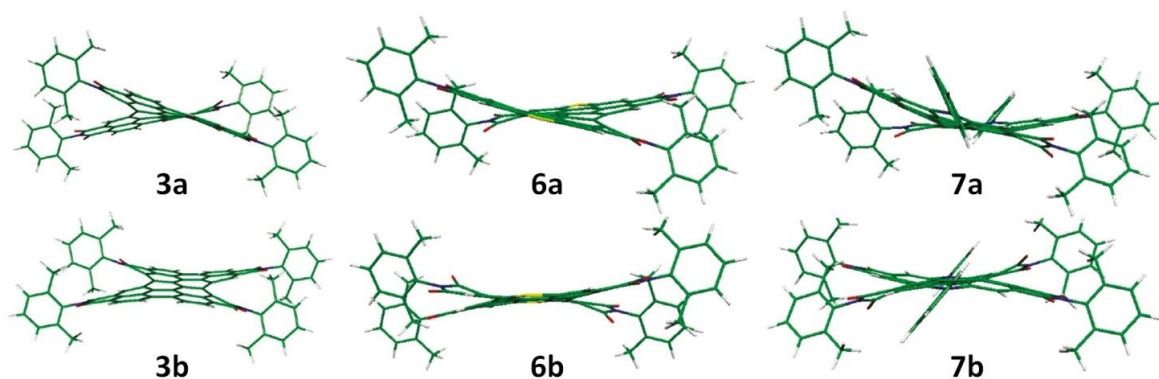


**Figure 6.9** Equilibrium structures of *trans* (a) and *cis* (b) conformers of **3**, **6**, and **7** computed at the B3LYP/3-21G\* level. Figure adapted from <sup>24</sup>.

For **3**, **6**, and **7**, low-energy *trans* and *cis* conformers were optimized, representing two different out-of-plane deformations of the two PBI moieties (Figure 6.9). As shown in Figure 6.9, PBI moieties in the *trans* conformer of **3** are planar, while in the *cis* conformer, their aromatic cores are forced to be bent by the steric congestion in non-bay regions. In the *trans* conformer of **6**, the aromatic core of each PBI unit is almost planar, while in the *cis* conformer, the PBI moieties exhibit a shallow bowl-shaped structure. In contrast with the *trans* conformer of **6**, each PBI unit in the *trans* structure of **7** is twisted, and, compared to the *cis* conformer of **6**, the bowl shape of the PBI moieties in the *cis* structure of **7** is strongly enhanced. These changes are justified by the larger strain induced by pyrrole rings with respect to thiophene rings. Notably, for S- and N-diPBI, the computed energies of *trans* and *cis* configurations are much closer than those of diPBI **3** (see Table 6.1), indicating that the incorporation of S and N atoms increases the stability of *cis* conformers while decreasing that of *trans* conformers, leading ultimately to a more stable *cis* conformer for **7**.

Crystals of S- and N-diPBI suitable for single-crystal X-ray structure analysis were obtained at room temperature. As proved by the crystal structures and the temperature-dependent <sup>1</sup>H NMR experiments, only the *cis* conformers of **6** and **7** were obtained in the products of Stille-type and Buchwald reactions.<sup>34-35</sup> The equilibrium structures predicted for the *cis* conformers of **6** and **7** are in close agreement with their crystal structures, which have crystallographically imposed inversion symmetry (Figure 6.10); moreover, much shallower PBI bowls were correctly predicted for **6**. The curvature was evaluated by the method of  $\pi$ -orbital axis vector analysis (POAV1)<sup>36</sup> based on the geometry obtained from the X-ray analysis. In S-diPBI, the highest local curvature, 2.9°, is found on C19 (C19A) that is in the

imide rings, and the average pyramidalization angle (PA) for the carbons of the central benzene ring in the perylene core is 1.0°. Compared with **6**, the PAs for most carbons in the aromatic core of **7** are much higher, indicating the strongly enhanced bowl-shaped structures induced by pyrrole rings. As shown by the crystal structure of **7**, the highest local curvature, 4.7°, is found on C10 (C10A), corresponding to one of the  $\beta$ -carbons in the pyrrole rings, and the average PA for the carbons of the central benzene ring in the perylene core is 3.1°. These results are in agreement with the computed structures.<sup>24</sup>

**Table 6.1** B3LYP/3-21G\* absolute energies, relative energies, MO energies, HOMO-LUMO gaps and optical gaps ( $\Delta E_{S_0-S_1}$ ) of *cis* and *trans* conformers of **3**, **6**, and **7**. First reduction potentials measured as half-wave potentials *vs.* Fc/Fc<sup>+</sup> in CH<sub>2</sub>Cl<sub>2</sub> solution, with scan rate of 0.1 V s<sup>-1</sup> and TBAPF<sub>6</sub> (0.1 M) as electrolyte.<sup>24</sup>

	Absolute Energy (a.u.)	Relative Energy (kcal/mol)	$E_{\text{HOMO}}$ (eV)	$E_{\text{LUMO}}$ (eV)	$E_{\text{LUMO}+1}$ (eV)	$\Delta E_{\text{H-L}}$ (eV)	$\Delta E_{S_0-S_1}$ (eV)	$E_{1^{\text{st-red}}}$ (V)
<i>cis</i> <b>3</b>	-3875.90077962	+5.32	-5.99	-4.07	-3.27	1.92	-	-
<i>trans</i> <b>3</b>	-3875.90926192	0.00	6.04	-4.06	-3.28	1.98	1.82	-0.46
<i>cis</i> <b>6</b>	-4666.18889074	+2.61	-6.17	-4.04	-3.29	2.13	1.97	-0.62
<i>trans</i> <b>6</b>	-4666.19304338	0.00	-6.19	-4.04	-3.30	2.15	1.99	-
<i>cis</i> <b>7</b>	-4443.14849145	-0.10	-5.85	-3.71	-2.99	2.14	1.95	-0.73
<i>trans</i> <b>7</b>	-4443.14833135	0.00	-5.87	-3.73	-3.03	2.14	1.97	-

Not only do they significantly alter the structures of the aromatic core, but the introduction of heteroatoms to diPBI skeletons also induces highly ordered superstructures. Interestingly, unique ribbons of S-diPBI **6** were observed in the crystal structure (Figure 6.11), similarly with those found in the crystal of **9**. The inversion-related pairs of S-diPBI molecules in the crystal of **6** are linked by C3-H3···O1 hydrogen bonds with H···O distances of 2.29 Å, C-H···O angles of 134.7°, and S1···O1 intermolecular contacts with S···O distances of 3.06 Å. The probable reason for the formation of ribbons in **6** is the subtle influence of sulfur atoms on the molecular electronic structure.

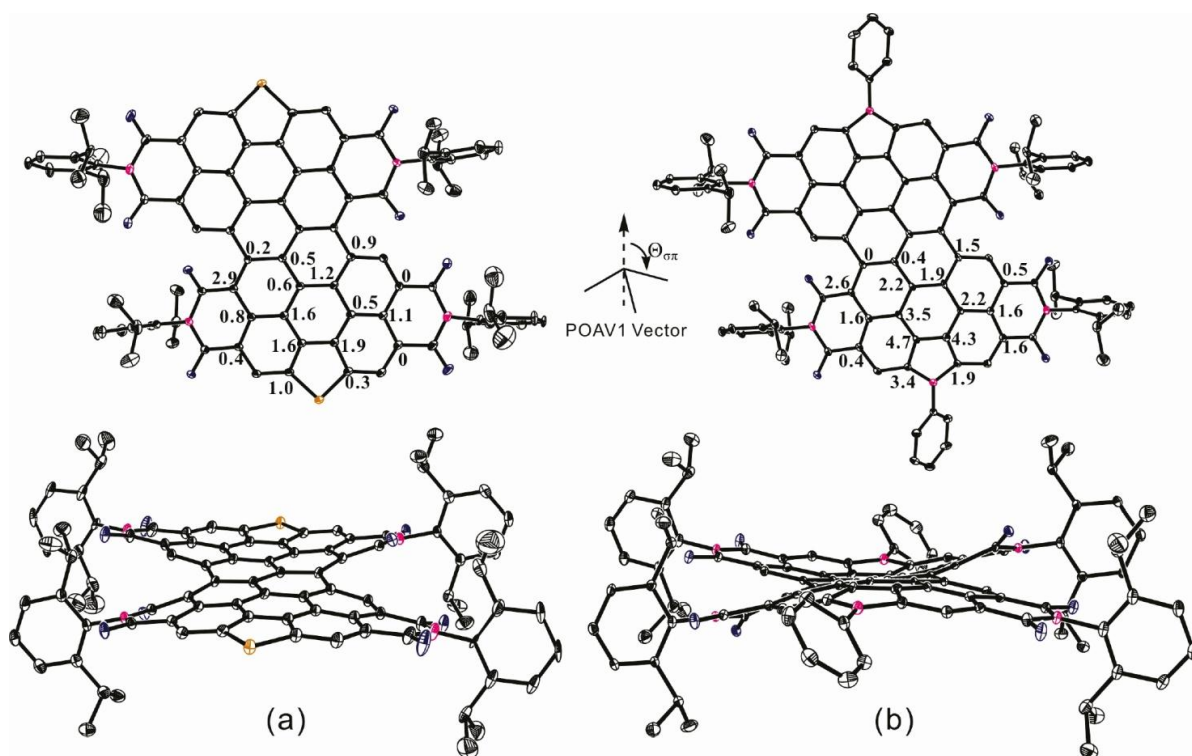


**Figure 6.10** ORTEP drawing of the molecular structures of (a) 6 and (b) 7 with 30% probability ellipsoids. POAV1 pyramidalization angles ( $\theta_{\sigma\pi} - 90$ ) of one PBI unit based on the crystal structures of 6 and 7 are given: (top) top view and (bottom) side view. Figure adapted from <sup>24</sup>.

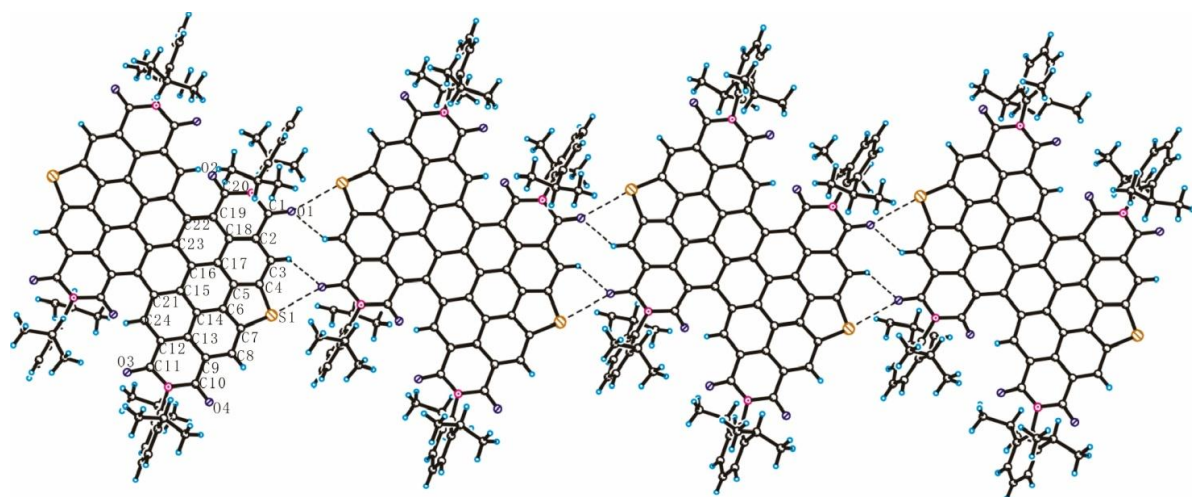


**Figure 6.11** Intermolecular interactions in the crystal structure of 6. Figure adapted from <sup>24</sup>.

The introduction of S and N atoms to diPBI skeletons leads to a remarkable change in the electronic absorption spectra. The blue-black solution of S-diPBI 6 exhibits three major

absorption bands at 411, 584, and 633 nm ( $\epsilon_{\max} = 90500 \text{ M}^{-1} \text{ cm}^{-1}$ ) with a blue shift of 51 nm relative to **3**, as a reflection of the expanded aromatic core (Figure 6.12) with a five-atom ring. Compared with **3**, N-diPBI **7** displays hypsochromically shifted spectra with five major bands at 414, 430, 574, 620, and 670 nm ( $\epsilon_{\max} = 77100 \text{ M}^{-1} \text{ cm}^{-1}$ ). As revealed by the absorption spectra, the energy of the lowest allowed electronic transition, namely the optical gap, increases with the incorporation of heteroatoms in bay regions.

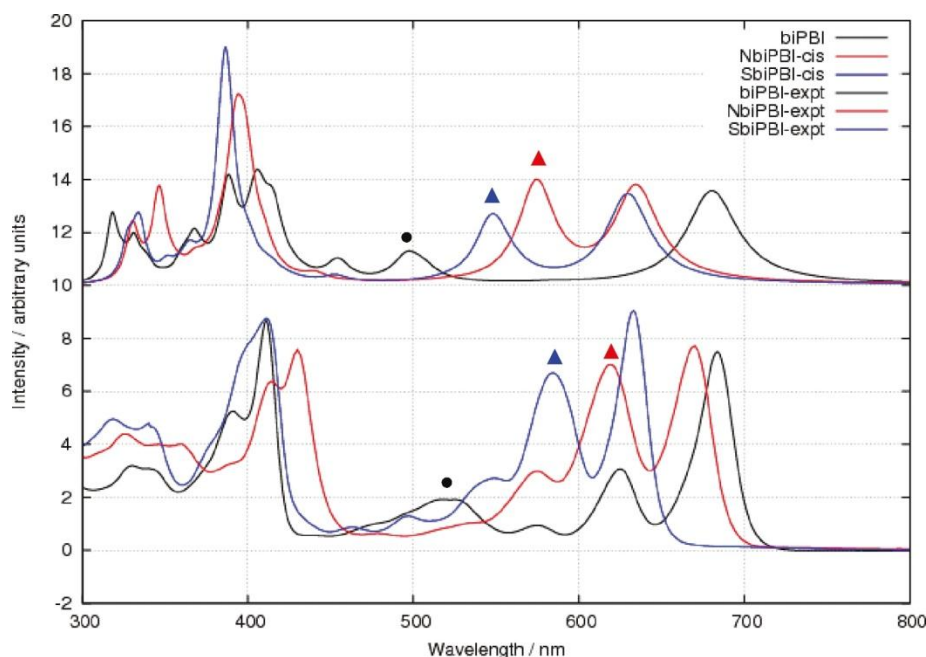


**Figure 6.12** (top) The TD-B3LYP/3-21G\* calculated absorption spectra (vibronic structure not included) of **3** (black), **6** (blue), and **7** (red) at the optimized *cis* structures. (bottom) Absorption spectra of **3** (black), **6** (blue), and **7** (red) in  $\text{CHCl}_3$ . Figure adapted from <sup>24</sup>.

The TDDFT calculated absorption spectra of **6** and **7** agree very well with the observed counterpart although the excitation energy of the  $S_0 \rightarrow S_1$  transition of **7** is overestimated. The overestimate results from the limited basis set we were forced to use because of the size of the systems. Calculations on similar heteroderivatives of smaller sizes show that an almost perfect match between computed and observed energies is obtained employing the larger 6-31+G\*\* basis set.

The comparison between computed and observed spectra shows an interesting feature characterizing the bowl-shaped heteroderivatives featuring five-member rings. The shallow maximum observed for **5** at *ca.* 510-520 nm (black dot in Figure 6.12) disappears for **6** and **7** and at the same time a new electronic transition appears at lower energies (red and blue

triangles in Figure 6.12), in the region of the 0-1 vibronic band associated with the first electronic transition. Inspection of the wavefunctions associated with these (black dot and red, blue triangles) electronic transitions shows a similar orbital nature. The red shift in bowl-shaped derivatives results from the modulation of molecular orbital energies (and shapes) induced by the presence of the heteroatoms forming the five-membered rings.

Referring to Figure 6.13, it can be seen that the incorporation of heteroatoms modifies the shapes of the frontier orbitals of **6** and **7** compared with those of **3** although they conserve essentially the same parentage. The energies of LUMO and LUMO+1 of **6** and **7** are less negative than those of **3** because of the expanded  $\pi$ -system by heteroatoms (Table 6.1).

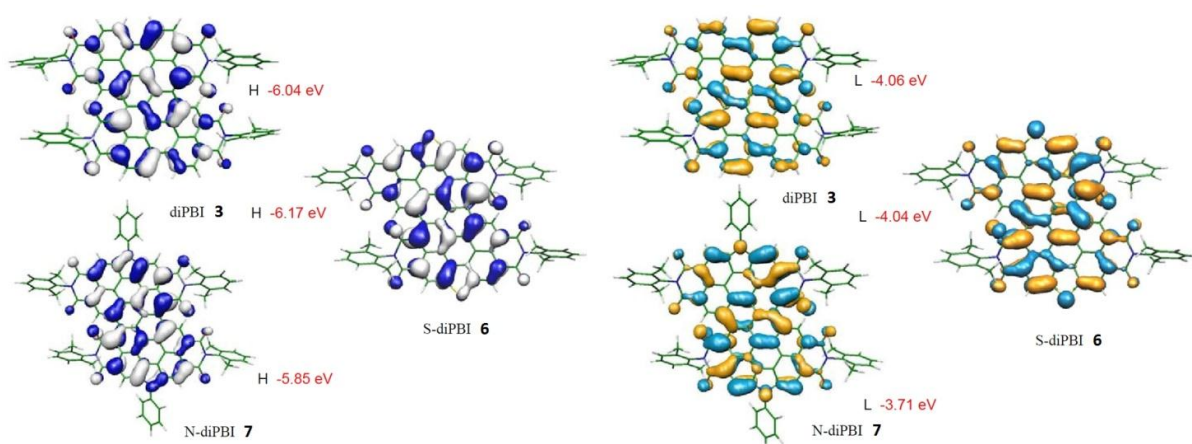


**Figure 6.13** Comparison between computed frontier orbitals (left) HOMO and (right) LUMO of *trans* **3**, *cis* **6**, and *cis* **7** showing the dominant orbital parentage across diPBI derivatives. Figure adapted from <sup>24</sup>.

Similar to **3**, the cyclic voltammograms of **6** and **7** exhibit four reduction waves,<sup>24</sup> revealing that both **6** and **7** are easily reduced and can accept up to four electrons. The half-wave reduction potentials *vs.* Fc/Fc<sup>+</sup> are -0.62, -0.90, -1.60, and -1.73 V for **6** and -0.73, -1.01, -1.65, and -1.85 V for **7**. Compared with **3**, the first reduction potentials of **6** and **7** are more negative, suggesting an increased LUMO energy associated with the expansion of the conjugated system through the incorporation of a pentagonal ring, in agreement with the computed results (Table 6.1). Due to the stronger electron-donating properties of nitrogen atoms compared to sulfur atoms, **7** shows a smaller electron affinity than **6**, in agreement with the calculated LUMO energies. Thus, the electrochemical properties as well as frontier

orbital energies can be easily modulated by incorporating different heteroatoms into bay regions of diPBI.

In light of the accessibility to synthesis and functionalization, the unique doubly bowl-shaped structures, the controllable curvatures, and the easily tunable optical and electrochemical properties, heterocyclic annelated diPBIs are promising not only for basic research in molecular engineering, but also for applications in material science.

### 6.1.5 $\pi$ -conjugation effects and mixed-valence features in diPBIs

In the remainder of this Section, we mainly compare the structural, optical, and electrochemical properties of the singly, doubly, and triply bay-linked diPBIs shown in Figure 6.3, particularly focusing on the effects of the extension of the  $\pi$ -conjugation over the PBI units, and on the mixed-valence nature of such compounds when negative charges are added electrochemically. Indeed, as for the former, it is shown that the degree of interaction in both the neutral and the reduced forms of the linked PBIs is qualitatively doubly-linked < singly-linked  $\ll$  triply-linked, due to the different degree of twisting and flexibility between the two moieties; only triply-linked diPBI shows totally delocalized wavefunctions over the entire  $\pi$ -system. As for the latter, through a combined spectroelectrochemical and computational study, it is demonstrated the mixed-valence nature of these diPBIs, whose Robin-Day classes are thus assigned.

Singly-linked dimer **1** show much broader and more complicated bands than the parent PBI monomer **8** (Figure 6.14). Also, the spectrum of **1** shows a pronounced red-shift of the onset of absorption (590 nm compared to 540 nm for **8**). The red shift and the broadening can be interpreted by a combination of effects: first, owing to the flexibility of singly-linked dimers and trimers, a number of slightly different reciprocal orientations of the PBI units are expected. These, in turn, may be associated with different exciton couplings of localized PBI transitions that overall broaden and red shift the spectrum.

The significant Stokes shift and lower fluorescence quantum yield ( $\lambda_{em} = 605$  nm,  $\Phi_{fl} = 0.15$ ), compared to parent PBI monomer **8** ( $\lambda_{em} = 534$  nm,  $\Phi_{fl} = 1.0$ ),<sup>37</sup> are also a consequence of this

exciton coupling if one considers that several twisted conformers will contribute to the spectrum. Indeed, the angle between the two PBI  $\pi$ -systems is *ca.*  $70^\circ$  for the gas phase optimized geometry, but owing to the flexibility of singly linked derivatives one expects that a number of different reciprocal orientations of the two PBI units will be populated at room temperature, which follow neither the simple *J* or *H* type behavior of chromophore aggregates.<sup>38</sup>

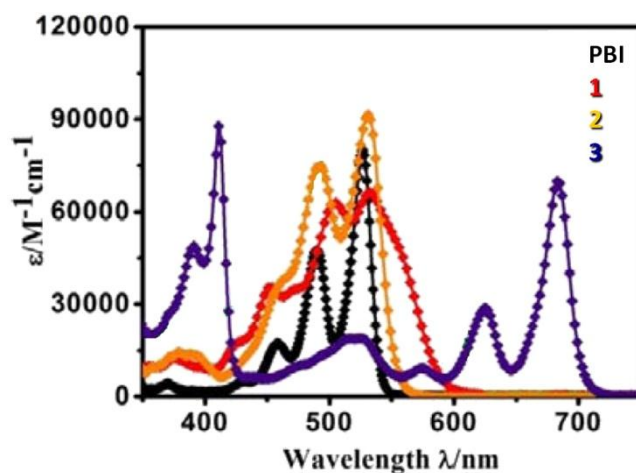


**Figure 6.14** UV-Vis absorption spectra: PBI **8** (black), singly-linked **1** (red), doubly-linked **2** (orange), and triply-linked **3** (violet) in chloroform. Figure adapted from <sup>13</sup>.

Much in contrast, the absorption spectrum of doubly-linked diPBI **2** appears to be very similar to monomer **8**, just slightly more diffuse and with an onset at *ca.*  $550\text{ nm}$  (Figure 6.14). This startling observation becomes easily comprehensible if one considers the structure which is in fact much more rigidly twisted than in **1** - our computational results indicate an almost orthogonal orientation of the two PBI  $\pi$ -systems, as already observed for tetrachlorinated doubly-linked diPBI **4** (Section 6.1.3). In contrast to **1**, the broadening is reduced because the structure of **2** is forced to be rigidly twisted by the presence of the double link. Also the fluorescence spectrum of **2** is not much shifted from that of **8**, with the highest fluorescence quantum yield ( $\Phi_{fl} = 0.44$ ) among all linked diPBIs.

The triply-linked diPBI **3** behaves much different than either **8**, **1**, and **2**. It features the longest absorbance maximum at  $684\text{ nm}$ ,<sup>12a</sup> bathochromically shifted by about  $4350\text{ cm}^{-1}$  relative to that to **8**, and pronounced vibronic progressions. These properties can hardly be explained by excitonic interactions and are due to extensive conjugation over the whole  $\pi$ -system of **3**. This is also visible by the MO coefficients of HOMO-1 and LUMO which include

the three CC single bonds connecting the two PBIs which form a rigid and almost planar "step ladder" superstructure. The fluorescence has a small Stokes shift ( $170\text{ cm}^{-1}$ ) but an almost negligible quantum yield (0.02).

The cyclic voltammograms (CVs) were measured in  $\text{CH}_2\text{Cl}_2$  containing  $\text{Bu}_4\text{NPF}_6$  (0.1 M) as the electrolyte and referenced against ferrocene/ferrocenium redox couple. The electrochemical data in  $\text{CH}_2\text{Cl}_2$  are summarized in Table 6.2. The cyclic voltammograms of **1**, **2**, and **3** showed well-defined, single-electron, four reversible reduction waves (Figure 6.15). Differential pulse voltammetry experiments show that each wave corresponds to the transfer of a single electron.<sup>13</sup> Compared with PBI, the half-wave reduction potentials *vs.*  $\text{Fc}/\text{Fc}^+$  were -0.83, -0.98, -1.14, and -1.25 V for **1**, -0.80, -0.96, -1.07, and -1.22 V for **2**, and -0.46, -0.73, -1.49, and -1.66 V for **3**, indicating the much higher electron affinity of triply-linked diPBI as a reflection of substantial electronic coupling between the adjacent PBI units, whereas **1** and **2** displayed much smaller shift, further supporting the electronic decoupling of these non-conjugated oligo-PBIs. LUMO levels estimated by reduction half-wave potentials are -4.33 eV for **1**, -4.36 eV for **2**, and -4.70 eV for **3**, largely decreasing by nearly 0.3 eV from highly twisted diPBIs (**1** and **2**) to more planar diPBI (**3**).

**Table 6.2** Optical and electrochemical properties of bay-linked oligo-PBIs versus those of PBI **8**.<sup>13</sup>

	$\lambda_{\text{max}}^{\text{abs}}$ (nm) <sup>a</sup>	$\epsilon$ ( $M^{-1}\text{ cm}^{-1}$ ) <sup>a</sup>	$\lambda_{\text{max}}^{\text{flu}}$ (nm) <sup>b</sup>	$\Phi_{\text{fl}}$ <sup>c</sup>	$E_{1\text{r}}$ (V) <sup>d</sup>	$E_{2\text{r}}$ (V) <sup>d</sup>	$E_{3\text{r}}$ (V) <sup>d</sup>	$E_{4\text{r}}$ (V) <sup>d</sup>	$E_{\text{LUMO}}$ (eV) <sup>e</sup>	$E_{\text{g}}$ (eV) <sup>f</sup>
<b>PBI</b>	527	80900	534	1.00	-0.96	-1.22	-	-	-4.20	2.30
<b>1</b>	533	66200	605	0.15	-0.83	-0.98	-1.14	-1.25	-4.33	2.09
<b>2</b>	531	91600	552	0.44	-0.80	-0.96	-1.07	-1.22	-4.36	2.25
<b>3</b>	684	87000	692	0.02	-0.46	-0.73	-1.49	-1.66	-4.70	1.85

<sup>a</sup> Measured in dilute  $\text{CHCl}_3$  solution ( $1.0 \cdot 10^{-5}\text{ M}$ ). <sup>b</sup> Measured in dilute  $\text{CHCl}_3$  solution ( $1.0 \cdot 10^{-6}\text{ M}$ ). <sup>c</sup> Average deviation for  $\Phi_{\text{fl}}$ ,  $\pm 0.04$ , determined with **8** (N,N'-di(2,6-diisopropylphenyl)perylene-3,4:9,10-tetracarboxylic acid bisimide,  $\Phi_{\text{fl}} = 1.00$  in  $\text{CHCl}_3$ ) as the standard. <sup>d</sup> Half-wave potential in  $\text{CH}_2\text{Cl}_2$  solution. <sup>e</sup> LUMO (eV) estimated by the half-wave reduction potentials with  $E(\text{Fc}/\text{Fc}^+ \text{ in } \text{CH}_2\text{Cl}_2) = 5.16\text{ V vs. vacuum}$ .<sup>13</sup> <sup>f</sup>  $E_{\text{g}}$  (eV) calculated by the onset of absorption in  $\text{CHCl}_3$  solution.

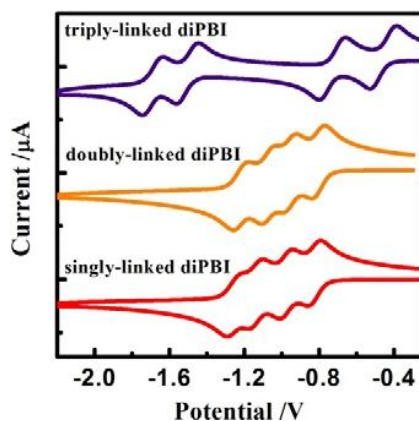


**Figure 6.15** Reductive cyclic voltammograms of **1** (red), **2** (orange), and **3** (violet) in  $\text{CH}_2\text{Cl}_2$  with a scan rate of  $100 \text{ mVs}^{-1}$  vs.  $\text{Fc}/\text{Fc}^+$  and  $\text{Bu}_4\text{NPF}_6$  ( $0.1 \text{ M}$ ) as electrolyte. Figure adapted from <sup>13</sup>.

In order to get more insight into the electronic structure of charged diPBIs **1**, **2**, and **3**, we performed UV-Vis-NIR spectroelectrochemical experiments in  $\text{CH}_2\text{Cl}_2/\text{Bu}_4\text{NPF}_4$  ( $0.2 \text{ M}$ ). In these experiments, the spectra are recorded at specific electrical potentials applied to a polished platinum disk electrode. Owing to the relatively large redox potential separations of the four redox processes for each compound, there are potentials at which a specific radical ion can almost exclusively be generated (in all cases more than 80%). The recorded spectra at these potentials are thus taken as that of the "pure" radical ion without further deconvolution. These spectra are given in Figure 6.16 for **1**, **2**, and **3** vs. wavenumbers for better comparison with computed spectra.

First inspection of the spectroelectrochemistry of **1** and **2** reveals very similar behavior up to the spectra of the tetra-anion which is due to their twisted structure. For both compounds, reduction to the radical monoanions results in a decrease of the lowest energy transition at *ca.*  $20000 \text{ cm}^{-1}$  to roughly 50% of its original intensity (if one takes the integral of the band), while new transitions rise between  $10000$  and  $17000 \text{ cm}^{-1}$ . Upon reduction to the radical dianion, the band at  $20000 \text{ cm}^{-1}$  disappears almost completely while that between  $10000$  and  $17000 \text{ cm}^{-1}$  doubles its intensity. Further reduction to the tri-anion again leads to *ca.* 50% decrease of the band at  $10000$ - $17000 \text{ cm}^{-1}$  and to rise of a new band between  $14000$  and  $22000 \text{ cm}^{-1}$ . The latter band doubles at reduction to the tetra-anion while that at  $10000$ - $17000 \text{ cm}^{-1}$  vanishes.

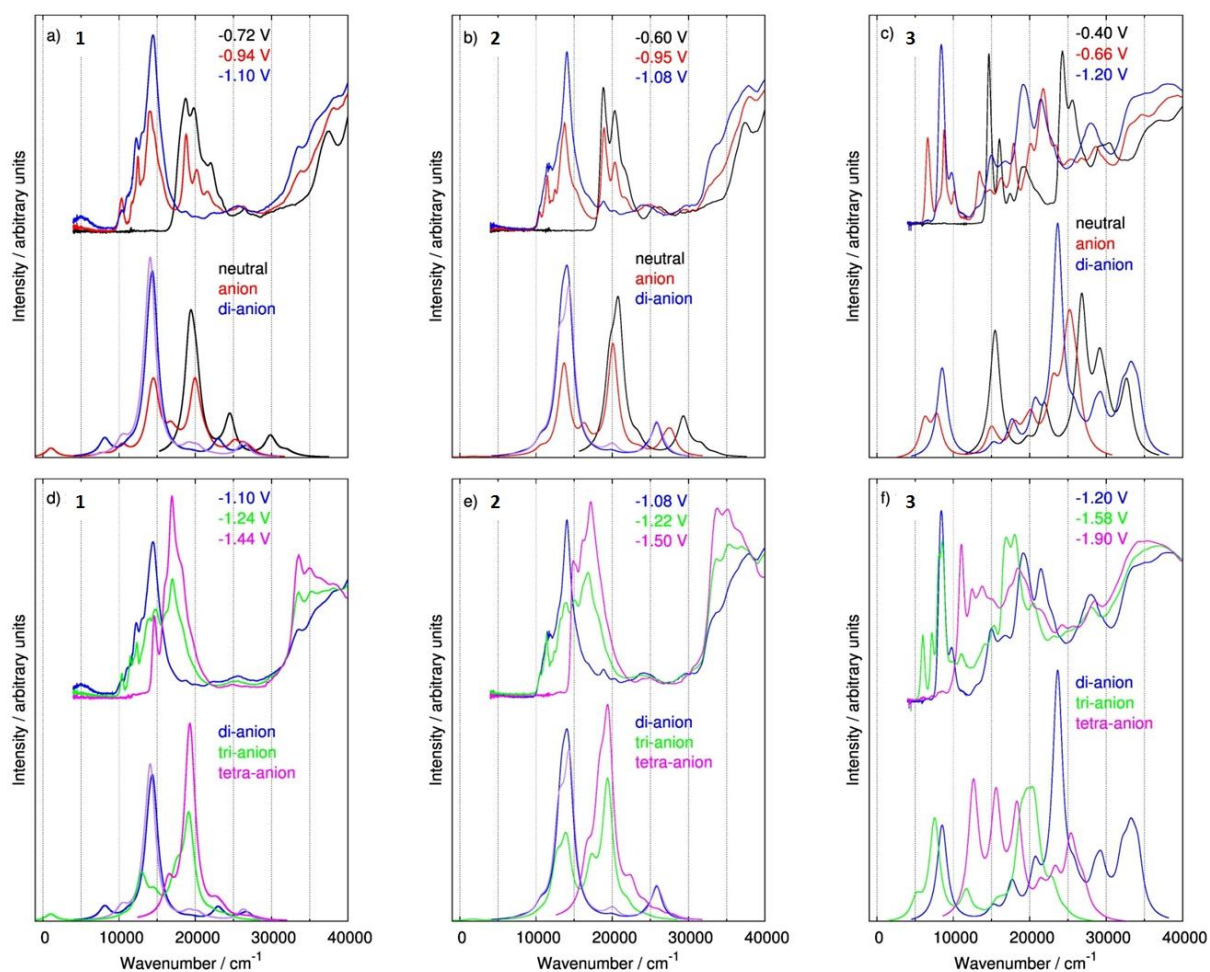


**Figure 6.16** Comparison between observed and computed electronic spectra of (a,d) **1**, (b,e) **2**, and (c,f) **3**. (top) Spectroelectrochemistry in  $\text{CH}_2\text{Cl}_2/\text{Bu}_4\text{NPF}_6$  (0.2 M), potentials at which the spectra are measured are given *vs.*  $\text{Fc}/\text{Fc}^+$ . (bottom) TD-CAM-B3LYP/6-31G\* computed spectra rigidly shifted to the red by  $2500\text{ cm}^{-1}$ . Figure adapted from <sup>13</sup>.

These observations suggest practically non-interacting PBI units in **1** and **2** whose spectroscopic properties are additive. In other words, any charge added to **1** or **2** is completely localized at either of the two PBI units.

However, particularly for the di-anion of **1** but also visible in **2** a weak transition at even lower energy than those mentioned above rises at *ca.*  $5000\text{ cm}^{-1}$  which is too near to the accessible spectroscopic window of the solvent to be visible completely in its shape. A similar band, though much less intense, is also visible at the same energy for the mono-anion and the tri-anion of **1** and **2**. These bands result from the interaction of the two PBI units and are charge transfer (CT) bands in nature (*vide infra*). Those CT bands in the mono-anion and

tri-anion of **1** and **2** are referred to as intervalence charge transfer (IV-CT) bands typical of MV class II compounds. Unfortunately, these bands are very weak and their maximum is beyond the accessible spectroscopic window. Thus, we were unable to evaluate electronic couplings from these IV-CT bands by *e.g.* Mulliken-Hush theory.<sup>39</sup>

Much in contrast to **1** and **2**, diPBI **3** shows differing spectra for each redox state which cannot be reconstructed from independent units. For the mono-anion a very structured band between 6000 and 11000  $cm^{-1}$  rises which is replaced by a much more intense and sharp band between 7500 and 11000  $cm^{-1}$  for the di-anion. The tri-anion again shows band down to 5000  $cm^{-1}$  which has a series of new bands at 10000  $cm^{-1}$  and higher energy. This behavior clearly shows that in the triply linked and rigid diPBI **3** the charges introduced by stepwise reduction interact strongly, which proves delocalization of these charges within the whole diPBI.

However, a detailed experimental analysis of the spectra is difficult as the number of state involved and their electronic origin is unknown. Furthermore, the spin multiplicity of each redox state (*e.g.*, singlet or triplet for the di-anion, doublet or quartet for the tri-anion and singlet, triplet or quintet for the tetra-anion) is unknown but may result in distinguishable absorption spectra that may serve in comparison of theory and experiment to unequivocal assignments. Thus, we performed quantum-chemical calculations at DFT level in order to address the above mentioned questions.

As mentioned above, our structure optimizations yield a twisted structure for diPBI **1**, an almost orthogonal structure for **2**, and an almost planar structure for **3** (Figure 6.17). The striking observation of an even stronger twist in **3** shows that multiple linkages can induce a stronger twist because of more structural strain.

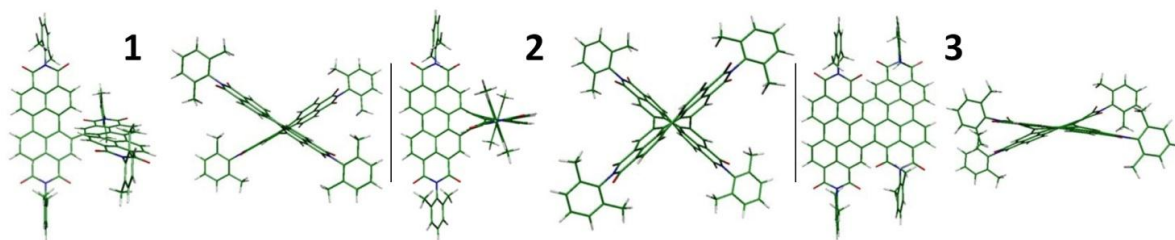


**Figure 6.17** CAM-B3LYP/6-31G\* optimized geometries of the neutral ground states of diPBIs **1**, **2**, and **3**; frontal and side views are shown. Figure adapted from <sup>13</sup>.

The different degrees of electronic communication in *n*-type singly, doubly, and triply bay-linked diPBI can be quantified by considering the computed energy splitting between LUMO and LUMO+1 orbitals of the neutral species (Figure 6.18).<sup>40</sup> Such splitting, which correspond to twice the electronic coupling  $V$  according to the energy-splitting-in-dimer (ESD) method combined with Koopmans' theorem (KT),<sup>41</sup> amounts to  $7813\text{ cm}^{-1}$  (CAM-B3LYP/6-31G\*) for **3**. Thus, the electronic coupling  $V$  between the two PBI chromophores is of the order of  $3900\text{ cm}^{-1}$  which should be compared with the intramolecular reorganization energy  $\lambda_i$  associated with the PBI anion formation, amounting to about  $0.28\text{ eV}$  or *ca.*  $2300\text{ cm}^{-1}$  in the gas phase.<sup>42</sup> <sup>43</sup> Therefore, triply-linked diPBIs are expected to be Robin-Day class III systems in the gas phase and in non-polar solvent such as the employed  $\text{CH}_2\text{Cl}_2$ .

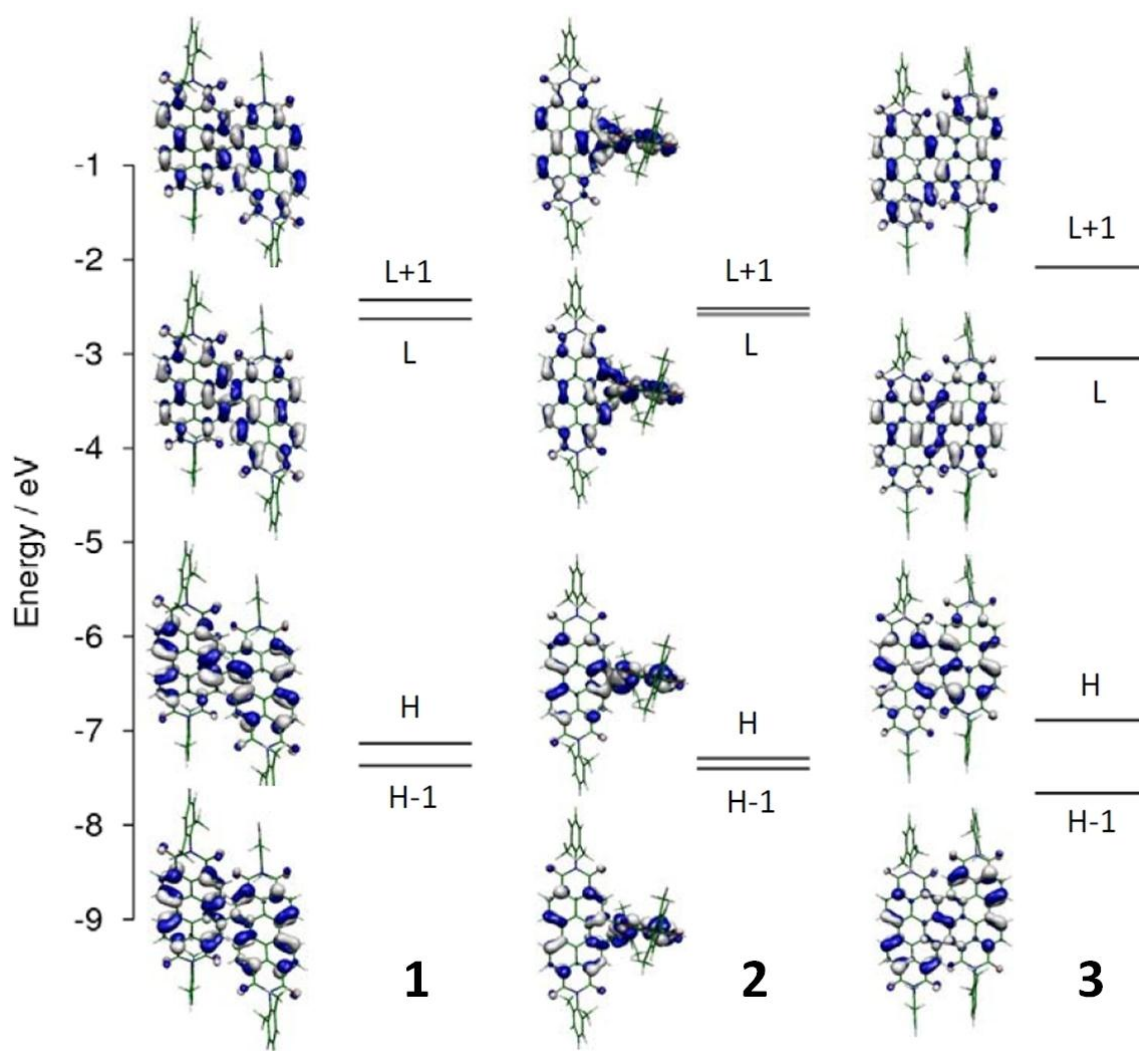


**Figure 6.18** CAM-B3LYP/6-31G\* frontier molecular orbitals of neutral **1**, **2**, and **3**. The large electronic communication of **3** compared to **1** and **2** results in a large energy split of LUMO/LUMO+1 and HOMO/HOMO-1 pairs of orbitals. Figure adapted from <sup>13</sup>.

For doubly-linked and singly-linked diPBIs the situation is more critical, since the electronic coupling diminishes to  $809\text{ cm}^{-1}$  for singly-linked **1** and to  $255\text{ cm}^{-1}$  for doubly-linked **2**, indicating that the systems should localize the charge on a single PBI (Robin-Day class II) unit rather than allowing full delocalization.

Indeed, one-electron localization was predicted for both the mono- and the tri-anionic forms of **1** and **2**, in accordance with their modest electronic couplings compared to **3**. Detailed bond lengths displaying the charge localization are collected in Figure 6.19 for **2**. The symmetry breaking of the atomic structure of the mono-anion (red), indicating localization of the electron on a single PBI unit, is clearly evident by comparison with the bond lengths of the neutral (black) and di-anion structures (blue). Similarly for the tri-anion, the bond lengths indicate localization of one electron on one PBI unit and of two electrons on the other PBI unit. Similar results are obtained for **1**,<sup>13</sup> while a gradual geometry change delocalized over the two PBI units is predicted for the triply-linked **3**.<sup>13</sup>

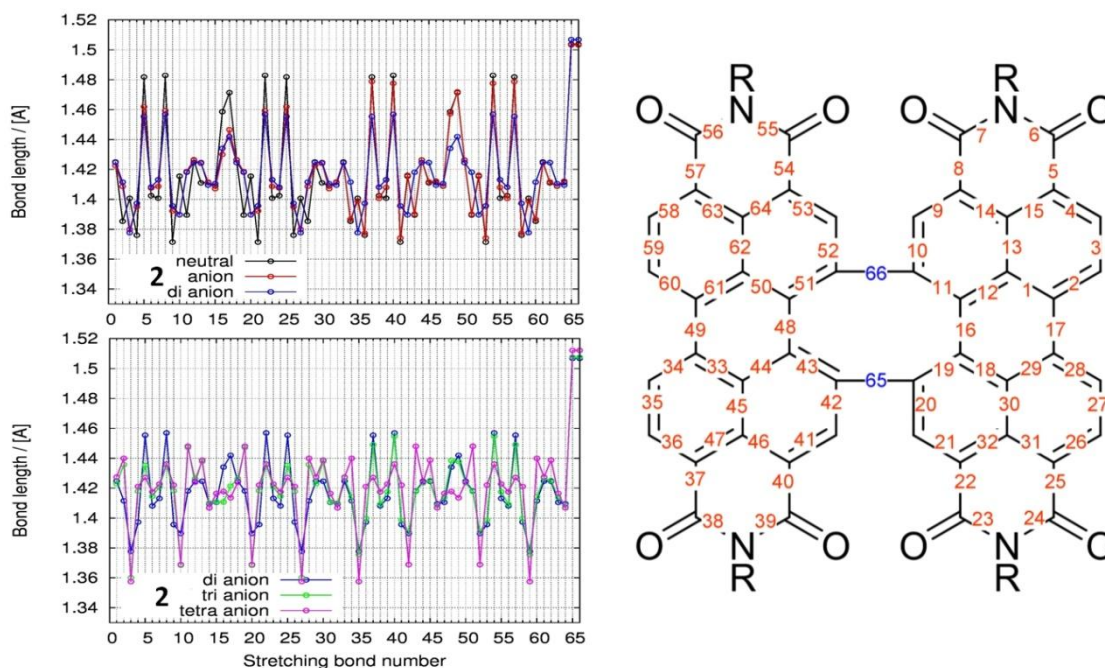


**Figure 6.19** CAM-B3LYP/6-31G\* equilibrium bond lengths for the neutral and anionic species of **2**. Figure adapted from <sup>13</sup>.

The small electronic communication of the PBI units in **1** and **2**, responsible for charge localization in mono- and tri-anions, also implies a biradical character of the di-anion. To determine the role of biradicaloid contributions to the di-anion (and tetra-anion form) of **1**, **2**,

and **3**, the stability of the CAM-B3LYP/6-31G\* closed-shell (CS) wavefunction was determined at the optimized geometry. Instability was found only for **1** and **2** in their di-anionic forms, whose UCAM-B3LYP broken symmetry (BS) equilibrium geometry was therefore determined and employed to compute the electronic absorption spectra. The BS stable structure of **1** and **2** resulted to be more stable than the CS structure by 10.21 *kcal mol<sup>-1</sup>* and 11.67 *kcal mol<sup>-1</sup>*, respectively, and almost degenerate with the triplet state (Table 6.3).

While for the di-anions of **1** and **2** the triplet and singlet states are predicted to be very close in energy, the triplet state of the di-anion of **3** is computed to be 11.86 *kcal mol<sup>-1</sup>* (0.51 *eV*) above the singlet state, and therefore it can be safely concluded that the di-anion is its singlet state. Apart from the di-anionic species, the lowest energy spin state of the other anionic forms is confirmed to be a singlet state (for tetra-anions) and the doublet for tri-anions, with higher spin states being generally more than 1.0 *eV* above the lowest energy state (Table 6.3). Therefore, electronic absorption spectra were computed for the most stable spin state of all the species considered except for the di-anion for which the spectrum of the triplet state was also evaluated for **1** and **2** and is reported in purple in Figure 6.16.

**Table 6.3** Relative energies of different spin states for the neutral and anionic forms of **1**, **2**, and **3**. From CAM-B3LYP/6-31G\* calculations.<sup>13</sup>

Spin state	Relative Energy ( <i>eV</i> )			Spin state	Relative Energy ( <i>eV</i> )	
	neutral	di-anion	tetra-anion		mono-anion	tri-anion
<b>singly-linked</b>						
singlet CS	0.00	+0.44	0.00			
singlet BS	-	0.00 <sup>a</sup>	-	doublet	0.00	0.00
triplet	+1.70	+0.00	+2.10	quartet	-	+1.44
<b>doubly-linked</b>						
singlet CS	0.00	+0.51	0.00			
singlet BS	-	0.00 <sup>b</sup>	-	doublet	0.00	0.00
triplet	+1.40	+0.00	+1.36	quartet	-	+1.38
<b>triply-linked</b>						
singlet CS	0.00	0.00	0.00			
singlet BS	-	-	-	doublet	0.00	0.00
triplet	-	+0.51	+0.79	quartet	-	-

<sup>a</sup> spin contamination:  $S^{*2} = 1.049$  after annihilation 0.615; <sup>b</sup> spin contamination:  $S^{*2} = 1.072$  after annihilation 0.621.

Inspection of Figure 6.16 shows a remarkable agreement between computed and observed spectra which suggests that the optimized atomic structures and, more specifically, the localization *vs.* localization pattern provided by CAM-B3LYP calculations is not only consistent with the computed magnitude of electronic couplings discussed above, but also with the electronic absorption features observed in the spectroelectrochemical investigation.

In agreement with the experimental results, the reduction to the mono-anion of **1** and **2** results in intensity decrease of the band at 20000  $cm^{-1}$  accompanied by the appearance of a number of new electronic transitions in the 15000  $cm^{-1}$  region. The appearance and disappearance of electronic transitions upon further reduction is closely reproduced by the calculations. The comparison between computed and observed data confirms the similarity of the spectral signatures of **1** and **2** and the localization of charges induced by their reduced electronic communication.

The spectra of the di-anionic forms of **1** and **2** deserve some additional comment: for each species, in Figure 6.16, we report both the purple spectrum computed for the triplet state and the blue spectrum computed for the BS singlet state. The two spectra look very similar in account of the similar predicted geometries for BS singlet and triplet. Nevertheless, for the singlet state a weak feature not computed for the triplet is found at about 7500  $cm^{-1}$ . This feature is well visible as a weak isolated band in the spectrum of **1**, while it is just a shoulder in the spectrum of **2**. This band has the same origin for both compounds and is due to a charge transfer (CT) excitation from the localized molecular orbitals as depicted in Figure 6.20a for the singly-linked compound. In this respect, the term "charge transfer" might be somewhat misleading as in total, no charge is transferred and there is no change of dipole moment upon excitation. However, the individual MO contributions of excitations are clearly CT in nature which prompted us to call this type of excitation "quasi-CT". Interestingly, the experimental spectra of the di-anion show a feature at 5000  $cm^{-1}$  which is slightly more intense for **1** than for **2** and that can be attributed to the CT transition. Therefore, even considering possible inaccuracies in the description of BS singlet states due to spin contamination, based on the comparison between computed and experimental spectra we can conclude that only the singlet state of the di-anions of **1** and **2** accounts for the weak CT band observed in the spectroelectrochemical study.

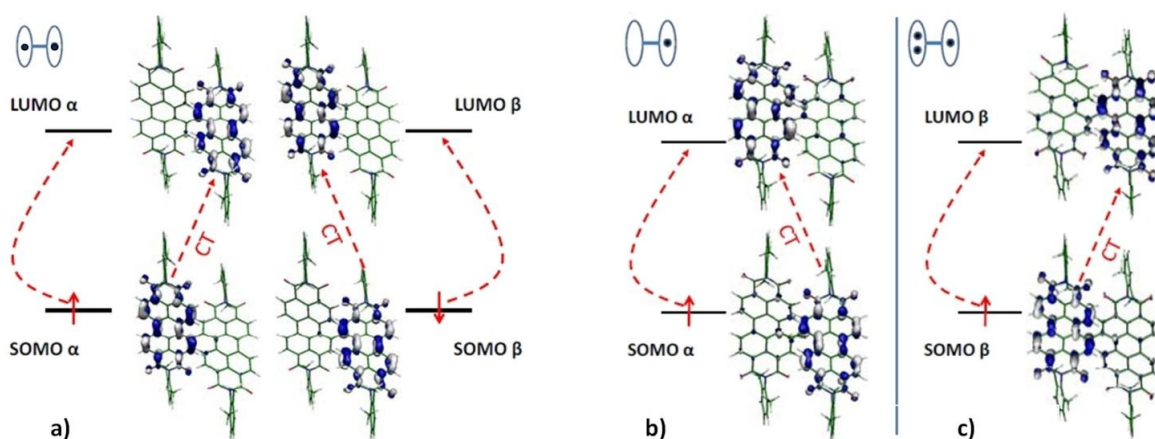


**Figure 6.20** (a) The localized nature of UCAM-B3LYP/6-31G\* SOMO and LUMO ( $\alpha$  and  $\beta$ ) orbitals of the BS biradical structure of the di-anion of **1**. The two electronic excitations responsible for the low energy (*ca.*  $7500\text{ cm}^{-1}$  computed value, *ca.*  $5000\text{ cm}^{-1}$  observed value) quasi-CT transition are indicated by dashed red arrows. (b-c) The localized nature of (b) the SOMO and LUMO ( $\alpha$ ) orbitals of the mono-anion of **1** and (c) the SOMO and LUMO ( $\beta$ ) orbitals of the tri-anion of **1**. These orbitals are involved in the electronic excitation responsible for the low energy (*ca.*  $1000\text{ cm}^{-1}$  computed value) CT transition indicated by the dashed red arrow. From UCAM-B3LYP/6-31G\* calculations. A schematic representation of electron localization on the singly linked diPBI is shown in the top left corner of each graph. Figure adapted from <sup>13</sup>.

A similar weak feature, shifted to even lower energies (at about  $1000\text{ cm}^{-1}$ ) is computed for the mono- and tri-anionic forms of **1** and **2** and is due to an IV-CT excitation as depicted in Figure 6.20b,c for the singly-linked diPBI. The experimental counterpart of the computed CT band is indeed observed in the low energy portion of the spectra collected in Figure 6.16. The analogy of MO excitations in the mono- and tri-anions of **1** (Figure 6.20b,c) also supports our assignment of the low energy band of the di-anion (Figure 6.20a) as a CT excitation.

The electronic transitions of **3** are determined by the strong electron interaction between the two PBI units and are therefore remarkably different from those of **1** and **2**. The close agreement between computed and observed spectra suggests that the degree of electronic coupling is realistically accounted for by the CAM-B3LYP calculations also for **3**.

To summarize, we demonstrated that the singly and doubly bay-linked diPBIs are electronically almost decoupled, but show weak IV-CT excitations in the NIR which result from weak interactions between the two PBI moieties of the mono- and tri-anionic forms of **1** and **2**, respectively. In this regard, the observation of such a quasi-CT band in the di-anions of **1** and **2** is surprising in view of their symmetry but it is explained by a mixture of two CT excitations of the  $\alpha$  and  $\beta$  electrons. However, the anions of **3** show excitations that are due to the delocalized wavefunction of the  $\pi$ -system.

Much in contrast to our initial expectation, the degree of interaction in both the neutral and the reduced forms of the linked PBIs does not follow the number of linkers but is qualitatively doubly-linked < singly-linked  $\ll$  triply-linked, due to the different degree of twisting between the two PBIs moieties.

For the first time in literature, to the best of our knowledge, perylene bisimide derivatives such as diPBIs have been considered in terms of their mixed-valence characteristics.

## 6.2 N-ANNULATED RYLENES

PBIs are not the only perylene derivatives we investigated. By repeating N-annulated perylene units along the short side of the  $\pi$ -system, they were recently synthesized bis-N-annulated quaterrylenes<sup>44</sup> and tri-N-annulated hexarylenes,<sup>45</sup> from the perspective of producing well-defined functionalized graphene nanoribbons through the synthesis of poly(*peri*-N-annulated perylene). Like the oligomers of perylene bisimide discussed in Section 6.1, the computational study of these rylene derivatives was strongly motivated by the collaboration with Prof. Wang, who synthesized the compounds<sup>45</sup> with his group at the Beijing National Laboratory for Molecular Science, Institute of Chemistry, Chinese Academy of Sciences. In this Section, it is shown that tri-N-annulated hexarylenes dyes display remarkably large dipole moments likely associated with the formation of *H* aggregates, as suggested by the sensible concentration dependence of the measured UV-Vis spectra. It is proposed that the combination of  $\pi$ - $\pi$  stacking interactions and dipole-dipole interactions may favor the formation of highly ordered supramolecular structures, resulting in enhanced charge carrier mobilities.

### 6.2.1 Background

Graphene nanoribbons (GNRs), in which the lateral quantum confinement opens an electronic gap that is a function of the ribbon width, have opened the way to a breakthrough in carbon-based nanoelectronics.<sup>46</sup> Driven by these, a great effort has been devoted to developing methods for the preparation of graphene nanoribbons: physical, top-down techniques are available like lithographic patterning of graphene sheets<sup>47</sup> or longitudinal unzipping of multiwalled carbon nanotubes;<sup>48</sup> but there is also the bottom-up strategy offered by synthetic chemistry.<sup>49</sup>

The copper-mediated condensation of PBIs along the bay region (short molecular axis) was used to construct graphene-type nanoribbons that are functionalized by arrays of imide groups (Figure 6.2).<sup>12a</sup> However, due to the two possible coupling positions, there are structural isomers of oligo-PBIs, which hinder further attempts toward the effective synthesis of higher homologues and structurally perfect poly(bay-PBIs),<sup>11</sup> unless peculiar

stratagems (e.g., the preliminary formation of a singly-linked basic array, see Section 6.1.1) are developed.<sup>13</sup>

Poly(*peri*-N-annulated perylene) can be regarded as perfect graphene nanoribbons incorporating nitrogen atoms into the armchair edge structures, providing ideal model compounds for chemically modified graphene ribbons with large dipoles. In this contribution, we present tri-N-annulated hexarylenes containing three space-demanding, branched alkyl chains and a variety of end-cap pending groups (Figure 6.21) to guarantee their good processability, which represent a new approach toward the rational synthesis of graphene nanoribbons with well-defined edges.<sup>45</sup>

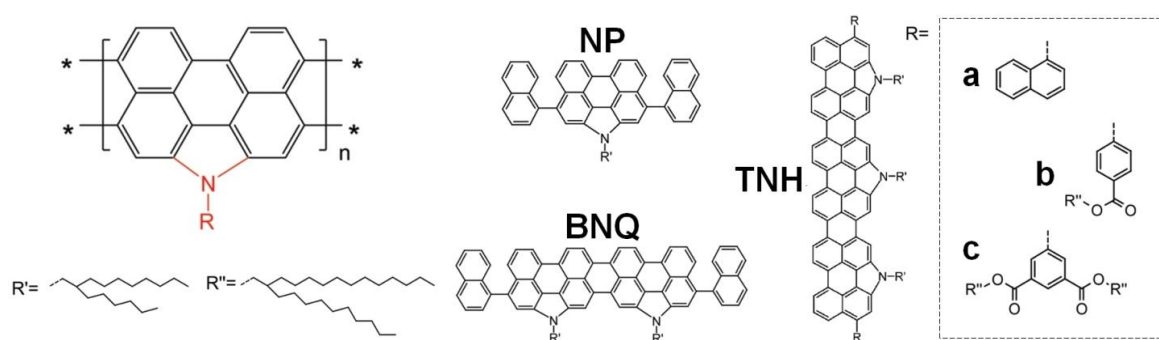


**Figure 6.21** Chemical structures of the synthesized N-annulated perylene (NP), bis-N-annulated quaterrylene (BNQ), and tri-N-annulated hexarylene (TNH); depending on the end group **a**, **b**, or **c**, TNHa, TNHb, or TNHc is obtained, respectively. Figure adapted from <sup>45</sup>.

### 6.2.2 Computational details

The chosen models for N-annulated rylenes did not include the naphthyl substituents, since these contribute negligibly to the final structural and electronic properties of the extended conjugated chromophores. Atomic structures were optimized with DFT calculations using the B3LYP hybrid functional with the basis set limited to 3-21G owing to the large dimension of the chromophores. The small basis set results were validated with additional calculations carried out with the 6-31G\* basis set. Molecular orbital shapes and energies discussed in the text are those calculated at the optimized structures. Orbital pictures were prepared with Molekel 4.3 visual software.

Electronic excitation energies and oscillator strengths were computed with TDDFT calculations for the 15 lowest singlet excited electronic states. In plotting computed electronic

spectra, a Lorentzian line width of 0.1 eV was superimposed on each computed intensity to facilitate the comparison with experimental spectra. The Franck-Condon (FC) vibronic structure<sup>50</sup> associated with electronic transitions was evaluated along the lines described in<sup>51</sup>. Assuming the harmonic approximation, negligible Duschinsky effect and identical frequencies in the  $K$  and  $J$  states, we obtained for each  $i$ -th mode, the displacement parameters  $B_i$  relative to the  $S_0 \leftrightarrow S_n$  transition. The latter are as (*cfr.* Eq. (4.30) in Section 4.5.2):

$$B_i = \sqrt{\frac{\omega_i}{\hbar}} \{\mathbb{X}_K - \mathbb{X}_J\} \mathbb{M}^{1/2} \mathbb{l}_i \quad (6.1)$$

where  $\mathbb{X}_K$  and  $\mathbb{X}_J$  are the  $3N$  dimensional vector of the equilibrium Cartesian coordinates of the  $H$ -th (here,  $S_0$ ) and  $J$ -th ( $S_n$ ) states, respectively;  $\mathbb{M}$  is the  $3N \times 3N$  diagonal matrix of the atomic masses;  $\mathbb{l}_i$  is the  $3N$  vector describing the mass-weighted Cartesian coordinates of the normal mode  $Q_i$  of the neutral or charged state. HF (ground state) and CIS (excited state) optimized geometries, vibrational frequencies and normal coordinates were employed to evaluate the  $B_i$  parameters that were scaled by 0.71 because of the known overestimate by HF/CIS levels of theory. In the harmonic approximation and assuming identical frequencies in the two electronic states, the FC intensity of a band corresponding to the  $\nu = \{\nu_1, \nu, \dots, \nu_N\}$  vibrational quantum in the excited state is given by:

$$I_{K_0, J_\nu} \propto \prod_i \langle 0_i | \nu_i \rangle^2 = \prod_i e^{-\gamma_i \frac{(\nu_i)^{\nu_i}}{\nu_i!}} \quad (6.2)$$

where (*cfr.* Eq. (4.29) in Section 4.5.2)

$$\gamma_i = \frac{1}{2} (B_i)^2 \quad (6.3)$$

Because of the large dimension of the systems investigated, the vibronic structure in absorption spectra was determined employing vibrational frequencies and normal coordinates of the ground state.

To model the possible aggregates, we considered a dimer and a trimer maximizing the dipole-dipole interaction, with molecules at a distance of 3.5 Å. It is interesting to note that the orientation determined by the attractive dipole-dipole interaction implies a parallel orientation dipole moments, which is typical for H aggregates. All QM calculations were performed with the Gaussian03 package.

### 6.2.3 GNRs featuring large dipoles and H aggregation

The B3LYP/3-21G optimized geometries of **NP**, **BNQ**, and **TNH** are collected in Figure 6.22. It is seen that the extended conjugation results in a large planar carbon skeleton. The computed dipole moments for the three systems, oriented along the short molecular axis as shown in Figure 6.22, are 2.69, 5.08, and 7.41 *D*. The remarkably large dipole moment of **TNH** may result in an increased ability to form aggregates. The frontier molecular orbitals in Figure 6.23 indicate a sensible reduction of the electronic gap, consistent with the remarkable red shift of the absorption spectrum of **TNH** in comparison to **NP** and **BNQ** (*vide infra*). We note that the energy of the HOMO level increases considerably, which may result in exceptional electron-donating properties of **TNH**.

**TNHs** are dark green solids and are soluble in common organic solvents. Room-temperature absorption spectra of **NP**, **BNQ**, and **TNHa-c** in tetrahydrofuran (THF) are shown in Figure 6.24. In sharp contrast, the spectra of **TNHs** display a drastic bathochromic shift (403 *nm*, 173 *nm*) compared with those of **NP** and **BNQ**, which reflects how the ladder-type conjugated structure leads to a great degree of planarity and correspondingly large delocalization of electronic wave functions with an absorption maximum at 846 *nm*. Interestingly, the introduction of sterically bulky end groups has a strong influence on the absorption coefficient as a reflection of the strong aggregation of **TNH** (*vide infra*).

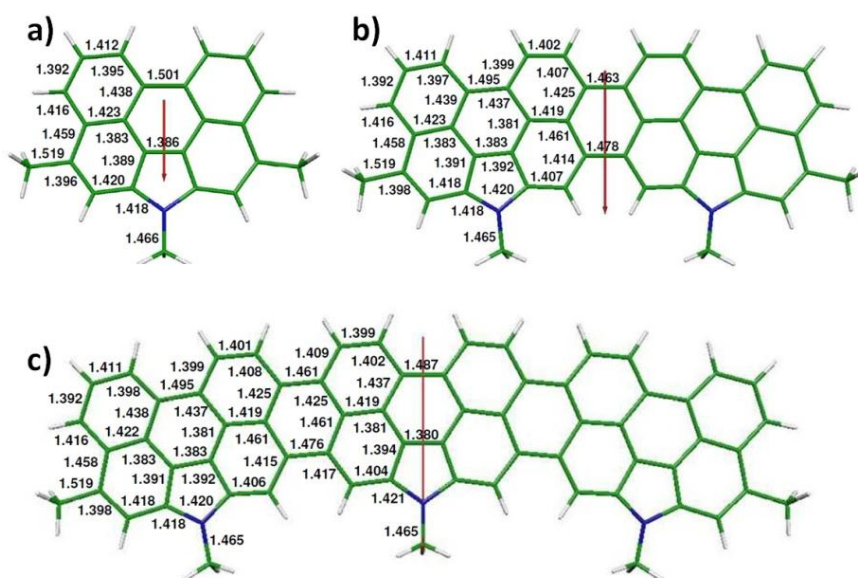


**Figure 6.22** B3LYP/3-21G equilibrium geometries of the neutral ground states of (a) **NP**, (b) **BNQ**, and (c) **TNH** models. The red arrow indicates the permanent dipole moment of the molecule. Figure adapted from <sup>45</sup>.

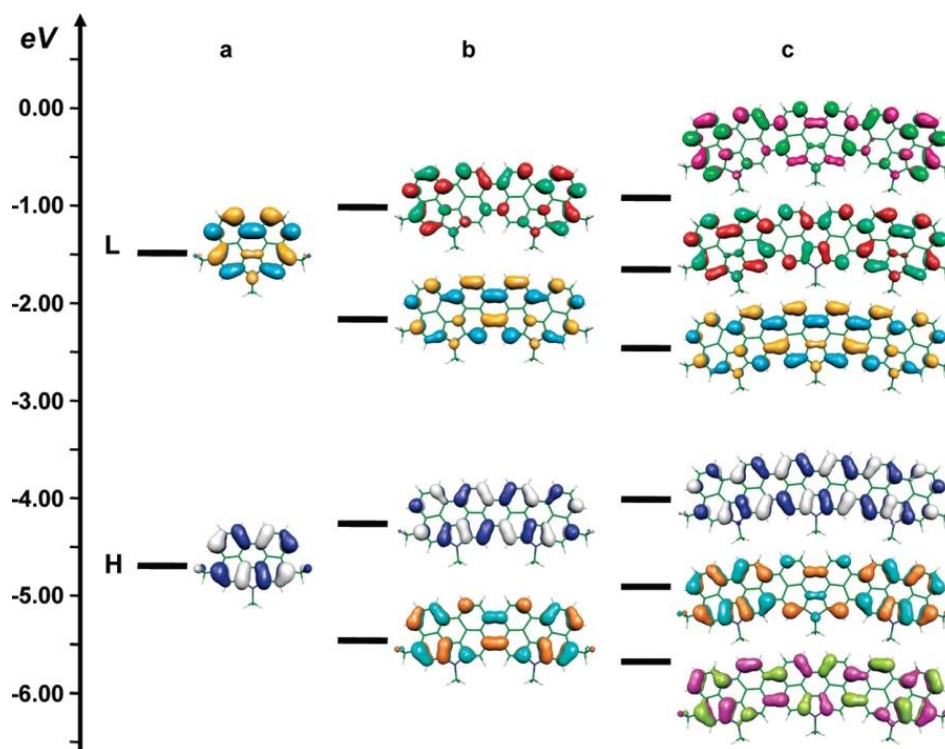


**Figure 6.23** B3LYP/3-21G frontier molecular orbitals of (a) NP, (b) BNQ, and (c) TNH. Figure adapted from <sup>45</sup>.

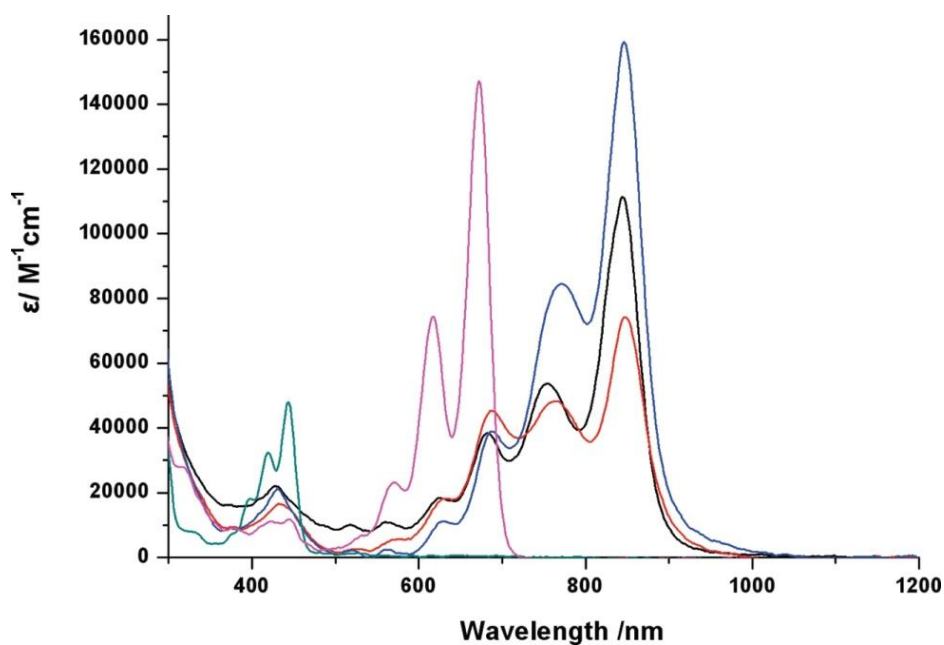


**Figure 6.24** UV-Vis absorption spectra of NP (cyan), BNQ (magenta), TNHa (black), TNHb (red), and TNHc (blue) in THF ( $1 \cdot 10^{-6} M$ ). The apparent reduction of absorptivity for TNHa-c is due to the fact that only a fraction of the monomer is present, while the remaining TNH is present in the form of aggregate. Figure adapted from <sup>45</sup>.

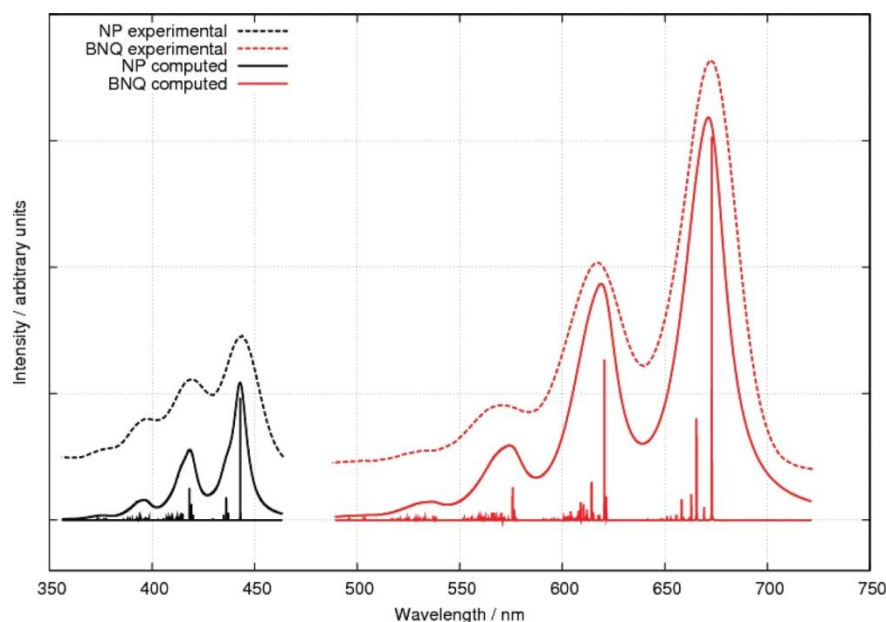


**Figure 6.25** Comparison between observed (dashed) and computed (solid) spectra (including computed vibronic structure) for **NP** in black and **BNQ** in red. The fine structure shown under the broad computed spectra represents the FC activity contributions to each broad band. The origins of the computed spectra were translated to the origins of the respective experimental spectra. Figure adapted from <sup>45</sup>.

The simulated vibronic spectra of **NP** and **BNQ** are compared with the experimental counterparts in Figure 6.25, from which it is clear that computed activities agree very nicely with the observed vibronic structure. On the basis of calculations, we can formulate an assignment of the most prominent FC structure in the two spectra (Table 6.4); as a demonstration, in Figure 6.26 we report for **NP** the normal coordinates mainly contributing to the largest computed FC activity. The peaks observed at 443, 418, 396, and 375 nm in the experimental absorption spectrum of **NP** correspond to a separation of *ca.* 1350  $cm^{-1}$ . The observed peak separation is nicely reproduced by the simulated spectra, indicating the activity of a number of vibrations with frequencies ranging between 1238 and 1336  $cm^{-1}$ . In addition, band shapes are modulated by the activity of a low-frequency mode at *ca.* 350  $cm^{-1}$ , which describes an in-plane expansion of the whole molecule along its long molecular axis. For **BNQ** the most active vibration is computed at *ca.* 1250  $cm^{-1}$ , but band shapes are modulated by the remarkably active vibration at 166  $cm^{-1}$  in the acoustic phonon region, corresponding to the molecular expansion in the long molecular axis whose activity has been documented in other PAH systems.<sup>52</sup>

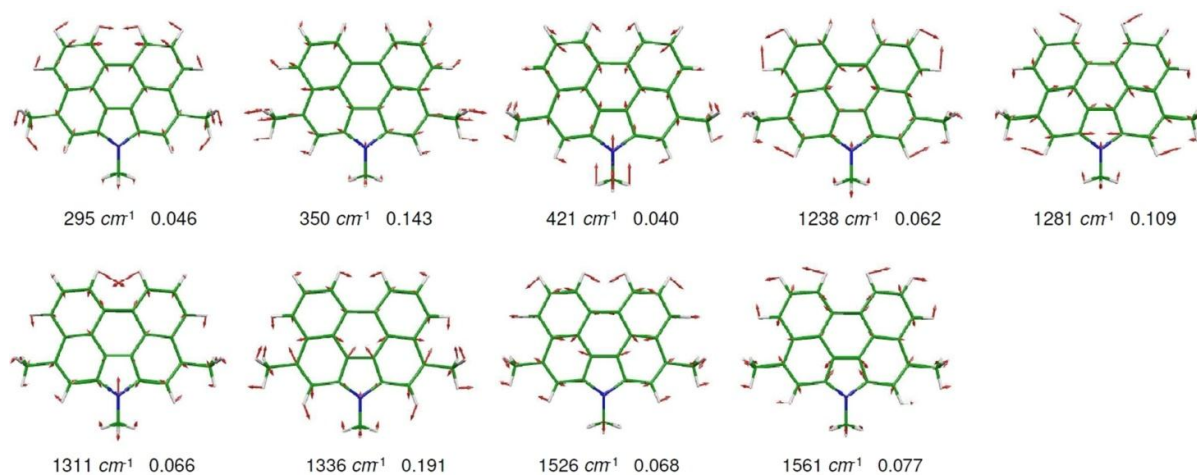


**Figure 6.26** Normal coordinates associated with the largest computed FC activity in the spectrum of **TNH**. The vibrational frequency and the associated  $\gamma_i$  value are indicated for each normal mode. Figure adapted from <sup>45</sup>.

**Table 6.4** Franck-Condon activity parameters computed for the lowest energy intense transition of the three N-annulated rylenes investigated.<sup>45</sup>

NP		BNQ		TNH	
$\nu_i$ ( $cm^{-1}$ ) <sup>a</sup>	$\gamma_i$ <sup>b</sup>	$\nu_i$ ( $cm^{-1}$ ) <sup>a</sup>	$\gamma_i$ <sup>b</sup>	$\nu_i$ ( $cm^{-1}$ ) <sup>a</sup>	$\gamma_i$ <sup>b</sup>
295	0.046	48	0.026	117	0.708
350	0.143	82	0.037	1104	0.029
421	0.040	166	0.394	1197	0.027
1238	0.062	226	0.068	1224	0.167
1281	0.109	1228	0.041	1233	0.031
1311	0.066	1232	0.066	1239	0.171
1336	0.191	1243	0.026	1244	0.116
1526	0.068	1253	0.414	1524	0.062
1561	0.077	1525	0.059	1561	0.028
1644	0.030	1561	0.045		

<sup>a</sup> Computed frequencies  $\nu_i$  were scaled by 0.9. <sup>b</sup> Only  $\gamma_i > 0.025$  are shown.

The observed spectrum of **TNH** (Figure 6.24) is similar to those of **NP** and **BNQ**, although it shows a strong dependence on substituents. In addition, the relative intensity distribution

among the observed bands is sensibly concentration dependent (Figure 6.28). Thus, the apparent reduction of the observed absorptivity for **TNH<sub>a-c</sub>** (Figure 6.24) must be due to the fact that only a fraction of the **TNH** monomer is present, while the remaining amount is in the form of aggregate. Indeed, the large computed ground-state dipole moment (cyan arrows in Figure 6.27) induces a remarkable dipole-dipole interaction which justifies the formation of aggregates. Because the transition dipole moment is directed along the long molecular axis, while the permanent dipole is directed along the short molecular axis, the aggregates are expected to be *H* type (aggregates showing hypsochromically shifted bands).

To model the spectroscopic features associated with aggregates, we considered a dimer and a trimer maximizing the dipole-dipole interaction, oriented as shown in Figure 6.27 with molecules at a distance of 3.5 Å. Accordingly, the TDDFT computed vertical excitations show a blue shift of the intense excitonic transition (Table 6.5). Assuming for simplicity, similar vibronic structures for the spectra of the monomer and the aggregate, the computed results are compatible with the intensity dependence of the second, third, and higher bands in the observed absorption spectrum as a function of concentration (Figure 6.28).

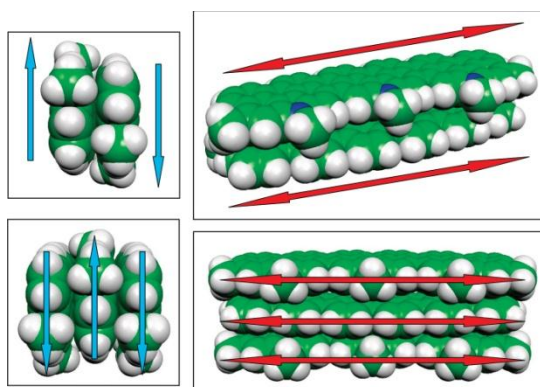


**Figure 6.27** Dimer (top) and trimer (bottom) of **TNH** as examples of *H* aggregates. Cyan arrows represent the directions of dipole moments. Red arrows represent the directions of the  $S_0 \rightarrow S_1$  transition dipole moments of each molecule. Figure adapted from <sup>45</sup>.

We note in passing that the apparently different aggregation behaviors by **TNH<sub>a-c</sub>** are not related to the electronic properties of the substituents but rather to their steric hindrance. Indeed, quantum-chemical calculations carried out for **TNH<sub>b,c</sub>** show similar dipole moments. However, the large dimensions and the directions of the substituents in **TNH<sub>c</sub>**

(with respect to the rylene plane) are likely to force the molecules even farther apart, thereby reducing the efficiency of aggregation.

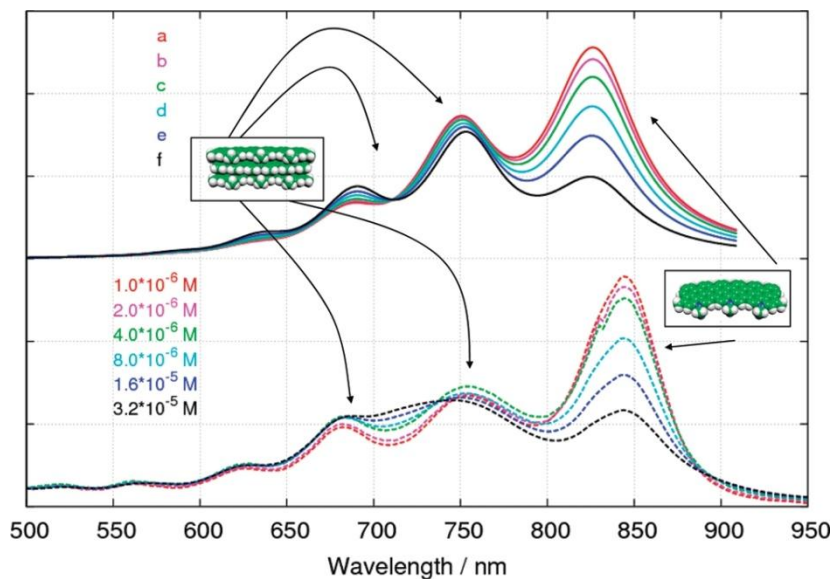


**Figure 6.28** Comparison between observed (bottom) and simulated (top) absorption spectra of TNH. The computed spectra were obtained by superimposing, in different, proportions, the spectra of the monomeric and trimeric species with their associated FC structures. Figure adapted from <sup>45</sup>.

**Table 6.5** TD-B3LYP/3-21G computed vertical excitation energies, oscillator strengths, wavefunction analysis, frontier orbital energies and transport gap of NP, BNQ, TNH, and TNH dimer and trimer.<sup>45</sup>

TD-B3LYP 3-21G	$\Delta E_{\text{optic}}$ (eV)	$f$	wavefunction	$E_{\text{HOMO}}$ (eV)	$E_{\text{LUMO}}$ (eV)	$\Delta E_{\text{H-L}}$ (eV)
NP	3.08	0.34	0.63(H → L)	-4.78	-1.48	3.30
BNQ	2.01	1.22	0.61(H → L)	-4.25	-2.20	2.06
TNH	1.57	2.30	0.59(H → L)	-4.05	-2.49	1.56
TNH dimer	1.67	3.39	-0.35(H → L) 0.45(H-1 → L+1)	-3.76	-2.29	1.47
TNH trimer	1.71	4.25	-0.16(H → L+1) 0.32(H-1 → L)	-3.56	-2.17	1.39

In summary, since the transition dipole moment associated with the allowed electronic transition is polarized along the long molecular axis, the extension of conjugation is reflected not only in a bathochromic shift of the first transition but also in a strong enhancement of its intensity. At the same time, the large dipole moment (directed along the short molecular axis) favors aggregation of the larger dye (TNH), which is reflected by a decrease of its

observed intensity in absorption in combination with a marked concentration dependence of the spectrum, displaying increased intensity on the blue side of the first maximum, consistent with the computed results indicating the formation of *H* aggregates.

These dyes display remarkably large dipole moments that may favor the formation of highly ordered supramolecular structures, resulting in enhanced charge carrier mobilities (see Sections 6.6 and 6.7).

## 6.3 TETRACENE DIIMIDES

There are many reasons to be interested in tetracene diimides. For instance, such air-stable *n*-type NIR dyes arise as suitable molecular materials for organic photovoltaics. In this Section, particular attention is focused on the structure-property relationships on which such promising characteristics rely. From this perspective, it is shown how the structural mix of a *p*-type core with *n*-type features leads to hybrid opto-electronic properties as well. Also this investigation was carried out as part of the collaboration with Prof. Wang and his group at the Beijing National Laboratory for Molecular Science, Institute of Chemistry, Chinese Academy of Sciences, who synthesized and experimentally characterized the compounds.<sup>53</sup>

### 6.3.1 Background

The design and synthesis of acenes have attracted considerable interests owing to their potential applications as *p*-type organic semiconductors in organic electronics, such as field-effect transistors, organic light-emitting diodes, and solar cells.<sup>54</sup> Typically, tetracene and pentacene derivatives have been the subject of intense study because of the unique electronic properties associated with their  $\pi$ -bond topology.<sup>55</sup> One efficient approach to optimize the performance of acenes is to integrate functional groups into the parent molecules to improve their stability and processability.<sup>22b,56</sup> However, the systematic change of effective functional groups on acenes poses a great challenge since there are a very few synthetic methodologies that can serve this purpose.

Compared with aryl, alkynyl-substituted, and other functionalized groups, introduction of strong electron-withdrawing substituents to acenes is believed to be very crucial to invert the majority carrier sign to achieve efficient electron transport.<sup>58</sup> Perylene tetracarboxylic bisimides (PBIs) and naphthalene tetracarboxylic diimides (NDIs), which combine *p*-type perylene or naphthalene aromatic cores with strong electron-withdrawing tetracarboxylic diimides substituents, were used as promising building blocks for most extensively investigated *n*-type semiconductors.<sup>58</sup> Thus, a similar strategy is expected to create new series of acene tetracarboxylic diimides as new *n*-type building blocks.

Herein, we present a new family of air-stable and NIR tetracene derivatives functionalized by tetracarboxylic diimide substituents,<sup>53</sup> depicted in Figure 6.29.

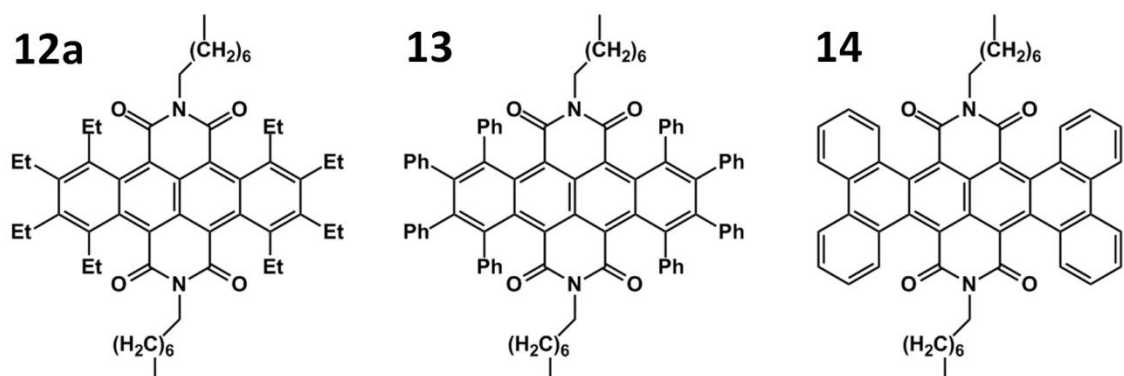


**Figure 6.29** Chemical structures of the recently synthesized<sup>53</sup> tetracene diimides **12a**, **13**, and **14**. Derivative **12c** is analogous to **12a** but featuring  $-\text{CH}_2(\text{CF}_2)_2\text{CF}_3$  instead of  $-\text{CH}_2(\text{CH}_2)_6\text{CH}_3$ . Figure adapted from<sup>53</sup>.

### 6.3.2 Computational details

Atomic structures of tetracene, and models of **NDI**, **12** and **14** featuring methyl substituents instead of the R1 and R2 groups, were optimized with DFT calculations using the B3LYP hybrid functional with the 6-31G\* basis set. Precisely, we built: a model for **NDI** featuring only hydrogen substituents on the naphthalenic core and methyl groups at the imide positions; a model for **TDI 12** (labeled **12p**; "p" as "planar") featuring hydrogens on the tetracenic core and methyl groups at the imide positions; more realistic models for **12** featuring methyl substituents at the tetracenic core positions instead of ethyl substituents; models for **14** featuring methyl substituents instead of the alkyl units at the imide positions. Molecular orbital shapes and energies of discussed in the text are those calculated at the optimized *cis*-structures. Orbital pictures were prepared with Molekel 4.3 visual software. Electronic excitation energies and oscillation strengths were computed for the fifty lowest singlet excited electronic states of the investigated compounds with TDDFT calculations. In plotting computed electronic spectra, a Lorentzian linewidth of 0.1 eV was superimposed to each computed intensity to facilitate the comparison with experimental spectra. The computed spectra did not include the vibron structure associated with electronic bands and as a result they show a reduced number of bands compared with the experimental spectra. All QM calculations were performed with the Gaussian09 package.

### 6.3.3 NIR dyes TDIs

To determine the molecular structure of tetracene diimide (TDI) derivatives, crystal of **12c** suitable for single-crystal X-ray structure analysis was obtained by slow evaporation of a solution of dichloromethane and methanol at room temperature.<sup>59</sup> As can be seen from Figure 6.30, the crystal structure reveals that the molecule has crystallographically imposed inversion symmetry. Owing to the steric encumbrance effect between oxygen atoms and neighboring group, the tetracene core is found to be markedly non-planar as well as the two imides rings with dihedral angles of 30-32°. The heliciform structure revealed by the crystal structure corresponds indeed to the lowest energy computed structure (B3LYP/6-31G\*) of **12** and **14**. Precisely, while **12p** holds an essentially planar tetracene core and is useful to make a direct comparison with the oligoacene, **12** and **14** display a remarkably non-planar structure which indicates that the addition of peripheral aromatic units to the original NDI core leads to an out-of-plane twisting of the tetracene core, driven by the steric congestion between alkyl substituents and the neighboring oxygen atoms. Interestingly, **12** and **14** show two equilibrium structures of similar energy (Table 6.6) corresponding to heliciform and non-heliciform arrangements of the peripheral phenyl (in **12**) or phenantrenic (in **14**) units, very similarly to what previously observed for triply-linked triPBI derivatives.<sup>11</sup>

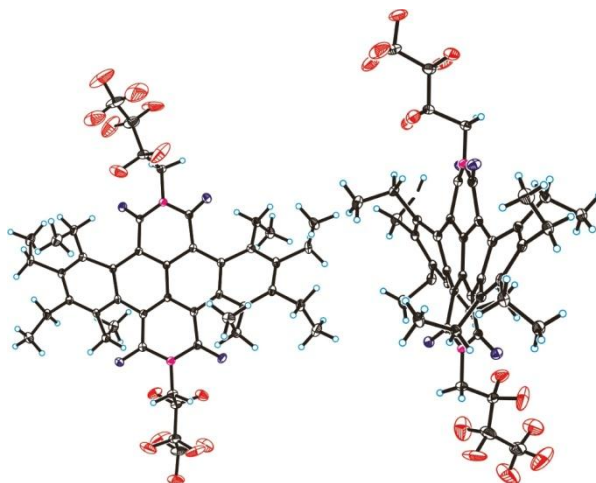


**Figure 6.30** Molecular structure of **12c**, the X-ray structure along the crystallographic *b* axis (right), the X-ray structure along the crystallographic *c* axis (left). Figure adapted from <sup>53</sup>.

The absorption spectra of **12a** and **13** in chloroform are shown in Figure 6.31, showing broad absorption which covers the whole visible and NIR region, rendering them as "full-absorption dyes" and therefore potential objects in solar cells. Compared with their all-

carbon parent, tetracene (474 nm),<sup>60</sup> those TDIs broad and significantly red-shifted spectra and have higher molar extinction coefficient in the visible-NIR region. The remarkable difference between TDIs and tetracene in their absorption peaks and intensities reflect the substantial electronic effect of the attachment of strong electron-withdrawing diimide groups. Furthermore, in contrast with NDI (380 nm),<sup>61</sup> which show absorption only in the UV region, the fusion of two additional aromatic rings also leads to much more red shift in absorption as a reflection of a larger extensive conjugation over the electronic system (*vide infra*).

The absorption spectra of **14** lead to a sensible change. The purple-red solution of compound **14** exhibits a major absorption band at 584 nm with a blue shift of 176 nm relative to **13** ( $\lambda_{\text{max}} = 740 \text{ nm}$ ), as a reflection of the interruption of tetrabenzene units to the effective conjugation along the cores of the TDI.

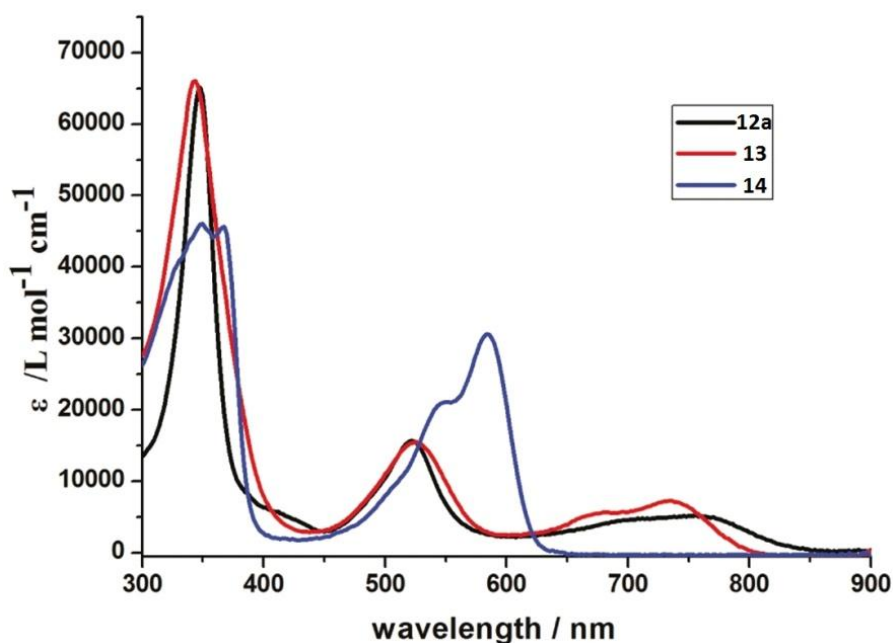


**Figure 6.31** UV-Vis-NIR absorption spectra of **12a** (black), **13** (red), and **14** (blue) in chloroform. Figure adapted from <sup>53</sup>.

An analysis in terms of the orbital nature of the TD-B3LYP/6-31G\* computed electronic transitions of **12** and other TDI derivatives (see Tables 6.6-8 and Figures 6.33-34) sheds more light on the nature of the lowest energy transitions (and specifically the NIR transitions of TDIs). The computed excitation energies show that the lower energy portion of the absorption spectra of **12** (and the other derivatives) and **14** is dominated by two low-lying

transitions, the first of which is weaker than the second one, considerably more intense (see also Tables 6.6-8). The lowest energy and weaker transition (responsible for the NIR absorption of TDIs) corresponds always to the HOMO  $\rightarrow$  LUMO excitation.

The HOMO orbital of all the TDI derivatives is dominated by the tetracenic HOMO nature, while the LUMO orbital shows the typical character of diimide derivatives (see Figures 6.32,35 and Table 6.7). Therefore, the low energy transition of TDI derivatives is a new transition reflecting the peculiar frontier orbital nature. While for **12** the  $S_0 \rightarrow S_1$  transition is well separated in energy from the next, higher intensity transition, the two excitations are almost degenerate for **14** (Table 6.6). Interestingly, the second (more intense) transition of TDIs is also dominated by a  $\pi \rightarrow \pi^*$  electronic excitation from an occupied orbital of tetracenic nature to the LUMO (see Figure 6.36 and Table 6.8).

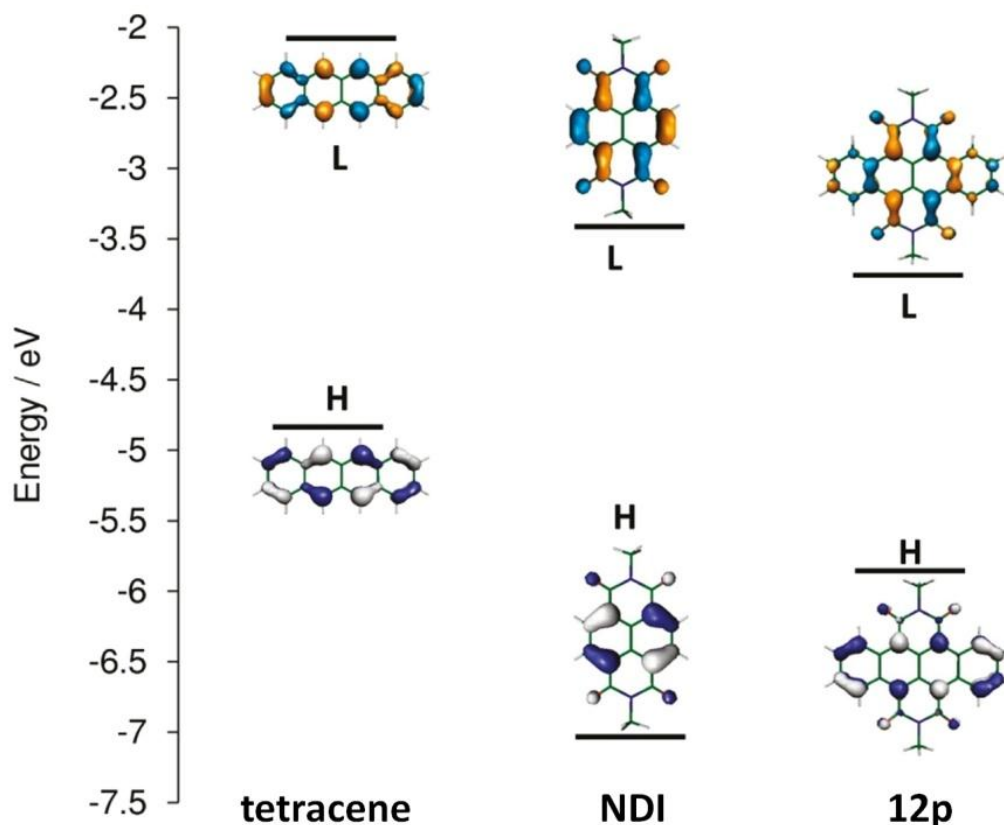


**Figure 6.32** Energies and shapes of B3LYP/6-31G\* frontier orbitals (HOMO and LUMO) of tetracene, NDI, and a planar model of **12**. Figure adapted from <sup>53</sup>.

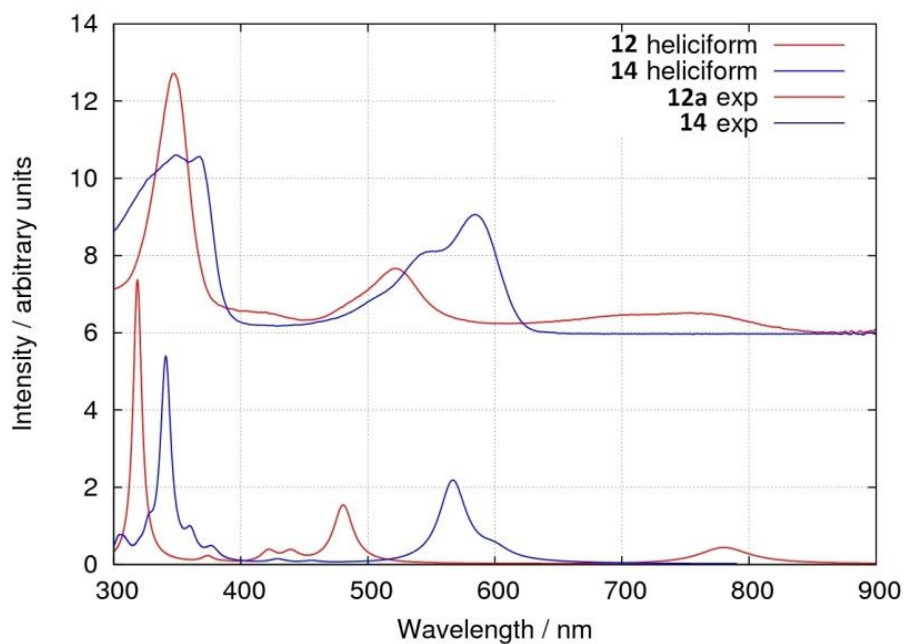


**Figure 6.33** Comparison between computed and observed UV-Vis-NIR absorption spectra. (bottom) TD-B3LYP/6-31G\* calculated absorption spectra of **12** (red) and **14** (blue) in their more stable heliciform structure. (top) Absorption spectra of **12a** (red) and **14** (blue) in  $\text{CHCl}_3$ . Figure adapted from <sup>53</sup>.

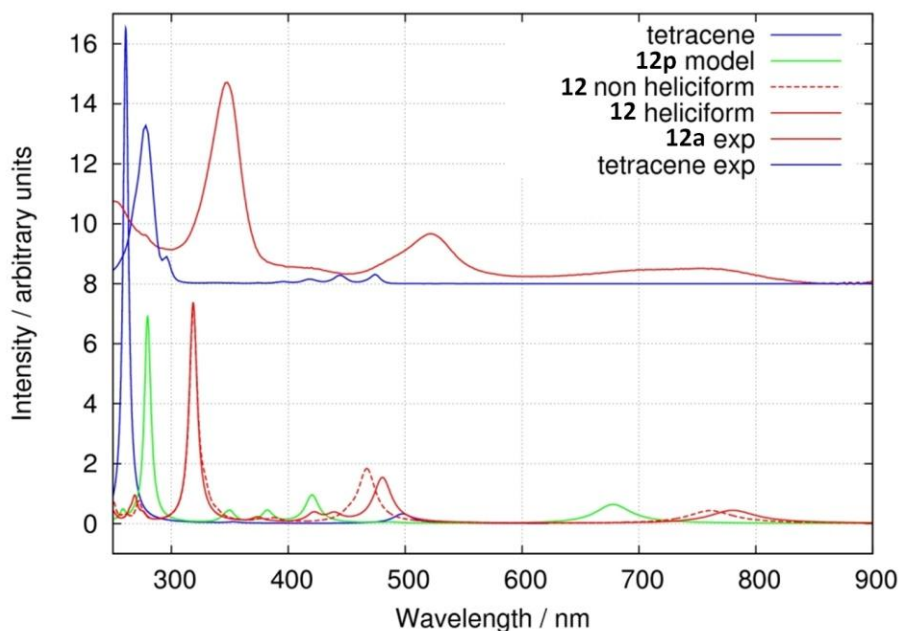


**Figure 6.34** Comparison between computed and observed UV-Vis-NIR absorption spectra. (bottom) TD-B3LYP/6-31G\* calculated absorption spectra of **12** (red), **12p** (green), and tetracene (blue). (top) Absorption spectra of **12a** (red) and tetracene (blue) in  $\text{CHCl}_3$ . Figure adapted from <sup>53</sup>.

**Table 6.6** B3LYP/6-31G\* absolute energies, relative energies, optical gaps (lowest allowed electronic transitions from TDDFT B3LYP/6-31G\* calculations), and the second most important electronic transition in absorption spectra.<sup>53</sup>

B3LYP/6-31G*	Absolute Energy (a.u.)	Relative Energy (kcal/mol)	$E(S_0 \rightarrow S_1)$			$E(S_0 \rightarrow S_n)$		
			<i>eV</i>	<i>nm</i>	oscillator strength	<i>eV</i>	<i>nm</i>	oscillator strength
<b>NDI</b>	-1026.22606730	-	3.20	388	0.000	3.39	366	0.295
<b>tetracene</b>	-693.165811512	-	2.49	498	0.050	4.75	261	2.593
<b>12p</b>	-1333.46912455	-	1.83	678	0.100	2.95	420	0.147
heliciform <b>12</b>	-1647.94405901	0.00	1.59	780	0.068	2.58	481	0.237
non-heliciform <b>12</b>	-1647.94218269	+1.18	1.63	761	0.067	2.65	467	0.280
heliciform <b>14</b>	-1948.00952802	0.00	2.07	599	0.042	2.19	567	0.335
non-heliciform <b>14</b>	-1948.00862499	+0.57	2.12	584	0.042	2.25	552	0.344

**Table 6.7** MO energies (*eV*) of  $\pi$  orbitals and HOMO-LUMO gaps of **NDI**, tetracene, and TDIs **12** and **14**. From B3LYP/6-31G\* calculations at optimized geometries.<sup>53</sup>

	HOMO-2	HOMO-1	HOMO	LUMO	$\Delta E_{H-L}$
<b>NDI</b>			-7.04	-3.41	3.63
<b>tetracene</b>	-6.41	-6.33	-4.85	-2.08	2.78
<b>12p</b>	-7.14 <sup>b</sup>	-6.77	-5.86	-3.76	2.09
<b>12<sup>a</sup></b>	-6.36 (-6.35) <sup>b</sup>	-6.01 (-6.00)	-5.31 (-5.31)	-3.38 (-3.33)	1.92 (1.98)
<b>14<sup>a</sup></b>	-6.22 (-6.21)	-5.95 (-5.95) <sup>b</sup>	-5.83 (-5.84)	-3.36 (-3.30)	2.47 (2.54)

<sup>a</sup> In parenthesis the values for the non-heliciform isomer of **12** and **14**. <sup>b</sup> This molecular orbital bears a parentage with the tetracenic HOMO-2 orbital, see also Figure 6.36.

The spectra reported in Figures 6.33,34 deserve some additional comment. First, the electronic transitions were calculated for heliciform and non-heliciform structures of **12** and **14** and for the reference compounds tetracene, **NDI**, and **12p**, and the orbital nature of low-lying electronic transitions were identified. The computed spectra of **12** and **14** are compared with the observed absorption spectra in Figure 6.33. It is seen that the TDDFT calculated bands agree very well with the most prominent observed features in the experimental spectra. The computed spectrum of **12** is slightly blue shifted compared with the observed spectra, but it should be kept in mind that the calculations were carried out with methyl

groups as substituents. The smaller number of bands in the computed spectra is due to the limited number of computed excitation energies and to the neglect of vibronic structures associated with the electronic transitions.

**Table 6.8** Orbital nature of the low-lying electronic states of TDI derivatives.<sup>53</sup>

B3LYP/6-31G*	$E(S_0 \rightarrow S_1)$				$E(S_0 \rightarrow S_n)$		
	<i>eV</i>	oscillator strength	$\Delta E_{exp}$ optical gap ( <i>eV</i> )	Dominant electronic excitation	<i>eV</i>	oscillator strength	Dominant electronic excitation
<b>12p</b>	1.83	0.100		(H → L)	2.95	0.147	(H-2 → L)
heliciform <b>12</b>	1.59	0.068	1.64	(H → L)	2.58	0.237	(H-2 → L)
non-heliciform <b>12</b>	1.63	0.067		(H → L)	2.65	0.280	(H-2 → L)
heliciform <b>14</b>	2.07	0.042	2.12	(H → L)	2.19	0.335	(H-1 → L)
non-heliciform <b>14</b>	2.12	0.042		(H → L)	2.25	0.344	(H-1 → L)

<sup>a</sup> Taken from the lowest energy maximum in absorption spectra.

In Figure 6.34 we compare the observed and computed spectra of **12** and tetracene. Interestingly, it can be seen that the spectra simulated for the heliciform and non-heliciform forms of **12** are very similar, with the less stable structure responsible for the slightly blue shifted spectrum. The spectrum of **12** is however very different from both that of tetracene and that of **NDI**. Therefore, an analysis in terms of the orbital nature of the electronic transitions of **12** and other TDI derivatives can shed more light on the observed differences and on the nature of the NIR transitions in TDI derivatives.

Because the lowest allowed transition is dominated by the H → L single excitation, the optical gaps determined from absorption spectra are expected to reflect the trend in the HOMO-LUMO (transport) gaps. This can be seen by comparing optical and transport gaps reported in Table 6.7-8.

While for **12** the  $S_0 \rightarrow S_1$  transition is well separated in energy from the next, higher intensity transition, the two excitations are almost degenerate for **14** (Table 6.6). Interestingly, the second transition is also dominated by a  $\pi \rightarrow \pi^*$  electronic excitation from an occupied orbital bearing strong parentage with a tetracene to the LUMO which is instead dominated by the diimide characted (Figures 6.33,35). This is more clearly seen in Figure 6.36 and Table 6.8 where the HOMO orbitals and the occupied orbitals involved in the above discussed

excitation are depicted for all the TDI derivatives and for tetracene itself. From Figure 6.36 it can be seen that the HOMO-2 orbital of tetracene (green-magenta lobes) correlates very closely with the HOMO-2 orbital of **12p**, and also with the HOMO-2 orbital of the more realistic model **12**. The HOMO-2 → LUMO excitation determines the intensity of the bands observed at *ca.* 584 nm for **14**.

It can be concluded that extension of the aromatic core of NDI to TDI originates new electronic transitions because of the availability of higher energy HOMO levels dominated by the tetracenic nature of the core.

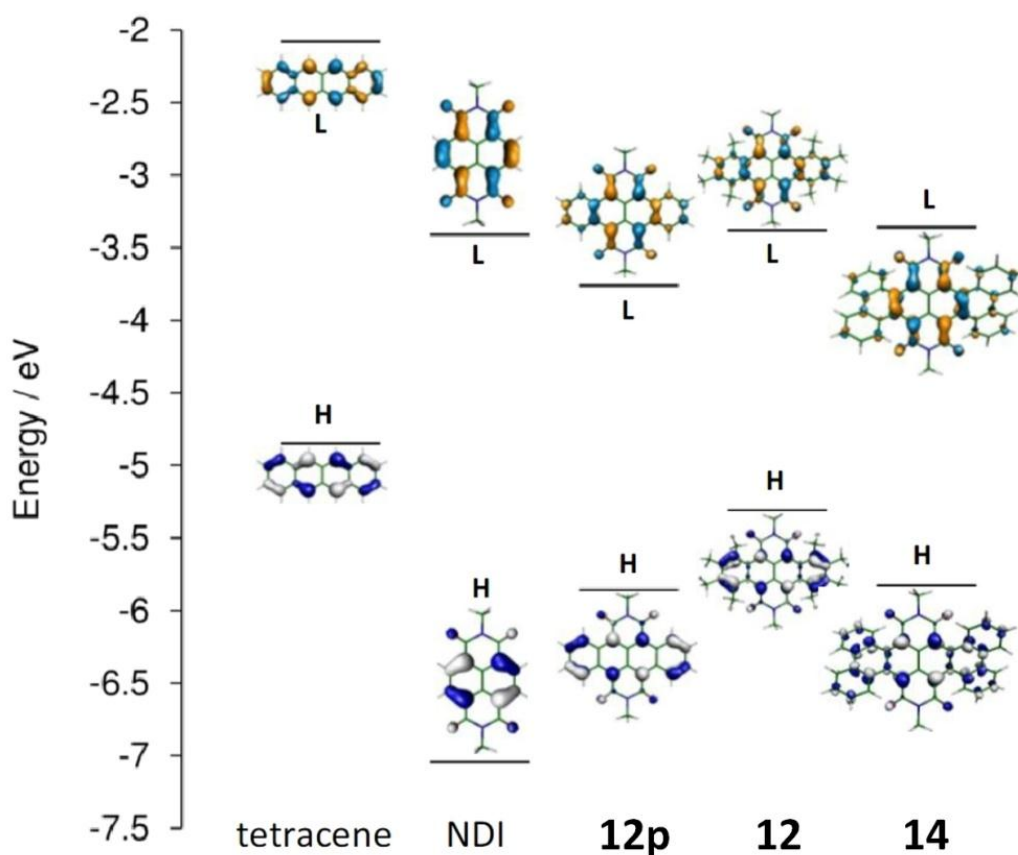


**Figure 6.35** Energies and shapes of B3LYP/6-31G\* frontier orbitals (HOMO and LUMO) of tetracene, NDI, **12p**, **12**, and **14** showing the dominant orbital parentage across TDI derivatives. The orbital shapes of the non-heliciform structures of **12** and **14** are very similar to those of the heliciform species. Figure adapted from <sup>53</sup>.

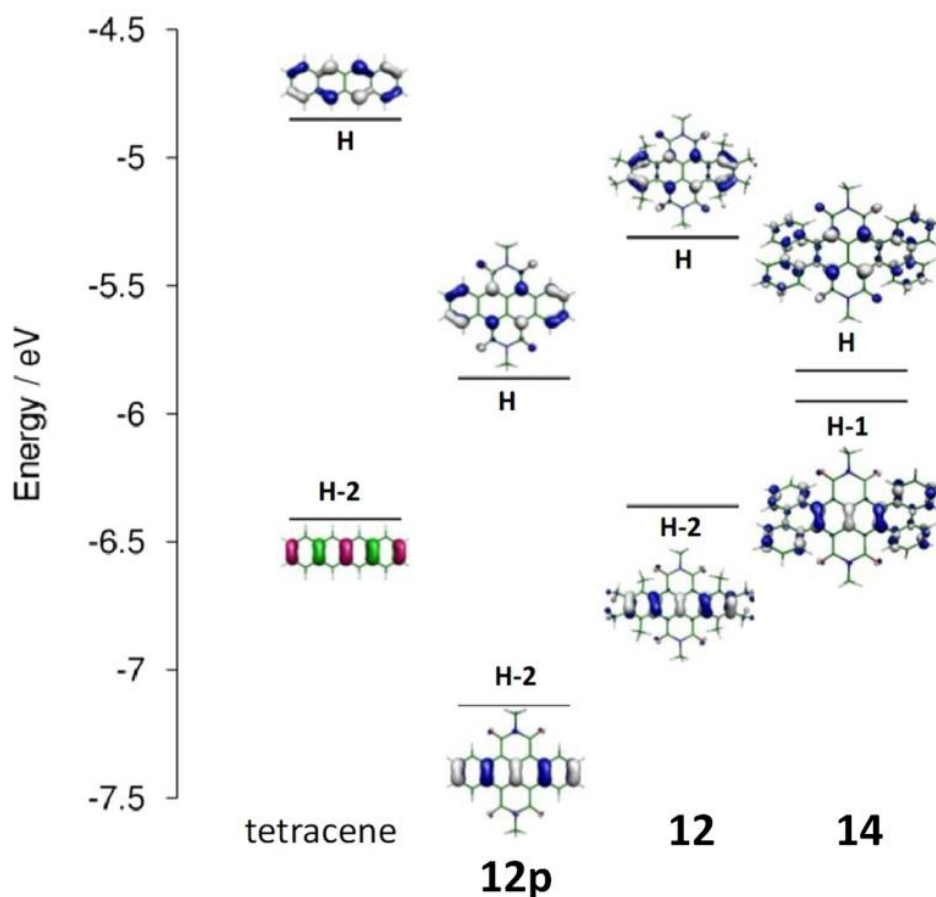


**Figure 6.36** Energies and shapes of B3LYP/6-31G\* occupied orbitals (HOMO, HOMO-2 (tetracene, **12p**, **12**) and HOMO-1 (for **14**)) involved in the low-lying excitations of the investigated compounds. The comparison shows the dominant orbital parentage with tetracene across TDI derivatives. Figure adapted from <sup>53</sup>.

The redox properties of the TDIs were studied by cyclic voltammetry in CH<sub>2</sub>Cl<sub>2</sub> (in *V vs.* Ag/AgCl). The half-wave reduction potentials of the representative compounds are -0.63, -1.11 *V* for **NDI**; -0.40, -0.73 *V* for **12a**; and -0.32, -0.64 *V* for **14**. The first reduction potentials of these TDIs are much less negative than those of parent **NDI** (Table 6.9), thus, revealing the extremely strong electron-accepting abilities, and the first reduction potential of **12c** is less negative by about 0.1 *V* than the other alkyl substituted TDIs, which is probably due to the introduction of semiperfluoroalkyl chains.

The optical band gaps and LUMO energy levels of these compounds were calculated based on UV-Vis-NIR absorption data and the onset potential of the first reduction wave. It is worth mentioning that the band gap of these TDIs are much smaller than the gap of **NDI**

( $\lambda_{\max} = 380 \text{ nm}$ , optical gap is  $3.12 \text{ eV}$ ), which could be related to the increasing conjugation length, and the LUMO levels fall into  $-4.0$  to  $-4.2 \text{ eV}$  indicating that all of them could be served as candidates for air-stable  $n$ -stable semiconductors. Notably, the value of the gaps are comparable to the HOMO-LUMO gap of heptacene,<sup>62</sup> which means that the introduction of electron-withdrawing tetracarboxylic diimides can reduce the gaps more efficiently than the fusion of rings.

All the TDIs show good solubility in common organic solvents such as dichloromethane, chloroform, toluene, and tetrahydrofuran. They exhibited very good stability on exposure to light and air condition, whereas the tetracene is an air and light sensitive material, that is, the introduction of strong electron-withdrawing imides groups into the tetracene improved their photo-oxidative resistance significantly and make them to be stable  $n$ -type semiconductors and NIR dyes.

**Table 6.9** Opto-electronic properties of TDIs and energy levels of representative compounds.<sup>53</sup>

	$\lambda_1 \text{ (nm)}^a$	$E_{1r} \text{ (V)}^b$	$E_{\text{LUMO}} \text{ (eV)}^c$	$E_{\text{HOMO}} \text{ (eV)}^d$	$E_g \text{ (eV)}^e$
NDI <sup>f</sup>	380	-0.63	-3.90	-7.02	3.12
<b>12a</b>	756	-0.40	-4.06	-5.54	1.48
<b>12c</b>	774	-0.29	-4.17	-5.50	1.43
<b>13</b>	737	-0.35	-4.12	-5.68	1.56
<b>14</b>	584	-0.32	-4.14	-6.13	1.99

<sup>a</sup>  $\lambda_1$  as peak of the Vis-NIR regions. <sup>b</sup> Half-wave redox potential (in  $V$  vs  $\text{Ag}/\text{AgCl}$ ) measured in  $\text{CH}_2\text{Cl}_2$  with a scan rate of  $0.1 \text{ V/s}$ . <sup>c</sup> Calculated by measuring the onset potential of the first reduction wave. <sup>d</sup> Estimated from LUMO levels and  $E_g$ . <sup>e</sup> Obtained from the edge of the absorption spectra. <sup>f</sup> **NDI**:  $N,N'$ -di ( $n$ -octyl)-naphthalene-1,2:6,7-tetracarboxylic bisimide.

In conclusion, a new family of stable low band gap TDIs has been designed and synthesized.<sup>53</sup> In light of their unique structure and admirable photophysical and electro-optical properties, this new molecular skeleton is promising candidate for air-stable  $n$ -type semiconductors and solar cell materials.

## 6.4 QUINOIDAL OLIGOTHIOPHENES

In this Section, evidence of the biradicaloid and polyenic character of quinoidal oligothiophenes is reported by proving at the CASSCF//CASPT2 computational level the presence of a low-lying double exciton state responsible for the weak features observed in the NIR absorption region of the longest members of this class of molecules. The energy lowering of this state, accompanying the length increase in the oligomers, causes a displacement of the ground-state equilibrium geometry toward more biradicaloid structures because of the more efficient  $S_0$ - $S_1$  state mixing. Furthermore, it is shown that the doubly excited state is strongly coupled to the ground electronic state, and the coupling is mediated by a collective mode dominated by the out-of-phase stretching of adjacent CC bonds, recently shown to govern the Raman activity. All together, this evidence offers a unified view of the low-lying electronic states for quinoidal oligothiophenes and polyenes.<sup>29</sup>

This study was performed in the framework of a collaboration with Prof. Castiglioni and her group at the Department of Chemistry, Materials, and Chemical Engineering, Politecnico di Milano, where the investigated oligomers were synthesized and experimentally characterized.<sup>29</sup>

### 6.4.1 Background

Developments in organic electronics, following a bottom-up chemical approach, have contributed to an increase in the number of potential semiconductors and to tuning of their properties. Among others, ambipolar organic semiconductors<sup>63</sup> are emerging as interesting materials owing to their flexibility and their use in a variety of device architectures in different areas of organic electronics.<sup>64</sup>

Recently, synthesized quinoidal oligothiophenes (QOTs)<sup>28,65</sup> have been shown to be promising materials for their proven amphoteric properties<sup>63c,64c-e,65b,66</sup> and also because the longer members in the series show near-infrared (NIR) absorption features, driven by the reduction of their HOMO-LUMO energy gap, that make them of potential use in the field of organic photodetectors.<sup>67</sup> NIR absorptions are desirable, for instance, to increase the efficiency of solar cells, as proposed in recent work.<sup>68</sup>

Another signature of the energy gap decrease occurring in longer QOTs is their more marked biradicaloid character,<sup>65a,c</sup> whose role in determining the dispersion of the Raman bands was discussed in a recent work<sup>28</sup> for the **2P-nT** series shown in Figure 6.37 and in a number of studies on related QOT systems.<sup>65a,c</sup> In these previous works, the properties of the ground state were determined mainly using density functional theory (DFT), and it was concluded that a closed-shell (CS) configuration satisfactorily describes the shorter members more markedly quinoid, whereas a broken symmetry<sup>69</sup> (BS) biradicaloid configuration is the stable solution for longer chromophores.

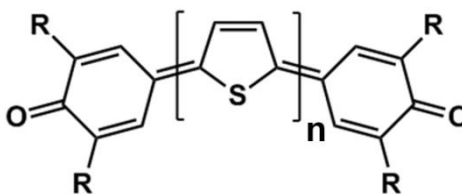


**Figure 6.37** Structural formula of the quinoid molecules **2P-nT** experimentally investigated ( $R$ =tert-butyl) and the model systems considered for computations ( $R$ =H), where  $n=0,1,2$ . Figure adapted from <sup>29</sup>.

It is known that perfect biradicals are characterized by the presence of three singlet states and one triplet state arising from the occupation of two electrons in a pair of degenerate orbitals.<sup>70</sup> The four states, degenerate in the Hückel approximation, split as electron repulsion is considered explicitly;<sup>71</sup> however, because they originate from intra-shell electron promotions, they lie within a relatively low energy range.

In homosymmetric biradicaloids,<sup>70</sup> the two orbitals are not degenerate, and the three singlet states correspond to the ground electronic state, to a singly excited ( $H \rightarrow L$ ) state (single-exciton state), and to a doubly-excited ( $H, H \rightarrow L, L$ ) state. Therefore, one signature of the biradicaloid character is the presence of a low-lying excited singlet state dominated by the doubly-excited ( $H, H \rightarrow L, L$ ) electronic configuration,<sup>72</sup> that is, a double-exciton state because simultaneous promotion of two electrons from occupied to unoccupied orbitals occurs.

The importance of double-exciton states has been emphasized in a very recent quantum chemical study<sup>73</sup> that has revealed how, in pentacene, whose biradicaloid character was suggested in other studies,<sup>74</sup> a dark double-exciton state governs singlet fission. This process,<sup>70,75</sup> which is more likely to occur in biradicaloids,<sup>70</sup> has recently received renewed

interest because it enables the generation of a pair of charge separated triplet states and provides a strategy to generate two electron-hole pairs from a single photon,<sup>70,73,76</sup> thereby increasing the efficiency of dye-sensitized solar cells.

Dark double-exciton states are well-known to characterize the electronic structure and spectroscopy of polyenes and related systems<sup>77</sup> and were previously identified as two triplet states coupled to one singlet.<sup>77b,78</sup>

Therefore, the presence of a double-exciton state may reveal either a biradicaloid or a polyenic character or both, and tuning its location compared with that of the lowest triplet is essential for the optimization of dyes for solar cells.<sup>70</sup> It should also be noted that the interplay between biradicaloid and polyenic character determines the magnitude of the third-order nonlinear optical properties, as discussed in recent work.<sup>79</sup>

Herein we consider the QOTs **2P-2T** and **2P-1T** and investigate, with high-level quantum chemical methods, their low-lying excited electronic states seeking more explicit signatures of their biradicaloid character, and we show that the pattern of low-lying singlet excited states resembles closely that of polyenes, with a double-exciton state becoming the lowest excited singlet state as the length of the oligomer increases. For comparison, the shortest oligomer in the series, not featuring thiophene rings, **2P-0T** (Figure 6.37), is also considered.

#### 6.4.2 Computational details

The chosen models for quinoid molecules did not include the tert-butyl substituents since these contribute negligibly to the final structural and electronic properties of the extended conjugated chromophores. Atomic structures (Figures 6.38-39) were optimized with DFT calculations using the B3LYP hybrid functional with the 6-31G\* basis set. Molecular orbital shapes and energies reported in Figure.40 were calculated at the DFT optimized structures. Orbital pictures were prepared with Molekel 4.3 visual software.

For **2P-2T** the closed-shell (CS) ground-state wavefunction resulted to be unstable as previously found for the tert-butyl substituted analogue.<sup>28</sup> Accordingly, the broken symmetry (BS) UB3LYP/6-31G\* equilibrium structure was determined and resulted to be more stable than the CS structure by 1.06 *kcal mol*<sup>-1</sup>, in agreement with previous results.<sup>28</sup>

Electronic excitation energies, oscillator strengths and the equilibrium structure of the strongly dipole allowed excited state (Figures 6.38-39) were computed with TDDFT calculations employing the Gaussian09 suite of programs. The nature of the critical points determined by quantum-chemical structure optimizations was assessed by evaluating vibrational frequencies at the optimized geometries. Excited state vibrational frequencies were also employed to estimate the vibrational contributions to the Franck-Condon (FC) activity in electronic absorption spectra. The FC vibronic structure associated with electronic transitions was evaluated as reported in Section 6.2.2. The vibrational coordinates and frequencies displaying the largest  $\gamma$  values are collected in Figures 6.42. In plotting computed electronic spectra, a Lorentzian line-width of the order of 0.1 eV was superimposed to each computed intensity to facilitate the comparison with experimental spectra. For **2P-2T** three ground-state geometries were taken into account to simulate the absorption spectrum: the CS quinoid structure, the strongly biradicaloid BS structure and an intermediate structure between the two. A comparison of the 2P-2T  $S_0 \rightarrow S_2$  simulated spectra using different  $S_0$  geometries (Figure 6.43) shows that a quinoid ground state leads to a too pronounced FC progression with an overestimated 0-1/0-0 ratio whilst an underestimate is predicted employing the computed BS geometry, suggesting that a biradicaloid ground-state character is required to account for the reduced FC progression, with the chosen intermediate biradicaloid structure appearing as the most adequate solution.

Because the double-exciton state is dominated by the (H,H  $\rightarrow$  L,L) doubly excited configuration, a multiconfiguration approach was required to describe this state. To this end, equilibrium structures of ground and double-exciton states (Figures 6.44-45) were obtained from quantum-chemical calculations carried out at state average (SA)-CASSCF/6-31G\* level of theory.<sup>80</sup> CAS energies were corrected with single state - single reference (SS-SR)-CASPT2 second-order perturbation calculations.<sup>81</sup> State-averaged calculations were carried out using the same weight for the lowest three singlet states in geometry optimization calculations of ground and double-exciton states, and for the calculation of potential energy profiles. The active space comprised generally 12 electrons in 12  $\pi$  orbitals (12,12) and the CAS was restricted to 8 electrons in 8  $\pi$  orbitals (8,8) for the calculations of the  $S_0$  and  $S_1$  potential energy profiles. CASPT2 energy corrections were evaluated for the full space of configurations, and level shifts, required to avoid intruder state problems, of 0.1 and 0.2 were applied to correct CAS(8,8) energies and CAS(12,12) energies, respectively.

The biradical character of the ground-state wavefunction of **2P-1T** and **2P-2T** was determined as determined as twice the weight of the doubly-excited configuration.<sup>74b</sup>

Derivative couplings between ground and double-exciton states were evaluated at the SA-CASSCF(12,12)/6-31G\* ground state equilibrium structures with a state-average over the lowest three singlet states.

For the **2P-2T** oligomer, several structures were generated by displacing the SA-CASSCF(12,12)/6-31G\* ground-state equilibrium structure along the out of phase CC stretching mode  $\mathcal{A}$  responsible for ground-state Raman activity.<sup>28</sup> In keeping with our previous study,<sup>28</sup> the ground-state normal coordinate employed to displace the geometry was calculated at B3LYP/6-31G\* level of theory. SA-CASSCF(8,8) and CASSCF(12,12)/6-31G\* energies (the latter only for the ground state), as well as subsequent SS-SR-CASPT2 corrected energies, were evaluated at each  $\mathcal{A}$  displaced structure. A level shift of 0.2 was applied to all the CASPT2 calculations to avoid intruder state problems.

The same set of normal coordinates and frequencies were employed to determine the vibrational contributions of the projection of the  $S_0$ - $S_1$  geometry change (Figure 6.49) and of the  $S_0$ - $S_1$  derivative coupling (Figure 6.50).

To explore the suitability of **2P-2T** and **2P-1T** as regard the singlet fission process,<sup>71</sup> SA-CASSCF(12,12)/6-31G\*  $S_0 \rightarrow S_1$ ,  $S_0 \rightarrow T_1$ , and  $S_0 \rightarrow T_2$  vertical excitation energies were calculated at SA-CASSCF(12,12)/6-31G\* ground-state equilibrium structure. State averaging was done over four states, namely the lowest two singlet and the lowest two triplet states. SS-SR-CASPT2 corrected energies were calculated with a level shift of 0.2.

All CASSCF and CASPT2 calculations were run with the MolPro suite of programs.

### 6.4.3 Biradicaloid and polyenic character in QOTs

The DFT computed ground state structures and frontier molecular orbitals of the model systems employed in the calculations follow closely those of the tert-butyl substituted analogues<sup>28</sup> (Figures 6.38-40).

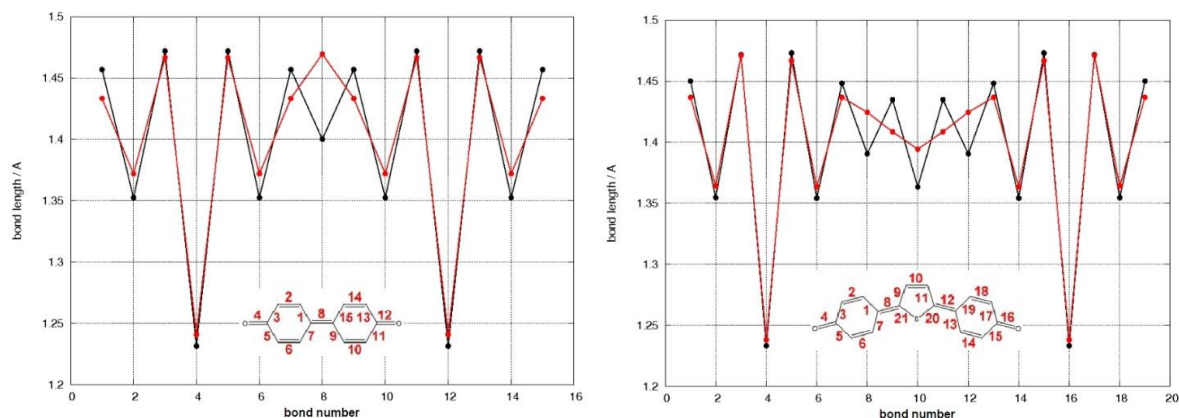


**Figure 6.38** Comparison between the optimized structures of  $S_0$  (B3LYP/6-31G\*)(black) and of the bright state  $S_2$  (TD-B3LYP/6-31G\*)(red) for (left) **2P-0T** and (right) **2P-1T**. Only selected bond lengths are reported, according to the bond numbering in the inset. Figure adapted from <sup>29</sup>.

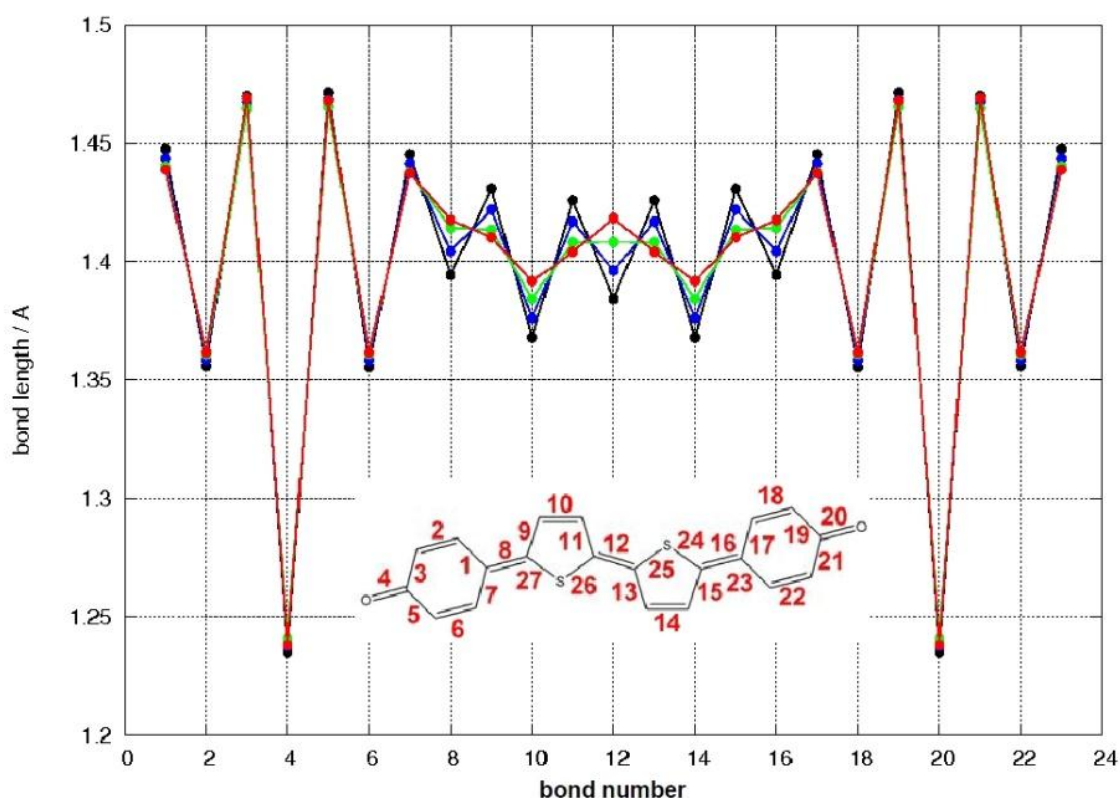


**Figure 6.39** Comparison between the optimized structures of  $S_0$  and of the bright state  $S_2$  (TD-B3LYP/6-31G\*)(red) for **2P-2T**. Only selected bond lengths are reported, according to the bond numbering in the inset. For the ground state, the unstable B3LYP/6-31G\* CS quinoid structure (black), the stable UB3LYP/6-31G\* BS biradicaloid structure (green) and the intermediate structure employed to simulate the  $S_0 \rightarrow S_2$  absorption spectrum in Figure 6.41 (blue), are reported. Figure adapted from <sup>29</sup>.

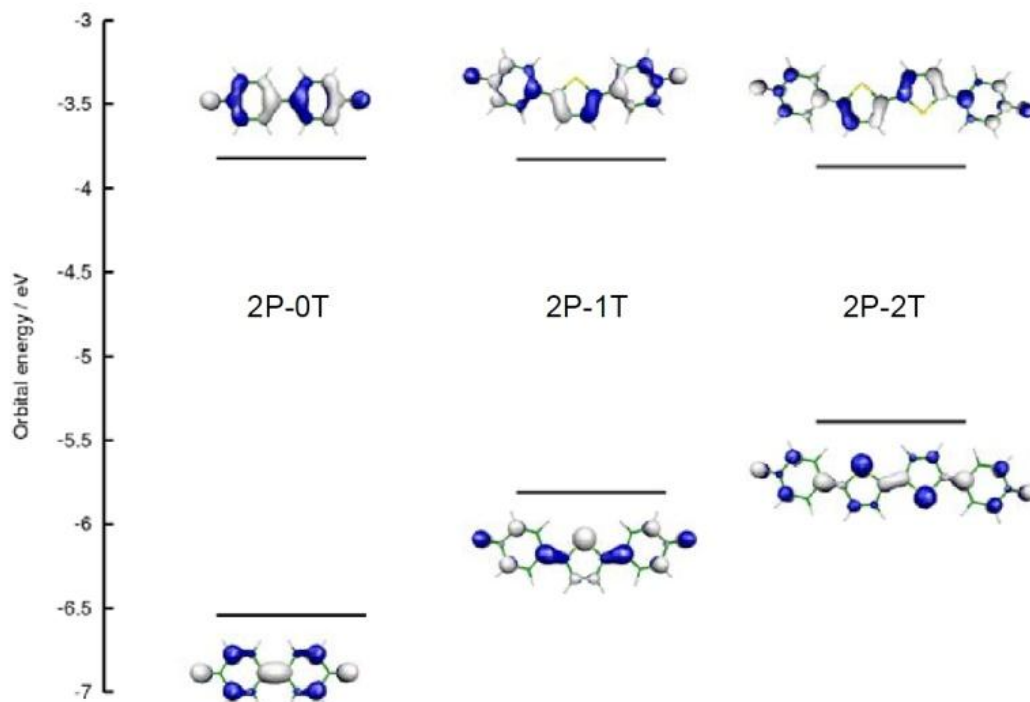


**Figure 6.40** B3LYP/6-31G\* frontier molecular orbital shapes and energy levels of **2P-0T**, **2P-1T**, and **2P-2T** at their equilibrium structures. Figure adapted from <sup>29</sup>.

The TDDFT vertical excitation energies (Table 6.10), in line with previous calculations for similar quinoid systems,<sup>28,65a,c</sup> reveal a low-lying strongly allowed excited state for all systems investigated, accounting for the strong feature observed in experimental absorption spectra (Figure 6.41). This is the bright, single-exciton state dominated by the (H→L) excitation, hereafter labeled the  $S_2$  state.

**Table 6.10** TD-B3LYP/6-31G\* computed vertical excitation energies, oscillator strengths and wavefunction analysis of **2P-0T**, **2P-1T**, and **2P-2T** at their CS equilibrium structures.<sup>29</sup>

TD-B3LYP 6-31G*	$\Delta E$ optical gap			$\Delta E_{exp}$ optical gap (nm) <sup>a</sup>	wavefunction
	eV	nm	oscillator strength		
<b>2P-0T</b>	3.25	382	1.01	420	0.7(H→L)
<b>2P-1T</b>	2.44	508	1.34	544	0.7(H→L)
<b>2P-2T</b>	1.98	627	1.86	658	0.7(H→L)

<sup>a</sup> The energy of the most intense vibronic feature is reported.

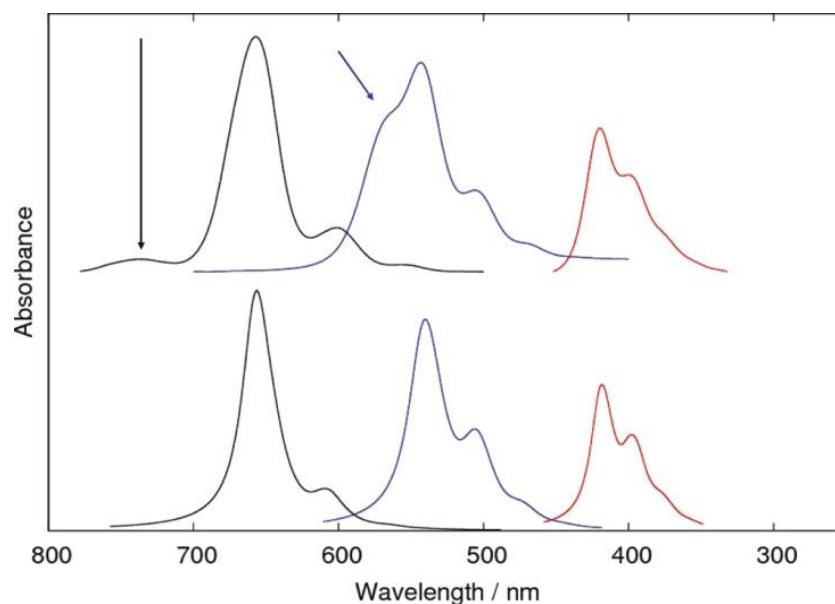


**Figure 6.41** Comparison between observed (top) absorption spectra in *n*-hexane and TDDFT/6-31G\* computed (bottom) FC structure associated with the  $S_0 \rightarrow S_2$  strongly allowed electronic transition of **2P-2T** (black), **2P-1T** (blue), and **2P-0T** (red). The origins of the computed spectra were translated to the origins of the respective experimental spectra. The arrows indicate features in the experimental spectra assigned to the double-exciton state. Figure adapted from <sup>29</sup>.

A comparison between the TDDFT/6-31G\* equilibrium structure of  $S_2$  and that of  $S_0$  in Figures 6.38-39 reveals a marked bond length change localized in the central thiophenic molecular region. The Franck-Condon (FC) vibronic structure<sup>50b,d</sup> associated with the strongly allowed electronic transition of **2P-0T**, **2P-1T**, and **2P-2T**, evaluated along the lines described in previous work,<sup>51b</sup> is compared with the experiments in Figure 6.41, from which it is clear that computed vibronic activities agree nicely with the observed structure. The observed intensities increase monotonically with the oligomer size less markedly than the computed oscillator strengths (Table 6.10), owing to incomplete solubility of the longer oligomers in *n*-hexane. Therefore, to facilitate the comparison with observed data, the computed spectra of **2P-2T** and **2P-1T** in Figure 6.41 were rescaled with respect to those of **2P-0T** following the observed trend rather than according to computed transition dipole moments. On the basis of calculations, we can formulate an assignment of the most prominent FC structure in the spectra, which results to be associated with the normal coordinates collected in Figures 6.42.

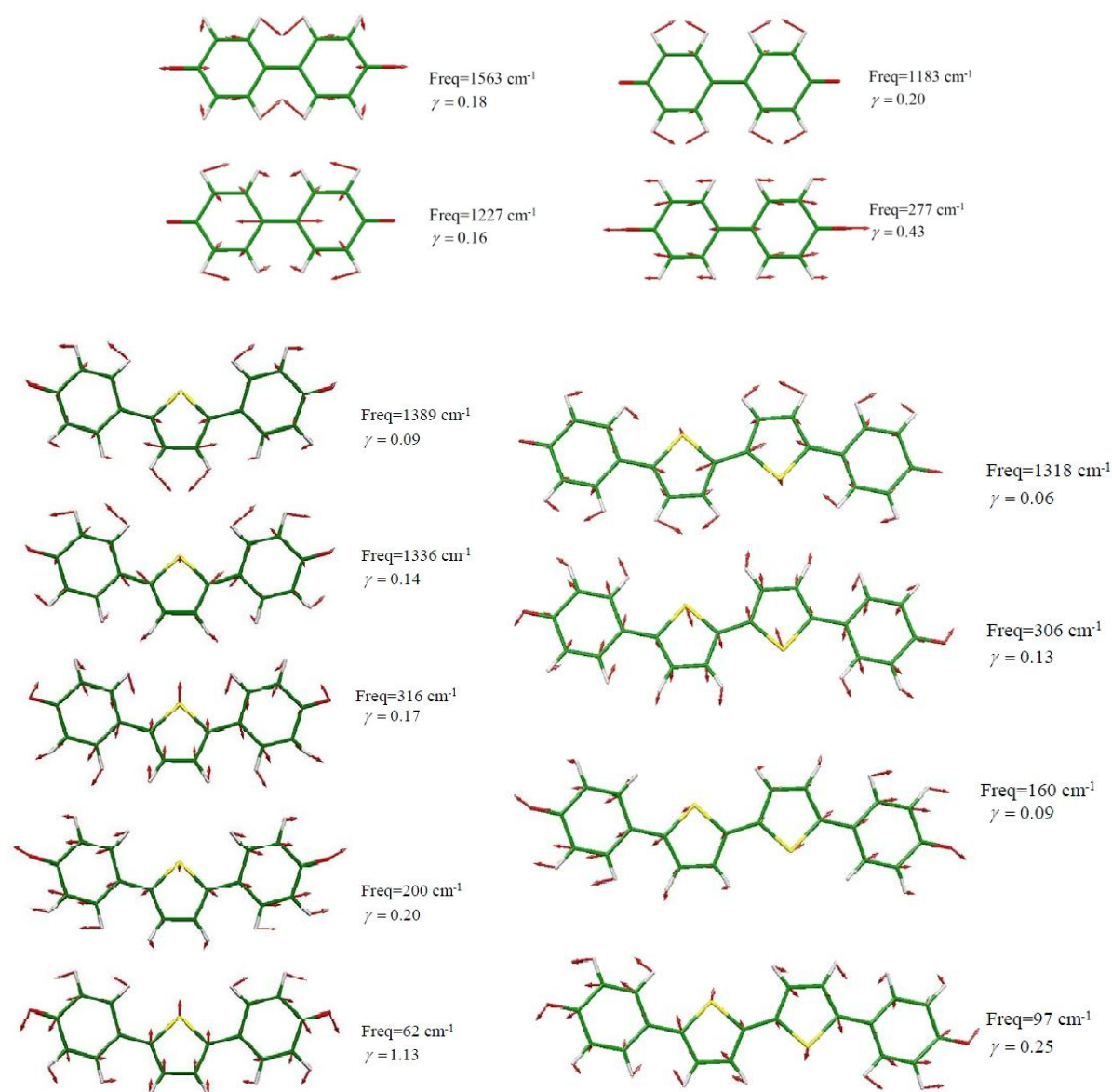


**Figure 6.42** Excited state normal coordinates and frequencies (TD-B3LYP/6-31G\*, scaled by 0.97) associated with the largest computed FC activity ( $\gamma_i$  parameters) in the  $S_0 \rightarrow S_2$  absorption spectrum of **2P-0T** (up), **2P-1T** (bottom, left), and **2P-2T** (bottom, right). The scaled vibrational frequency and the associated  $\gamma_i$  value are indicated for each normal mode. Only modes with  $\gamma_i > 0.1$  are reported. Figure adapted from <sup>29</sup>.

Figure 6.41 shows that there is a nice agreement between computed and observed vibronic structures. In particular, the peaks observed at 420, 400, and 381 nm in the experimental absorption spectrum of **2P-0T** correspond to a separation of *ca.* 1200-1300  $\text{cm}^{-1}$ . The observed peak separation is nicely reproduced by the simulated spectra, indicating the activity of two vibrations (Figure 6.42) with computed frequencies of 1183 and 1227  $\text{cm}^{-1}$ , dominated by the

stretching of CC bonds undergoing remarkable elongation upon excitation. Similarly, the peaks observed at 544, 507, and 473 nm for **2P-1T** and at 658, 602, and 559 nm for **2P-2T** correspond to a separation of *ca.* 1300-1400  $cm^{-1}$  reproduced by the simulated spectra through the activity of two major vibrations with computed frequencies of 1336 and 1389  $cm^{-1}$  for the former and 1318  $cm^{-1}$  for the latter, also dominated by CC stretching. Note that the higher frequencies of the active modes of **2P-2T** and **2P-1T** compared with **2P-0T** are in line with their less marked CC bond length changes upon excitation (Figures 6.38-39). Band shapes are further modulated by the activity of a number of low frequency modes.

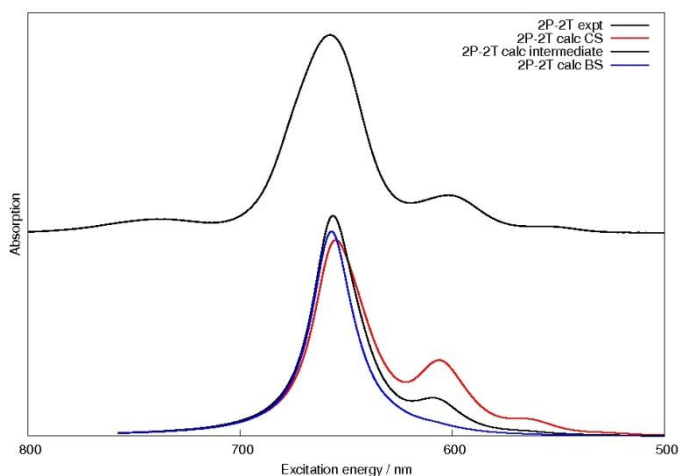


**Figure 6.43 2P-2T:** Comparison between the experimental absorption spectrum (top, black) and the computed FC structure (bottom) employing: the quinoid CS ground-state structure (red), the strongly biradicaloid BS ground-state structure (blue), and the intermediate biradicaloid structure between the two (black). Figure adapted from <sup>29</sup>.

The FC activity is experimentally more pronounced for **2P-0T**, whereas it appears considerably reduced for **2P-2T**, as demonstrated by the larger 0-1/0-0 intensity ratio for the former compared with the other two chromophores. Although functionals featuring different amounts of HF exchange might be explored, this effect is reproduced by the B3LYP/6-31G\* calculations employing, for **2P-2T**, a ground-state geometry intermediate between the markedly quinoid CS and the strongly biradicaloid BS structures computed at the DFT level. All computed spectra predict the FC activity in the correct frequency region, and, for **2P-2T**, the most active mode, dominated by the out-of-phase stretching of adjacent CC bonds<sup>77c,82</sup> mainly located on the thiophenic molecular region, clearly reveals the  $\mathcal{A}$  character<sup>28</sup> of the mode governing Raman activities.<sup>28</sup> Interestingly, the above results indicate that a

biradicaloid ground-state structure is required for **2P-2T**, not only to account for its Raman activity<sup>28</sup> but also to reconcile its reduced FC activity in the absorption spectrum compared with the shorter members (Figure 6.43).

Despite the correct extension of the simulated FC progression associated with the strongest transition in absorption, the arrows in Figure 6.41 show that for **2P-1T** and **2P-2T**, additional bands at lower energies are observed. Interestingly, very similar spectral features characterize the longer members of QOTs end-capped with different terminal groups.<sup>63c,65a</sup> This observation excludes a possible role of  $n \rightarrow \pi^*$  excitations due to the oxygen atoms in our systems to account for the weak features. Furthermore, there is no evidence of aggregation from either the experimental or the computational investigations; therefore, we propose that the low-energy shoulders in the NIR for **2P-2T** and in the visible for **2P-1T** are due to a different class of excited electronic states that characterize these biradicaloids systems regardless of their terminations.

According to the excited-state pattern typical for biradicaloids,<sup>70</sup> we explored, at the CASSCF//CASPT2 level,<sup>83</sup> the so-far ignored location of the singlet excited state dominated by the (H,H $\rightarrow$ L,L) double excitation. Interestingly, whereas the CASSCF ground-state structure of **2P-1T** compares well with the DFT result, the CASSCF structure of **2P-2T** is more markedly quinoid than the UB3LYP BS structure (Figures 6.44-45), as confirmed by the identical biradical character<sup>74b</sup> (*ca.* 8%) predicted by CASSCF for both oligomers. The modest biradical character of **2P-2T** results from the unrealistically large energy difference between the ground and the double-exciton states at the CASSCF level. An almost doubled biradicaloid character is recovered for  $S_0$  once CASPT2 corrections are taken into account. As it will be shown, the CASPT2 correction drives energy differences between the two states to realistic values and forces a displacement of the  $S_0$  state minimum toward a more marked biradicaloid structure. Indeed, the CASPT2 corrected adiabatic excitation energies compare well with the experimentally determined low-energy features in the *n*-hexane absorption spectra (Table 6.10). Their CASSCF-computed transition dipole moments are much smaller than those of the  $S_0 \rightarrow S_2$  transition and support their assignment to the weak transition to the double exciton state, hereafter labeled the  $S_1$  state. Notably, the presence of a low-lying double-exciton state is strongly reminiscent of polyenes.<sup>77b-d,78</sup> Although a similarity between oligoenes and oligothiophenes<sup>82b,84</sup> and between oligoenes and dioxide oligothiophenes<sup>85</sup> has been previously suggested, to the best of our knowledge this is the first reported evidence of

a similarity in the low-lying singlet electronic state pattern between polyenes and quinoidal oligothiophenes. In passing, we note that the CASPT2 energy of the lowest triplet state of both **2P-1T** and **2P-2T** is compatible with singlet fission because the  $E(S_1) > 2E(T_1)$  requirement<sup>71</sup> is satisfied, although undesired inter-system crossing to the  $T_2$  state might occur (Table 6.11).

The bond length changes upon excitation to  $S_1$  (Figure 6.46) follow a pattern very similar to the bond length differences between the quinoid CS and the biradicaloid BS structures (Figure 6.47). These, in turn, overlap with the mode dominated by the collective vibrational coordinate  $\mathcal{R}$ , featuring out-of-phase oscillation of adjacent CC bonds in the thiophenic molecular region and responsible for the Raman activity of these systems.<sup>28</sup>

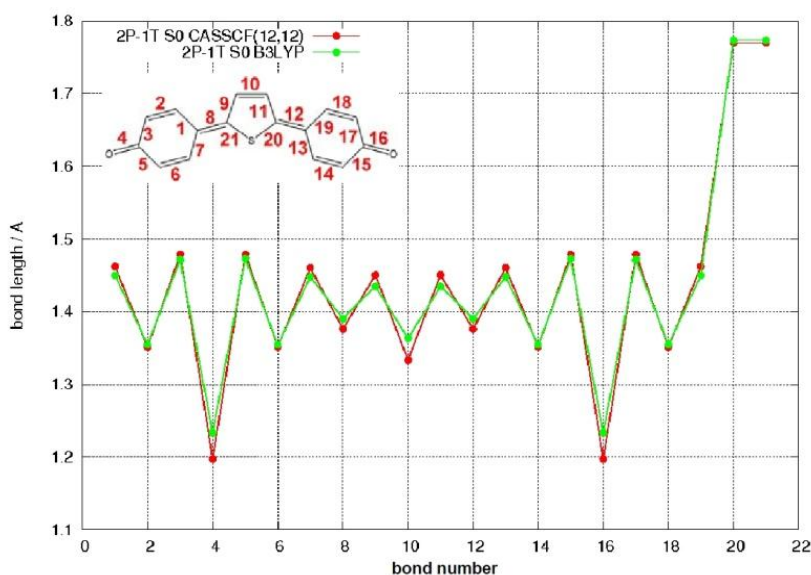


**Figure 6.44** Comparison between the ground state equilibrium structures of **2P-1T** computed at CASSCF(12,12)/6-31G\* (red) and B3LYP/6-31G\* (green) levels. Figure adapted from <sup>29</sup>.

**Table 6.11** Comparison between CASPT2-corrected  $S_0 \rightarrow S_1$  adiabatic excitation energies (eV) and observed weak features in the absorption spectra.<sup>29</sup>

	adiabatic	exp ( <i>n</i> -hexane)
<b>2P-1T</b>	1.97	2.19
<b>2P-2T</b>	1.38	1.68 <sup>a</sup>

<sup>a</sup> Very likely this weak feature is not the origin of the  $S_0S_1$  transition, which is expected to be located at even lower energies; see for instance the weak features in the spectra of related quinoid systems.<sup>63c</sup>

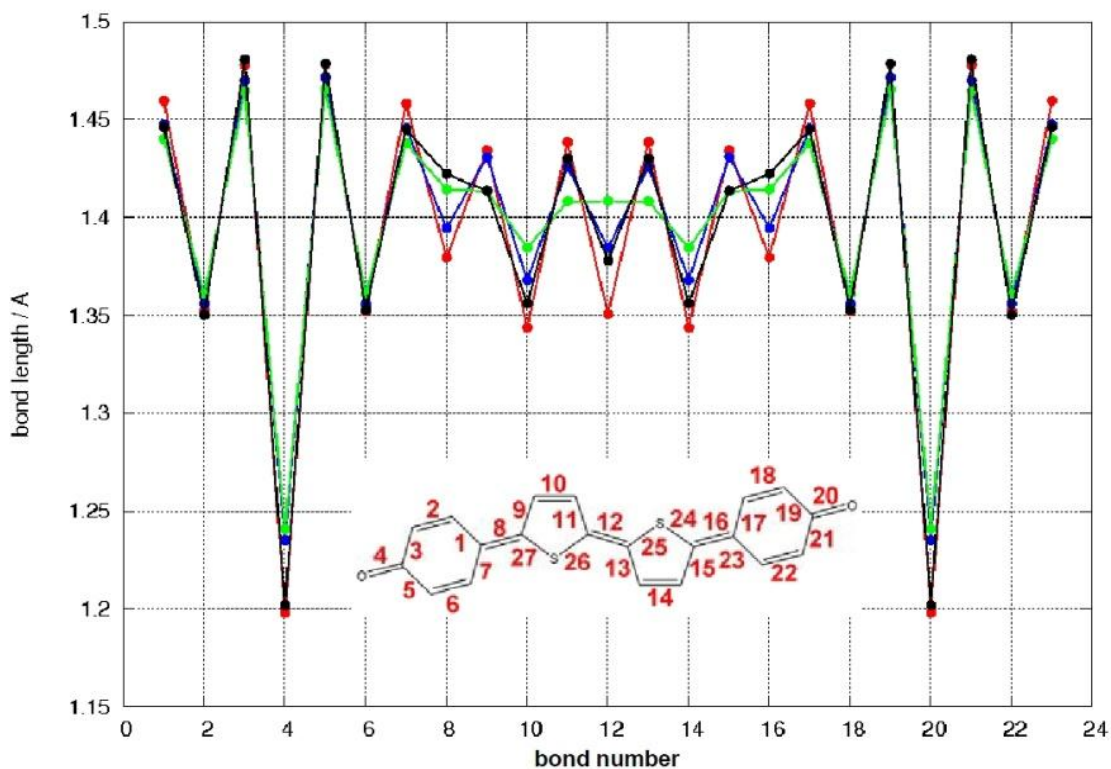


**Figure 6.45** Comparison of **2P-2T** ground-state equilibrium structures computed at CASSCF(12,12)/6-31G\* (red), B3LYP/6-31G\* (CS structure) (blue), UB3LYP/6-31G\* (BS structure) (green, and CASPT2 (black) levels. The black structure was determined as the  $\mathcal{N}$ -displaced structure corresponding to the CASSCF(12,12)/6-31G\* + CASPT2 minimum energy. Figure adapted from <sup>29</sup>.

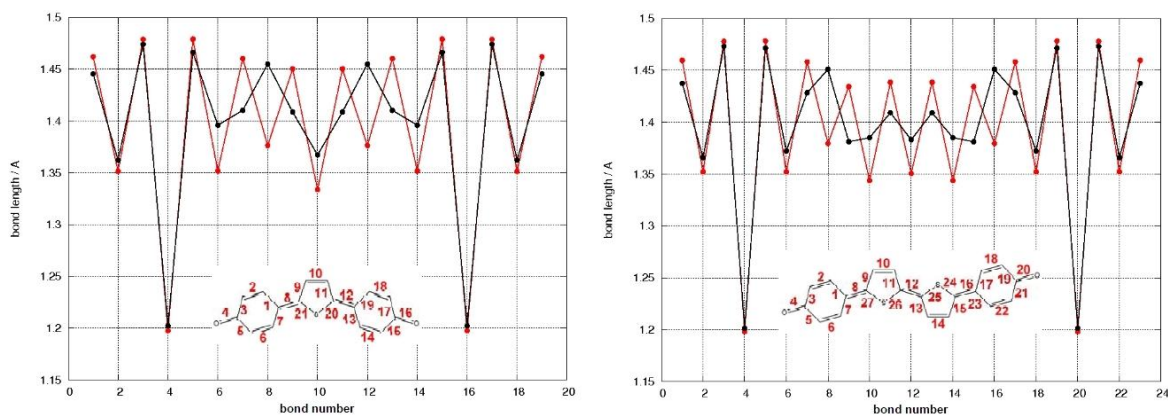


**Figure 6.46** Comparison between the equilibrium structures of  $S_0$  (red) and of the double-exciton state  $S_1$  (black) computed at CASSCF(12,12)/6-31G\* level for (top) **2P-1T** and (bottom) **2P-2T**. Only selected bond lengths are reported, according to the bond numbering in the inset. Figure adapted from <sup>29</sup>.

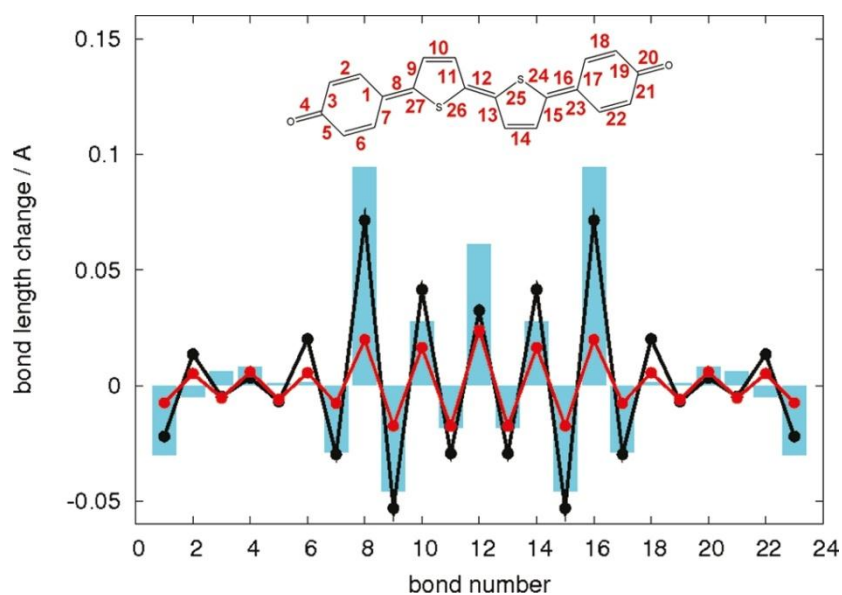


**Figure 6.47 2P-2T:** Bond length changes upon excitation to the double-exciton  $S_1$  state from CASSCF(12,12)/6-31G\* calculations (black) and upon moving from the ground-state quinoid CS to the biradicaloid BS structure obtained at the B3LYP/6-31G\* level (red). The bond length changes overlap closely with the displacements (cyan) of the Raman active out-of-phase CC stretching mode (the  $\mathcal{A}$  mode, B3LYP/6-31G\* level) which is mainly localized on the thiophenic molecular region. Figure adapted from <sup>29</sup>.

Figure 6.47 suggests that we can generate increasingly biradicaloid ground-state geometries by displacing the initial CASSCF optimized ground-state structure of **2P-2T** along the mode dominated by the  $\mathcal{A}$  character. This is done in Figure 6.48 where the potential energy profiles (PEPs) of both the ground and  $S_1$  states are computed at CASSCF and CASPT2 levels for displacements along the  $\mathcal{A}$  mode starting from the CASSCF optimized ground-state structure. As expected, the minimum on the CASSCF  $S_0$  PEP coincides with the origin of the graph. In contrast, the minimum on the CASPT2-corrected  $S_0$  PEP is displaced toward a more biradicaloid structure (corresponding to a displacement of *ca.*  $0.20 \text{ \AA } amu^{1/2}$  along the  $\mathcal{A}$  mode in Figure 6.48 and a biradicaloid character of *ca.* 14%) as a result of the dramatic  $S_1$ - $S_0$  energy reduction. The CASPT2 results in Figure 6.48 reconcile the computed with the observed  $S_1$ - $S_0$  energy difference for **2P-2T**. On the other side, the displacement of the  $S_0$  minimum occurring upon inclusion of the CASPT2 correction exemplifies the effect of the energy gap decrease accompanying the conjugation length increase for the longer members of the QOT families. In other words, the displaced  $S_0$  minimum justifies the increased

biradicaloid character resulting from the extension of conjugation in longer members of quinoidal chromophores.

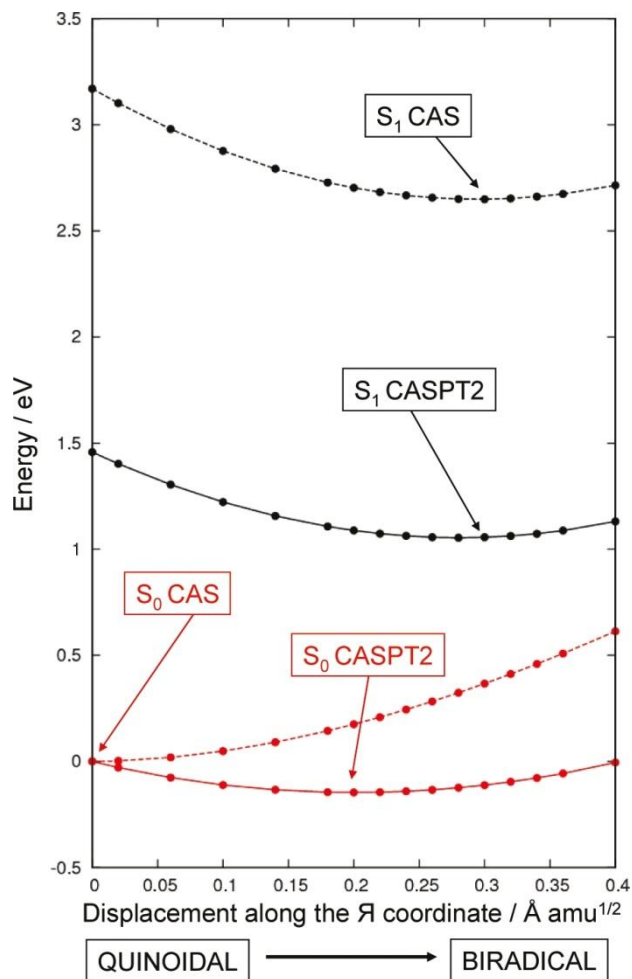


**Figure 6.48** Potential energy profiles of  $S_0$  and  $S_1$  along the  $\mathcal{Y}$  coordinate at CASSCF level and including CASPT2 corrections. The red and black arrows indicate the minima on the CASSCF and CASPT2 profiles. The  $S_0$  minimum is located at a more biradicaloid structure at the CASSCF//CASPT2 level. Figure adapted from <sup>29</sup>.

Having proven the effect of the  $S_0$ - $S_1$  energy difference in determining the biradicaloid character of the ground state, to strengthen further the analogy with polyenes, we explored the role of the out-of-phase CC stretching mode in coupling these two states. Projection of the computed  $S_0$ - $S_1$  geometry changes on ground-state normal coordinates shows the largest contribution for the mode dominated by the  $\mathcal{Y}$  character (Figure 6.49), and a similar trend is obtained by projecting the CASSCF computed derivative couplings between  $S_0$  and  $S_1$  on the same set of normal coordinates (Figure 6.50). Therefore, the out-of-phase oscillation of

adjacent CC bonds is responsible for the largest coupling between the two electronic states as it is well known for polyenes.<sup>77c,82a,86</sup>

In this regard, we notice that the CASPT2 results for **2P-2T** indicate an excited-state reorganization energy associated with the  $S_0 \rightarrow S_1$  excitation (Figure 6.51) larger than the ground-state contribution. This observation further supports the presence of a remarkable coupling between the two states, which might result in an unusual excited state frequency increase compared with the ground state, as previously demonstrated for polyenes and carotenoids.<sup>77c-d,86</sup>

In summary, high-level quantum chemical calculations have been carried out to investigate the excited electronic states of QOTs, and the major features in the vibronic structure associated with the transition to the lowest bright excited state have been reproduced. The study has revealed the double-exciton nature of their lowest excited electronic state, responsible for the weak features appearing in measured absorption spectra, and a possible compatibility of these biradicaloids with singlet fission. The energy location of the double-exciton state on one side controls the biradicaloid character of the ground-state geometry, and on the other side it discloses a typical polyenic character further emphasized by the evidence of a strong vibronic coupling between  $S_0$  and  $S_1$ , thereby offering a parallel view of low-energy transitions in polyenes and quinoidal oligothiophenes.

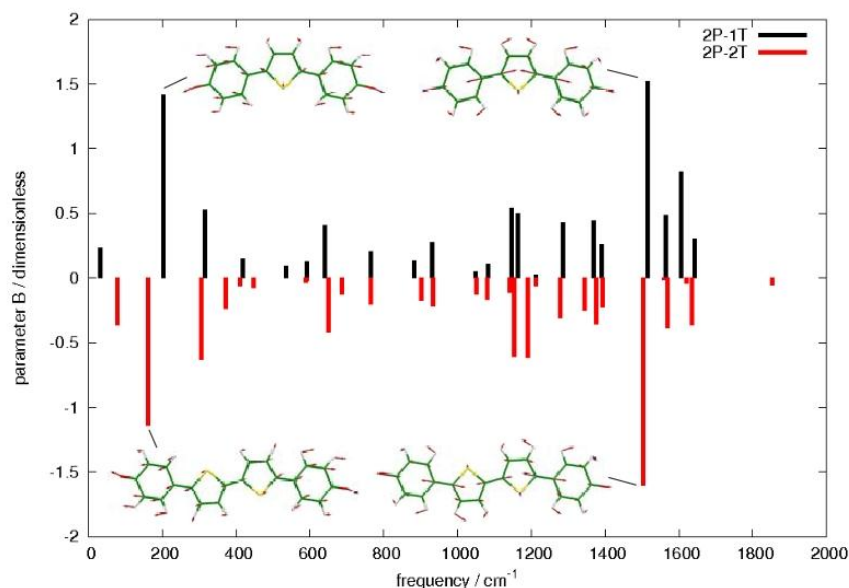


**Figure 6.49** Projection of the  $S_1-S_0$  geometry change (CASSCF(12,12)/6-31G\* level) over ground state normal modes (dimensionless  $B$  parameter). Contributions for **2P-1T** (black) and **2P-2T** (red). Vibrational frequencies, scaled by 0.97, were computed at B3LYP/6-31G\* level. The largest contribution in the high frequency region is due, for both molecules, to the mode dominated by the  $\mathcal{A}$  character. Figure adapted from <sup>29</sup>.

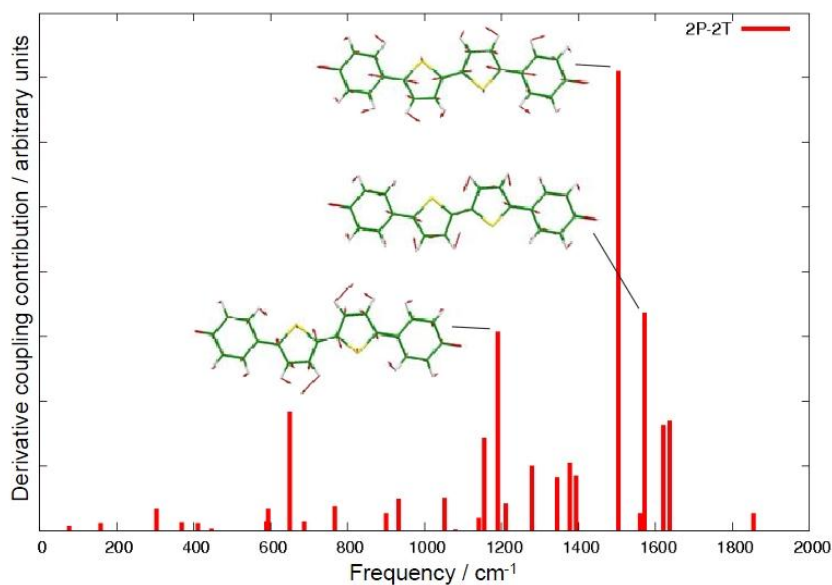


**Figure 6.50** Projection of the CASSCF(12,12)/6-31G\* computed derivative coupling between  $S_0$  and  $S_1$  over ground-state normal modes. Vibrational frequencies, scaled by 0.97, were computed at B3LYP/6-31G\* level. The largest contribution in the high frequency region is due to the mode dominated by the  $\mathcal{A}$  character. Figure adapted from <sup>29</sup>.

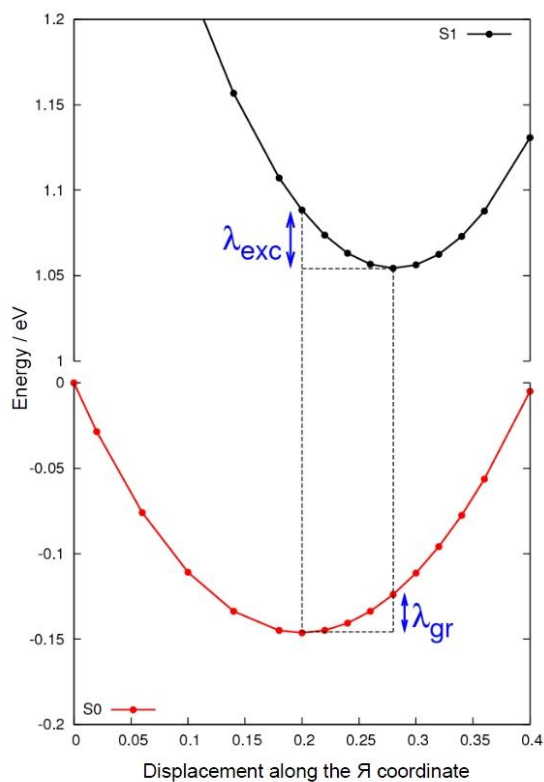


**Figure 6.51 2P-2T:** Reorganization energies ( $\lambda_{gr}$  and  $\lambda_{exc}$ ) associated with the  $S_0 \rightarrow S_1$  excitation from CASSCF(8,8)/6-31G\* + CASPT2 calculations. The largest value of  $\lambda_{exc}$  compared to  $\lambda_{gr}$  suggests a frequency increase in the  $S_1$  state of the mode dominated by the  $\mathcal{A}$  character, as it is well known for polyenes. Figure adapted from <sup>29</sup>.

## 6.5 OXYGEN DOPED PICENE

In this Section, it is discussed the modification induced by oxygen gas to the electronic structure of highly crystalline picene films with a standing-up orientation grown epitaxially on the Ag(110) surface. It is suggested that the highest two picene orbitals are inverted due to the strong interactions between the singly occupied oxygen  $\pi$  orbital and the highest occupied orbital of picene.<sup>87</sup> Therefore, by inactivating trap states, the exposure to oxygen grants picene thin films higher hole drift mobility, like a sort of *p*-type doping.

This study was motivated by the strong recent interest in the peculiar properties of oxygen doped picene, and by the collaboration with Prof. Friedlein and his group at the School of Materials Science, Japan Advanced Institute of Science and Technology, Nomi, Ishikawa, who prepared the materials and performed ultraviolet photoelectron spectroscopy measurements.<sup>87</sup>

### 6.5.1 Background

In general, electronic properties of most organic semiconductors are highly sensitive to the atmospheric environment and in particular to the exposure to oxygen ( $O_2$ ). For example, oxidation of crystalline rubrene has a significant effect on the charge transport since impurities form new states within the original gap.<sup>88</sup> As found for a number of rather small molecules and polymers,<sup>89</sup> molecular oxygen can also adsorb physically and cause *p*-doping of the organic semiconductors which has a pronounced effect on the conductivity.<sup>90</sup> Although much effort has been devoted to studying the effects associated with the incorporation or reaction of oxygen species on the transport characteristics of organic semiconductors,<sup>91</sup> progress is still limited since the underlying fundamental mechanisms are only partially understood.

An isomer of pentacene called picene, the molecular structure of which is depicted in the inset of Figure 6.52, has recently shown some remarkable and unusual transport properties.<sup>92</sup> As active materials in organic field-effect transistors, pristine thin films exhibit a hole mobility of more than  $3 \text{ cm}^2 \text{ V}^{-1} \text{ s}^{-1}$ . More fascinating, the mobility is enhanced up to  $5 \text{ cm}^2 \text{ V}^{-1} \text{ s}^{-1}$  upon exposure to  $O_2$  gas at 500 Torr.<sup>92b-c</sup> These unique phenomena inspired us to study the changes of electronic structure induced by the interaction between oxygen and picene. Here

the epitaxial growth is reported of highly crystalline picene films with a standing-up orientation on the Ag(110) surface that provide an ideal platform for the study of the electronic structure. The Ag(110) surface was chosen due to its low symmetry and the good matching of multiples of lattice parameters with those reported for the bulk<sup>92a</sup> of picene. Changes of electronic properties caused by the incorporation of molecular oxygen into the interstitial sites within the film were studied by ultraviolet photoelectron spectroscopy (UPS) and DFT based calculations.

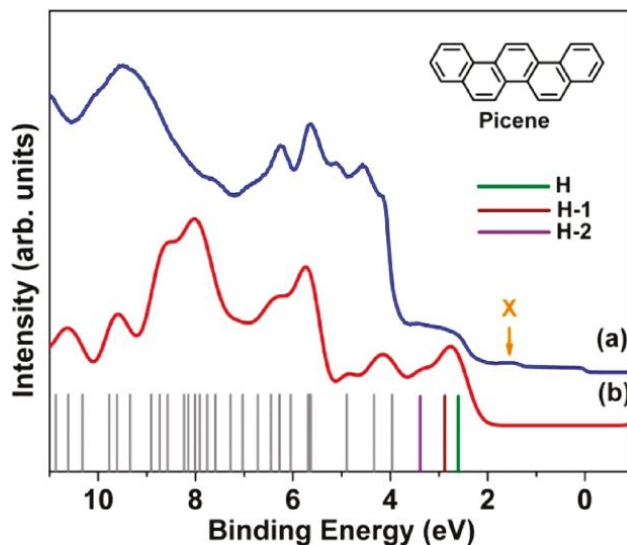


**Figure 6.52** (a) UPS spectrum of the picene/Ag(110) multilayer film measured with respect to  $E_F$  and (b) a simulated spectrum derived from calculated molecular orbital energies, shown at the bottom. H, H-1, and H-2 denote the three highest occupied molecular orbitals, HOMO, HOMO-1, and HOMO-2, respectively. Feature "X" is attributed to trapping states (*vide infra*). The molecular structure of picene is shown in the inset. Figure adapted from <sup>87</sup>.

### 6.5.2 Computational details

UPS spectra of pristine picene were simulated by using the B3LYP/6-31G\* computed molecular orbital eigenvalues. A Gaussian broadening of 0.25 eV was added to the computed peaks to facilitate the comparison with the experimental spectra. Previous investigations have shown that this level of theory provides simulations of UPS spectra in excellent agreement with the observed spectra.<sup>93</sup> The computed UPS spectra were rigidly shifted by 2.9 eV to match the observed spectra. Atomic structures of the complexes formed between picene and one or three oxygen molecules were optimized with DFT calculations using the M06 hybrid functional<sup>94</sup> with the 6-31G\* basis set and the Gaussian 09 suite of programs.

Additional calculations were carried out with other long-range corrected DFT functionals and also employing the MP2 level of theory, with similar results.

### 6.5.3 Effect of O<sub>2</sub> to the electronic structure of highly crystalline picene thin films

Upon deposition of picene on Ag(110), the work function ( $\phi$ ) decreases by about  $0.60 \pm 0.05$  eV to a value of  $\phi = 4.25 \pm 0.10$  eV. Saturation at a nominal film thickness of about 13.8 Å is consistent with the completion of the first molecular layer (1 ML) with a "standing-up" molecular orientation. With increasing thickness, the UPS valence band spectrum changes (Figure 6.53). The intensity of the feature related to the Ag (3d) band is gradually suppressed. As shown for the spectrum of the pristine multilayer film in Figure 1, several adsorbate-induced spectral features appear in the binding energy range between 2 and 8 eV. The separation between these features corresponds well to the spacing of B3LYP/6-31G\* calculated energy levels<sup>19</sup> of the picene molecule (shown at the bottom) which in turn agree with those of recent calculations.<sup>20</sup> The sharpness of the features between about 4 and 6 eV indicates the formation of highly ordered thin films on Ag(110). In the low-binding energy region of the pristine multilayer film shown in Figure 6.52, spectral features at about 2.60, 2.96, and 3.50 eV, denoted H, H-1, and H-2, relate to the three highest occupied molecular orbitals, HOMO, HOMO-1, and HOMO-2, respectively. Additionally, a weak spectral feature centered at the binding energy of 1.55 eV, denoted "X", may be recognized as part of a tail at the low-binding energy side of the HOMO. This feature is certainly a signature of trapping states caused by structural defects associated with the formation of the multilayer and not by impurities since it is not detected for thicknesses below 16 Å. At the Fermi level,  $E_F$ , a step-like feature is visible even for the multilayer films with a nominal thickness of about 35 Å. Since multilayer films are not expected to be metallic, electronic states at  $E_F$  should derive from the non-vanishing contribution of the substrate or from interfacial states associated with the first layer. It is therefore concluded that the growth proceeds in multilayer islands. This conclusion is also supported by Atomic Force Microscopy measurements (Figure 6.54) showing an island-like multilayer film with a profile containing protrusions up to 10 nm deep.

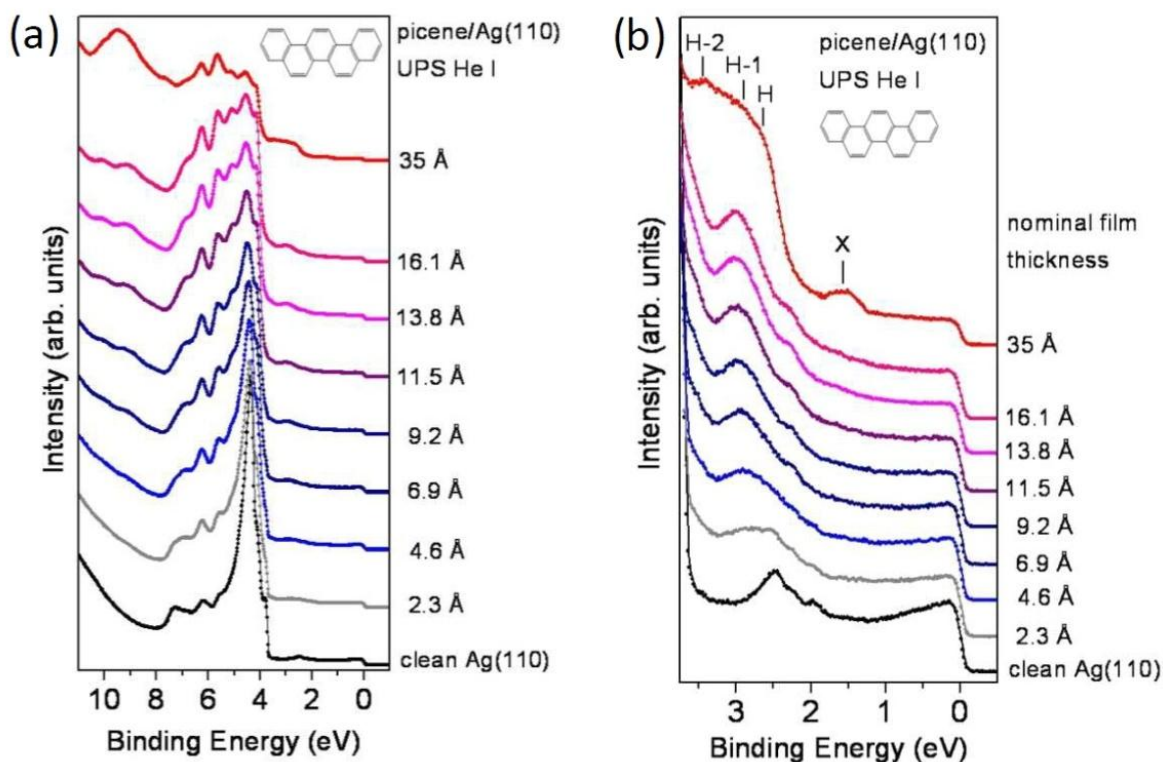


**Figure 6.53** Evolution of the valence band photoelectron spectra of picene/Ag(110) as a function of the nominal film thickness, in a wider (a) and a narrower range (b). The corresponding spectra of the clean Ag(110) surface are included for comparison. Figure adapted from <sup>87</sup>.

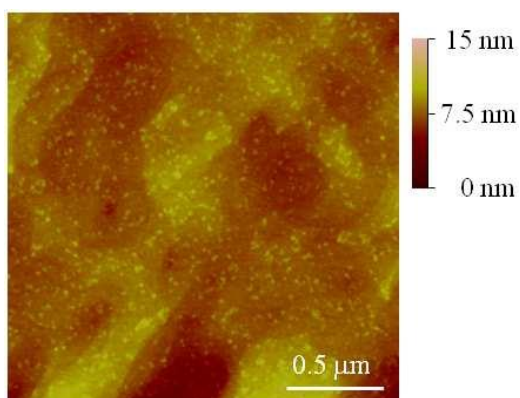


**Figure 6.54** Topographic TM-AFM image of a multilayer picene film on Ag(110), after exposure to air.<sup>87</sup> The image shows an island-like multilayer film with a profile containing protrusions up to 10 *nm* deep. Within the islands, small grains are visible. The formation of these small grains could have been caused by the exposure to oxygen or air and do not necessarily exist in the pristine films. Figure adapted from <sup>87</sup>.

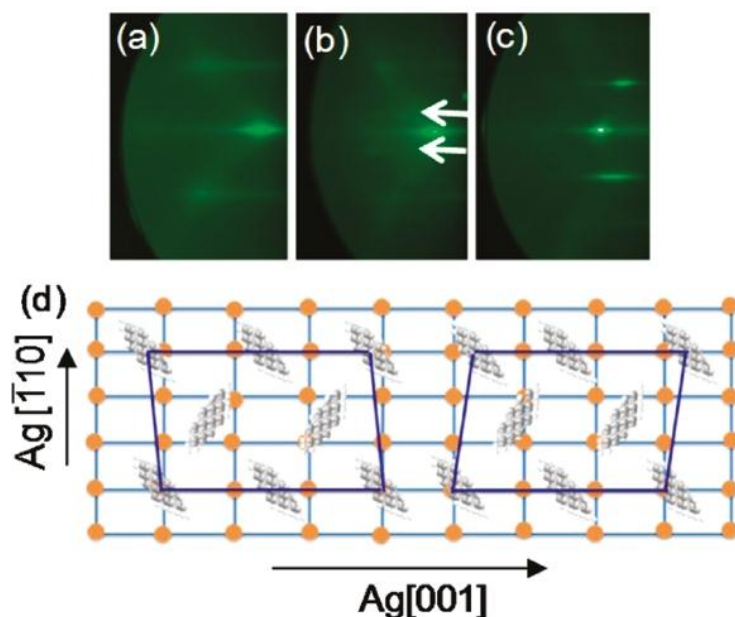


**Figure 6.55** RHEED pattern of (a) the Ag(110) surface and (b) picene ML film on Ag(110), with the electron beam directed along the Ag[001] direction and of (c) a picene ML film on Ag(110), with the electron beam directed along the Ag[-110] direction. (d) Schematic representation of the picene ML unit cell with respect to the underlying Ag(110) lattice. Figure adapted from <sup>87</sup>.

Reflection high-energy electron diffraction (RHEED) images of the Ag(110) surface and of a monolayer picene film are shown in Figures 6.55a and 6.55b, respectively. The patterns obtained with the electron beam directed along the Ag[001] crystallographic direction represent the reciprocal periodicity along the [-111] direction. Upon deposition of the molecules, additional streaks with a spacing of one-third of the original ones appear as indicated with white arrows. The clear RHEED pattern comprising narrow and elongated side streaks is both an indication of a high degree of crystallinity of the picene films and of a good epitaxial relationship with the Ag(110) surface. In the [-110] direction, the picene unit cell is three times larger than that of the substrate. In the [001] direction (Figure 6.55c), no additional streaks related to the picene lattice are observed. Since the lattice constants in the relevant *a-b* plane of bulk picene<sup>92a</sup> would match with multiples of those of the Ag(110) surface, additional streaks should be expected in the case of a rectangular thin film unit cell. On the other hand, small deviations of 2° to 4° of the unit cell vector from the [-110] direction would lead to the observed pattern and a monoclinic film structure. A model of the as-derived in-plane unit cells of coexisting twin domains is shown in Figure 6.55d. The length of the unit cell vectors within the *a-b* plane of 8.79 and 12.12 Å is consistent with a unit cell of

an epitaxial monolayer containing four molecules. In subsequent layers, this ML unit cell naturally gives rise to a unit cell that would be half the size in the [001] direction once the contact to the Ag surface is lost. Additional confidence in the proposed model is found in the fact that the nearest-neighbor molecular distance of about 5.16 Å is similar to that in bulk material.

Note that picene thin films on Ag(110) exhibit a standing-up orientation from the very beginning. This is markedly distinct to monolayer thin films of pentacene and of other aromatic molecules on the same surface where the molecular plane is parallel to the substrate surface.<sup>95</sup> The orientational difference may indicate a particular molecule-substrate interaction governed by epitaxy conditions. For the following discussion related to the effect of oxygen on the electronic properties, details of the structure model are important as there is a strong resemblance of the thin film structure with that of the bulk material. In particular, O<sub>2</sub> molecules may occupy interstitial sites within the *a-b* plane similar to those used by K-atoms in superconducting K-intercalated picene.<sup>92a</sup> It is logical to assume that the oxygen guest species would be in the form of weakly interacting oxygen molecules since other forms of oxygen may not undergo reversible reactions. Covalent bonds to the picene molecules would have already formed prior to the introduction of the molecules into the vacuum systems. Due to the particular w-shaped chemical structure, picene molecules are actually predicted to be resistant against quinone formation.

In Figure 6.56 are shown UPS spectra obtained after stepwise exposure to oxygen gas, at selected exposure times. With increasing partial pressure,  $\phi$  increases steadily by a final amount of about  $0.70 \pm 0.05$  eV that is obtained after exposure to 1 bar for 35 min. In the valence band region shown in Figure 6.56a and 6.56b, spectral features centered at about 4.60, 5.10, 5.64, and 6.26 eV remain pinned to  $E_F$  while others at 7.65 and 9.20 eV and those in the range of 2-4 eV, denoted the H, H-1, and H-2, shift toward a lower binding energy. Even more, as clearly visible in Figure 6.56b, the shift is different for each of the latter three  $\pi$  levels. Such orbital-specific properties must reflect special interactions between picene  $\pi$  orbitals and incorporated oxygen atoms within the *a-b* plane of the film. The picene films remain ordered after exposure to oxygen gas pressures of up to at least  $3.4 \cdot 10^{-4}$  mbar which is proven by the persistence of the RHEED patterns (not shown) characteristic of the pristine film. This indicates that the O<sub>2</sub> molecules are incorporated at interstitial sites allowing the above-mentioned unique electronic interactions. Note that the unit cell of pristine picene is

significantly larger than those of herringbone-stacked oligoacene films where intercalants sit in between molecular layers.<sup>96</sup> The increase of  $\phi$  upon exposure to oxygen gas and the pinning of the majority of electronic levels to the Fermi level are consistent with a *p*-type doping of the films related to an effective partial electron transfer from the molecules to the oxygen atoms. In this picture, the pinning level may be related to the now partially unoccupied HOMO, and the change of  $\phi$  could reflect changes of the chemical potential of the films as it does for alkaline-metal intercalated films of polyaromatic hydrocarbons.<sup>97</sup>

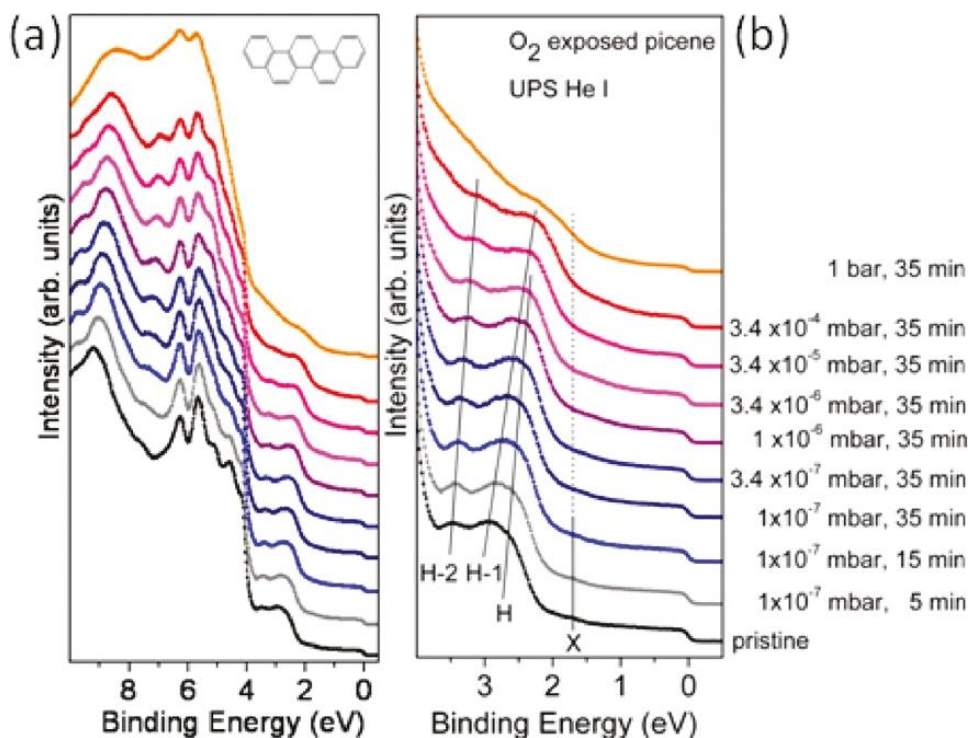


**Figure 6.56** Evolution of the valence band photoelectron spectra of the picene/Ag(110) multilayer film as a function of the oxygen exposure time and pressure, in a wider (a) and narrower (b) range. The corresponding spectra of the pristine picene film are included for comparison. Figure adapted from <sup>87</sup>.

As the transport of positive charge carriers in organic materials does occur mainly via electronic states related to the HOMO, a more careful look at the associated spectral features and their behavior upon exposure to oxygen gas is required. As shown in Figure 6.56b, in pristine picene films, H and H-1 are split by only about 0.3 eV. While both features shift toward a lower binding energy, the one related to the HOMO-1 exhibits a much larger shift surpassing the original HOMO at exposures in the  $10^{-4}$  mbar range. The transfer of spectral weight toward a lower binding energy continues upon exposure to oxygen gas at ambient

conditions (1 bar for 35 min). Even if it is difficult to distinguish individual features from the observed trends, it may then be concluded that (i) the original HOMO-1 becomes itself the highest occupied orbital (ii) at energies in the vicinity of the original trapping states related to the feature X at 1.55 eV. The appearance of a new frontier orbital at energies close to the feature X has important consequences for the transport of positive charge carriers. Indeed, structural traps related to the former HOMO or any other traps associated with X may then become inactive since the charge transport will occur via states related to the original HOMO-1. This explains why picene thin films exhibit a higher hole drift mobility under ambient conditions as compared to the pristine material in vacuum.<sup>92c</sup> Note that apart from the improved charge transport in the bulk, also the barrier for hole injection from the metal to the film is reduced by almost 1 eV which leads to a higher performance by devices as well.<sup>98</sup> The inversion of frontier orbitals due to the interaction with molecular oxygen is a strong effect that deserves particular attention. In the case of free aromatic molecules, theoretical studies agree in predicting a weak interaction dominated by van der Waals forces and a preferential orientation of the O<sub>2</sub> molecular axis parallel to the molecular plane.<sup>99</sup> With regard to the aromatic sextet underlying aromatic hydrocarbon compounds, two possible orientations of O<sub>2</sub> parallel to the molecular plane may be called orthogonal ( $\perp$ ) and parallel ( $\parallel$ ) by referring to the fact that in  $\parallel$  the O<sub>2</sub> molecule lies along a line connecting two opposite carbon atoms while in  $\perp$  it is perpendicular to such a line. Guided by the oxygen orientation, the singly occupied  $\pi$  orbital of oxygen, with lobes perpendicular to the molecular plane, interacts only with one of the two highest occupied picene orbitals. The orbital interacting with oxygen is slightly mixed with the O<sub>2</sub>  $\pi$  orbital and pushed toward a lower energy while the other one is not affected.

In the case of benzene, theoretical studies agree in predicting an equilibrium distance of O<sub>2</sub> from the molecular plane of about 3.2 Å, a weak interaction dominated by van der Waals forces and a preferential orientation of the O<sub>2</sub> molecular axis parallel to the benzene plane.<sup>99</sup> Experimentally, it was not possible to isolate the complex between O<sub>2</sub> and anthracene in a supersonic free jet confirming the weakness of the interaction between the two components.<sup>100</sup> In the solid state, interaction may be stronger.

For benzene, as sketched in Figure 6.57, two possible orientations of O<sub>2</sub> parallel to the molecular plane may be called orthogonal ( $\perp$ ) and parallel ( $\parallel$ ). Guided by the oxygen orientation, the singly occupied  $\pi$  orbital of oxygen, interacts only with one of the two

degenerate HOMO orbitals. The benzene orbital interacting with oxygen is slightly mixed with the  $\pi$  orbital of  $O_2$  and pushed toward lower energy while the other one is not affected.

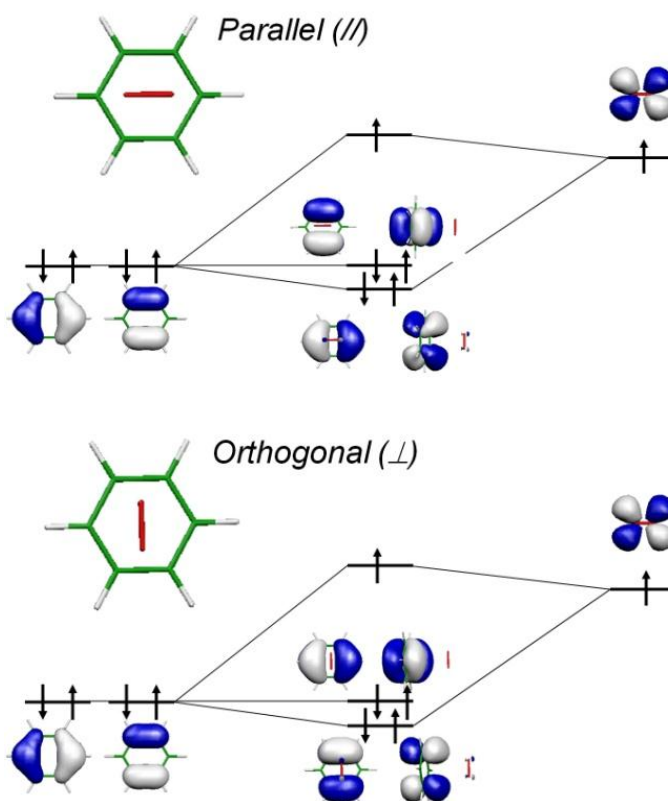


**Figure 6.57** Qualitative orbital interaction scheme for both orientations ( $//$  and  $\perp$ ) of  $O_2$  in benzene- $O_2$  complexes. To simplify the scheme, only one of the two singly occupied orbitals of  $O_2$  is shown. Figure adapted from <sup>87</sup>.

For complexes maximizing the interaction with the picene HOMO, oxygen molecules will be in the  $\perp$  position. For this case, as shown in Figure 6.58a, it is the HOMO which is lowered. If the interaction is sufficiently strong, or if the distance between oxygen and picene molecules is forced to be reduced (as compared to the gas phase), this eventually may lead to an inversion of the original HOMO and HOMO-1 orbitals of picene.

In Figure 6.58b and 6.58c are shown the results of calculations on complexes with either one or three oxygen molecules, respectively. All the computed complexes between oxygen molecules in their triplet state and picene are characterized by intermolecular distances between oxygen and picene on the order of 3.2 Å. The  $\perp$  complex with three  $O_2$  molecules on the same side is the most stable (by about 2.6 kcal mol<sup>-1</sup>). For these calculated structures, the energetic effect on the picene HOMO orbital is modest and does not lead to the

experimentally observed proximity of the HOMO and HOMO-1 orbitals. The behavior changes for three oxygen molecules sandwiched in  $\perp$  positions between two picene molecules, the optimized structure shown in Figure 6.58c. For appropriate distances between the two picene molecules close to those in the solid state, the interaction with oxygen leads to a strong displacement of the HOMO orbital. As the geometry optimization for the free complex reaches the minimum energy, the interaction becomes weaker and the energy displacement of the HOMO is reduced. Nevertheless, the calculated results are in qualitative agreement with the experimental observations with respect to the orbital inversion providing details of the exact mechanism behind the peculiar electronic changes following the incorporation of molecular oxygen within the *a-b* plane of the picene crystal.

In summary, highly crystalline picene films with a standing-up orientation were grown epitaxially on the Ag(110) surface. Upon exposure to oxygen gas, the O<sub>2</sub> molecules incorporate at interstitial sites within the *a-b* plane consisting of layers of standing molecules. Energy levels related to the highest three occupied molecular orbitals shift toward a lower binding energy which results in the inactivation of traps and the reduction of the charge injection barrier by about 1 eV. Additionally, strong interactions between the singly occupied oxygen  $\pi$  orbital and the highest occupied orbital of picene may lead to an inversion of the original HOMO and HOMO-1. The appearance of a new frontier orbital and the inactivation of traps explain the higher hole mobility of picene OFETs under an oxygen atmosphere as compared to those made of pristine material in vacuum. This result is significant for the understanding and control of environmental factors as needed for applications in organic devices.

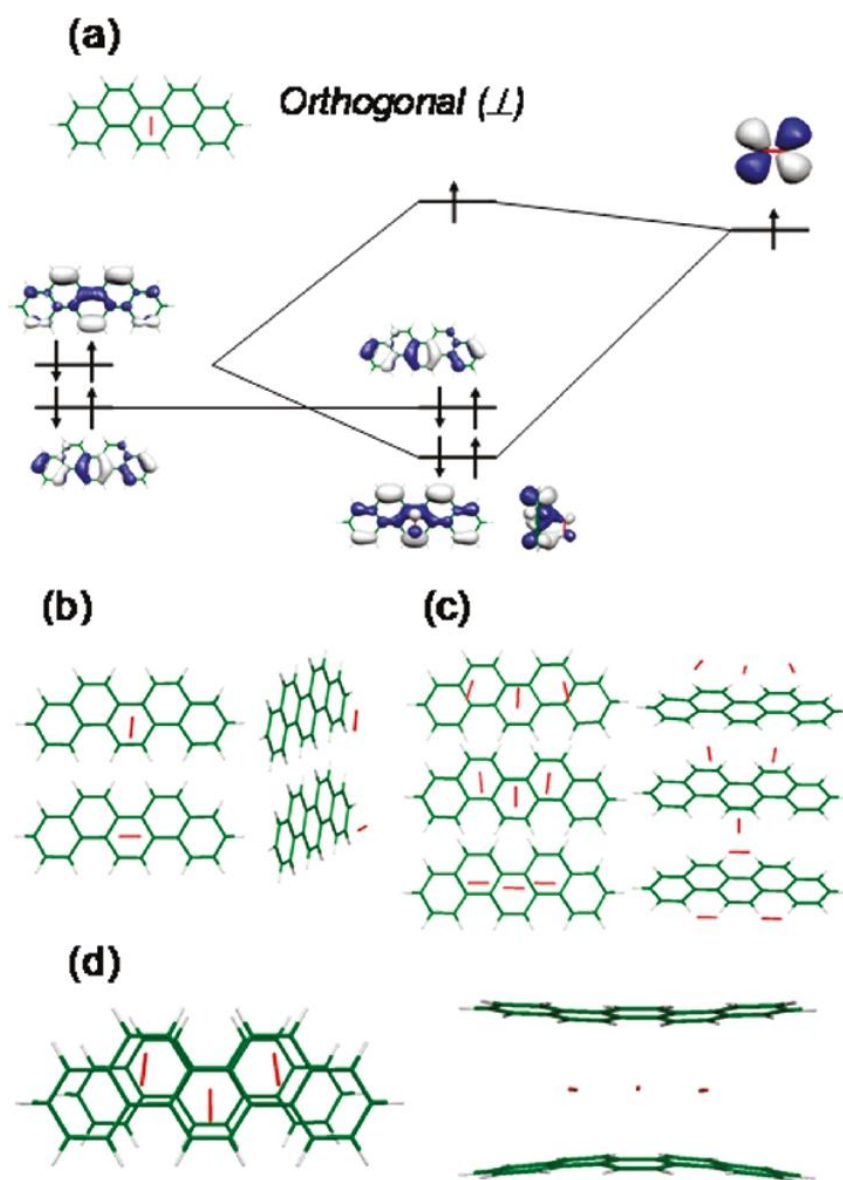


**Figure 6.58** (a) Qualitative orbital interaction scheme for a picene-O<sub>2</sub> complex maximizing the interaction between oxygen and the HOMO orbital of picene. To simplify the scheme only one of the two singly occupied orbitals of O<sub>2</sub> is shown. Quantum-chemically optimized structures determined for several complexes of oxygen with picene: (b) picene+O<sub>2</sub> ( $\parallel$  and  $\perp$  complexes); (c) picene + three O<sub>2</sub> ( $\parallel$  and  $\perp$  complexes, with the  $\perp$  complex featuring the three oxygens on the same side being the most stable structure); and (d) three  $\perp$  O<sub>2</sub> sandwiched between two picenes. Figure adapted from <sup>87</sup>.

## 6.6 RESISTIVE MEMORIES BASED ON BENZOQUINONES AND PENTACENE

The electrical bistability behavior of 2,3-dichloro-5,6-dicyano-1,4-benzoquinone along with two additional benzoquinone derivatives and pentacene is investigated in this Section by computing intra- and intermolecular charge transfer parameters and by comparing the efficiency of bulk charge transport and charge injection at the electrode/organic interface in the presence of neutral and charged molecular species.<sup>101</sup> The bulk charge transport is modeled assuming a charge hopping regime and by computing hopping rates and mobilities. Molecular dynamics simulations are carried out to estimate the effect of thermal disorder on charge transfer integrals. The efficiency of the interface transport is estimated by comparing the electron affinities of benzoquinone derivatives and the ionization potential of pentacene with the work function of commonly employed electrodes. It is shown that the observed memory effect can be rationalized in terms of an interplay of the two transport mechanisms by showing that the OFF state is dominated by interface limited phenomena and the ON state may be determined also by bulk transport limited phenomena.<sup>101</sup> While the contribution of collective effects cannot be ruled out for the macroscopic memory phenomenon, we show that, at a molecular level, sizable intramolecular reorganization energies are fundamental for the efficiency of the device, provided their magnitude does not hamper the charge transport across the device. It is suggested that control over molecular parameters might be exploited to design more efficient resistive molecular memories.<sup>101</sup>

### 6.6.1 Background

Organic electronics has been a field of intense research interest for the last couple of decades. Besides light emitting diodes, photovoltaic devices, and field effect transistors, recently, conjugated organic materials displaying memory effects have received considerable attention. Memory effects can be driven by several physical phenomena.<sup>102</sup> Here, we refer to organic based devices in which the memory effect is induced by an electrical stimulus.<sup>103</sup> In these devices, two stable conducting states (hereafter labeled OFF and ON states) exist at the same applied voltage, and one can switch from one state to the other by applying a suitable voltage. Once the device is in the ON state, for instance, it retains its high conductivity until a specific action (reset) is taken by a reverse voltage that erases the ON state and returns the device in its OFF state.<sup>104</sup> The rationalization of the change in conductivity is still under

debate: in some cases, there is evidence of extrinsic mechanisms (presence of metal filaments, metal nanoparticles) not due to the properties of the molecular material.<sup>103,105</sup> In others, however, there is strong evidence that the mechanism is intrinsic, driven by the nature of the organic material. In some cases, it has been explained in terms of structural rearrangements (conformational changes),<sup>106</sup> or electronic changes induced by redox reactions,<sup>107</sup> or both.<sup>108</sup> Further evidence supporting the intrinsic molecular mechanism has been provided by modifying the organic molecule with electron-withdrawing groups (EWG) of different strength and monitoring associated changes in ON/OFF ratios.<sup>107a,109a</sup> One such example is Rose Bengale for which the resistive memory efficiency (ON/OFF ratio) has been shown to increase with the strength of EWGs.<sup>109</sup> Other studies using devices built with different layers of the deposited organic material have also pointed to the intrinsic molecular character of the phenomenon, and at the same time have shown that collective effects are relevant. Indeed, in the case of a single molecular layer, the device was shown to display a threshold switching phenomenon, which becomes a resistive memory behavior<sup>109b</sup> only by increasing the number of layers of the organic species and hence sustaining more efficiently the charge density on the device.<sup>109b</sup> Among molecular systems, diphenyl bithiophene derivatives have been shown to display electrical bistability,<sup>110</sup> and in a recent computational study<sup>111</sup> it was shown that the different electrical behavior observed for *Z* and *L* isomers can be associated with a different efficiency of level alignment at the interface electrode/semiconductor. Diphenyl bithiophene derivatives are quite complex molecular systems, with flexible degrees of freedom that can mask or modulate the resulting electric properties. To date, the simplest organic molecule displaying electrical memory behavior<sup>104a,107a,112</sup> is 2,3-dichloro-5,6-dicyano-1,4-benzoquinone (**DDQ**) (Figure 6.59a). Evidence on the molecular nature of the phenomenon has been recently provided by the sensitivity of the ON state current to the work function of the electrodes employed to fabricate the device.<sup>104a</sup> Highly conductive organic semiconductors like pentacene have been employed to prepare organic bistable devices,<sup>104b</sup> but the memory effect was attributed to the inclusion of metal nanoparticles during electrode evaporation on top of the organic material.<sup>104b,113</sup> Indeed, there was no evidence of bistability by gently contacting pentacene on the electrode.<sup>104b</sup> These results call for a deeper understanding of the intramolecular and intermolecular parameters governing the intrinsic molecular memory effect, and this is the objective of this study. Among the processes governing the electrical (or resistive) memory function in molecular materials, the efficiency of carrier injection into the organic material at the electrode/organic interface and the charge transport within the organic semiconductor have to be considered as factors

limiting the current. In this contribution, we have considered these two processes and have performed a computational investigation to evaluate their relevance for the electrical bistability of **DDQ** and, to explore the effect of EWGs, two additional benzoquinone (BQ) derivatives, 2,3,5,6-tetrachloro-BQ (**TCQ**) (see Figure 6.59b) and 2,3,5,6-tetracyano-BQ (**TCN**) (see Figure 6.59c), each featuring only one type of the two EWGs of DDQ. For comparison, pentacene (**PNT**) is also considered (see Figure 6.59d).

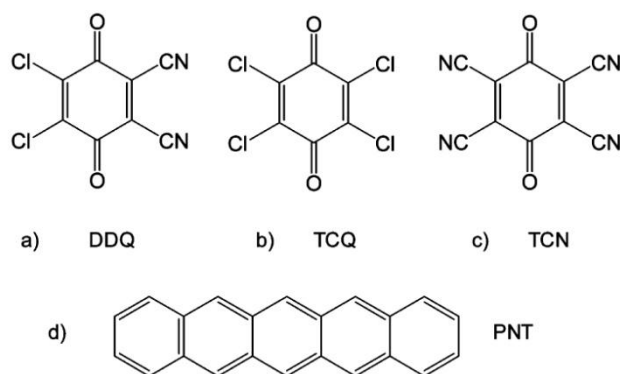


**Figure 6.59** Structural formula of the four molecules considered in this Section. Figure adapted from 101.

### 6.6.2 Computational details

Quantum chemical calculations, required to obtain equilibrium structures of the neutral species and molecular ions, were carried out at the B3LYP/6-31G\*\* level of theory (which corresponds to B3LYP/6-31G\* for BQ derivatives, because of the lack of light atoms). To estimate the ionization potential of pentacene, Koopmans' theorem was employed, while the vertical electron affinities (*VEA*) of **DDQ** and other BQ derivatives were directly estimated as energy differences between neutral and charged species both computed at the geometries optimized for the neutral ( $VEA_n$ ) or the charged ( $VEA_a$ ) species (see Section 4.2 and Figure 4.5). The nature of the critical points determined by quantum-chemical structure optimizations was assessed by evaluating vibrational frequencies at the optimized geometries. Vibrational frequencies were also employed to estimate the vibrational contributions to the intramolecular reorganization energies<sup>3,41</sup> (see Section 4.5.2).

The charge transfer integrals  $t_{ij}$  were computed with the INDO or CNDO Hamiltonians following the direct approach described in Section 4.5.1. The computed electronic couplings

$t_{ij}$  were transformed in an orthogonalized basis ( $V_{ij}$ ) as described in Section 4.5.1. All of the QM calculations were carried out with the Gaussian03 suite of programs.

Bulk charge transport was modeled by means of Pandora Suite (see Chapter 5) assuming a non-adiabatic hopping regime and defining charge transfer rate constants according to the Marcus-Levich-Jortner (MLJ) formalism. The dimers with distances lower than *ca.* 10 Å were considered. The different dimers selected for **PNT**, **DDQ**, **TCQ**, and **TCN** are shown in Figures 6.60, 6.61, 6.62, and 6.63, respectively. Herein, we have taken the outer-sphere reorganization energy  $\lambda_o$  as a parameter equal to 0.1 eV, in keeping with current studies.<sup>114</sup> Note that the absolute values of the rate constants can be strongly influenced by the chosen  $\lambda_o$  parameter. In addition, the validity of the non-adiabatic hopping model depends on the relative magnitude of the charge transfer integral  $V_{ij}$  and the reorganization parameter  $\lambda$ , with  $V_{ij}$  required to be considerably smaller than  $\lambda$ .<sup>41,115</sup> As it will be shown, we are within this limit only for the BQ derivatives, and for this reason the results on pentacene connected with the hopping assumption will not be presented in the following discussion. The temperature range is also relevant, because the hopping contribution dominates in the high temperature regime, which is the one considered in this work.

Charge mobilities were computed assuming a Brownian motion of the charge carrier.<sup>116</sup> The calculation of the macroscopic parameter was performed by considering the three-dimensional crystal structures of **PNT**,<sup>117a</sup> **DDQ**,<sup>117b</sup> **TCQ**,<sup>117c</sup> and **TCN**<sup>117d</sup> and by computing the diffusion coefficient  $D$  with the approximate relation<sup>116</sup> providing a qualitative estimate of  $D$ :

$$D = \frac{1}{2d} \sum_n (r_n)^2 k_n p_n \quad (6.4)$$

Herein,  $n$  runs over possible hopping events for a charge localized on a given molecular unit in the crystal,  $d$  is the dimensionality of the system,  $r_n$  is the distance between the starting molecule and the neighboring molecule in the hopping event, and finally  $p_n$  is the probability associated with the hopping, determined by the charge transfer rate constant  $k_n$  as:

$$p_n = \frac{k_n}{\sum_j k_j} \quad (6.5)$$

Hence, charge mobility  $\mu$  is readily obtained as:

$$\mu = \frac{eD}{k_B T} \quad (6.6)$$

To assess the importance of thermal motions in the modulation of the charge transfer integrals relevant for the charge transport, we run molecular dynamics simulations on a supercell ( $2 \times 2 \times 4$ ) of the crystal unit cell of **DDQ**.<sup>117b</sup> The dynamics of the system was studied with periodic boundary conditions employing the MM3 force field<sup>118</sup> and the Tinker code. It has been shown in recent studies that low frequency intermolecular vibrations can modulate the magnitude of the charge transfer integrals.<sup>119</sup> Thus, we froze all of the intramolecular degrees of freedom and kept the molecule in the cell rigid at its crystal structure while allowing intermolecular motions. We run MD simulations in the *NVT* ensemble at  $T=100$  and  $300$  K, using the Berendsen's algorithm<sup>120</sup> to simulate the presence of a thermal bath. The integration time step was set to  $1$  fs. The transfer integrals between LUMO orbitals were evaluated every  $60$  fs for the different dimers identified in the crystal of **DDQ** (Figure 6.61). Fourier transforms of the autocorrelation function of the transfer integrals were also evaluated to extract the phonon frequencies, leading to more effective coupling modulation.<sup>119,121</sup>

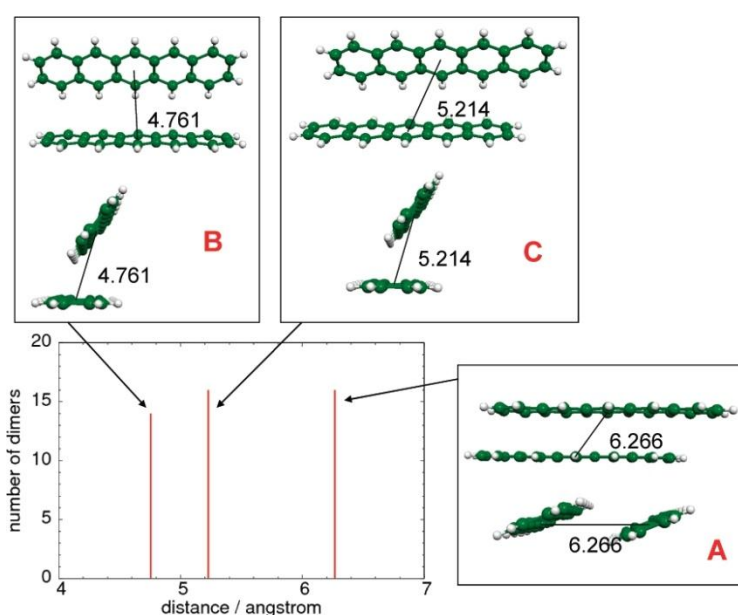


**Figure 6.60** Molecular dimers of **PNT** extracted from the crystal supercell ( $3 \times 2 \times 2$ ) and considered in the simulation of hopping events. Distances from centers of mass are in Å. Figure adapted from <sup>101</sup>.

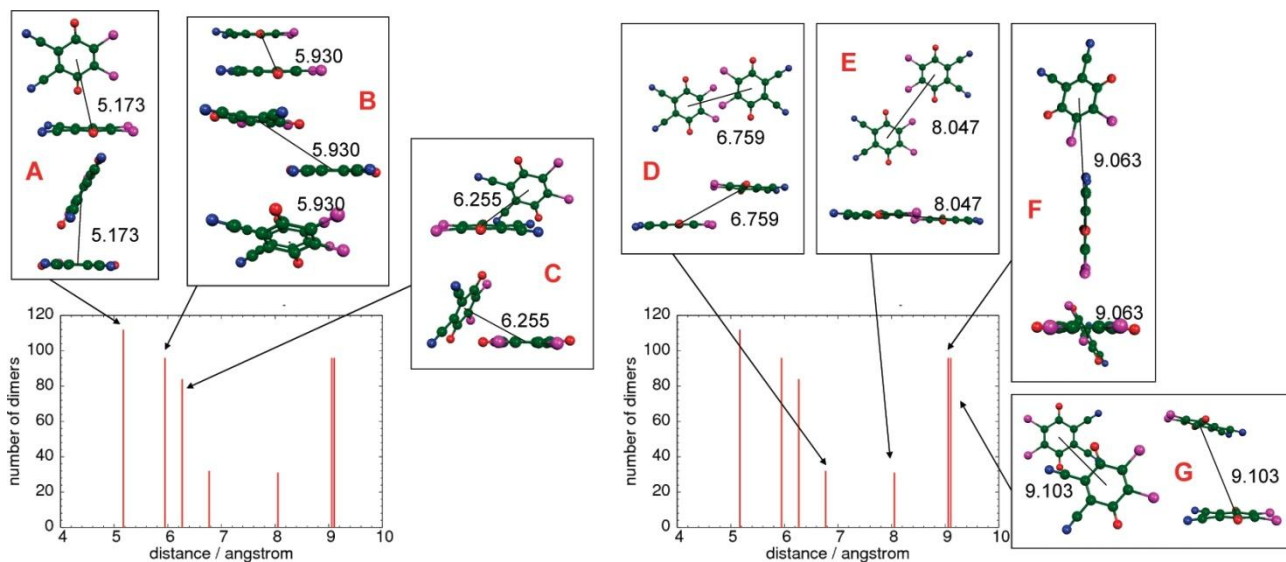


**Figure 6.61** Molecular dimers of DDQ extracted from the crystal supercell (2x2x4) and considered in the simulation of hopping events. Distances from centers of mass are in Å. Figure adapted from <sup>101</sup>.

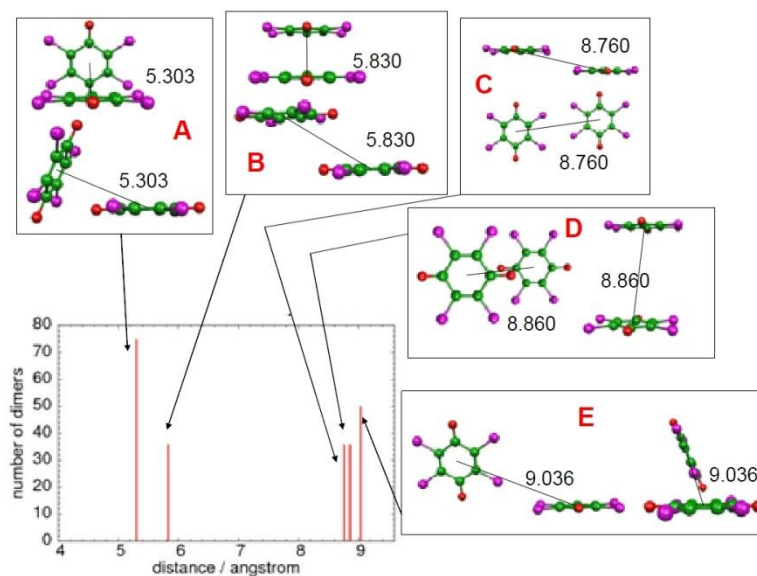


**Figure 6.62** Molecular dimers of TCQ extracted from the crystal supercell (3x3x3) and considered in the simulation of hopping events. Distances from centers of mass are in Å. Figure adapted from <sup>101</sup>.

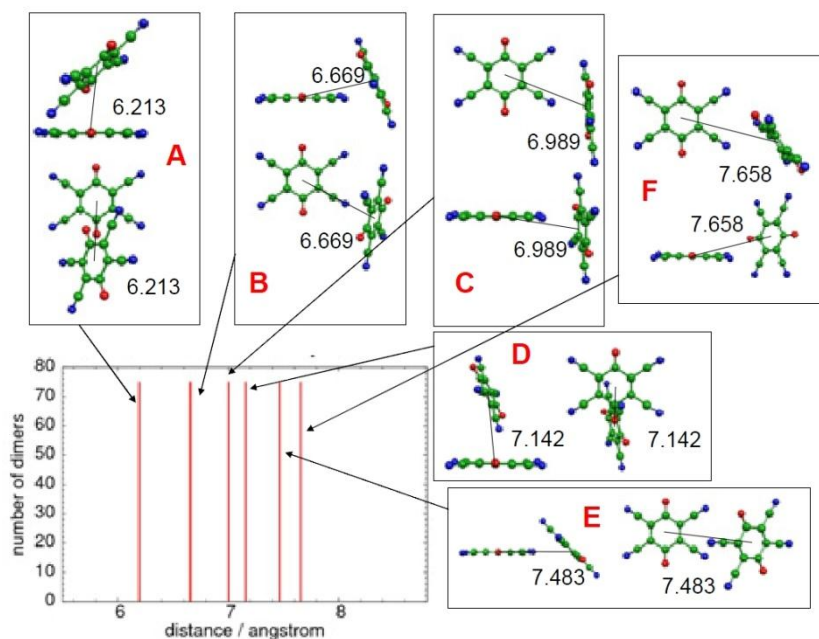


**Figure 6.63** Molecular dimers of TCN extracted from the crystal supercell (3x3x3) and considered in the simulation of hopping events. Distances from centers of mass are in Å. Figure adapted from <sup>101</sup>.

### 6.6.3 DDQ as a resistive molecular memory

The molecular memory device configuration is made by a layer of the organic molecular semiconductor material sandwiched between two electrodes, usually indium-tin-oxide (ITO) and Al.<sup>104a</sup> Experiments on DDQ indicate that the redox process occurring at the electrode/organic semiconductor interface is a reduction,<sup>112b</sup> due to its electron-withdrawing properties in turn connected with its *n*-type semiconductor character. We assumed a reduction process for the other BQ derivatives, also characterized by the presence of the same EWGs of DDQ, while the relevant redox process was assumed to be an oxidation for PNT, due to its *p*-type semiconductor character.

The bistability of the memory device can be discussed by considering the two major processes that can contribute to the current-voltage characteristic shape. These are (i) the charge injection at the electrode-semiconductor interface and (ii) the charge transport across the organic material. In the following, we discuss the efficiencies of both processes on the basis of computed intramolecular and intermolecular parameters.

To discuss the injection across the electrode/organic material interface, we assume the validity of the Schottky rule<sup>122</sup> and compare the work function of the electrode with the relevant transport levels of the organic materials. Experimentally, those levels are obtained from photoelectron or inverse photoelectron spectra, and the electronic affinity (*EA*) and ionization potential (*IP*) of the solid material are conventionally associated with the one-electron levels measured from photoelectron experiments.<sup>123</sup>

Accordingly, we computed the  $VEA_n$  of BQ derivatives in the gas phase with B3LYP/6-31G\* calculations on neutral and charged species and compared them to the work function of common electrodes. The energy offset between the electrode/organic material levels determines the injection barrier. Experimental *EAs* of the solid phases of BQ derivatives are not known. However, it is known that when a molecule is part of a condensed phase of identical molecules, additional forces of interaction come into play, markedly altering the energetic of ionization and electron attachment. A major factor in this alteration is the stabilizing effect of the polarization. The polarization energy of stabilization in the organic crystal is qualitatively comparable to the solvation energy of ions in solution,<sup>124</sup> and it has been recently investigated by QM/MM calculations.<sup>114b</sup> Accordingly, we corrected the computed gas-phase values by assuming polarization effects of the order of 0.5 eV. A schematic representation of the electronic levels at the electrode/semiconductor interface is shown in Figure 6.64 for the BQs and in Figure 6.65 for **PNT**. Besides the computed gas-phase values of the  $VEA_n$  (dashed lines), comparing well with the results of previous calculations<sup>125</sup> and with the experimental data,<sup>126</sup> in Figure 6.64 we also indicate with solid lines the more realistic levels including the effect of polarization. For **PNT**, the *IP* was estimated directly from the B3LYP/6-31G\*\* HOMO energy because this is predicted, for a favorable error cancelation, quite close to the experimental *IP* of *ca.* 5.0 eV in the condensed phase.<sup>124</sup> From the computed levels, it is apparent that electron injection either from Al or from ITO will be an activated process for all of the systems studied except for **TCN** whose  $VEA_n$  level suggests a barrierless injection. In the figure, the red arrows indicate the electron injection assumed to occur from the Al electrode. The increased level alignment moving from **TCQ** to **TCN** is a result of the increased strength of EWGs.

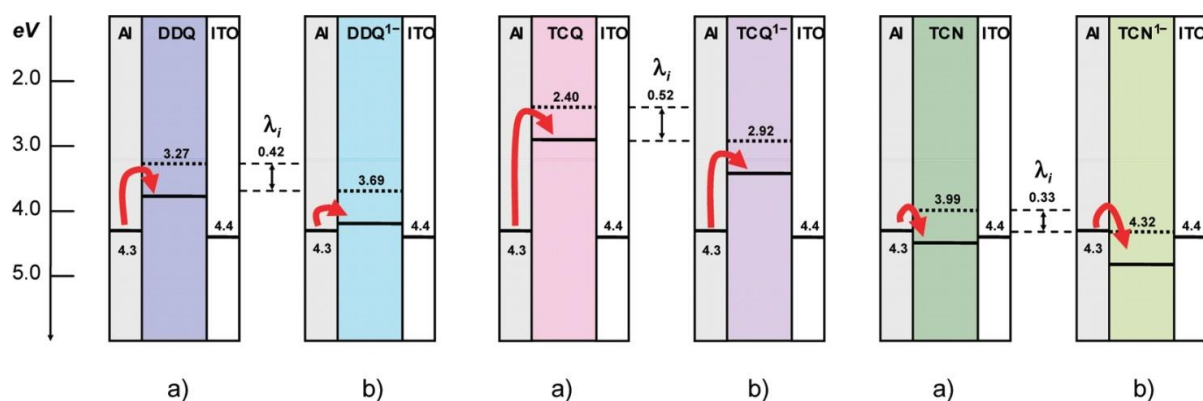


**Figure 6.64** B3LYP/6-31G\* computed ( $eV$ , dashed lines)  $VEA_n$  and (**b**) negatively charged ( $VEA_a$ ) species along with their difference corresponding to  $\lambda_i$ . DDQ (left), TCQ (center), and TCN (right). Comparison with the work function of ITO and Al electrodes ( $eV$ ).<sup>110a</sup> Solid lines below dashed lines represent schematically the stabilizing effect of polarization energy in the organic crystal.<sup>124</sup> Red arrows show the electron injection process from the electrode. Figure adapted from <sup>101</sup>.

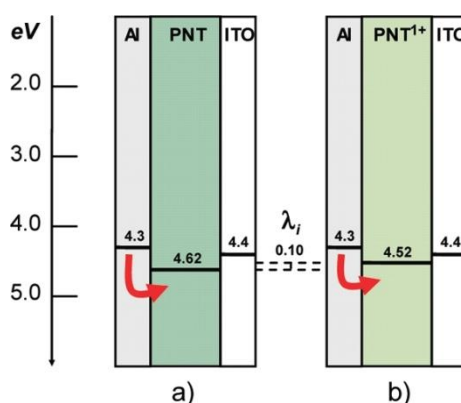


**Figure 6.65** B3LYP/6-31G\*\* HOMO energies ( $eV$ ) of PNT at the equilibrium structure of (**a**) neutral and (**b**) positively charged species along with their difference corresponding to  $\lambda_i$ . Comparison with the work function of ITO and Al electrodes ( $eV$ ).<sup>110a</sup> Red arrows show schematically the hole injection process from the electrode. Figure adapted from <sup>101</sup>.

As the voltage creates the reduced state, modified energy levels of the molecules have to be considered to discuss the charge injection at the interface. In some cases, these modified levels become better aligned with the electrode work functions. To estimate the modified alignment, we determined the  $VEA_a$  at the equilibrium structures of the charged species. The computed equilibrium structures of the four molecules in their neutral and charged

configurations are collected in Figures 6.66-69. For BQs, the major geometry change upon electron doping is the transition from a quinoid to a more benzenoid structure. For **PNT**, the geometry change induces elongation of the CC bonds mainly along the short molecular axis. The structural changes associated with negative charging of **DDQ** and other BQ derivatives are reflected in an increase of the  $VEA_a$  as compared to the  $VEA_n$  (see Figure 4.5).

A graphical representation of the relevant electronic levels associated with charging is given in Figure 6.64 for BQs, and in Figure 6.65 for **PNT**. It is seen that  $VEA_a$  increases in all cases, as compared to the  $VEA_n$ , the increase being inversely related with the strength of the EWGs. Accordingly, **TCQ** shows the larger increase and **TCN** shows the smaller. It should be noted that the  $VEA$  change (the reduction of the injection barrier for electrons) is equivalent to the reorganization energy  $\lambda_i$  associated with the charging process (see Figure 4.5). The computed  $EA$  changes suggest an improved level alignment at the heterojunction in the case of **DDQ** and **TCQ**. In contrast, for **TCN**, the computed  $VEAs$  suggest that alignment with the work function of the Al electrode should be already very efficient for the pristine BQ derivative. Thus, while for **DDQ** a remarkably increased charge injection at the electrode/organic interface is expected, such effect is not expected to be significant for **TCN**. Finally, in the case of **TCQ**, one expects the switch to occur at higher applied voltages. Furthermore, the sizable  $VEA_a$  increase upon charging (large  $\lambda_i$ ) that would play a positive role in determining the efficiency of the memory device is likely to be insufficient to sustain efficient charge injection (at low applied voltages), due to the large computed injection barrier. Estimates taking into account interfacial dipoles formation will be required to confirm this conjecture.<sup>127</sup> In summary, the appropriate  $VEA_n$  level alignment with the work function of the electrode, combined with a considerable  $VEA_a$  increase (a sizable  $\lambda_i$ ), seems to be better realized with **DDQ**, the only BQ derivative that has been shown to display the resistive memory effect<sup>104a,107a</sup>. The observed electrode-dependent ON (and OFF) state currents displayed by **DDQ**<sup>104a</sup> can be easily accounted for by the present interpretative scheme. According to the calculations, when charged molecules are created at the interface (for an applied voltage  $V$  above a threshold value), a sudden increase of current is expected as a result of the concomitant barrier reduction at the interface, following the change from  $VEA_n$  to  $VEA_a$ .

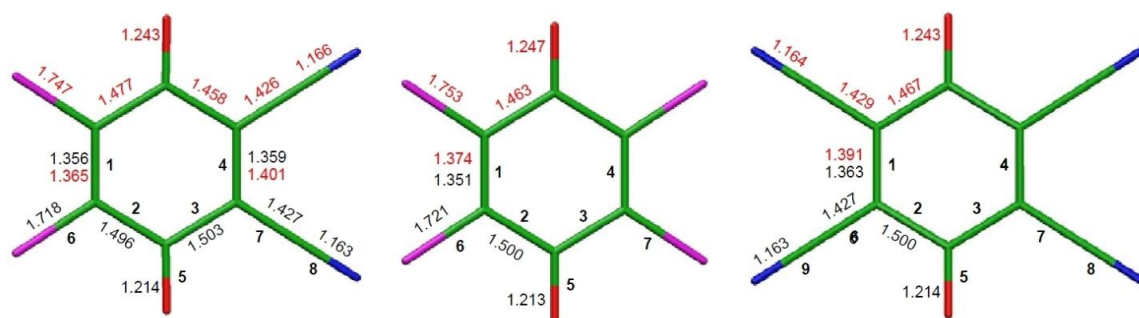


**Figure 6.66** Bond numbering (bold) and B3LYP/6-31G\* computed equilibrium bond lengths of DDQ (left), TCQ (center), and TCN (right) in the neutral (black) and negatively charged (red) state. Figure adapted from <sup>101</sup>.

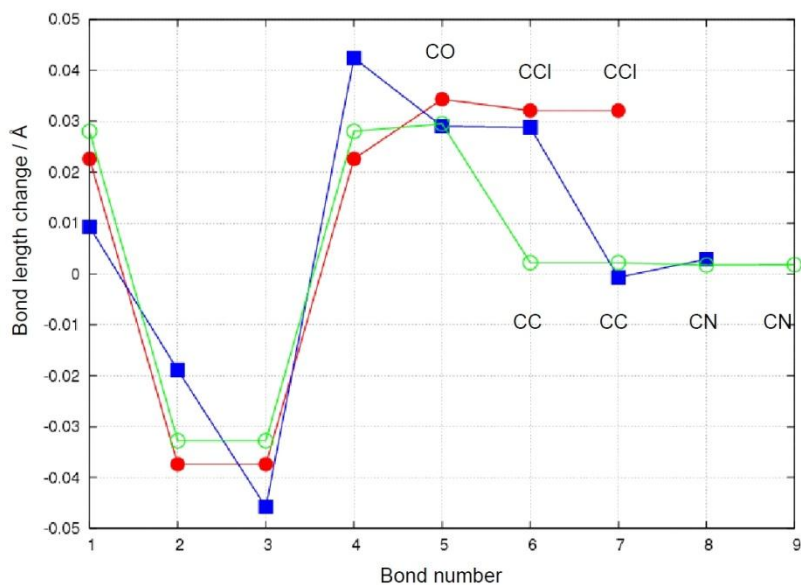


**Figure 6.67** Comparison between bond length changes in DDQ (blue), TCN (green) and TCQ (red) upon electron reduction (bond lengths of the charged molecule – bond lengths of the neutral molecule). Bond numbering is defined in Figure 6.66. Figure adapted from <sup>101</sup>.

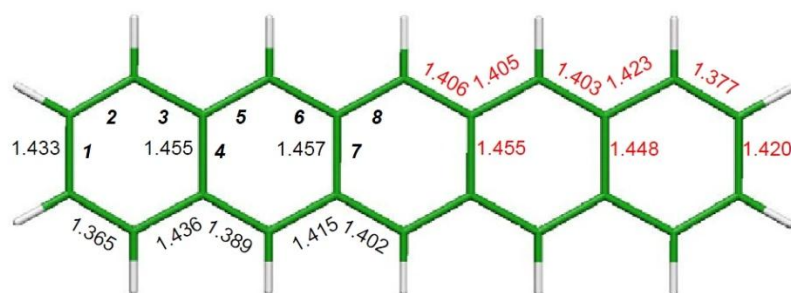


**Figure 6.68** CC bond numbering (bold) and B3LYP/6-31G\*\* computed equilibrium CC bond lengths of PNT in its neutral (black) and positively charged (red) state. Figure adapted from <sup>101</sup>.

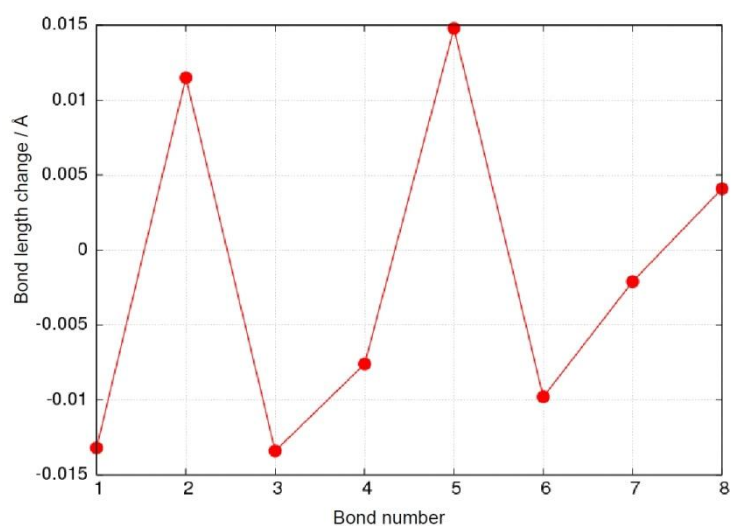


**Figure 6.69** Comparison between bond length changes in PNT upon electron oxidation (bond lengths of the charged molecule – bond lengths of the neutral molecule). Bond numbering is defined in Figure 6.68. Figure adapted from <sup>101</sup>.

From a mechanistic point of view, the charged species at the interface will transfer its electron to a nearby neutral molecule, farther away from the interface, through a hopping event that drives the electron current transport across the organic material. At the same time, before intramolecular relaxation occurs in the neutralized molecule at the interface, ultrafast electron transfer from the electrode is facilitated by the increased electron affinity of the molecule. Such ultrafast event would be facilitated by the formation of an electrode-organic molecule complex.<sup>127</sup>

Applying the same considerations as above to **PNT**, we can conclude that due to the minor HOMO level rearrangement occurring upon oxidation (Figure 6.65), a negligible change in hole injection at the electrode is expected. This conclusion, based on the intramolecular properties of **PNT**, is in agreement with the observed negligible memory effect displayed by **PNT** in the absence of other extrinsic mechanisms such as the inclusion of metal nanoparticles.<sup>104b</sup> To summarize, the examples considered above underscore the possible relevant role of the intramolecular reorganization parameter  $\lambda_i$  of the organic material in governing the efficiency of the resistive memory device. It should be noted that this conclusion agrees with the better memory performance of the Z form of diphenyl bithiophene derivatives.<sup>111</sup> A schematic macroscopic representation of the memory phenomenon taking into account the role of the intramolecular parameters is shown in Figure 6.70.

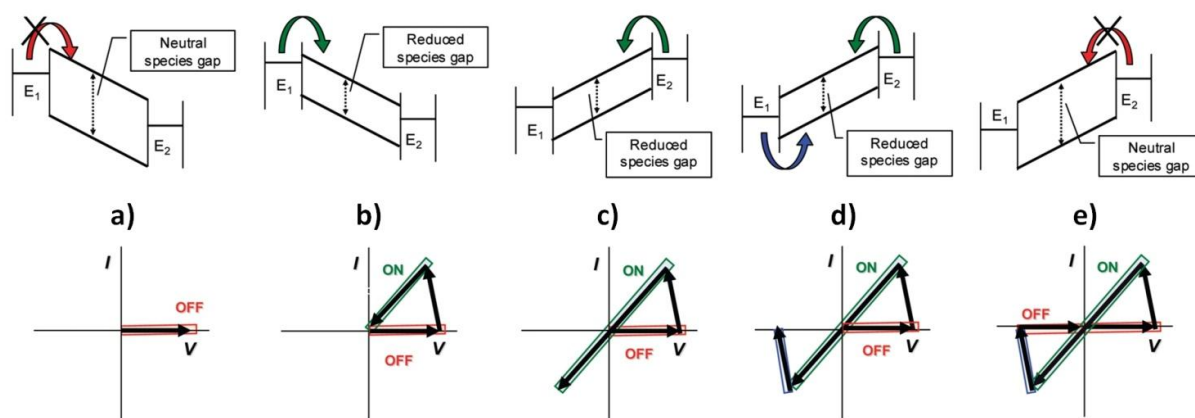


**Figure 6.70** Schematic macroscopic representation of the electric bistability of a memory device based on an *n*-type molecular semiconductor wafered between electrodes *E1* and *E2*. Device levels (top); schematic current-voltage (*I-V*) curve as a function of the voltage scan (bottom). The most relevant processes at the interface are indicated. (a) Initially the device is in its OFF state, and the transport gap is that of the pristine semiconductor. (b) As the applied voltage reaches the threshold value, the improved work function/*VEA* alignment favors electron injection. When charged species are at the interface, energy levels associated with the charged species have to be considered, further improving the electron injection. The system switches to the ON state. (c) As long as charge carriers are sustained in the device, the system stays in the ON state also for reverse applied voltages. (d) When the second (reverse) threshold voltage is reached, hole injection becomes competitive and neutralization of the charged species becomes significant, leading to a switch of the system back to the OFF state. (e) The transport gap reverts to that of the neutral species, and the system retains the OFF state. Figure adapted from <sup>101</sup>.

Besides the process at the electrode/organic interface, controlled by intramolecular parameters possibly governing the efficiency of the transition from the OFF to the ON state of the memory device, one has to consider also the charge transport across the organic material, whose efficiency will contribute to sustain charge density in the organic material, and hence the ON state. In this context, it should be noted that the sizable  $\lambda_i$  required for an efficient ON/OFF ratio plays against the efficiency of the charge transport as indicated by the MLJ rate constant formulation (see Eq.(4.19)). To further clarify this point, we modeled the charge transport process assuming a non-adiabatic hopping mechanism and computed the required parameters entering the MLJ formulation. The intramolecular reorganization energies  $\lambda_i$  are collected in Table 6.12, while the effective parameters employed in the calculation of rate constants are summarized in Table 6.13. The  $\lambda_i$  were evaluated with the AP method and by computing the HR parameters determining the vibrational FC factors. A detailed analysis of the vibrational contributions to the reorganization energies is provided in Figures 6.71-78. As discussed in the previous section, BQ derivatives show considerably larger  $\lambda_i$  as compared to **PNT**. These, on the other hand, agree with previous literature data<sup>128</sup>, for **PNT**. Because of the different FC contributions of **PNT** and BQs, the  $\omega_{eff}$  entering Eq. (4.19) is considerably different: 1317  $cm^{-1}$  for **PNT**, 780  $cm^{-1}$  (**DDQ**), 811  $cm^{-1}$  (**TCQ**), and 681  $cm^{-1}$  (**TCN**) for BQ derivatives (Table 6.13). The charge transport integrals  $V_{ij}$ , required to estimate the rate constants, are collected in Table 6.14, while the corresponding LUMO and HOMO orbitals are collected in Figure 6.79. The computed rate constants of BQs (a selection of the largest is collected in Table 6.15) were employed to estimate charge mobilities according to Eq. (6.4-6) and assuming a crystalline state for the layer of the organic material in the device. The temperature dependence of the computed mobilities is shown in Figure 6.80. It is seen that the three BQ derivatives show considerably smaller mobilities as compared to **PNT**, whose computed value at 300 K, using the same approach, is *ca.* 1.3  $cm^2 V^{-1} s^{-1}$ . The reduced mobilities can be attributed to the reduced electronic factors (the largest charge transfer integral of BQs is about one-half of the largest transfer integral of **PNT**) and the concomitant increase of the intramolecular reorganization energies whose effect is to depress the efficiency of the charge transfer event.

**Table 6.12** Intramolecular reorganization energies ( $eV$ ) computed for **DDQ**, **TCQ**, **TCN** (B3LYP/6-31G\*), and **PNT** (B3LYP/6-31G\*\*).<sup>101</sup>

	$\lambda_i^{AP,n}$	$\lambda_i^{AP,c}$	$\lambda_i^{HR,n}$	$\lambda_i^{HR,c}$	$\lambda_i^{AP}$	$\lambda_i^{HR}$
<b>PNT</b>	0.05	0.05	0.05	0.05	0.10	0.10
<b>DDQ</b>	0.21	0.21	0.21	0.21	0.42	0.42
<b>TCQ</b>	0.26	0.26	0.26	0.26	0.52	0.52
<b>TCN</b>	0.17	0.16	0.17	0.17	0.33	0.34

**Table 6.13** Effective frequency  $\omega_{eff}$  and associated HR factor  $S_{eff}$  employed in the evaluation of charge transfer rate constants of **DDQ**, **TCQ**, **TCN** (B3LYP/6-31G\*), and **PNT** (B3LYP/6-31G\*\*).<sup>101</sup>

	<b>PNT</b>	<b>DDQ</b>	<b>TCQ</b>	<b>TCN</b>
$\omega_{eff}$ ( $cm^{-1}$ )	1317	780	811	681
$S_{eff}$	0.57	4.42	5.22	3.98

**Table 6.14** Electronic coupling integrals  $V_{ij}$  ( $cm^{-1}$ ) of **DDQ**, **TCQ**, **TCN**, and **PNT**, computed for the most relevant dimers extracted from the crystal structures.<sup>101</sup>

dimer	<b>DDQ</b>		<b>TCQ</b>		<b>TCN</b>		<b>PNT</b>	
	distance ( $\text{\AA}$ )	$V_{ij}^{LUMO^a}$	distance ( $\text{\AA}$ )	$V_{ij}^{LUMO^a}$	distance ( $\text{\AA}$ )	$V_{ij}^{LUMO^a}$	distance ( $\text{\AA}$ )	$V_{ij}^{HOMO^b}$
A	5.173	-436	5.303	-494	6.213	-190	4.761	-807
B	5.930	387	5.830	417	6.668	23	5.214	557
C	6.255	-161	8.760	35	6.989	35	6.266	395
D	6.759	24	8.860	0	7.142	171		
E	8.047	-40	9.036	-48	7.483	-29		
F	9.063	-24			7.657	40		
G	9.103	0						

<sup>a</sup> Charge transfer integrals were evaluated at CNDO level. The interaction was determined between the LUMO orbitals of the two molecules belonging to the dimer. <sup>b</sup> Charge transfer integrals evaluated at INDO level. The interaction was determined between the HOMO orbitals of the two molecules belonging to the dimer.

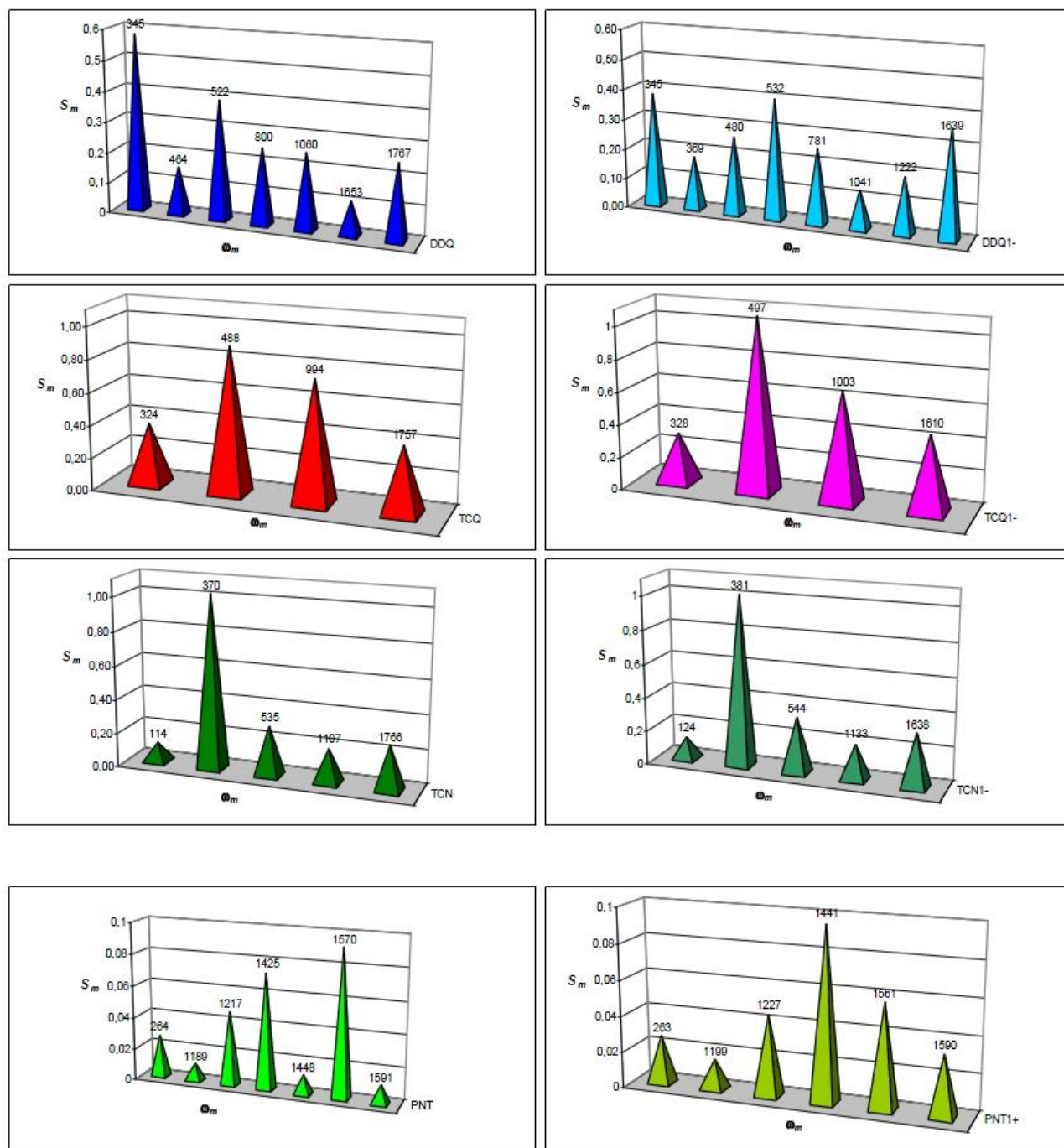


**Figure 6.71** Pictorial representation of the largest FC (HR) parameters associated with vibrational frequencies of the neutral and charged species of (from the top) DDQ, TCQ, TCN, and PNT. From B3LYP/6-31G\*\* calculations. Figure adapted from <sup>101</sup>.

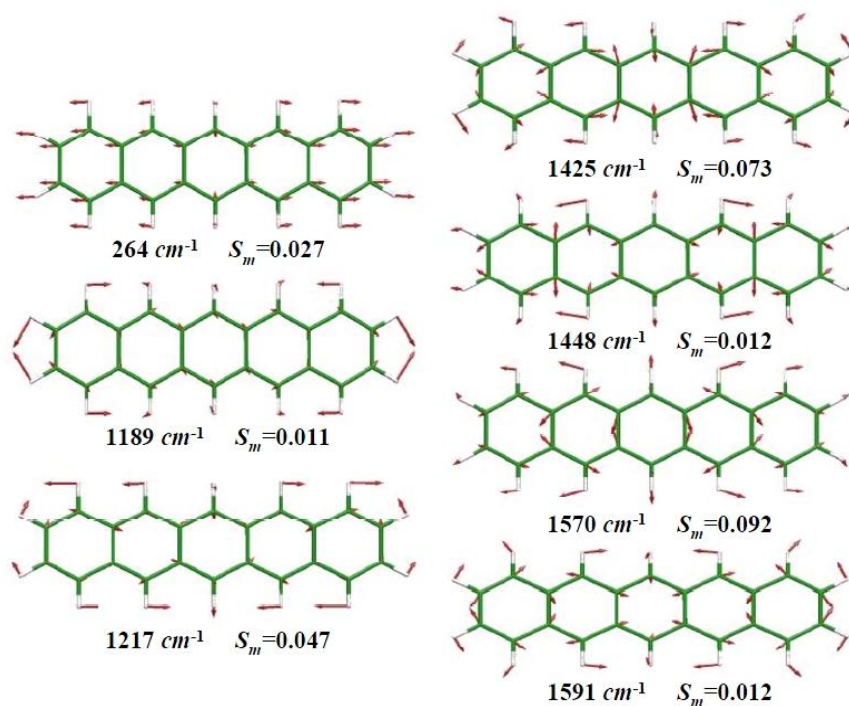


**Figure 6.72** B3LYP/6-31G\*\* normal modes and vibrational frequencies associated with the largest HR parameters of PNT. Figure adapted from <sup>101</sup>.

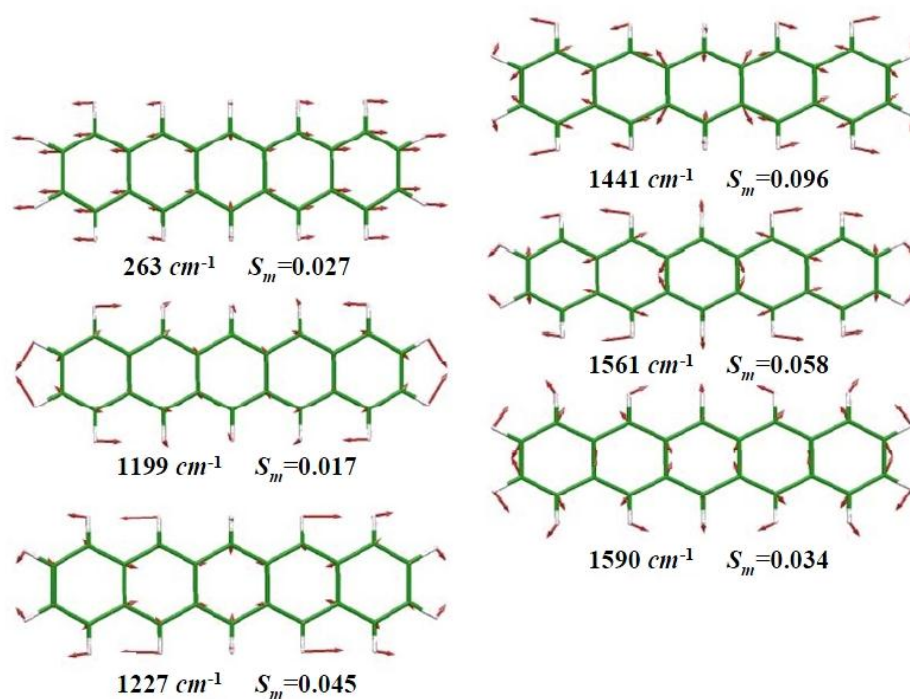


**Figure 6.73** UB3LYP/6-31G\*\* normal modes and vibrational frequencies associated with the largest HR parameters of PNT<sup>1+</sup>. Figure adapted from <sup>101</sup>.

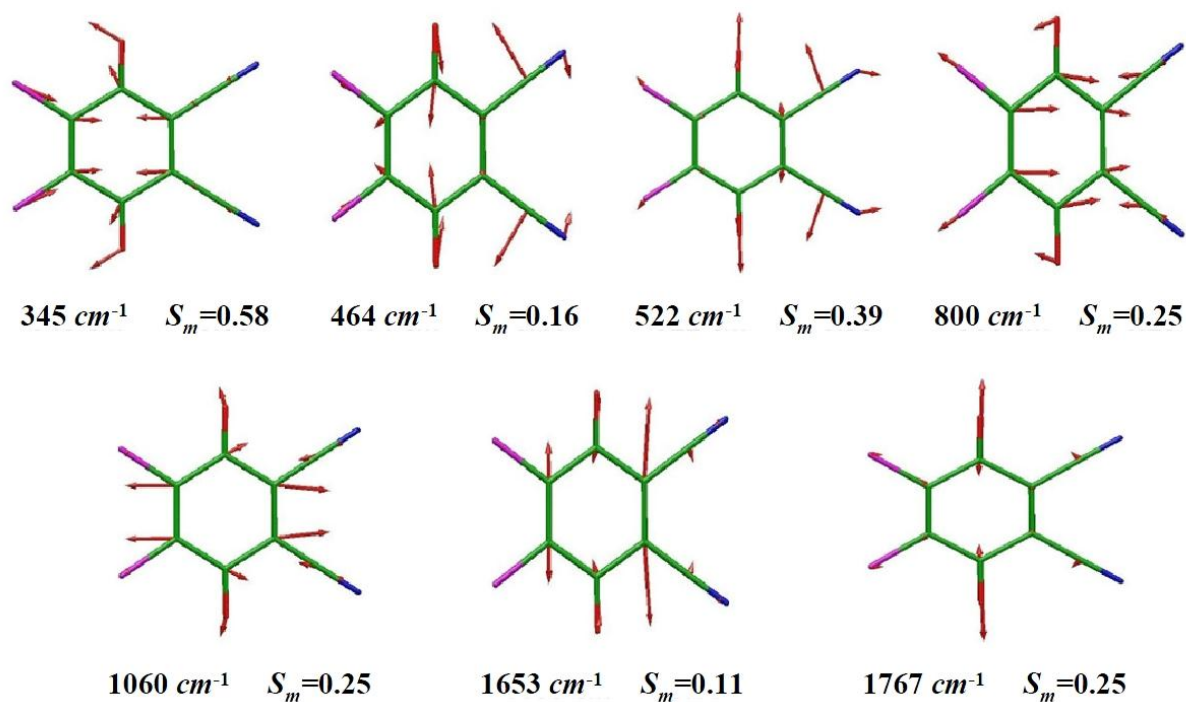


**Figure 6.74** B3LYP/6-31G\* normal modes and vibrational frequencies associated with the largest HR parameters of DDQ. Figure adapted from <sup>101</sup>.

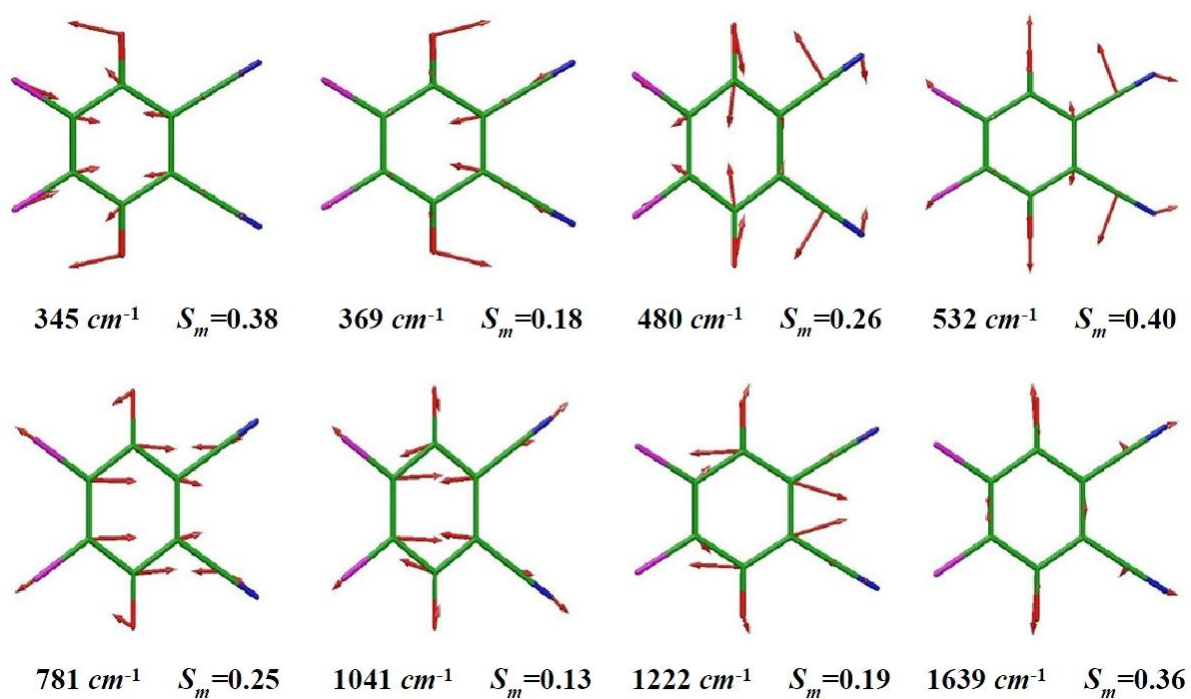


**Figure 6.75** UB3LYP/6-31G\* normal modes and vibrational frequencies associated with the largest HR parameters of DDQ<sup>1</sup>. Figure adapted from <sup>101</sup>.

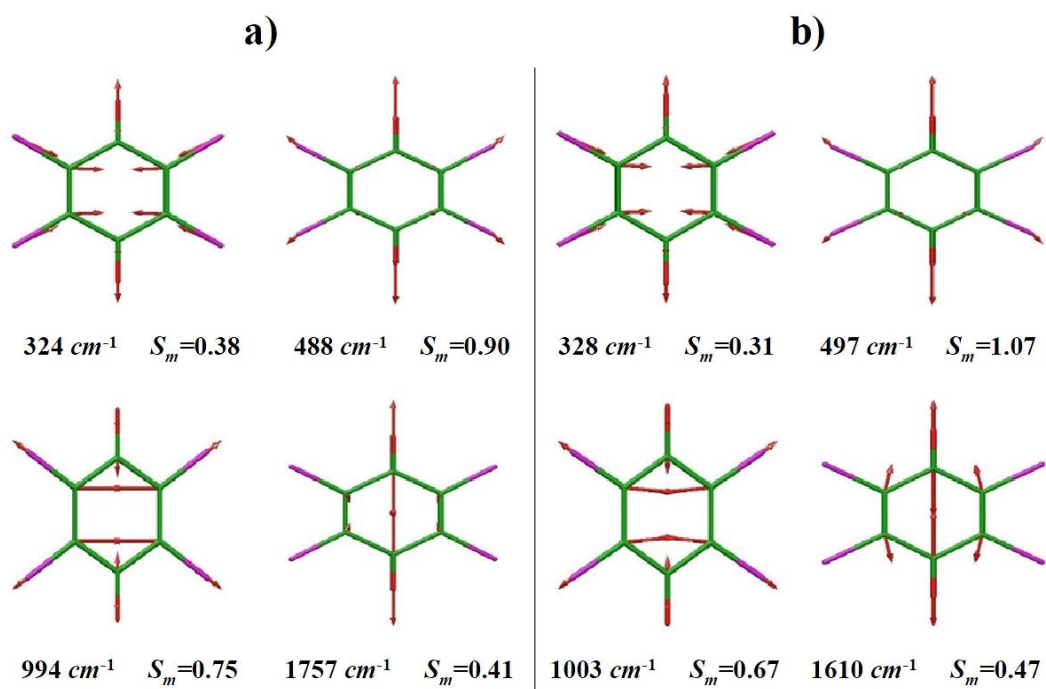


**Figure 6.76** (U)B3LYP/6-31G\* normal modes and vibrational frequencies associated with the largest HR parameters of TCQ (a) and TCQ<sup>-</sup> (b). Figure adapted from <sup>101</sup>.

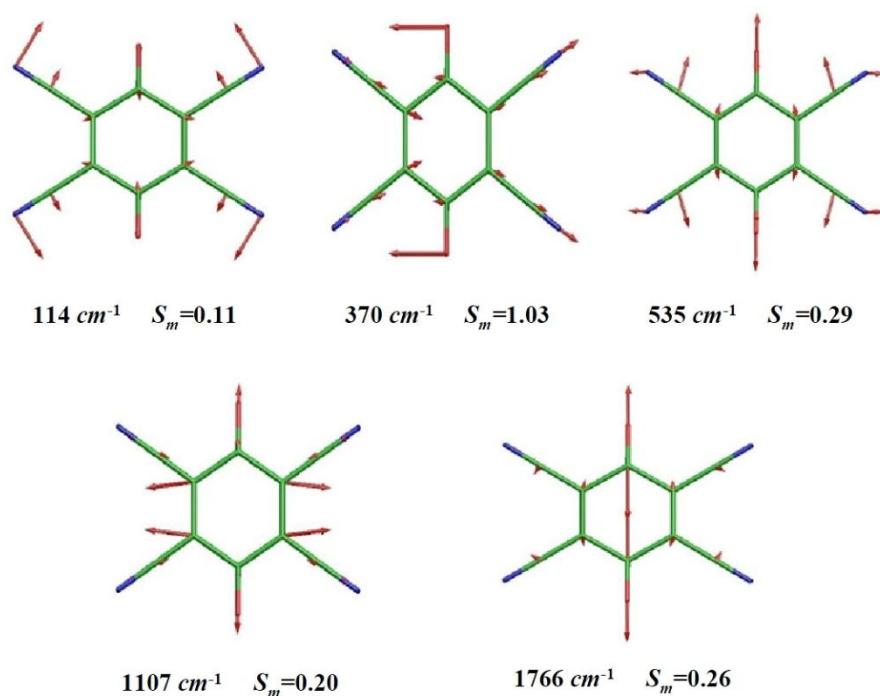


**Figure 6.77** B3LYP/6-31G\* normal modes and vibrational frequencies associated with the largest HR parameters of TCN. Figure adapted from <sup>101</sup>.

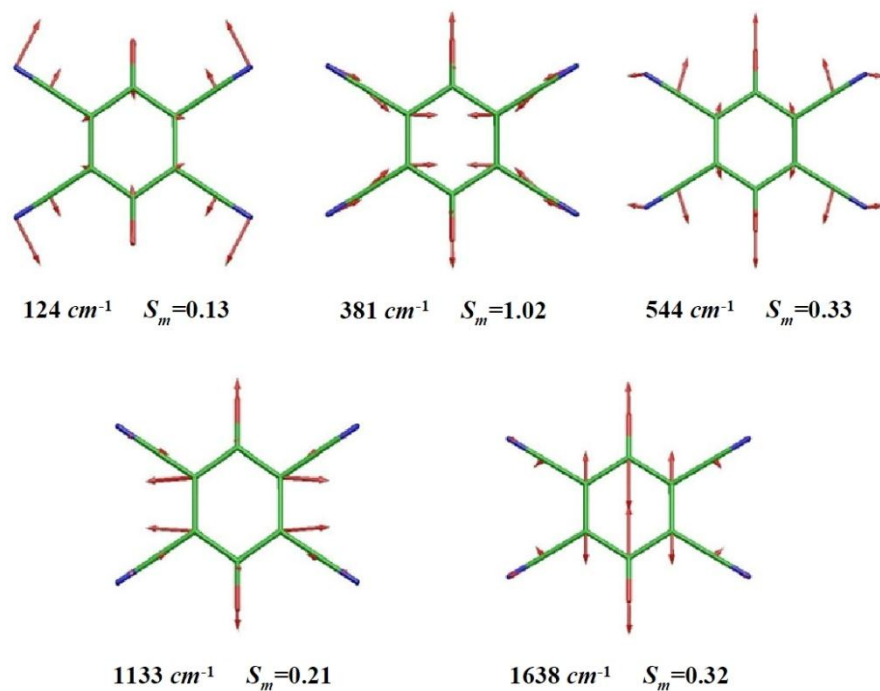


**Figure 6.78** UB3LYP/6-31G\* normal modes and vibrational frequencies associated with the largest HR parameters of TCN<sup>1-</sup>. Figure adapted from <sup>101</sup>.

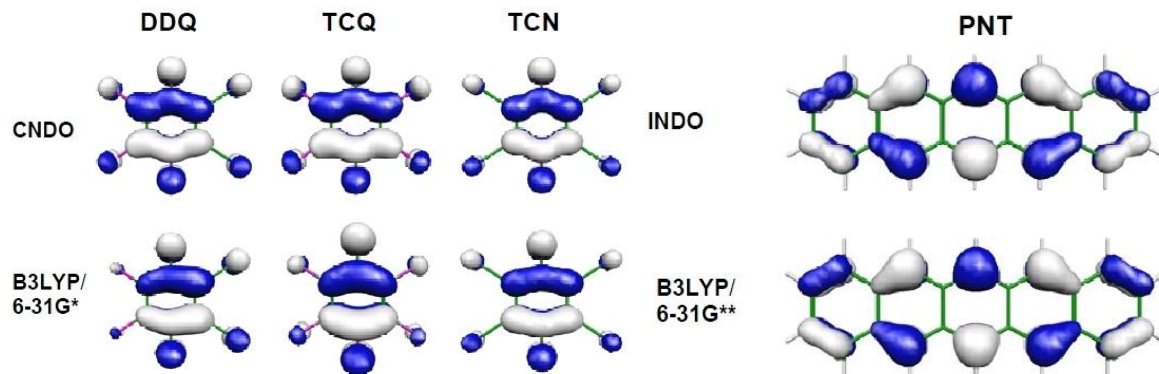


**Figure 6.79** (left) The LUMOs of BQs involved in the calculations of  $V_{ij}$ , computed at semiempirical and B3LYP levels of theory. (right) The HOMO of PNT involved in the calculations of  $V_{ij}$ , computed at semiempirical and B3LYP levels of theory. Figure adapted from <sup>101</sup>.

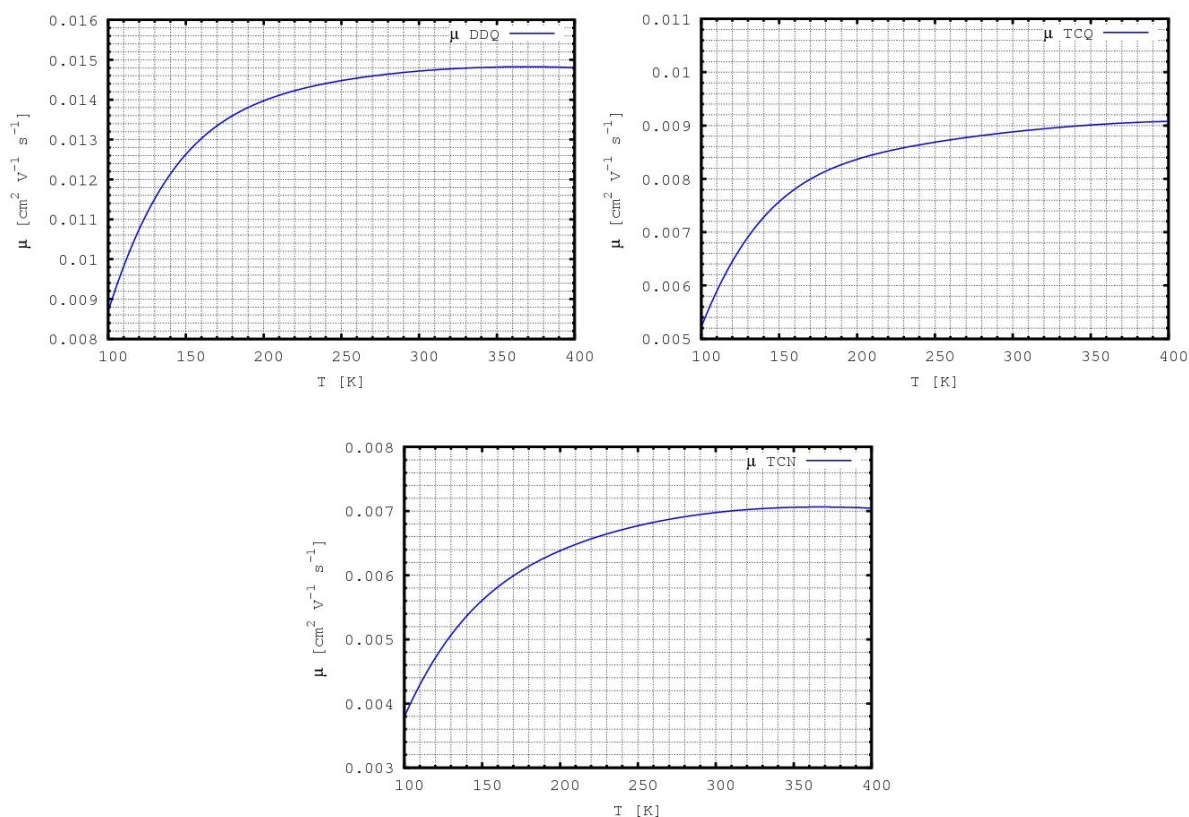


**Figure 6.80** Computed charge mobilities of DDQ (top left), TCQ (top right), and TCN (bottom) as a function of the temperature. Figure adapted from <sup>101</sup>.

The mobilities were computed assuming the values of the  $V_{ij}$  computed at the crystal geometry. However, it has been shown that the effect of thermally induced disorder on the  $V_{ij}$  can be substantial.<sup>119,121b</sup> Accordingly, we run MD simulations at 100 and 300 K and evaluated the charge transfer integrals for a series of sampled configurations. The thermally induced dynamic effects can be appreciated by inspecting Figure 6.81 showing broad Gaussian distributions of the computed  $V_{ij}$  values (see also Figure 6.82), as it was shown in previous studies on oligoacenes.<sup>119,121</sup> It is seen that  $V_{ij}$  values are subject to oscillations of the same magnitude of the integrals and that the width of the Gaussian distribution increases with temperature. It can be concluded that the thermal disorder effects on  $V_{ij}$  are a very general property encompassing high mobility and less efficient organic semiconductors. More detailed information on the frequencies of the intermolecular modes modulating the charge transport integrals can be extracted from the Fourier transforms of the autocorrelation functions of the  $V_{ij}$  shown in Figure 6.81b. Similarly to previous studies on the more efficient oligoacene semiconductors,<sup>119,121</sup> we find that low frequency intermolecular modes in the

range 20-80  $cm^{-1}$  modulate the integrals. Interestingly, computed rate constants (Table 6.15) are of the order of  $1 \div 10 \cdot 10^{11} s^{-1}$ , indicating that nuclear motions, associated with frequencies in the range of few tens of  $cm^{-1}$  as those modulating the  $V_{ij}$ , can effectively contribute to alter the charge transfer rate constants and the computed mobilities.

**Table 6.15** Selection of the largest computed MLJ charge transfer rate constants  $k_{eT}$  (at 300 K) of DDQ, TCQ, and TCN.<sup>101</sup>

dimer	DDQ		TCQ		TCN	
	distance (Å)	$k_{eT}$ ( $s^{-1}$ )	distance (Å)	$k_{eT}$ ( $s^{-1}$ )	distance (Å)	$k_{eT}$ ( $s^{-1}$ )
A	5.173	$9.0 \cdot 10^{11}$	5.303	$5.6 \cdot 10^{11}$	6.213	$2.8 \cdot 10^{11}$
B	5.930	$6.8 \cdot 10^{11}$	5.830	$4.0 \cdot 10^{11}$		
C	6.255	$1.2 \cdot 10^{11}$				
D					7.142	$2.3 \cdot 10^{11}$

It is clear, however, that the effect of the sizable intramolecular reorganization parameters computed for BQ derivatives is to depress the mobilities as compared to those of highly conductive oligoacenes.<sup>119,121</sup> Thus, we can conclude that the balance between efficient ON/OFF ratio and efficient transport in the bulk is strongly influenced by the intrinsic molecular properties of the organic material. In the case of **PNT**, the small  $\lambda_i$  value favors the efficient charge transport but disfavors the ON/OFF ratio in memory devices. In contrast, for **DDQ** the appropriate combination seems to be realized, and it results in a favorable ON/OFF ratio without compromising the charge transport across the organic material. The reorganization energy parameters are sizable also for **TCQ** and **TCN**, but in these cases inefficient level alignment (**TCQ**) or too efficient injection in the pristine material (**TCN**) is expected to result in less efficient memory effects. It can be speculated that, for a memory device, if the  $\lambda_i$  becomes even larger, the gain in the ON/OFF ratio will be negatively compensated by the hampered charge transport of the highly trapped charge carriers across the organic material.

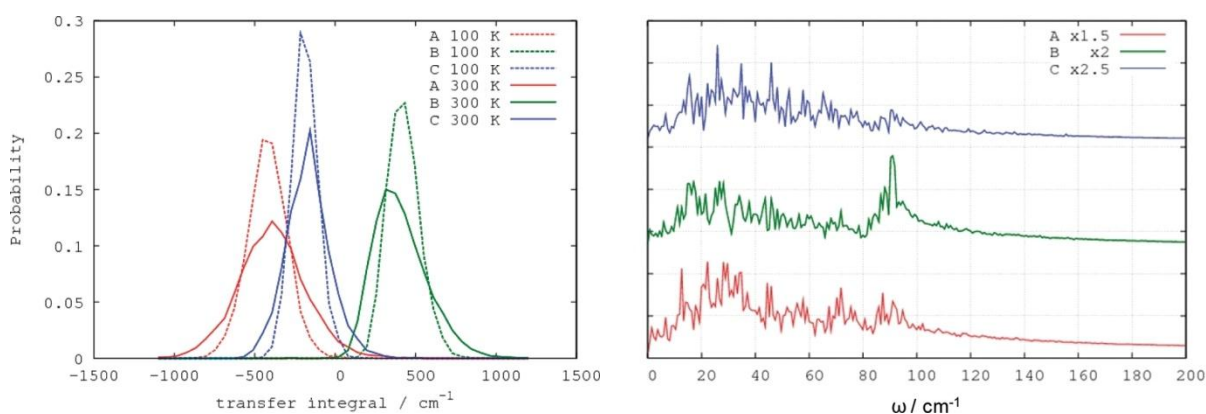


**Figure 6.81** Thermal disorder effects on the distribution of the largest computed charge transfer integrals of **DDQ** (left) evaluated at two temperatures (100 and 300 K) and Fourier transforms of the autocorrelation function of the transfer integrals computed at 300 K (right) underscoring the low frequency active modes responsible for the modulation of the charge transfer integrals. Figure adapted from <sup>101</sup>.

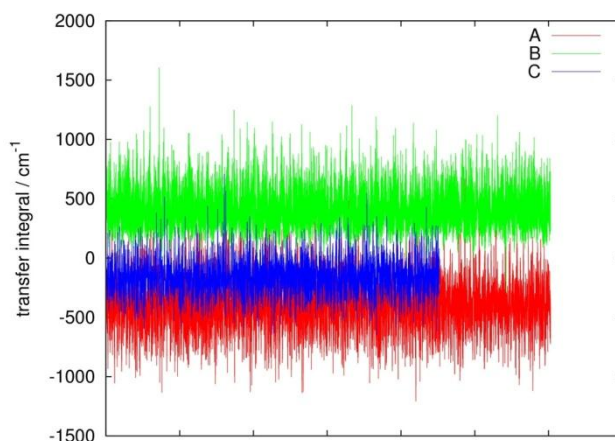


**Figure 6.82** Fluctuations of the computed charge transfer integrals of **DDQ** (due to thermal motions,  $T = 300$  K) as a function of the simulation time (overall 90 ps after equilibration). Integrals corresponding to dimers *A*, *B* and *C* of **DDQ** are shown. Figure adapted from <sup>101</sup>.

In summary, we have investigated, by means of computed intra- and intermolecular parameters, the intrinsic molecular nature of the memory effect displayed by **DDQ**, **TCQ**, and **TCN**, a series of BQ derivatives exhibiting EWGs of different strength, and **PNT**, an example of a highly conducting oligoacene. Two relevant processes have been considered: the efficiency of the charge injection at the electrode/organic interface and the charge transport across the organic material.

Concerning the first process, calculations suggest that the OFF state is injection limited, determined by the activated process of charge injection in most of the systems investigated. The strength and the number of EWGs improve level alignment of the pristine material and reduce the barrier to electron injection. With regard to the switching from the OFF (low conductivity) to the ON (high conductivity) state, the systems investigated underscore the relevant role of the intramolecular reorganization energy  $\lambda_i$  in governing the efficiency of the resistive memory device, in particular the ON/OFF ratio, through the modulation of the level alignment in the presence of charged species at the interface. Indeed, when charged species are at the interface, energy levels associated with the charged species have to be considered, further improving the electron injection. The increased alignment has been shown to be related to a sizable reorganization energy  $\lambda_i$ .

Employing the MLJ formalism to estimate the efficiency of the charge hopping mechanism, it has been shown that the sizable  $\lambda_i$  providing an efficient ON/OFF ratio, combined with moderate electronic coupling integrals  $V_{ij}$ , depresses the bulk charge transport of **DDQ** and other BQ derivatives as compared to the highly conductive **PNT**. To extend our understanding of the charge transport mechanism in these semiconductors, we have evaluated the effect of thermally induced disorder on computed charge transfer integrals. Similarly to previous studies on oligoacene semiconductors, we have found that low frequency intermolecular modes in the range 20-80  $cm^{-1}$  modulate the integrals.

The role of molecular parameters disclosed by this study might be exploited for tuning the bistability behavior of new molecular-based semiconductors and to gain control of the memory phenomenon by appropriate design rules.

## 6.7 FLUOROALKYLATED AND CHLORINATED PERYLENE BISIMIDES

In this Section, the Pandora Suite QM/MD/KMC integrated approach is applied to investigate the subtle interplay between intramolecular and intermolecular contributions to the charge carrier propagation in three fluoroalkylated<sup>42</sup> and four chlorinated<sup>43</sup> perylene bisimide derivatives. *n*-type strengthening obtained through the introduction of such electron-withdrawing groups is discussed, along with the role played by the flexible substituents within the intra- and intermolecular charge transfer parameters. It is shown that structural asymmetries result in both anisotropic conduction and a dimer-trapping retardation effect responsible for the limited mobilities of columnar core-twisted PBI derivatives.<sup>42-43</sup> In addition, such an effect is not mitigated by thermally induced electronic coupling fluctuations since these are shown to be drastically reduced in core-twisted PBI compared to planar-core derivatives.<sup>43</sup>

### 6.7.1 Background

The interest in organic electronics has increased considerably over the last couple of decades. The goal of organic-based electronics and opto-electronics is the fabrication of devices at reduced cost featuring new functionalities, such as flexibility, that are more difficult to achieve with inorganic semiconductors.<sup>129</sup> Because of their high band gap and low electronic affinity, most of the "classical" organic semiconductors are *p*-type or hole transporting. Among *n*-type organic semiconductors,<sup>130</sup> core fluorinated copper phthalocyanines,<sup>131</sup> perfluorinated pentacene,<sup>132</sup> and cyano-substituted terthienoquinoid derivatives<sup>132-133</sup> have displayed electron mobilities of the order of 0.1-0.2  $cm^2 V^{-1} s^{-1}$ . Recently, remarkable electron mobilities have been measured for naphthalene bisimide derivatives<sup>58a,134</sup> and for several derivatives of perylene bisimide dyes.<sup>64a-b,135</sup> The solid state packing and functional properties of PBIs can be tailored by the introduction of appropriate substituents in the imide position or by core substitution in the bay region.<sup>58c-d,136</sup> Core substitution contributes to modulate electron affinity and therefore electron injection along with molecular  $\pi$ -stacking properties. Substitution with strong electron-withdrawing groups such as fluorine and others<sup>10f,58d,136a-b,137</sup> at the imide position not only lowers significantly the LUMO level of the resulting molecule thereby improving electron injection but also improves the ambient stability of organic thin-film transistors (OTFT) since self-segregation of densely packed

fluorocarbon chains provides a kinetic barrier to the diffusion of oxygen and other ambient oxidants to the active channel area.<sup>58a,d</sup>

A thorough analysis of the charge transport properties of halogenated PBIs has been presented in recent work.<sup>58d,138</sup> It has been shown that chlorination, similarly to fluorination, is a viable route toward the design of *n*-type air-stable organic semiconductors.<sup>138</sup> However, moving from fluorine to chlorine and bromine, an increasingly twisted core is forced to the PBI which results generally in depressed mobilities that have been ascribed to unfavorable  $\pi$ - $\pi$  overlap between adjacent molecular units.

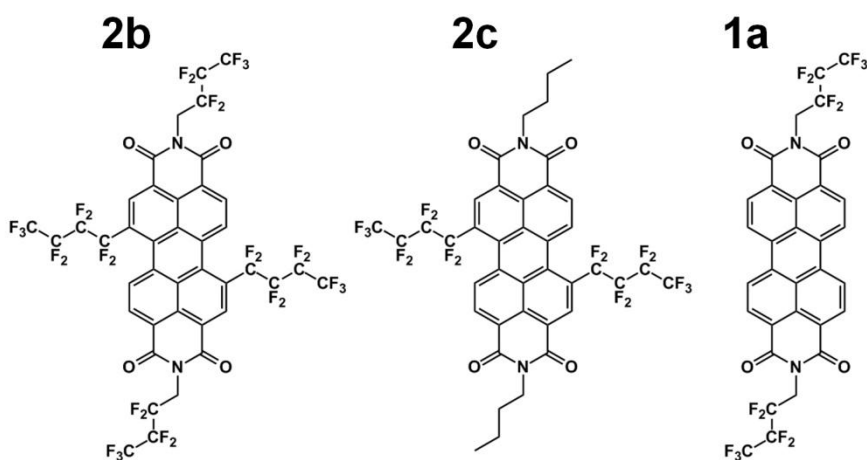


**Figure 6.83** Structural formula of the three fluoroalkylated PBIs. Figure adapted from <sup>42</sup>.

Recently, a convenient synthesis of core-perfluoroalkylated PBIs has been proposed<sup>10f</sup> along with the determination of a molecular packing arrangement in single crystals and preliminary charge mobility (*n*-type) measurements<sup>10f</sup> for the PBI derivatives labeled **2b** and **2c** in <sup>42</sup> and Figure 6.83. The observed mobilities are  $0.003 \text{ cm}^2 \text{ V}^{-1} \text{ s}^{-1}$  for compound **2b**,<sup>10f</sup>  $0.052 \text{ cm}^2 \text{ V}^{-1} \text{ s}^{-1}$  for compound **2c**,<sup>10f</sup> and  $1.42 \text{ cm}^2 \text{ V}^{-1} \text{ s}^{-1}$  for compound **1a**.<sup>58d</sup>

After we had investigated the combined effect of intra- and intermolecular properties on the charge transport of such fluoroalkylated PBI derivatives (**1a**, **2b**, and **2c**), we extended that study by considering three tetra-chlorinated PBIs (**1b**, **1d**, and **2d** in Figure 6.84) and the octa-chlorinated PBI (**8Cl** in Figure 6.84). In our discussion, we will compare the results on chlorinated derivatives with those obtained for the fluoroalkylated, particularly focusing on reference planar-core PBI derivative **1a**.

The charge mobility of **1d** and **2d** was measured in an OTFT configuration by vacuum-depositing a thin film of the organic semiconductor on a SiO<sub>2</sub> surface treated with *n*-octadecyl-triethoxy-silane (OTS) in the vapor phase (OTS-V) or in the solution phase (OTS-S).<sup>58d</sup> Despite its highly twisted aromatic core, the reported mobility of **2d** was 0.025 cm<sup>2</sup> V<sup>-1</sup> s<sup>-1</sup> for the OTS-V treatment and 0.28 cm<sup>2</sup> V<sup>-1</sup> s<sup>-1</sup> for OTS-S treatment (measurements in N<sub>2</sub> atmosphere). The reported mobility of **1d** in the OTFT configuration was 5 · 10<sup>-4</sup> cm<sup>2</sup> V<sup>-1</sup> s<sup>-1</sup> for the OTS-V treatment and 4 · 10<sup>-5</sup> cm<sup>2</sup> V<sup>-1</sup> s<sup>-1</sup> for the OTS-S treatment. The mobility of **1b** (0.045 cm<sup>2</sup> V<sup>-1</sup> s<sup>-1</sup>) was obtained from pulse radiolysis-time-resolved microwave conductivity (PR-TRMC) measurements.<sup>139</sup> Finally, the measured *n*-channel mobility<sup>58c</sup> of **8Cl** in N<sub>2</sub> atmosphere was reported to be 0.90 cm<sup>2</sup> V<sup>-1</sup> s<sup>-1</sup>, which shows that core-twisted PBI derivatives can still display large mobilities if accompanied by efficient intermolecular packing, in this case driven by the unsubstituted nitrogen.

The large variety of reported measurements for devices based on PBI derivatives exemplifies how intramolecular properties and packing effects cooperate to determine different charge transport properties. Molecular packing of PBI derivatives has been previously investigated both experimentally and theoretically, and charge transport models have been employed to investigate several PBI derivatives.<sup>42,140</sup>

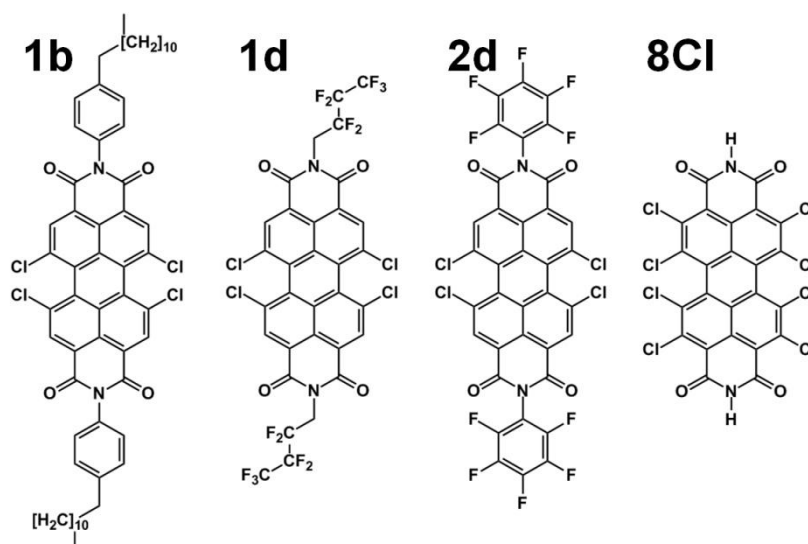


**Figure 6.84** Structural formula of the tetrachloro-substituted (**1b**, **1d**, and **2d**), and octachloro-substituted (**8Cl**) PBI derivatives. Figure adapted from <sup>43</sup>.

In the remaining of this text, the investigation on the fluoroalkylated PBIs is first shown, as it first revealed the importance of evaluating structural asymmetries delivering the dimer-trapping effect; then, the subsequent study on the chlorinated PBIs is discussed, whose main aim was to explore more closely the effect of core twisting, induced by chlorination, on intramolecular and intermolecular charge transport properties, also paying attention to the role of thermally induced dynamical effects.

Note that, although those two studies relied on the same assumptions (*e.g.*, non-adiabatic hopping model with Marcus-Levich-Jortner formalism) and were carried out by means of the same computational tools (Pandora Suite and related commercial software), the evaluation of some charge transfer parameters was not univocal. As a consequence, it would be meaningless a direct comparison between the values determined for the charge mobilities. From this perspective, I also point out that the purpose of this work is not to predict absolute values of charge mobilities, but rather to rationalize, in terms of intra- and intermolecular structure-property relationships, why different mobilities are obtained for different molecular and crystal architectures.

### 6.7.2 Computational details

Referring to Chapter 5, we adopted B3LYP/3-21G\* level for every calculation aimed at the determination of intra- and intermolecular parameters. For compounds **1a**, **2b**, and **2c**, further calculations at B3LYP/6-31G\* level were performed for comparison. All the QM calculations were carried out with the Gaussian09 (Gaussian03 for **2b**, **2c**, and the former evaluation on **1a**).

To the outer-sphere reorganization energy  $\lambda_o$  we set a value of 0.1 eV within the first study (**1a**, **2b**, and **2c**), and 0.01 eV within the second study (**1a**, **1b**, **1d**, **2d**, and **8Cl**), in keeping with current studies.<sup>141</sup> Note that the absolute values of the rate constants can be strongly influenced by the chosen  $\lambda_o$  parameter.

The single effective modes with frequency  $\omega_{eff}$  and Huang-Rhys factor  $S_{eff}$ , to be included in Eq. (4.19), were evaluated differently in the two studies (*vide infra*).

The charge carrier was propagated in a KMC scheme under the effect of an applied electric field only for **1a**, **1b**, **1d**, **2d**, and **8Cl**.

### 6.7.3 Charge transport phenomena in fluorinated PBIs

From the equilibrium structures of neutral and charged species, we estimated both electron affinities and intramolecular reorganization energies (see Figure 4.5) of the three species **1a**, **2b**, and **2c**. The inclusion of fluoroalkyl substituents in the bay region, for compounds **2b** and **2c**, leads to a marked twist of the perylene core, as well-known for other bay-substituted PBIs.<sup>142</sup> Fluoroalkyl substitution at both the imide and the bay positions lowers the energy of the lowest unoccupied molecular orbital (LUMO) level and increases the electronic affinity of the PBI derivative, thereby strengthening the *n*-type character of the semiconductor. This effect can be appreciated by considering the energies of the LUMO levels reported in Table 6.16 and the correspondingly computed vertical and adiabatic *EAs* in Table 6.16.

**Table 6.16** Frontier orbital energies and transport gap (at the optimized structures of the neutral species), *VEAs*, *AEAs*, AP intramolecular reorganization energies of **1a-model**, **1a**, **2b-2c-model**, **2b**, and **2c**, computed at the B3LYP/3-21G and B3LYP/6-31G\* levels. All values are given in *eV*.<sup>42</sup>

B3LYP 3-21G	$E_{\text{HOMO}}$	$E_{\text{LUMO}}$	$\Delta E_{\text{H-L}}$	$VEA_n$	$VEA_a$	<i>AEA</i>	$\lambda_i^{AP,VEA}$	$\lambda_i^{AP,n}$	$\lambda_i^{AP,c}$	$\lambda_i^{AP}$
<b>1a-model</b>	-6.08	-3.50	2.58	2.19	2.44	2.32	0.25	0.128	0.128	0.256
<b>1a</b>	-6.35	-3.78	2.57	2.49	2.80	2.65	0.31	0.154	0.155	0.309
<b>2b-2c-model</b>	-6.53	-3.91	2.62	2.63	2.91	2.77	0.28	0.141	0.142	0.283
<b>2b</b>	-6.77	-4.15	2.62	2.93	3.29	3.11	0.36	0.180	0.184	0.364
<b>2c</b>	-6.50	-3.88	2.62	2.66	3.00	2.83	0.34	0.172	0.167	0.339
B3LYP 6-31G*	$E_{\text{HOMO}}$	$E_{\text{LUMO}}$	$\Delta E_{\text{H-L}}$	$VEA_n$	$VEA_a$	<i>AEA</i>	$\lambda_i^{AP,VEA}$	$\lambda_i^{AP,n}$	$\lambda_i^{AP,c}$	$\lambda_i^{AP}$
<b>1a-model</b>	-6.00	-3.46	2.54	2.19	2.44	2.32	0.25	0.126	0.132	0.258
<b>1a</b>	-6.25	-3.72	2.53	2.47	2.77	2.62	0.30	0.148	0.150	0.298
<b>2b-2c-model</b>	-6.41	-3.81	2.60	2.56	2.86	2.71	0.30	0.148	0.150	0.298
<b>2b</b>	-6.67	-4.07	2.60	2.88	3.23	3.06	0.35	0.169	0.180	0.349
<b>2c</b>	-6.40	-3.80	2.60	2.61	2.94	2.78	0.33	0.164	0.166	0.330

The inclusion of fluoroalkyl chains (from **1a** to **2b**) in the bay region lowers the LUMO level by *ca.* 0.37 (B3LYP/3-21G) or 0.35 *eV* (B3LYP/6-31G\*) and similarly increases the adiabatic electron affinity (*AEA*, see Table 6.16) by 0.46 (B3LYP/3-21G) or 0.44 *eV* (B3LYP/6-31G\*). The substitution at the imide position with alkyl chains (compound **2c**), as compared with fluoroalkyl chains (**2b**), increases back the LUMO level by 0.27 *eV* and decreases the *AEA* by 0.28 *eV* at both levels of theory. Interestingly, the transport gap  $\Delta E_{\text{HOMO-LUMO}}$  is weakly

affected by the substitution and is identical for compounds **2b** and **2c**, while it is slightly smaller for compound **1a** as a result of the increased conjugation associated with the planar perylene chromophore in the latter.

The AP-computed intramolecular reorganization energies (collected in Table 6.16): 0.31, 0.36, and 0.35 *eV* for compounds **1a**, **2b**, and **2c**, respectively (values smaller by 0.01 *eV* with the 6-31G\* basis set) are relatively large, and a fraction of their magnitude can be attributed to the presence of the bay and imide flexible substituents. To investigate this effect in more detail, we carried out quantum-chemical calculations on model systems for the **1a**, **2b**, and **2c** compounds, featuring the minimal substituents mimicking the steric and electron-withdrawing effect of fluoroalkyl and alkyl substituents but at the same time reducing the number of flexible degrees of freedom. To this end, we selected the two model systems depicted in Figure 6.85, featuring a methyl group at the imide position in conjunction with (a) hydrogens in the bay region (**1a-model**) leaving a planar conjugated framework as for **1a** or (b) a CF<sub>3</sub> substituent (**2b-2c-model**) in the bay region, which should provide a realistic representation of compounds **2c** or **2b** with regard to their structural characteristics. Indeed, comparison between computed geometry changes upon electron transfer shows minimal differences between model and real systems,<sup>42</sup> thereby showing that the chosen models are realistic. Similarly, the frontier orbitals of the model and real systems are very similar (Figures 6.86-87). Interestingly, the intramolecular reorganization energies computed for the model systems are 0.26 (0.26) and 0.28 (0.30) *eV* for **1a-model** and **2b-2c-model**, respectively, at the B3LYP/3-21G (B3LYP/6-31G\*) levels of theory. These values, as those computed for the real systems, are in line with previously reported values for PBI derivatives.<sup>143</sup> The difference (0.05-0.08 *eV*) between the computed  $\lambda_i$  for model and real systems suggests that the presence of flexible substituents (in the real **1a**, **2b**, and **2c** systems) increases the intramolecular parameters, a factor that should be taken into account in the design of new species, because of its role in trapping charge carriers, thereby reducing the charge mobility. The computed vibrational contributions to the intramolecular reorganization energies collected in Figures 6.88-89 are indeed similar for model (**1a-model** or **2b-2c-model**) and correspondingly real (**1a** or **2b** and **2c**) systems except for the fact that in real systems a number of additional contributions are located in the low frequency region; hence, it can be attributed to the increased number of flexible (low frequency) degrees of freedom. Adapting the intramolecular effective parameters computed for model compounds to the respective real systems and including the exceeding contributions from low frequency modes into the

$\lambda_{class}$  parameter (Table 6.17), we estimated the rate constants of **1a**, **2b**, and **2c** according to Eq. (4.19).

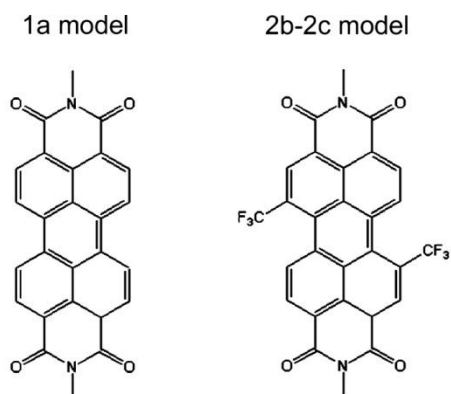


**Figure 6.85** Structural formula of the two model PBI derivatives. Figure adapted from <sup>42</sup>.

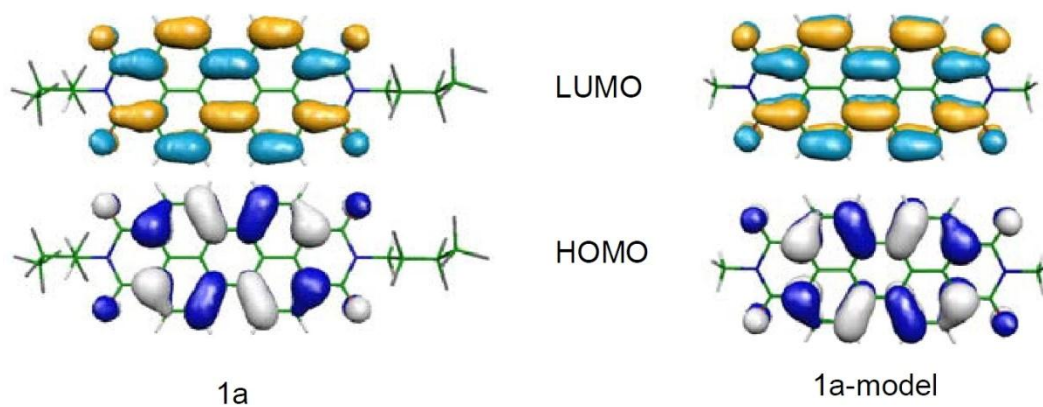


**Figure 6.86** The frontier molecular orbitals of **1a** (left) and **1a-model** (right). The LUMO orbitals were involved in the calculations of  $V_{ij}$  charge transfer integrals, computed at B3LYP/3-21G level of theory. Figure adapted from <sup>42</sup>.

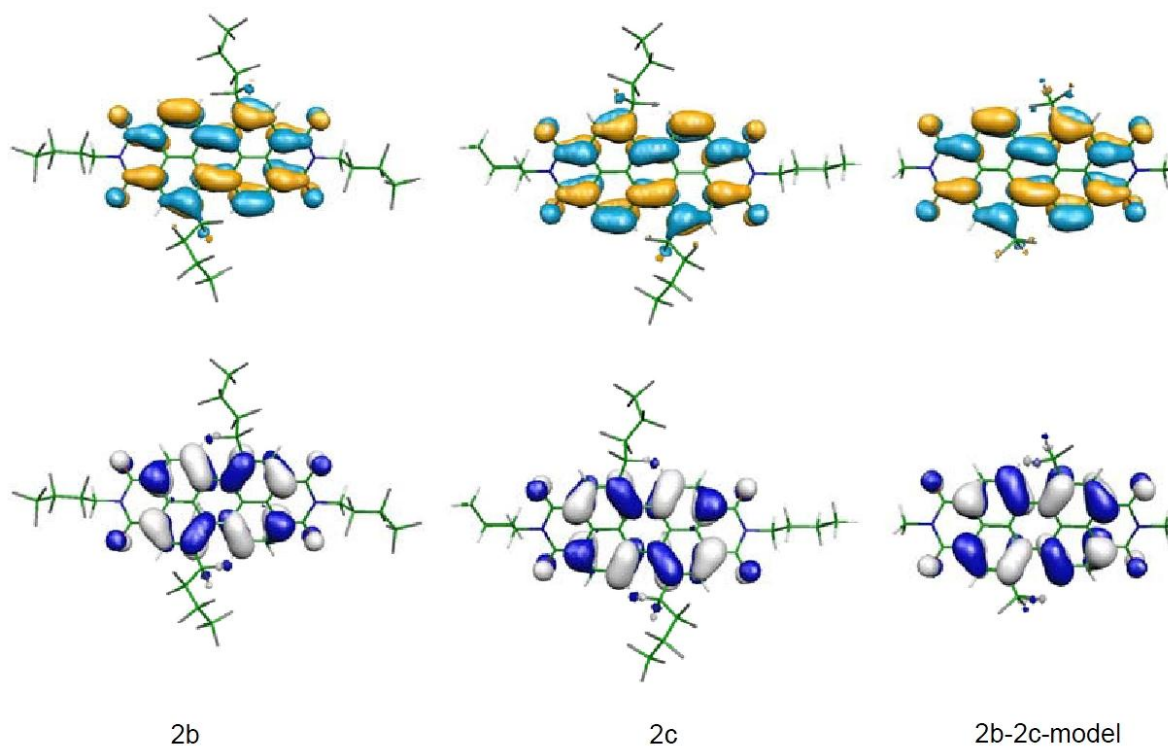


**Figure 6.87** The frontier molecular orbitals of **2b** (left), **2c** (middle), and **2b-2c-model** (right). The LUMO orbitals were involved in the calculations of  $V_{ij}$ , computed at B3LYP/3-21G level of theory. Figure adapted from <sup>42</sup>.

**Table 6.17** Effective frequency  $\omega_{eff}$  and associated HR factor  $S_{eff}$  employed in the evaluation of charge transfer rate constants of the three PBI derivatives **1a**, **2b**, and **2c**.<sup>42</sup>

B3LYP/3-21G	<b>1a-model</b>	<b>1a</b>	<b>2b-2c-model</b>	<b>2b</b>	<b>2c</b>
$\omega_{eff}$ ( $cm^{-1}$ ) <sup>a</sup>	992	992	858	858	858
$S_{eff}$ <sup>a</sup>	2.08	2.08	2.66	2.66	2.66
$\lambda_i^{HR}$ (eV)	0.256	0.309	0.283	0.364	0.339
Contribution to $\lambda_{class}$ for <b>real</b>		0.053		0.081	0.056
Total $\lambda_{class}$		0.153		0.181	0.156

<sup>a</sup> Only frequencies above  $150\text{ cm}^{-1}$  are considered in the calculation of the effective parameters for the model systems.

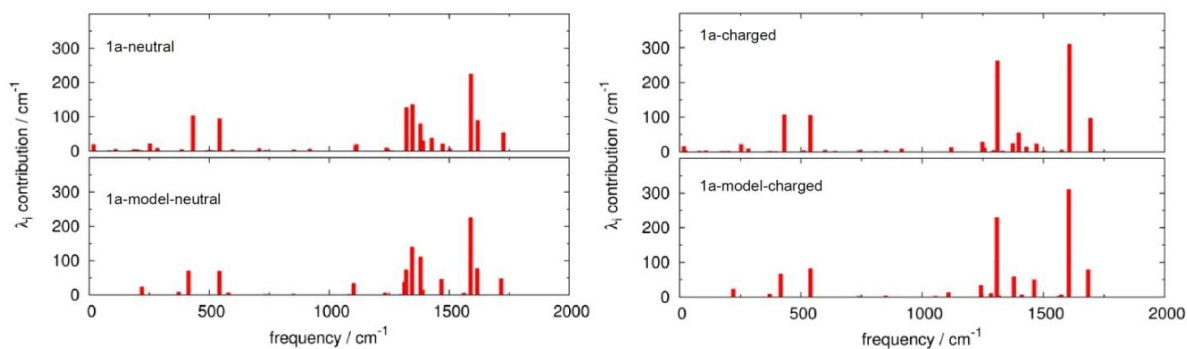


**Figure 6.88** The vibrational frequencies contributions to the computed  $\lambda_i^{HR}$  of **1a** (top) and **1a-model** (bottom) neutral (left) and charged (right) species. From B3LYP/3-21G calculations. It is seen that the contributions are very similar. Figure adapted from <sup>42</sup>.

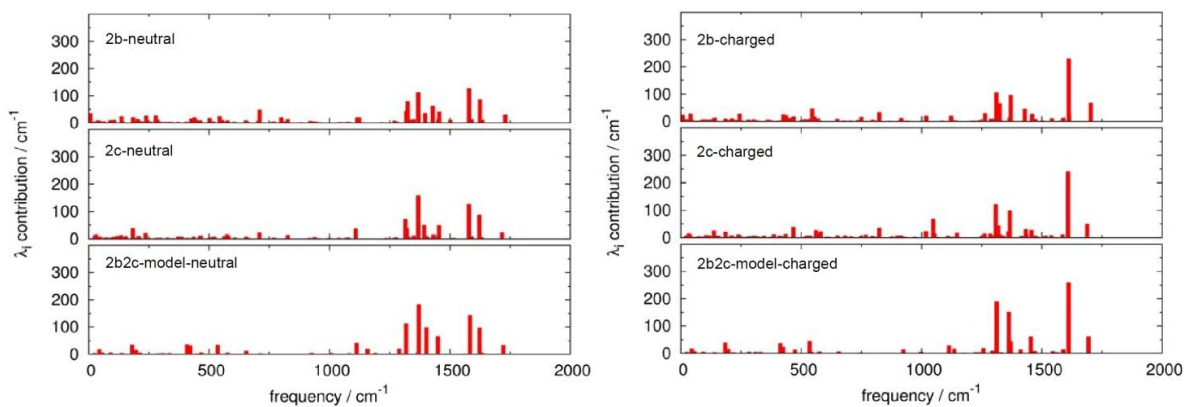


**Figure 6.89** The vibrational frequencies contributions to the computed  $\lambda_i^{HR}$  of **2b** (top), **2c** (middle), and **2b-2c-model** (bottom) neutral (left) and charged (right) species. From B3LYP/3-21G calculations. It is seen that the contributions are very similar. Figure adapted from <sup>42</sup>.

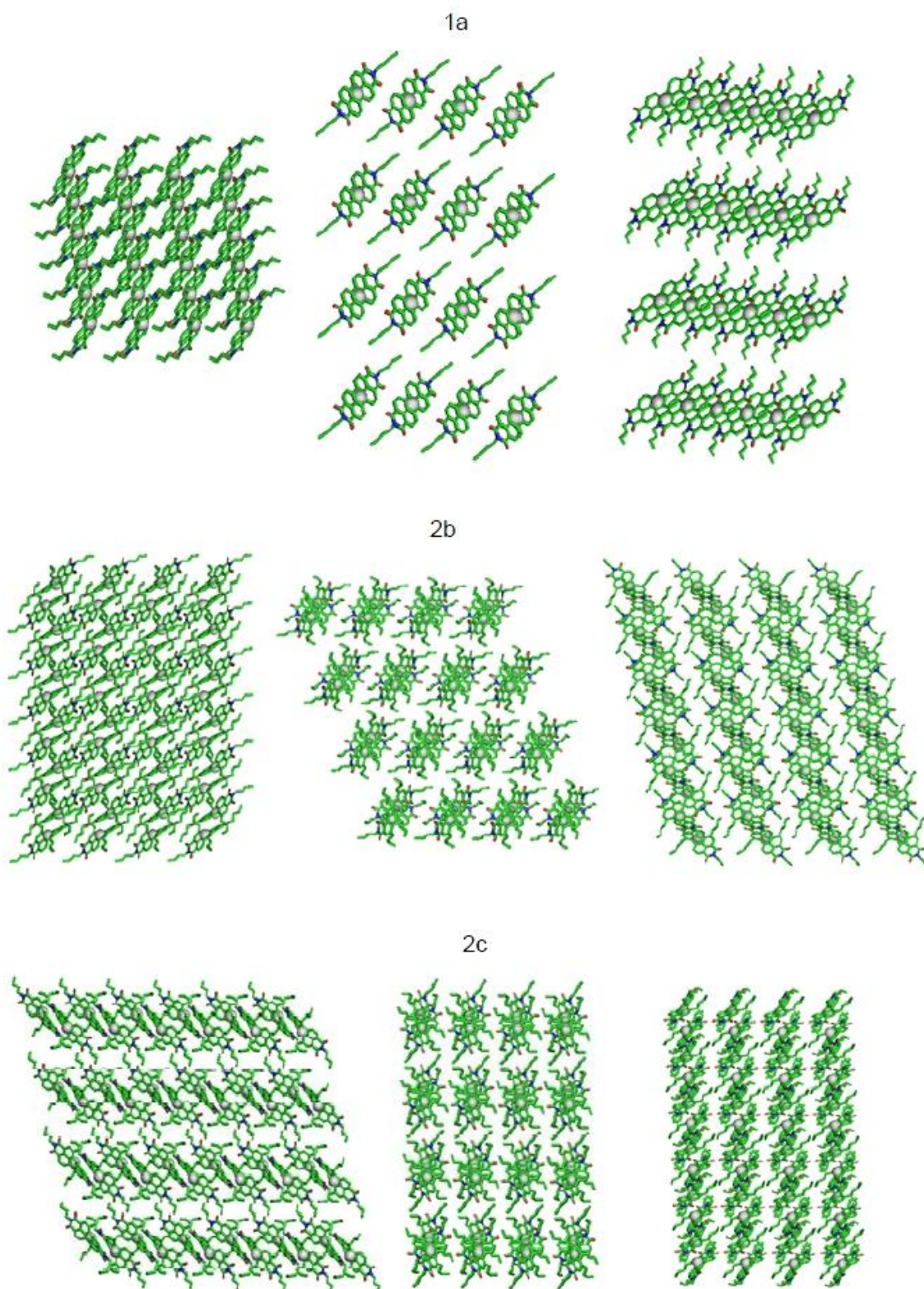


**Figure 6.90** Molecular crystals of **1a**, **2b**, and **2c** side and top views showing the presence of columns of  $\pi$ -stacked PBI molecules. The white spheres centered on each molecule represent the centers of mass; H and F atoms are omitted. Figure adapted from <sup>42</sup>.

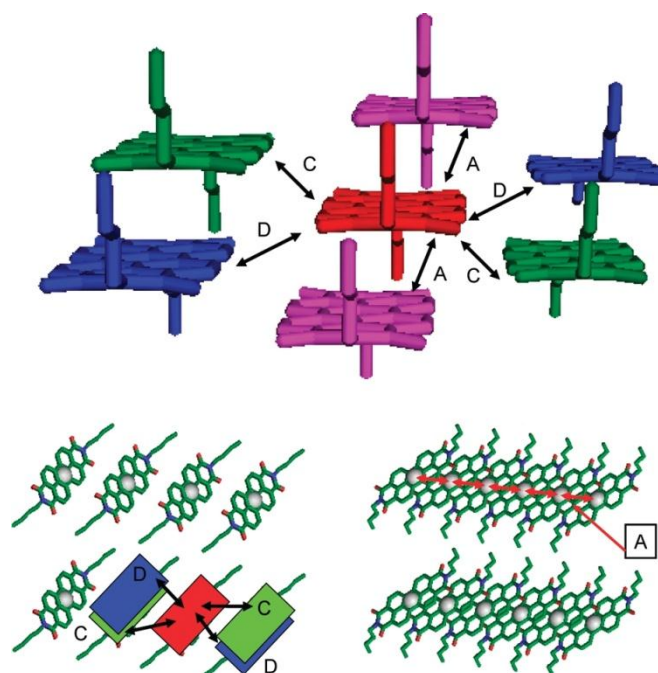


**Figure 6.91** Crystal of **1a**. (top) The possible intra- (magenta molecules) and *intercolumn* (green and blue molecules) paths taking as reference the red central molecule. The capital letters indicate the jumps that are active because of non-negligible charge transfer integrals. (bottom) Schematic indication of (left) the *intercolumn* paths C and D and (right) the *intracolumn* path A. The sequence of red arrows underscores that the jumps along the column are identical. The white spheres centered on each molecule represent the centers of mass, and hydrogen and fluorine atoms are omitted. Figure adapted from <sup>42</sup>.

The assumption of the hopping mechanism for the charge transport in crystals of PBI derivatives is justified because of the relatively large value of the  $\lambda_i$  parameter. To investigate the possible hopping paths, we extracted, for each crystal, all of the possible neighbors of a given molecule. The crystals of the PBI derivatives investigated in this work belong to the same triclinic *P-1* group. However, while there is only one site in the crystal of **1a**, there are two different sites (corresponding to the two enantiomers of the twisted PBI) for **2b** and **2c**. As for other PBI derivatives,<sup>58d,140a-b</sup> the tendency to form columns of  $\pi$ -stacked PBI units is clearly seen in Figures 6.90-93. Accordingly, the charge transport can be discussed in terms of *intracolumn* jumps and *intercolumn* jumps as pictorially shown in Figures 6.91-93. In Table 6.18, we collected the calculated charge transfer integrals for the various hopping paths in the three crystals. It is worth noting that while there is only one type of *intracolumn* jump (labeled A) for **1a** (Figure 6.91), there are two kinds of *intracolumn* jumps (labeled A and B) in the crystals of **2b** and **2c**, as graphically depicted with blue and red arrows in Figures 6.92-93.

The two jumps for **2b** and **2c** are due to the presence of two different molecular sites, which imply that given one molecular site, the jumps to a different one, in backward and forward directions, are characterized by different charge transfer integrals  $V_{ij}$ . Such difference is larger for **2b** than for **2c**.

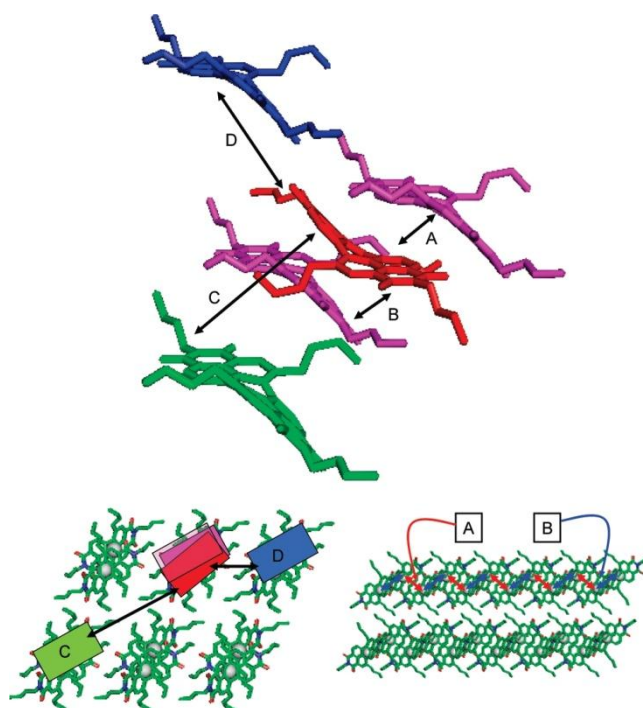


**Figure 6.92** Crystal of **2b**. (top) The possible intra- (magenta molecules) and *intercolumn* (green and blue molecules) paths taking as reference the red central molecule. The capital letters indicate the jumps that are active because of non-negligible charge transfer integrals. (bottom) Schematic indication of (left) the *intercolumn* paths C and D and (right) the *intracolumn* paths A (red arrows) and B (blue arrows). The sequence of red and blue arrows underscores that two different jumps (fast and slow) alternate along the column. The absence of the counterpart of jumps C and D in opposite directions, starting from the same red molecule, underscores the asymmetry that also characterizes *intercolumnar* jumps. The two different orientations of the rectangles reflect the presence of two different molecular sites in the crystal. Figure adapted from <sup>42</sup>.

**Table 6.18** *n*-type electronic coupling integrals  $V_{ij}^{\text{LUMO}}$  (B3LYP/3-21G) and charge transfer rate constant  $k_{eT}$  (at 300 K) for the most relevant dimers of **1a**, **2b**, and **2c** extracted from the crystal structures.<sup>42</sup>

crystal	dimer	intracolumn distance (Å)	$V_{ij}^{\text{LUMO}}$ ( $\text{cm}^{-1}$ )	$k_{eT}$ ( $\text{ps}^{-1}$ )	dimer	intercolumn distance (Å)	$V_{ij}^{\text{LUMO}}$ ( $\text{cm}^{-1}$ )	$k_{eT}$ ( $\text{ps}^{-1}$ )
<b>1a</b>	A	4.9104	-23	0.012	C	9.1891	338	2.3
			600 <sup>a</sup>	7.2	D	12.0472	-33	0.021
<b>2b</b>	A	6.2112	-772	5.2	C	13.2960	7	0.0005
	B	6.3033	282	0.7	D	15.1341	18	0.003
<b>2c</b>	A	5.8727	-465	2.7	C	10.6947	-10	0.001
	B	6.2298	603	4.4	D	11.8171	39	0.018
			<sup>a</sup> Estimated as an upper limit for $\sqrt{\langle (V_{ij})^2 \rangle}$		E	12.0177	9	0.001

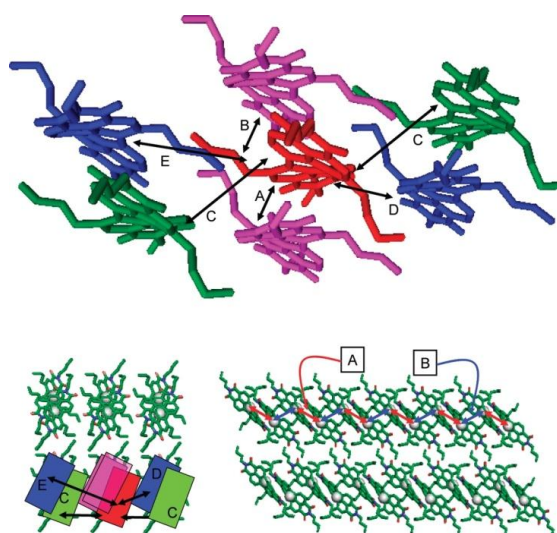


**Figure 6.93** Crystal of **2c**. (top) The possible intra- (magenta molecules) and *intercolumn* (green and blue molecules) paths taking as reference the red central molecule. The capital letters indicate the jumps that are active because of non-negligible charge transfer integrals. (bottom) Schematic indication of (left) the *intercolumn* paths C, D, and E and (right) the *intracolumn* paths A (red arrows) and B (blue arrows). The sequence of red and blue arrows underscores that two different jumps alternate along the column. The counterpart of jump D, in opposite direction starting from the same red molecule, is path E. The counterpart of jump C, in opposite direction starting from the same red molecule, is still path C since the molecular sites involved in the jump are of the same type. The white spheres centered on each molecule represent the centers of mass, and hydrogen and fluorine atoms are omitted. The two different orientations of the rectangles reflect the presence of two different molecular sites in the crystal. Figure adapted from <sup>42</sup>.

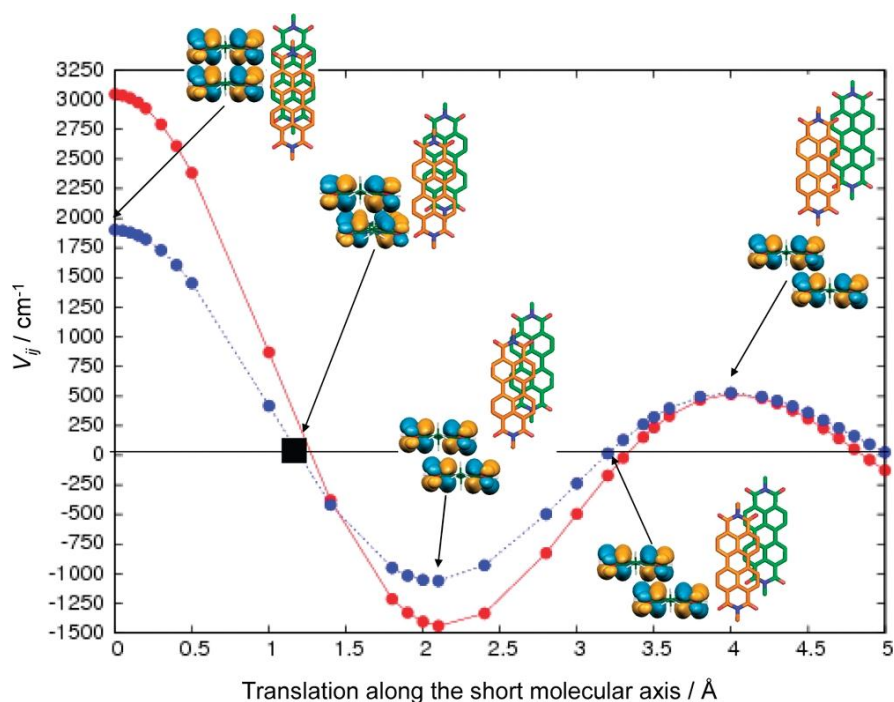


**Figure 6.94** Dependence of the charge transfer integral  $V_{ij}$  associated to the A jump of **1a**, as a function of the sliding along the short axis for selected values of the sliding along the long molecular axis, keeping the intermolecular distance fixed to the value observed in the crystal. The red curve corresponds to translation along the short axis, starting from a face to face dimer. The blue curve corresponds to translation along the short axis starting from the dimer configuration in the crystal of **1a**, which is represented by the black square in the figure. Figure adapted from <sup>42</sup>.

Inspection of Table 6.18 shows that the *intracolumn* jump for compound **1a** is associated with a remarkably small charge transfer integral. However, the optimal packing induced by intermolecular forces in organic crystals corresponds, in some cases, to minimization of the molecular orbital superposition; hence, it is not surprising that the charge transfer integral is minimal at the crystal structure. To quantify the relevance of this effect, we computed (see Figure 6.94) the charge transfer integral for a dimer of PBI starting from its face to face configuration and by translating one molecule with respect to the other along the long and short molecular axes. The configuration of the dimer in the crystal of **1a** corresponds to a translation of the long axis by *ca.* 3.4 Å and of the short axis by *ca.* 1.2 Å and is represented by the black square in Figure 6.94. The corresponding behavior of the  $V_{ij}$  integral as a function of the translation along the short axis is represented by the blue curve in Figure 6.94. It is seen that the translation is accompanied by a large variation in the charge transfer integral as expected because of the variation in the overlap between the LUMO orbitals of the two

molecules (shown in the insets of Figure 6.94). As a consequence, vibrational motions (and therefore thermally induced disorder) may lead to significant values of the *intracolumn* charge transfer integral.

A complete study of the dynamically induced modulation of charge transfer integrals is beyond the scope of this work and will be the subject of future investigations (see Section 6.7.4). However, preliminary molecular dynamics simulations (outlined in the Section 5.5) along the lines described in <sup>101</sup> indicate that the modulation of charge transfer integrals at *ca.* 300 K can be fitted with a Gaussian distribution whose  $\sigma$  is of the order of few hundreds  $cm^{-1}$ . Thus, we can account for the effect of thermally induced disorder by considering the thermalized limit<sup>144</sup> for this specific jump, that is, by injecting the  $\langle(V_{ij})^2\rangle$  value into the MLJ expression for the rate constant, as generally done in the description of biological systems, an approach whose derivation and validity has been recently discussed.<sup>144-145</sup> The thermalized limit is acceptable in this case since the frequency of intermolecular modes is larger than the hopping frequency for the A jump. Because  $\langle V_{ij} \rangle$  is almost negligible,  $\langle(V_{ij})^2\rangle \cong \sigma^2$  and jump A are expected to be more dramatically affected by thermal disorder. Thus, we run two set of KMC simulations, using both the static crystal value of  $V_{ij}$  and the estimated  $\sqrt{\langle(V_{ij})^2\rangle}$  value (assuming an upper limit of 600  $cm^{-1}$  for  $\sigma$ ) for the **1a** system (see Table 6.18).

Inspection of Table 6.18 and Figures 6.91-93 shows that, beside the *intracolumn* charge transfer integrals, also *intercolumn* jumps are active because of non-negligible electronic couplings. While the *intercolumn* distance is relatively large for crystals of **2b** and **2c**, because of the presence of alkylated substituents in the bay region, it is much closer in the crystal of **1a**. For instance, the most efficient *intercolumn* jump in **1a** must overcome 9.19 Å as compared with 11.82 Å for the crystal of **2c** and 13.30 Å for **2b**. The shortest distance in the case of **1a** is associated with a considerable charge transfer coupling of 338  $cm^{-1}$  for path C. In contrast, modest charge transfer integrals are computed for both **2b** and **2c** (see Table 6.18).

With the parameters discussed above, we computed the charge transfer rate constants (collected in Table 6.18) and injected them into the KMC scheme<sup>140a,146</sup> to estimate charge transport mobilities at 300 K. The absolute magnitude of charge mobilities can be influenced by the choice of the intra- and intermolecular parameters entering the definition of the

charge transport rate constant. Some of these parameters, such as the outer sphere contribution to the reorganization energy, are difficult to estimate<sup>114b</sup> and can affect the resulting values. In addition, the model assumes a perfect crystal structure without defects or microcrystalline boundaries while measurements are generally carried out in films whose exact morphology is not known. Thus, the purpose is not to reproduce the experimental values but to provide correct trends for relative values and to rationalize why different mobilities are obtained for different molecular and crystal architectures. In this sense, it is interesting to note (see Table 6.19) that the order of computed mobilities agrees with that experimentally found. More precisely, the smallest mobility is computed for compound **2b**; as observed, a larger mobility is computed for compound **2c**, and the largest value is computed for **1a**, in agreement with the observation. Notice that the correct order is also obtained without using the thermalized limit for the A jump of system **1a** (compare the computed charge mobilities in the fourth column of Table 6.19) or even assuming an identical value of the  $\lambda_{class}$  parameter (see Eq. (4.19)) for all of the systems investigated.

**Table 6.19** Computed electron mobilities  $\mu$  ( $cm^2 V^{-1} s^{-1} \cdot 10^2$ ) for the crystals of **1a**, **2b**, and **2c**; data averaged over 15 groups of 2000 trajectories.<sup>42</sup>

	only <i>intracolumn</i> paths, 10 <sup>6</sup> MC steps	<i>intracolumn</i> (thermalized limit) and <i>intercolumn</i> paths, 10 <sup>8</sup> MC steps	<i>intracolumn</i> and <i>intercolumn</i> paths, 10 <sup>8</sup> MC steps (10 <sup>7</sup> MC steps)
<b>1a</b>		8.00	4.21 (4.25)
<b>2b</b>	2.21		1.12 (1.12)
<b>2c</b>	5.88		1.91 (1.92)

We can analyze the computed mobilities in terms of charge transfer integrals, rate constants, and the arrangement of charge transfer paths available to each PBI derivative investigated. With regard to the electronic couplings, compound **2b** shows the largest value for an *intracolumn* jump. Nevertheless, its mobility is computed to be the lowest. The largest intramolecular reorganization energy of **2b** (Table 6.16) value may contribute to lower the efficiency of charge transport. However, the computed rate constant associated with jump A in Table 6.18 is larger than the largest  $k_{eT}$  of **2c**. The lower mobility of **2b** as compared to **2c** (and to **1a**) is mostly due to a *retardation effect* induced by the different charge transfer probabilities associated with *intracolumn* paths A and B along the same *intracolumn* direction. The alternation of A and B jumps along the column, schematically shown by red and blue

arrows in Figure 6.92, implies that the charge carrier can propagate along the column by alternating fast and slow jumps. As a result, the charge transport along one PBI column is retarded by the frequent oscillation of the charge trapped in a dimer and it "loses time" before it can find its way one molecule forward along the column. This effect is evident by inspecting a short portion of the KMC trajectory (Figure 6.95) showing the propagation of the charge for systems **2b**, **2c** and **1a** as a function of time. The comparison shows that, for system **2b**, the charge carrier is more frequently trapped (black rectangles in the Figure 6.95) inside the same dimer, without advancing. The effect is visible also for **2c**, although it is less extensive and frequent because of the lower asymmetry of A-B jump probability (see Table 6.18). Thus, asymmetry in the backward and forward charge transfer probabilities along a given direction leads to a retardation effect, which is larger for larger asymmetries, namely, for compound **2b** than for compound **2c**. Accordingly, for system **1a**, there is no trace of retardation effect in Figure 6.95. In passing, we note that such retardation effect is at the origin of a further remarkable discrepancy between the charge mobilities computed using the KMC procedure or employing the approximate formulation of the diffusion coefficient based on isotropic diffusion, often used in previous works.<sup>116,147</sup>

The asymmetry discussed for the *intracolumn* charge transfer probabilities of **2b** and **2c** and responsible for the retardation effect extends also to intercolumn paths if two different molecular sites (the two enantiomeric forms) form the dimer: In this case, the  $k_{eT}$  associated with the jump in one direction or in the opposite direction, starting from the same molecule, are not identical (see Table 6.18). In the case of **2b**, the *intercolumn* jumps associated with non-negligible charge transfer probabilities are indicated in Figure 6.92: The asymmetry effect is dramatic, and the jumps labeled C and D do not have a counterpart (negligible charge transfer probabilities) in the opposite direction, starting from the same red molecule in the Figure 6.92. In addition, the efficiency of *intercolumn* jumps in **2b** (and also **2c**) is modest (see Table 6.18) as compared to **1a**. As a result, jumps from the red molecule (in Figure 6.92) to nearby PBI columns occur only in one direction, and charge carriers for **2b** are expected to propagate mainly along columns of PBI stacked molecules, with seldom jumps from one column to another. This expectation is confirmed by the KMC simulations, as shown by the selected trajectories in Figure 6.96.

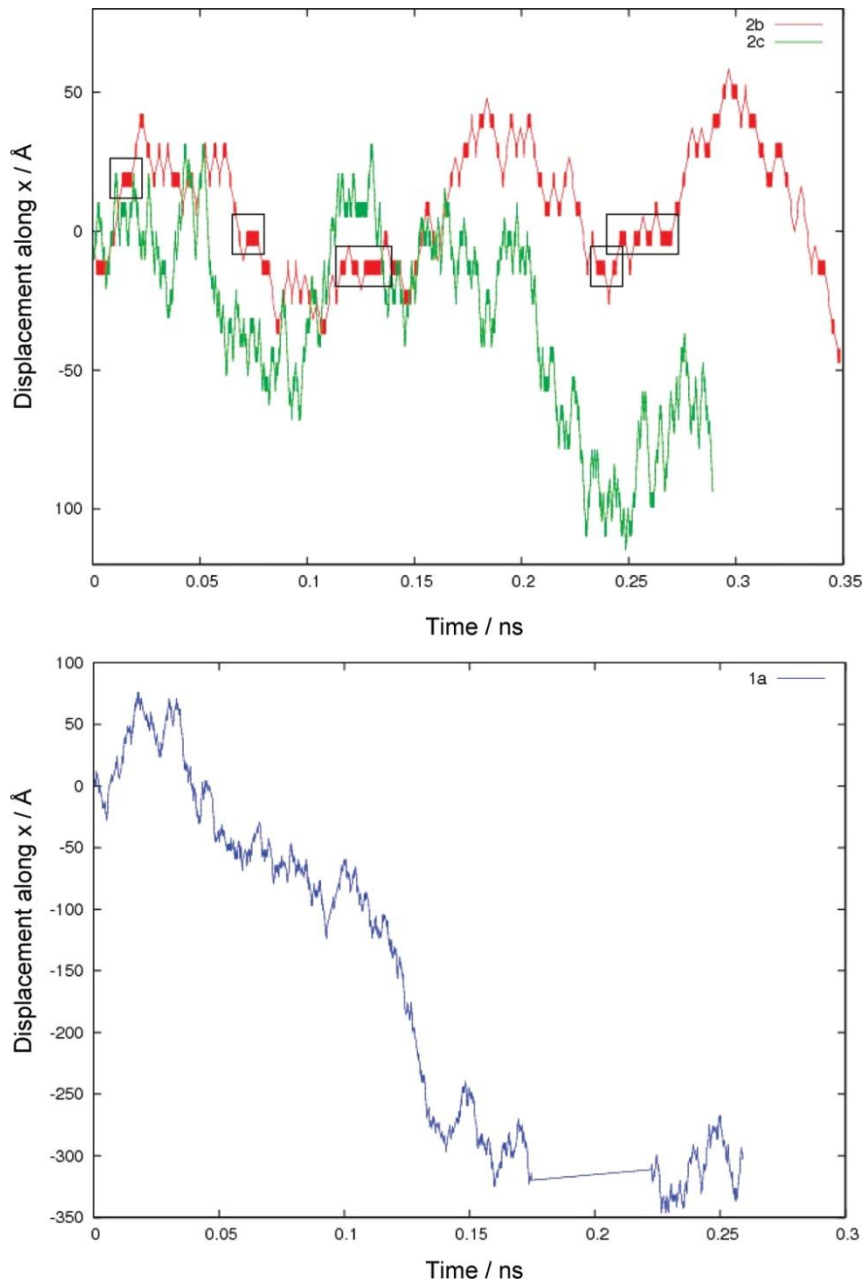


**Figure 6.95** (top) First 1000 steps of a KMC trajectory of a charge carrier propagating along a crystal of **2b** (red) and **2c** (green). The trajectory of **2b** shows frequent oscillations (some of which are enclosed in black rectangles) induced by the presence of markedly alternating fast and slow paths ABABAB along the column. These oscillations do not advance the charge carrier and induce a "dimer-trapping retardation effect". The charge is trapped several times and keeps oscillating back and forth in a dimer before it finds its way along the column. The retardation effect is less marked in **2c** because of the similar probability associated with paths A and B. (bottom) For comparison, the first 1000 steps of a carrier propagating in **1a** (blue), for which a single path A is repeated along the column, show no evidence of a retardation effect. Figure adapted from <sup>42</sup>.

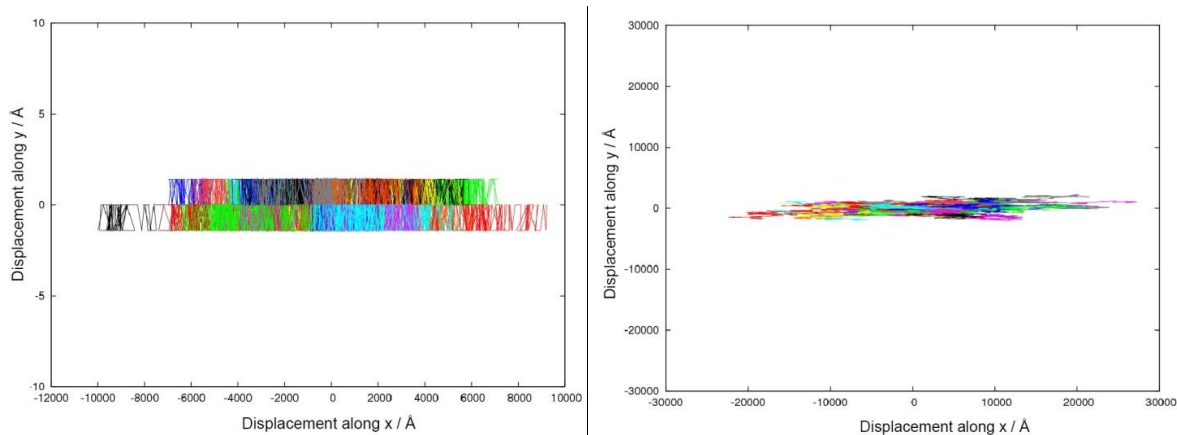


**Figure 6.96** (left) Representation of a number of KMC trajectories (in the  $x$ - $y$  plane) computed for system **2b** neglecting *intercolumn* jumps in the KMC simulations: The figure shows a perfectly monodimensional conduction of the charge along the  $x$  intra-column direction. (right) *Intercolumn* jumps are now included in the KMC simulations: The Figure shows still an approximately monodimensional conduction of the charge along the  $x$  intra-column direction. Figure adapted from 42.

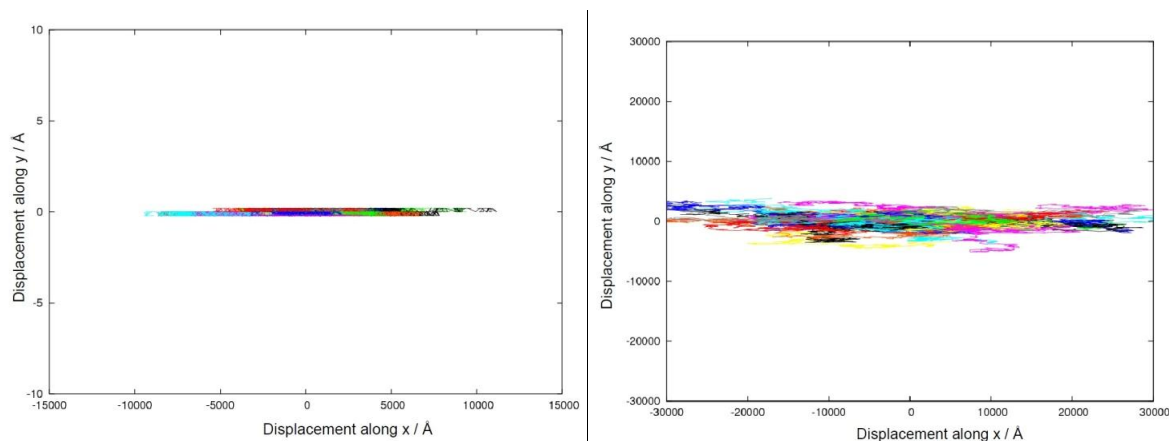


**Figure 6.97** (left) Representation of a number of KMC trajectories (in the  $x$ - $y$  plane) computed for system **2c** neglecting *intercolumn* jumps in the KMC simulations: The figure shows a perfectly monodimensional conduction of the charge along the  $x$  intra-column direction. (right) *Intercolumn* jumps are now included in the KMC simulations: The Figure shows still an approximately monodimensional conduction of the charge along the  $x$  intra-column direction. Figure adapted from 42.

The pattern of possible *intercolumn* jumps is slightly more symmetric for **2c**. In this case, as shown in Figure 6.93, the forward and backward jumps D and E are both associated with non-negligible charge transfer integrals and rate constants. We note, in passing, that the two jumps labeled C in Figure 6.93 are identical since the dimer involves two identical molecular sites (that is the same enantiomeric form) in the crystal. Nevertheless, even for **2c**, KMC simulations show a dominant charge propagation along the  $\pi$ -stacked PBI columns with less frequent jumps to nearby columns (Figure 6.97).

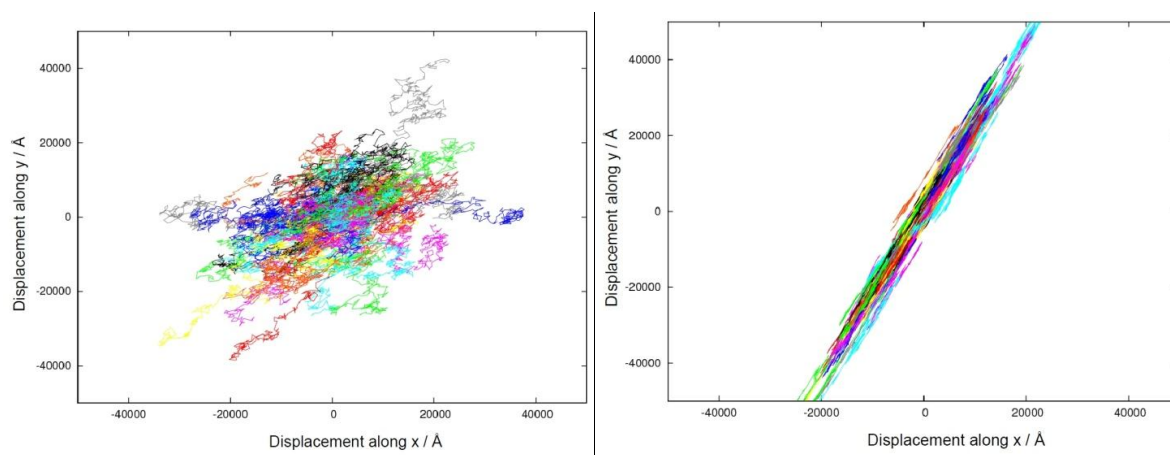


**Figure 6.98** (left) Representation of a number of KMC trajectories (in the  $x$ - $y$  plane) computed for system **1a** including *intercolumn* jumps and the thermalized value for the intra-column jump A: The figure shows an almost bidimensional conduction of the charge along the  $x$ - $y$  directions. (right) Herein the crystal value for intra-column probabilities are used: The figure shows an approximately monodimensional conduction along the inter-column jump direction. Figure adapted from <sup>42</sup>.

The large charge transfer integral associated with *intercolumn* path C of **1a** (Figure 6.91 and Table 6.18) implies that these *intercolumn* jumps are relatively efficient and, together with the *intracolumn* propagation along path A, lead to a quasi bidimensional conduction of the charge as seen in Figure 6.100, showing the path followed by the charge carrier in a series of KMC trajectories. In contrast, neglecting thermally induced disorder, a quasi monodimensional conduction would result along the *intercolumn* path C (Figure 6.98).

We can conclude that system **1a** shows the largest mobility because of its smaller intramolecular reorganization energies combined with large *intercolumn* and *intracolumn* charge transfer integrals and the absence of asymmetries inducing retardation effects. In contrast, systems **2b** and **2c** show similarly large charge transfer integrals whose effect is depressed by the presence of larger intramolecular reorganization energies (leading to reduced rate constants) combined with the retardation effect induced by the asymmetry of alternating fast and slow paths along the *intracolumn* direction. Although the order of computed charge mobilities is correct, the mobility of **2c** is computed to be *ca.* 2 times larger than that of **2b** while experimentally<sup>10f</sup> a ratio of 17 is found. This suggests that other factors are likely to influence the experimental values, such as, for instance, the presence of defects or traps.

#### 6.7.4 Structural and thermal effects on the charge transport of chlorinated PBIs

From the equilibrium structures of neutral and charged species, we estimated both electron affinities and intramolecular reorganization energies (see Figure 4.5) of the four chlorinated species **1d**, **2d**, **1b**, and **8Cl**. The inclusion of chlorine substituents in the bay region, for all compounds, leads to a marked twist of the perylene core, as well-known for other bay-substituted PBIs.<sup>58d,136c-e,138,142</sup> Chlorine substitution at the bay positions lowers the energy of the LUMO level (see Figure 6.99 for a graphical representation of frontier orbitals) and increases the electronic affinity of the PBI derivative, thereby strengthening the *n*-type character of the semiconductor. This effect can be appreciated by considering the energies of the LUMO levels of **1a** and **1d** reported in Table 6.20 and the correspondingly computed vertical and adiabatic *EAs* in Table 6.21. The inclusion of fluoroalkyl or fluoroaryl chains at the imide position (compare, for instance, **1b** and **2d**) in the bay region lowers the LUMO level by *ca.* 0.43 *eV* and correspondingly increases the adiabatic electron affinity (*AEA*, see Table 6.21) by 0.34 *eV*. The computed LUMO energies are in very good agreement with those estimated from experimental reduction potentials (Table 6.20). Interestingly, the transport gap ( $\Delta E_{H-L}$ ) is weakly affected by the substitution and is very similar for all tetrachlorinated compounds. The computed gap is slightly smaller for compound **1a** as a result of the increased conjugation associated with the planar perylene chromophore, and it is slightly larger for the octachloro derivative, owing to the increased twisting of the perylene core in the latter. Table 6.20 shows also that the transport gap decreases by about 0.30-0.35 *eV* upon doping.

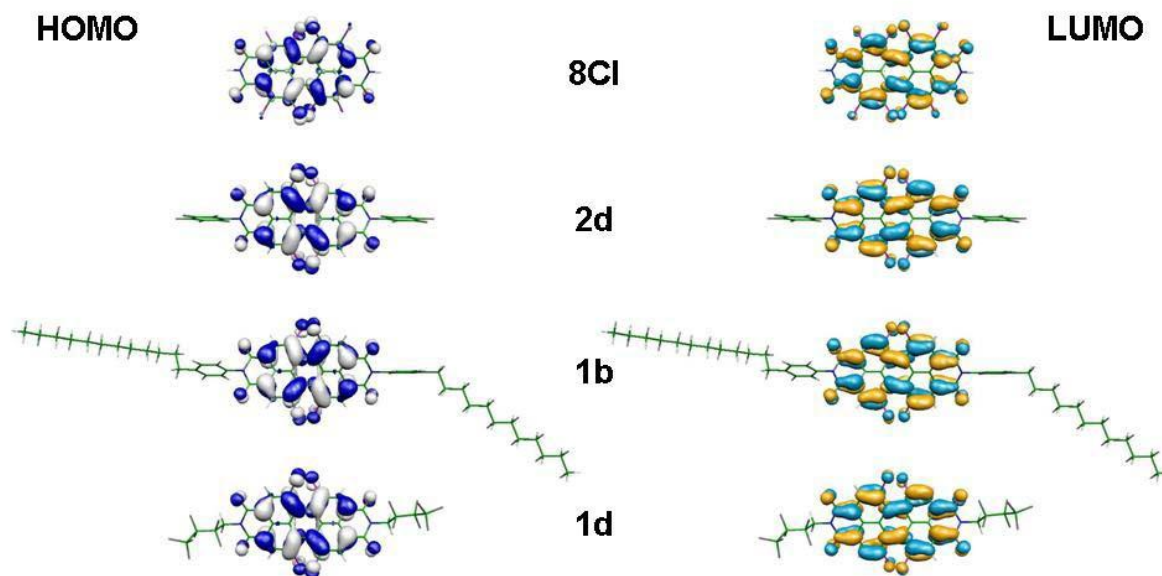


**Figure 6.99** The frontier molecular orbitals of **8Cl**, **2d**, **1b**, and **1d**. The LUMO orbitals were involved in the calculations of  $V_{ij}$  electronic coupling integrals, computed at B3LYP/3-21G\* level of theory. Figure adapted from <sup>43</sup>.

**Table 6.20** Frontier orbital energies of **8Cl**, **2d**, **1d**, and **1a** computed at the B3LYP/3-21G\* optimized structures of the neutral species along with the transport gaps computed at the optimized structures of the neutral and anionic species. All values are given in eV.<sup>43</sup>

B3LYP/3-21G*	$E_{\text{HOMO}}$	$E_{\text{LUMO}}$	$E_{\text{LUMO}}^{\text{a}}$	$\Delta E_{\text{H-L}}^{\text{geo-n}}$	$\Delta E_{\text{H-L}}^{\text{geo-a}}$
<b>8Cl</b>	-6.92	-4.18	-4.23 <sup>c</sup>	2.74	2.38
<b>2d</b>	-6.79	-4.17	-4.11 <sup>b</sup>	2.62	2.31
<b>1b</b>	-6.39	-3.74	-3.80 <sup>c</sup>	2.65	2.27
<b>1d</b>	-6.70	-4.08	-4.06 <sup>b</sup>	2.62	2.31
<b>1a</b>	-6.35	-3.78	-3.85 <sup>b</sup>	2.57	-

<sup>a</sup> LUMO energies estimated from experimental reduction potentials: <sup>b</sup> from <sup>58d</sup>, <sup>c</sup> from <sup>58c</sup>.

**Table 6.21** *VEAs*, *AEAs*, and AP intramolecular reorganization energies  $\lambda_i$  for **8Cl**, **2d**, **1d**, and **1b** computed at the B3LYP/3-21G\*. All values are given in *eV*.<sup>43</sup>

B3LYP 3-21G*	<i>VEA<sub>n</sub></i>	<i>VEA<sub>a</sub></i>	<i>AEA</i>	$\lambda_i^{AP,VEA}$	$\lambda_i^{AP,n}$	$\lambda_i^{AP,c}$	$\lambda_i^{AP}$
<b>8Cl</b>	2.98	3.29	3.14	0.31	0.157	0.157	0.313
<b>2d</b>	2.99	3.29	3.14	0.30	0.152	0.152	0.304
<b>1b</b>	2.63	2.97	2.80	0.34	0.171	0.170	0.341
<b>1d</b>	2.86	3.18	3.02	0.32	0.159	0.160	0.319
<b>1a</b>	2.49	2.80	2.65	0.31	0.154	0.155	0.309

The intramolecular reorganization energies (collected in Tables 6.21) fall in the region 0.30-0.34 *eV*, similarly to those of other PBI derivatives.<sup>42,143</sup> The computed values are relatively large compared with those of unsubstituted PBIs (of the order of 0.26 *eV*), owing to the presence of the bay and imide flexible substituents.<sup>42</sup> The computed vibrational contributions to the intramolecular reorganization energies collected in Figures 6.100-101 are similar for all the systems except for **8Cl** which shows a number of contributions with lower frequency because of the larger number of Cl substituents. The contributions from frequencies above 250 *cm*<sup>-1</sup> were employed to estimate the effective parameters of the single quantum mode in Eq. (4.19). The remaining contributions were included into the  $\lambda_{class}$  parameter<sup>42</sup> together with the outer-sphere term that was assumed to be 0.01 *eV* for all the systems investigated<sup>141</sup> (see Table 6.22). These parameters were employed to estimate the charge transfer rate constants of the PBI derivatives according to (Eq. 4.19).

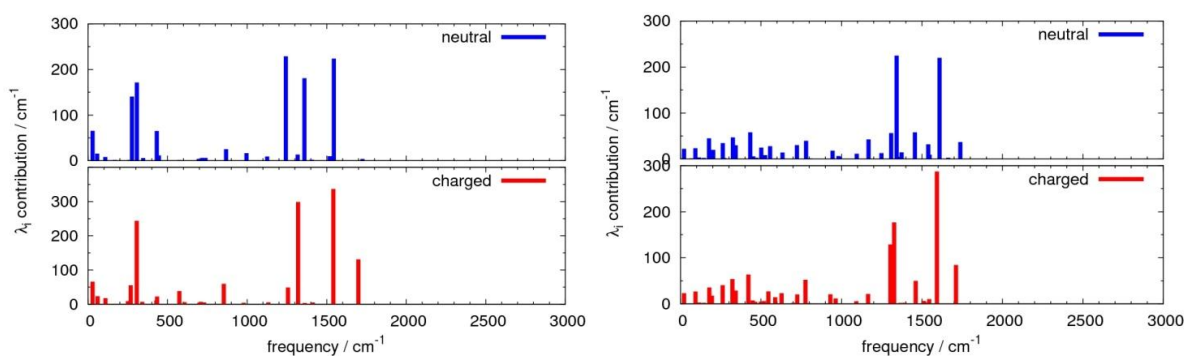


**Figure 6.100** The vibrational frequencies contributions to the computed  $\lambda_i^{HR}$  of: (left) **8Cl** neutral (top) and anionic (bottom) species; (right) **2d** neutral (top) and anionic (bottom) species. From B3LYP/3-21G\* calculations. It is seen that the contributions are very similar for the neutral and charged states. Figure adapted from <sup>43</sup>.

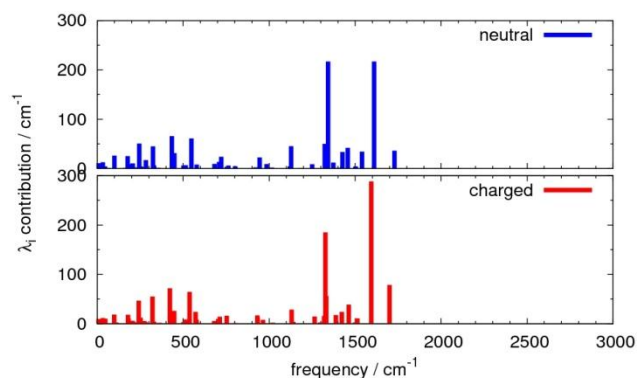


**Figure 6.101** The vibrational frequencies contributions to the computed  $\lambda_i^{HR}$  of: **1d** neutral (top) and anionic (bottom) species. From B3LYP/3-21G\* calculations. It is seen that the contributions are very similar for the neutral and charged states. Figure adapted from <sup>43</sup>.

**Table 6.22** Effective frequency  $\omega_{eff}$  and associated Huang-Rhys factor  $S_{eff}$  employed in the evaluation of charge transfer rate constants.<sup>43</sup>

B3LYP/3-21G*	<b>1a</b>	<b>1b</b>	<b>1d</b>	<b>2d</b>	<b>8Cl</b>
$\omega_{eff}$ ( $cm^{-1}$ ) <sup>a</sup>	930	839 <sup>b</sup>	840	837	655
$S_{eff}$ <sup>a</sup>	2.504	2.699 <sup>b</sup>	2.713	2.685	3.719
$\lambda_i^{HR}$ (eV)	0.309	0.341 <sup>b</sup>	0.319	0.304	0.313
Intramolecular $\lambda_{class}$	0.020	0.060	0.036	0.025	0.011
Total $\lambda_{class}$	0.030	0.070	0.046	0.035	0.021

<sup>a</sup> Only frequencies above 150  $cm^{-1}$  are considered in the calculation of the effective parameters for the model systems. <sup>b</sup> Mean values of those computed for **2d** and **1d** were reported for **1b**. A value of  $\lambda_o$  of 0.01 eV was assumed based on recent estimates.<sup>141</sup>

A summary of geometry changes upon doping for the chlorinated PBIs is depicted in Figure 6.102, from which it can be seen that the geometry change is very similar for all derivatives with a modest difference only for bonds 6, 7, 23, and 24 reflecting the effect of different imide substituents. The largest bond length variations occur for bonds 3, 10, 20, and 27 whose length decreases upon doping and for bonds 2, 11, 19, and 28 whose length increases upon doping. The charge transfer will be assisted by vibrational modes displaying a non-negligible projection over this geometry change, as confirmed by the inspection of modes exhibiting the largest contributions to the reorganization energy, most of which are computed to be above 1000  $cm^{-1}$  (Figure 6.103).

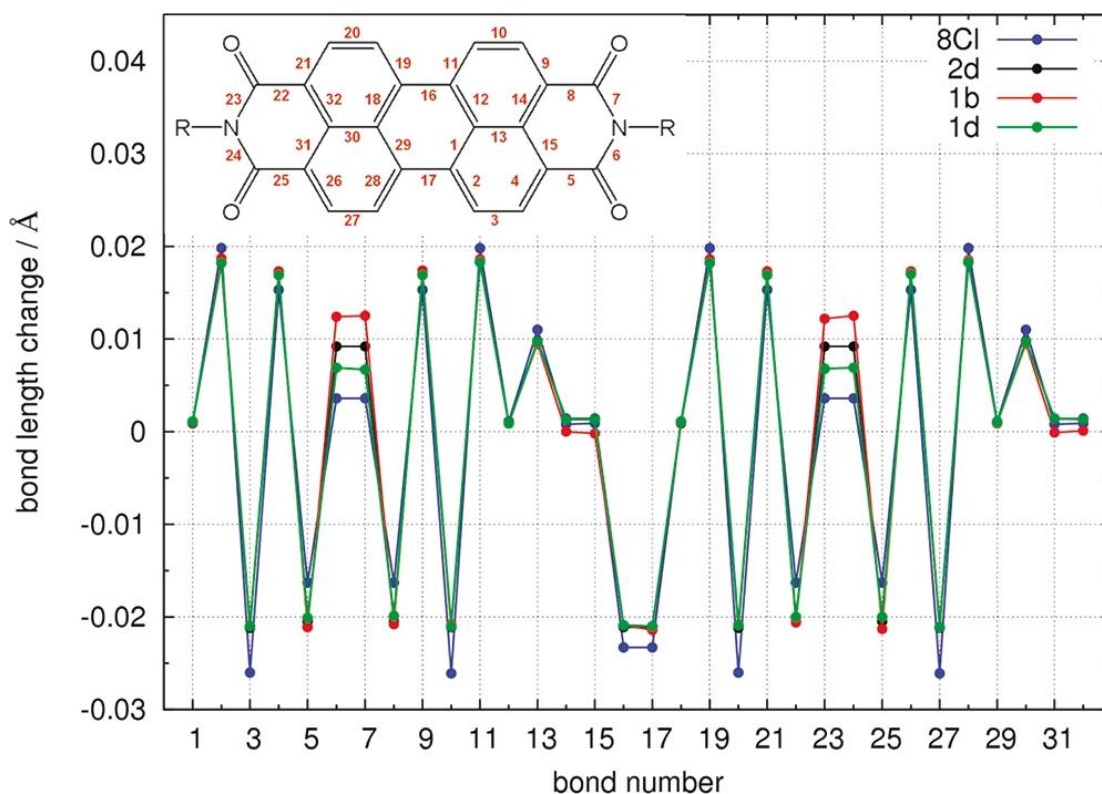


**Figure 6.102** B3LYP/3-21G\* computed bond length changes upon charging (anion-neutral) for **8Cl** (blue), **2d** (black), **1b** (red), and **1d** (green). Bond numbering as depicted in the inset. Figure adapted from <sup>43</sup>.

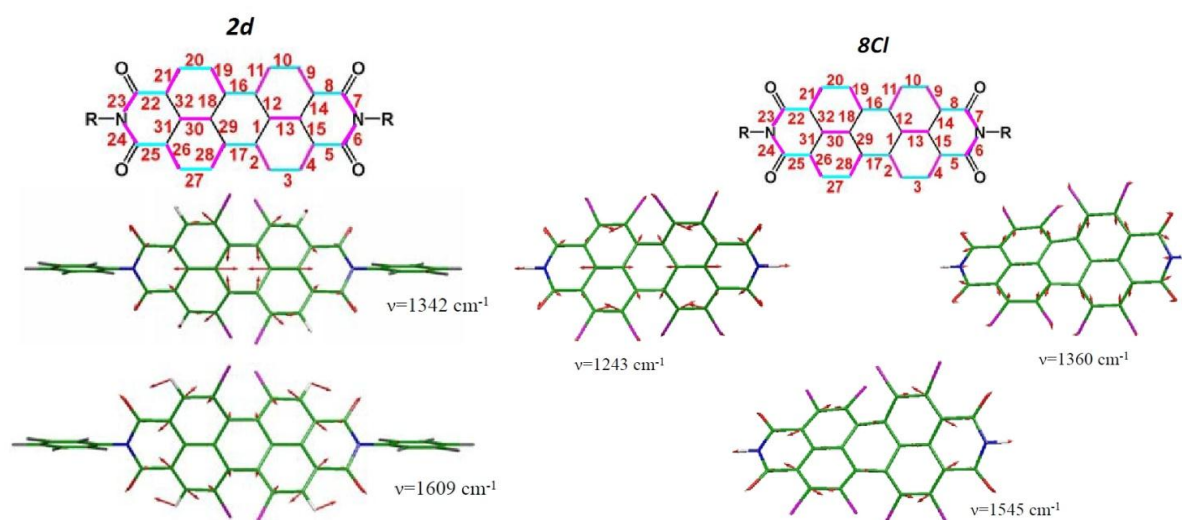


**Figure 6.103** Compounds **2d** (left) and **8Cl** (right). (top) Schematic representation of geometry change upon doping: (magenta) bonds whose length increases upon doping, (cyan) bonds whose length decreases upon doping. (bottom) Vibrational modes (neutral species) contributing most to the intramolecular reorganization energy. It can be seen that nuclear motions of the selected vibrations overlap with the computed geometry change. Figure adapted from <sup>43</sup>.

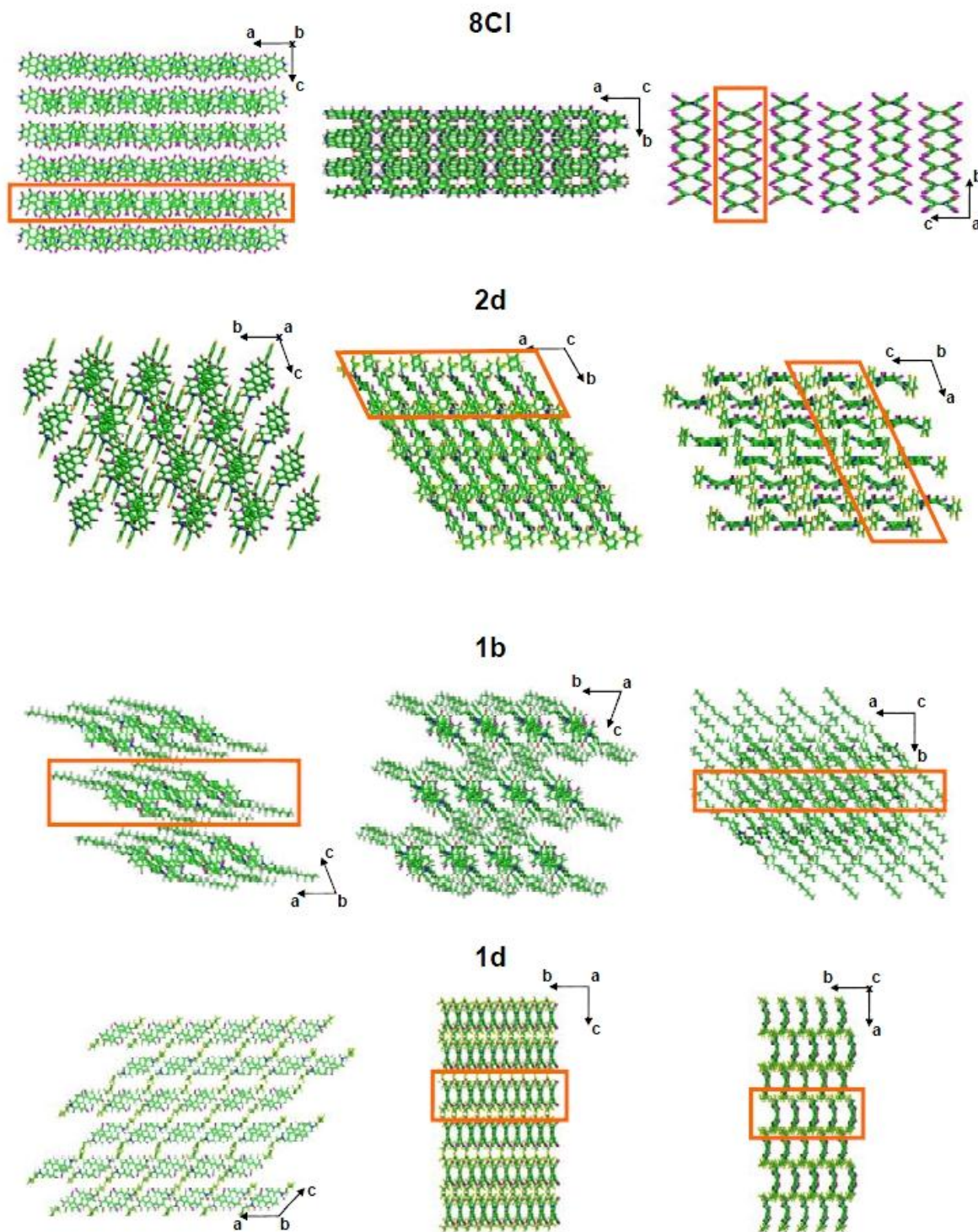


**Figure 6.104** Molecular crystals of **8Cl**, **2d**, **1b**, and **1d** side and top views showing the presence of columns (**2d**, **1b**, and **1d**) or walls (**8Cl**) of  $\pi$ -stacked PBI molecules. From top to bottom: **8Cl** belongs to the orthorhombic  $Pbcn$  space group; **2d** and **1b** belong to the triclinic  $P-1$  space group; **1d** belongs to the monoclinic  $C2$  space group. Figure adapted from <sup>43</sup>.

The assumption of the hopping mechanism for the charge transport in crystals of PBI derivatives is justified because of the relatively large value of their  $\lambda_i$  parameters, although the magnitude of most electronic couplings discussed below places these systems close to the limits of the non-adiabatic model.<sup>148</sup> Nevertheless, it should be noted that the emphasis here is not on absolute values of computed charge mobilities but on the structural motifs determining different charge transport properties and thermal fluctuations of electronic couplings.

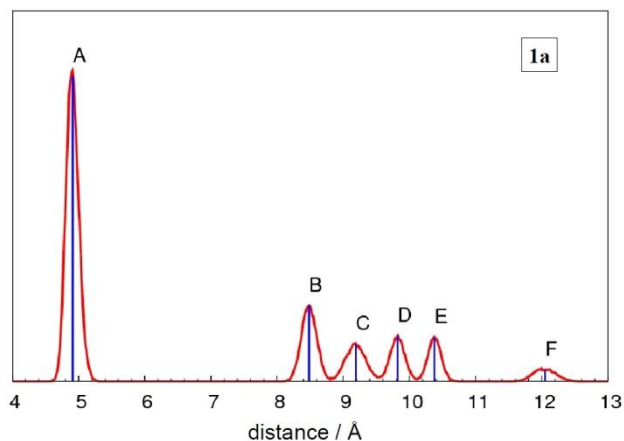


**Figure 6.105** PBI derivative **1a** comparison between: (red) radial distribution function of intermolecular distances between centers of mass, computed from MD simulations at 300 K; (blue) center of mass distances computed for the crystal structures. Figure adapted from <sup>43</sup>.

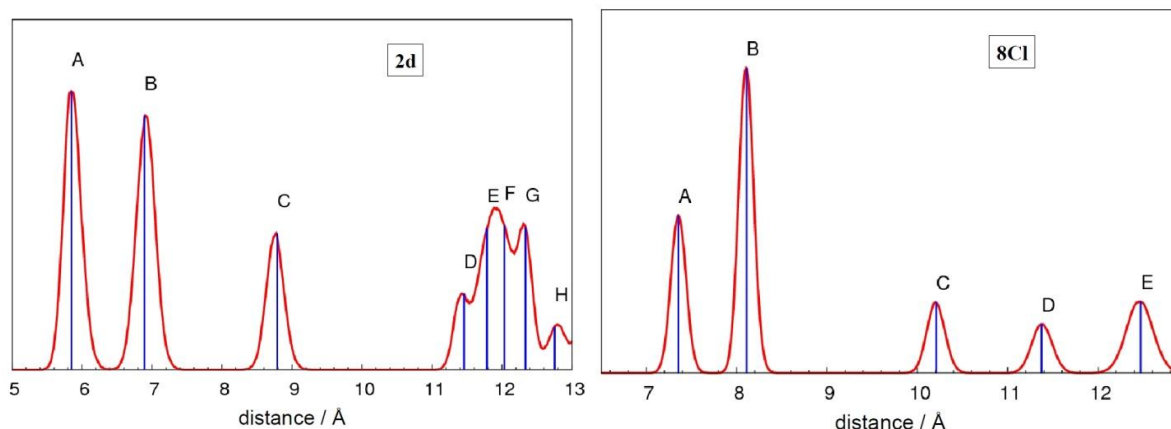


**Figure 6.106** PBI derivatives **2d** (left) and **8Cl** (right) comparison between: (red) radial distribution function of intermolecular distances between centers of mass, computed from MD simulations at 300 K; (blue) center of mass distances computed for the crystal structures. Figure adapted from <sup>43</sup>.

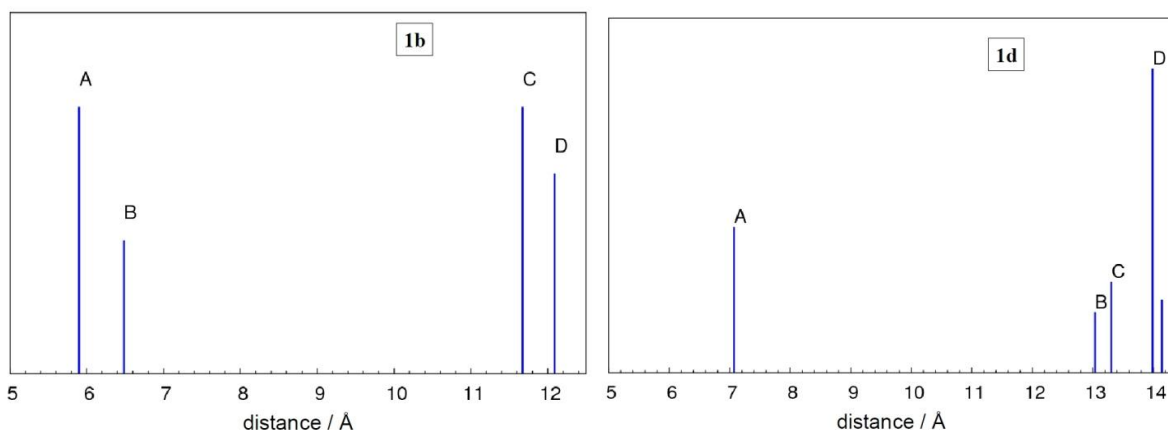


**Figure 6.107** PBI derivatives **1b** (left) and **1d** (right): center of mass distances computed at the crystal structure. Figure adapted from <sup>43</sup>.

To investigate the possible charge hopping paths we extracted, for each crystal (Figure 6.104), all the possible neighbors of a given molecule. The distribution of distances between centers of mass (at the crystal structure) along with the radial distribution functions extracted from MD simulations are collected in Figures 6.105-107. The paths for charge propagation were subsequently selected on the basis of their computed electronic couplings  $V_{ij}$  collected in Table 6.23. Only charge jumps associated with electronic couplings larger than  $30 \text{ cm}^{-1}$  were included in the KMC simulations.

The crystals of the PBI derivatives investigated in this work belong to the triclinic  $P-1$  group (**1a**, **1b**, **2d**), to the monoclinic group  $C2$  (compound **1d**), and to the orthorhombic group  $Pbcn$  (**8Cl**). As for other PBI derivatives,<sup>58d,140a-b,149</sup> the tendency to form columns of  $\pi$ -stacked PBI units is clearly seen for **1a**, **1b**, **1d**, and **2d** (Figure 6.104). In contrast, the **8Cl** PBI derivatives assemble in a slipped brickstone arrangement similarly to triisopropylsilylethynyl pentacene and related materials.<sup>22b,150</sup> Accordingly, the charge transport is discussed in terms of *intracolumn* jumps and *intercolumn* jumps for **1a**, **1b**, **1d**, and **2d** and in terms of *intrawall* and *interwall* jumps for **8Cl**.

**Table 6.23** Electronic couplings  $V_{ij}$  (computed at the static crystal structure) and charge transfer rate constants  $k_{eT}$  computed for the systems investigated at the B3LYP/3-21G\* level of theory.<sup>43</sup>

crystal	dimer	<i>intrawall</i> or <i>intracolumn</i> distance (Å)	$V_{ij}^{\text{LUMO}}$ ( $\text{cm}^{-1}$ )	$k_{eT}$ ( $\text{ps}^{-1}$ )	dimer	<i>interwall</i> or <i>intercolumn</i> distance (Å)	$V_{ij}^{\text{LUMO}}$ ( $\text{cm}^{-1}$ )	$k_{eT}$ ( $\text{ps}^{-1}$ )
<b>8Cl</b>	A	7.3585	28	-	C	10.2090	62	0.035
	B	8.1101	327	3.9	D	11.3724	27	-
					E	12.4691	-15	-
<b>2d</b>	A	5.8518	71	0.34	C	8.7899	229	3.59
	B	6.8950	-299	6.09	D	11.4571	10	-
					F	12.0337	14	-
					H	12.7513	0	-
<b>1d</b>	A	7.0704	46	0.11	B	13.0350	2	-
					C	13.3065	1	-
					D	13.9866	-4	-
<b>1b</b>	A	5.9016	136	0.67	D	12.0878	-31	0.035
	B	6.4839	-142	0.72				
<b>1a</b>	A	4.9104	400 <sup>b</sup>	14.5	C	9.1891	338	10.5
					F	12.0472	-33	0.9

We briefly recall that for **1a** there are two major charge paths to be considered (see Figure 6.91; note that, according to the new notation, closely on the basis of the radial distribution in Figure 6.105, dimers D are now referred to as F): the *intracolumn* path A along the *a* crystallographic axis and the *intercolumn* path C occurring in the *a-b* crystallographic plane. We showed previously<sup>42</sup> that the *intracolumn* charge transport is strongly affected by thermal effects that contribute significantly to the fluctuation of the  $V_{ij}$  electronic coupling which is otherwise remarkably smaller at the crystal structure. Here we report more extensive MD simulations followed by QM evaluation of electronic couplings. The resulting  $V_{ij}$  distribution is shown in Figure 6.108, and its fitting with a Gaussian function indicates a standard deviation  $\sigma$  of *ca.*  $350 \text{ cm}^{-1}$  with an average value of  $\langle V_{ij} \rangle = 155 \text{ cm}^{-1}$ , from which we extracted the thermalized value<sup>42,144,145b</sup> of *ca.*  $400 \text{ cm}^{-1}$  reported in Table 6.23 and employed to perform KMC simulations. The electronic coupling fluctuations were further analyzed by determining the Fourier transform of their autocorrelation function<sup>145b</sup> also reported in

Figure 6.108, showing active lattice vibration in the 10-50  $cm^{-1}$  frequency range. Using the static crystal value of the electronic coupling computed for path A of **1a** (ca.  $-23\text{ cm}^{-1}$ ),<sup>42</sup> we obtain a rate constant much smaller than  $1\text{ ps}^{-1}$ . Therefore, the frequency of most of the active lattice vibrations is larger than the hopping frequency, and the use of a thermalized value in the evaluation of the rate constant for path **1a** is justified. Note that this is the only case in which we made use, in this work, of the thermalized limit. Because of the magnitude of the largest charge transfer rate constants computed in this work (see Table 6.23), it can be argued that low-frequency modes may be too slow to follow the charge. We note, however, that the single effective mode describing non-classical contributions to the reorganization energy is always above  $830\text{ cm}^{-1}$  (except for **8Cl** for which it is still  $655\text{ cm}^{-1}$ ), while the classical modes contribute only to a minor extent to reorganization energies.

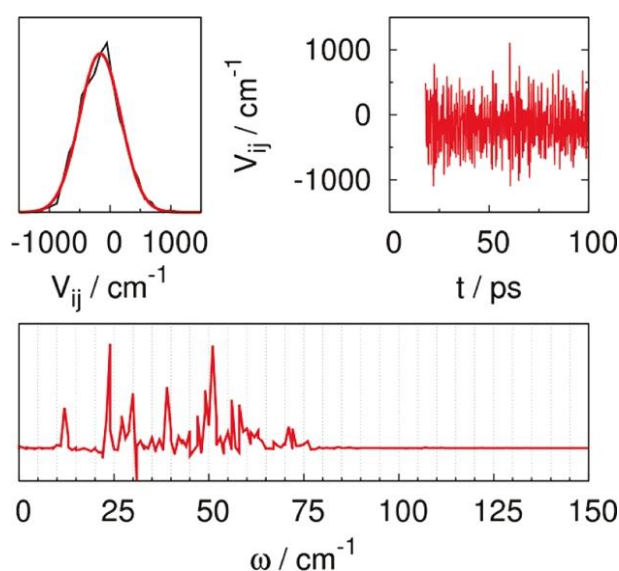


**Figure 6.108** Thermal disorder effects (300 K) on the distribution of the *intracolumn* electronic coupling associated with path A of **1a**. (top, left) Gaussian fitting of the B3LYP/3-21G\* computed dispersion of electronic couplings. (top, right) Dispersion of computed values as a function of simulation time. (bottom) Fourier transform of the autocorrelation function of the computed electronic couplings. Figure adapted from <sup>43</sup>.

To gain some information on the shape of the active lattice modes, we carried out rigid body vibrational frequency calculations on crystal supercells and examined graphically the eigenvectors associated with frequencies corresponding to peaks in the Fourier transforms. Typical lattice vibrations of **1a** falling in the correct frequency region are depicted in Figure 6.109. The intermolecular motion displaces pairs of adjacent PBI cores (belonging to a PBI

column) along the short or long molecular axis, thereby determining a change in  $\pi$ - $\pi$  stacking and orbital overlap which contributes to the observed integral fluctuation.

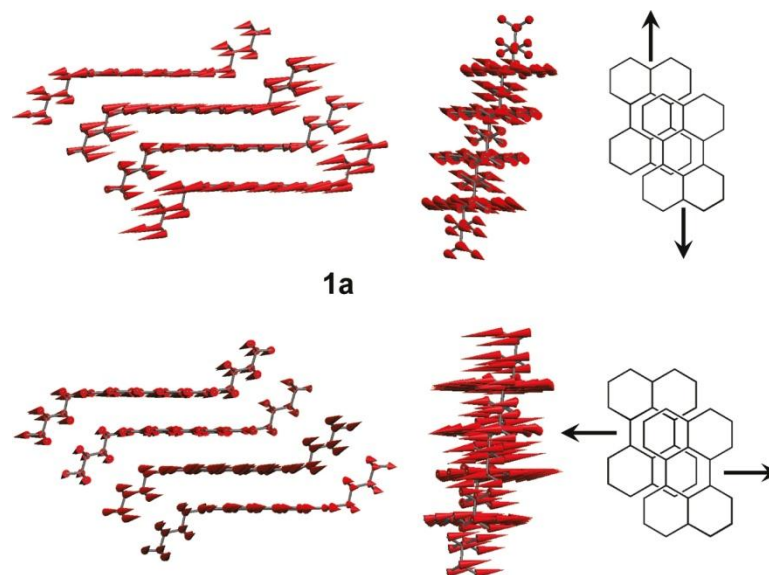


**Figure 6.109** Representative lattice vibrations (top,  $\omega=23\text{ cm}^{-1}$ ; bottom,  $\omega=31\text{ cm}^{-1}$ ) governing the modulation of *intracolumn* charge transfer A of **1a**. Figure adapted from <sup>43</sup>.

The large electronic coupling associated with the *intercolumn* path C of **1a** (see Figure 6.91 and Table 6.23) is competitive with that of the *intracolumn* propagation along path A, therefore leading to a quasi-bidimensional conduction of the charge in the *a-b* crystallographic plane, with a marked directionality along path C, as seen in Figure 6.110.

The computed electron mobility of **1a** is the largest among the PBI derivatives investigated (see Table 6.24) in agreement with the observation. From X-ray measurements on thin films, it has been suggested that in most cases the PBI derivatives adopt an edge-on configuration,<sup>58c</sup> namely, a perpendicular arrangement of the  $\pi$  conjugated cores with respect to the dielectric surface of the OTFT device. This is the optimal orientation for efficient charge transport between source and drain electrodes. For **1a** (and other PBI derivatives), the edge-on configuration is expected to correspond to layers of molecules oriented as in the *a-b* crystallographic plane since the most efficient charge transport occurs in this plane. For this reason, we explored the effect of application of an electric field along *a* and other directions selected in the crystallographic *a-b* plane. The computed TOF mobility along *a* is indeed large, owing to the favorable *intracolumn* path, but an even larger mobility is predicted by

applying the field in the  $a$ - $b$  plane along path C, thereby underscoring the importance of available *intercolumn* charge hopping paths.

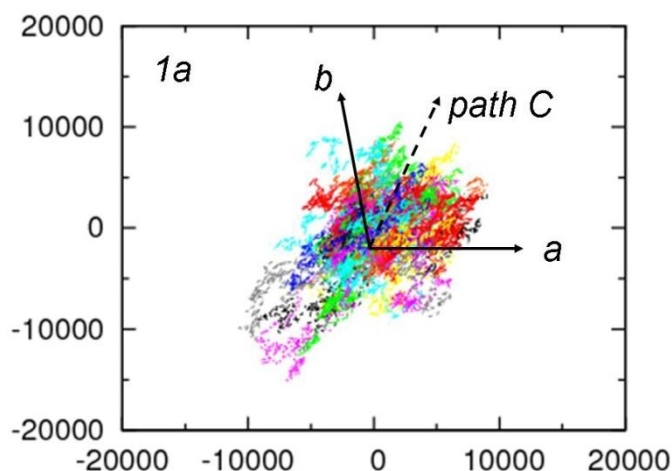


**Figure 6.110** Representation of a number of KMC trajectories (in the  $a$ - $b$  crystallographic plane) computed for system **1a**. The Brownian motion of the charge carrier shows an approximately bidimensional conduction in the  $a$ - $b$  plane corresponding to sequences of *intracolumn* and *intercolumn* jumps between PBI units. The direction of path C is also indicated. Figure adapted from <sup>43</sup>.

**Table 6.24** Computed electron mobilities  $\mu$  for the crystals of PBI derivatives **1a**, **1b**, **1d**, **2d**, and **8Cl**, and comparison with experimental data.<sup>43</sup>

	$\mu^a$ ( $cm^2 V^{-1} s^{-1}$ )	$\mu^b$ ( $cm^2 V^{-1} s^{-1}$ )	$\mu_{exp}$ ( $cm^2 V^{-1} s^{-1}$ )
<b>1a</b>	0.28	0.63 (path C); 0.40 ( $a$ -axis)	1.42 <sup>c</sup>
<b>1b</b>	0.012	-	0.045 <sup>d</sup>
<b>1d</b>	$4 \cdot 10^{-3}$	-	$4 \cdot 10^{-5c}$
<b>2d</b>	0.08	0.19 ( $y$ -axis); 0.11 ( $a$ -axis)	0.28 <sup>c</sup>
<b>8Cl</b>	0.11	0.30 ( $a$ -axis); 0.08 ( $b$ -axis)	0.91 <sup>e</sup>

<sup>a</sup> Charge mobility in the absence of applied electric fields. <sup>b</sup> Charge mobility for an electric field of  $10^5 V cm^{-1}$  directed as indicated in parentheses. <sup>c</sup> From <sup>58d</sup>. <sup>d</sup> From <sup>139</sup>. <sup>e</sup> From <sup>58c</sup>.

Moving to the tetrachlorinated derivative **2d**, inspection of Table 6.23 shows that the pattern of electronic couplings is similar to **1a** in that there are two major active channels for charge propagation: one *intracolumn* path along the  $a$ -axis and one *intercolumn* path via dimers C occurring in the  $a$ - $b$  plane (see Table 6.23, Figure 6.111, and Figure 6.106). While there is only

one type of *intracolumn* jump (labeled A) for **1a** and **1d**, there are two different *intracolumn* jumps (labeled A and B) in the crystals of **2d** (Figure 6.111, paths A and B indicated with red and blue arrows) and **1b**. The two *intracolumn* jumps of **2d** (and **1b**) originate from the presence of two different molecular sites in the crystal (corresponding to the two enantiomers of the core-twisted PBI) forming dimeric pairs. These have been envisaged as potential electron traps in previous experimental work<sup>58d</sup> and were proposed, in our previous investigation on fluorinated PBI derivatives<sup>42</sup> (see Section 6.7.3), to be responsible for a *retardation effect*. A similar problem arises along the *intercolumn* path since the counterpart of jump C in the opposite direction, starting from the same reference molecule, is jump H whose associated electronic coupling is negligible. Also the remaining charge transfer paths are associated with negligible couplings and were therefore neglected in the following KMC simulations.

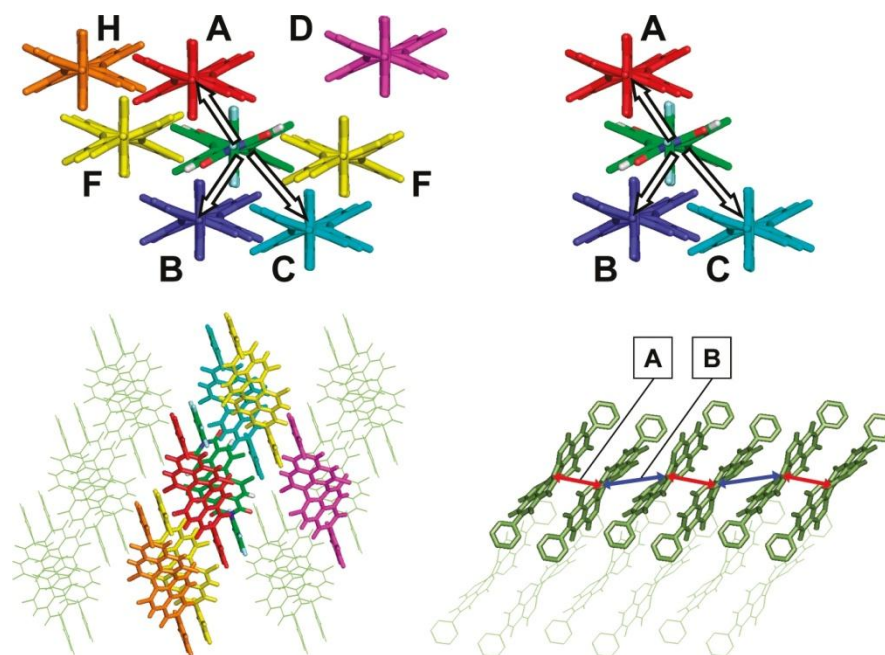


**Figure 6.111** Crystal of **2d**: (top, left) The possible *intracolumn* (blue and red molecules) and *intercolumn* (cyan, yellow, orange, and magenta molecules) paths taking as reference the green central molecule. (top, right) The jumps included in KMC simulations owing to non-negligible charge transfer integrals. (bottom, left) Top view of the *intracolumn* and *intercolumn* charge paths and (bottom, right) the *intracolumn* paths A (red arrows) and B (blue arrows). The sequence of red and blue arrows underscores that two different jumps (fast and slow) alternate along the *intracolumn* path. Figure adapted from <sup>43</sup>.

The charge propagation in crystals of **2d** occurs mainly in the crystallographic *a-b* plane (see Figure 6.112), following the available *intracolumn* paths A-B and the *intercolumn* path C. Therefore, the edge-on configuration experimentally detected in thin films is expected to correspond to layers of molecules oriented as in the *a-b* crystallographic plane, the plane on which the most efficient charge transport occurs. The *intracolumn* path sequence suffers from the dimer-trapping (retardation) effect<sup>42</sup> which results in frequent trapping of the charge on a molecular dimer. This originates from the difference in the forward and backward *intracolumn* charge transfer rates and reduces the charge mobility. Indeed, the two intracolumn jumps A and B of **2d** show a marked asymmetry, as indicated by the magnitude of computed electronic couplings and rate constants (see Table 6.23). This effect is evident by inspecting a short portion of the KMC trajectory (see Figure 6.113) showing the propagation of the charge along the *a* direction as a function of time. The figure on the top shows the trajectory obtained neglecting the *intercolumn* path. The trajectory of **2d** shows frequent oscillations induced by the presence of markedly alternating slow and fast paths A-B along the PBI column. These oscillations do not advance the charge carrier and determine the dimer-trapping or retardation effect. The charge is trapped several times and keeps oscillating back and forth in a B dimer before it finds its way along the column. The figure on the bottom shows the trajectory obtained when also *intercolumn* paths are taken into account. Because of the comparable charge transfer rate constant of jumps B and C, the *intercolumn* path offers an efficient escape to the charge that would be otherwise trapped along the PBI column. The charge escapes from the dimer-trapping sequence of *intracolumn* paths by jumping to a nearby PBI column through path C, that is, by sequences of B-C-B-C jumps. The resulting bidimensional charge propagation in the *a-b* plane, with a marked tendency along the crystallographic *b* direction (see Figure 6.112), results from the sequence of B and C jumps whose vectorial composition moves exactly along the *b*-axis.

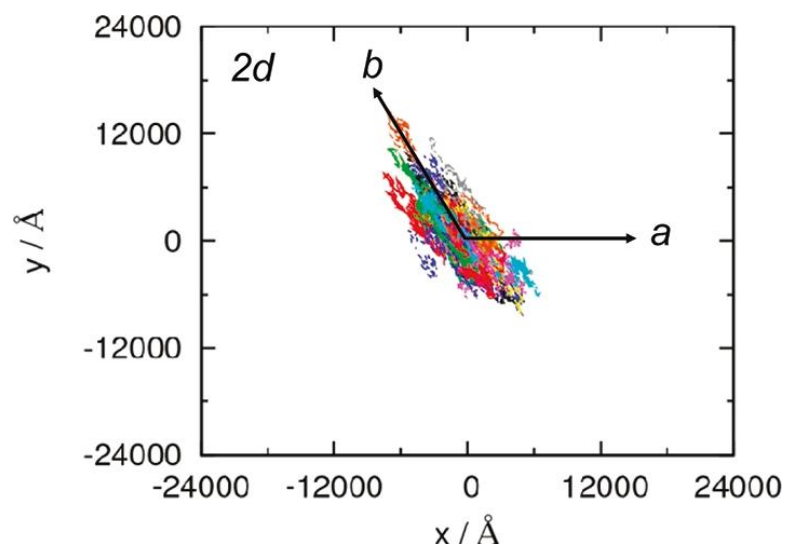


**Figure 6.112** Representation (in the  $x$ - $y$  Cartesian or  $a$ - $b$  crystallographic plane) of 50 randomly selected KMC trajectories computed for system **2d**. The Brownian motion of the charge carrier shows an approximately bidimensional conduction in the  $a$ - $b$  plane corresponding to sequences of *intracolumn* and *intercolumn* jumps between PBI units. Figure adapted from <sup>43</sup>.

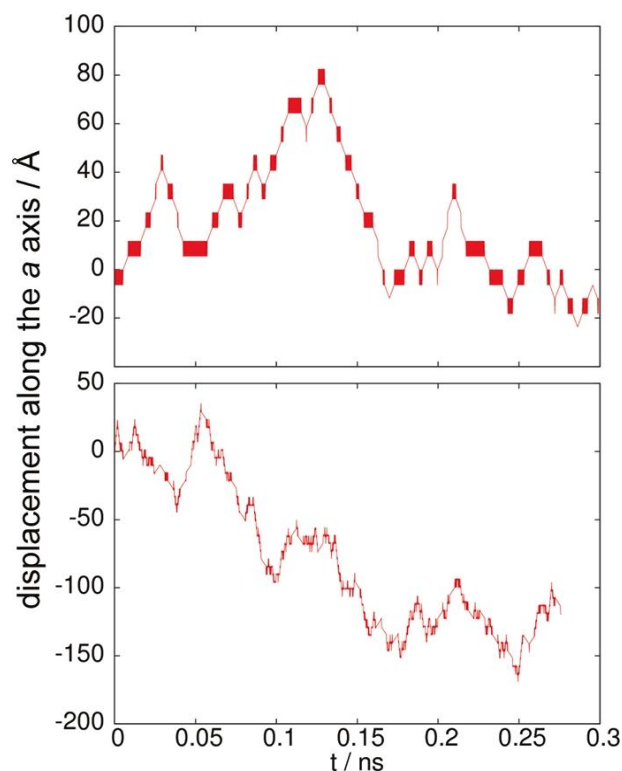


**Figure 6.113** Displacement along the  $a$  crystallographic axis (corresponding to the *intracolumn* charge transport channel) of a charge carrier propagating along a crystal of **2d**. The first 1000 steps of a KMC trajectory are shown. (top) KMC simulation including only *intracolumn* jumps A and B. (bottom) KMC simulation including *intracolumn* jumps A and B along with the *intercolumn* jump C. The KMC trajectory shows less evidence of trapping along  $a$ . Figure adapted from <sup>43</sup>.

Owing to the charge transport efficiency in the *a-b* crystallographic plane, likely corresponding to the orientation of the molecules in the film forming the OTFT device, we explored the magnitude of electron mobilities along directions selected in this plane, under the application of an electric field. Along the *intracolumn* direction *a*, the computed mobility is large (see Table 6.24), but an increase by a factor of 2 occurs by applying the field perpendicularly to a thereby indicating the relevant role played by the availability of efficient *intercolumn* paths, similarly to the charge propagation in crystals of **1a**.

To assess the role of thermally induced dynamical effects on core-twisted PBI derivatives, we carried out an analysis similar to what was done for the planar-core **1a** derivative, based on the integrated MD/QM approach, for the *intracolumn* charge paths of **2d**. Figure 6.114 shows the distribution of electronic couplings and their fitting with a Gaussian function. The computed standard deviation of the A electronic coupling ( $35 \text{ cm}^{-1}$ ) is astonishingly modest and is one-half the magnitude of the static crystal value, while the  $\sigma$  of the B integral fluctuation is  $72 \text{ cm}^{-1}$ , about one-fourth of its static crystal magnitude. Notably, these fluctuations are surprisingly smaller than those computed for path A of the planar-core PBI derivative **1a**.

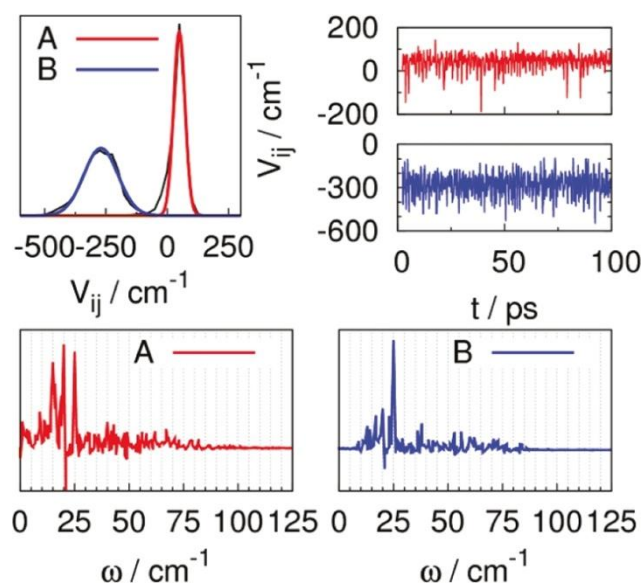


**Figure 6.114** Thermal disorder effects (300 K) on the distribution of the *intracolumn* electronic couplings associated with jump A and B of system **2d**. (top, left) Gaussian fitting of the B3LYP/3-21G\* computed dispersion for integral A (red) and B (blue). (top, right) Dispersion of computed values as a function of simulation time. (bottom) Fourier transform of the autocorrelation function of computed electronic couplings. Figure adapted from <sup>43</sup>.

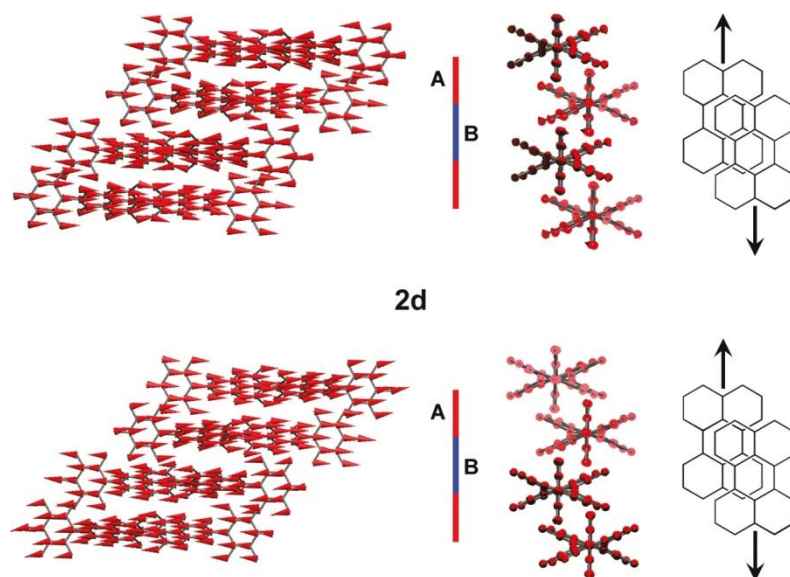


**Figure 6.115** Representative lattice vibrations (top,  $\omega=24\text{ cm}^{-1}$ ; bottom,  $\omega=24\text{ cm}^{-1}$ ) governing the modulation of *intracolumn* electronic couplings A and B of **2d**. Figure adapted from <sup>43</sup>.

The frequencies of the lattice vibrations governing the electronic-coupling modulation were determined from the Fourier transforms of the autocorrelation function of *intracolumn* electronic coupling (Figure 6.114) and fall in the  $15\text{-}30\text{ cm}^{-1}$  region. Inspection of the rigid-body lattice vibrations computed for supercells of **2d** shows a number of modes (Figure 6.115) in which pairs of adjacent PBIs (belonging to the same  $\pi$ -stacked column) oscillate in opposite directions, along the long molecular axis, thereby modulating the  $\pi$ -stacking and therefore the electronic coupling as already shown for **1a**. Note that, from computed radial distribution functions (Figures 6.105-106), the extent of *intermolecular* displacement has not decreased for **2d** compared to **1a**, at 300 K. Therefore, the reduced electronic coupling fluctuations of **2d** must be ascribed to a reduced efficiency of  $\pi$ -stacking and orbital overlap rather than to diminished *intermolecular* motions.

In conclusion, the electronic coupling fluctuations are modest (for both A and B paths) and slower than the hopping event (for path B), therefore we are not within the thermalized limit. In this case, each jump occurs at a rate determined by a member of the electronic coupling distribution, and more sophisticated models should be employed to propagate the charge.<sup>151</sup> However, since thermal fluctuations for **2d** are modest and  $\langle V_{ij} \rangle^2$  and  $\langle (V_{ij})^2 \rangle$  differ little, the impact of lattice vibrations is expected to be weak and will not overcome the asymmetry of the two *intracolumn* paths responsible for the dimer-trapping (or retardation) effect.

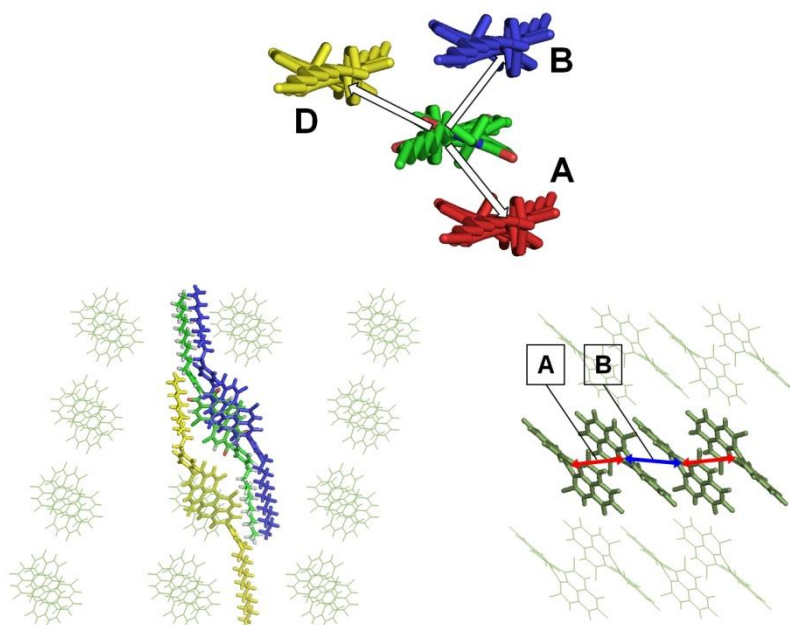


**Figure 6.116** Crystal of **1b**: (top) The possible *intracolumn* (blue and red molecules) and *intercolumn* (yellow molecule) paths taking as reference the green central molecule. The capital letters indicate the jumps that are active owing to non negligible charge transfer integrals. (bottom, left) Top view of the *intracolumn* and *intercolumn* charge paths and, (bottom, right) the *intracolumn* paths A (blue arrows) and B (red arrows). The sequence of red and blue arrows underscores that two different jumps alternate along the column owing to the presence of two different molecular sites (enantiomers) in the crystal. Figure adapted from <sup>43</sup>.

A remarkably reduced *intracolumn* path asymmetry is computed for compound **1b** (Figure 6.116). However the magnitude of *intracolumn* charge transfer integrals is considerably smaller than for **2d**, and the *intercolumn* paths are even less likely to be populated (the largest integral for *intercolumn* jumps is only  $31 \text{ cm}^{-1}$ , see Table 6.23) during charge propagation. As a result, a modest charge mobility is computed for this system, in good agreement with the PR-TRMC measurements<sup>139</sup> (taking into account that the experimental value includes also the contribution from hole mobility).

The crystal structure of **1d** includes only one enantiomer, thereby removing the dimer-trap obstacle, but it encloses also solvent molecules located between the cores of PBI columns. This forces large intermolecular distances for the *intracolumn* jump (about  $7.07 \text{ \AA}$ , compared to less than  $6 \text{ \AA}$  for **1b** and **2d**; see intermolecular distances in Figure 6.107), consequently reflected in small electronic couplings and rate constants. In addition, *intercolumn* jumps are also very unlikely because of the large distances (more than  $13 \text{ \AA}$ ) between molecular units

(Figure 6.117). On the basis of the computed electronic couplings, small mobilities are therefore simulated (see Table 6.24), although it should be considered that the structure of the vacuum-deposited film used to fabricate the device could be different from that of the solvent-embedded crystal<sup>58d</sup> on which simulations are based.

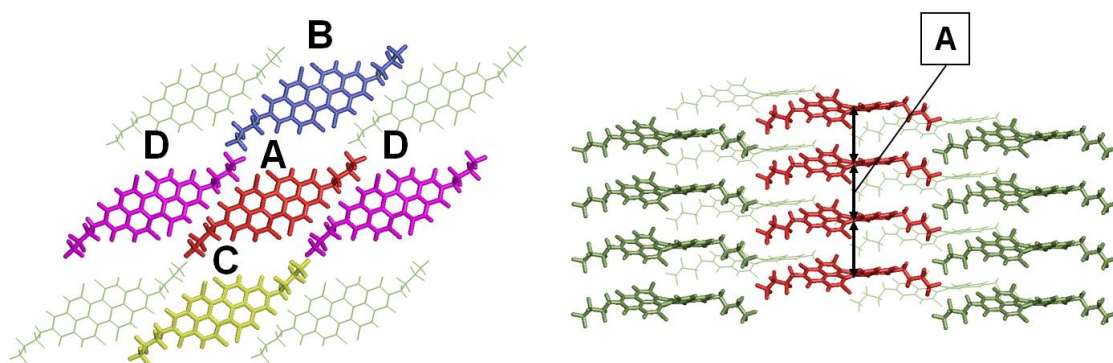


**Figure 6.117** Crystal of **1d**: Only *intracolumn* charge jump A is active owing to non negligible charge transfer integral. The sequence of black arrows underscores that only one type of jump determines the charge propagation along the column owing to the presence of one molecular site (enantiomer) in the crystal. Figure adapted from <sup>43</sup>.

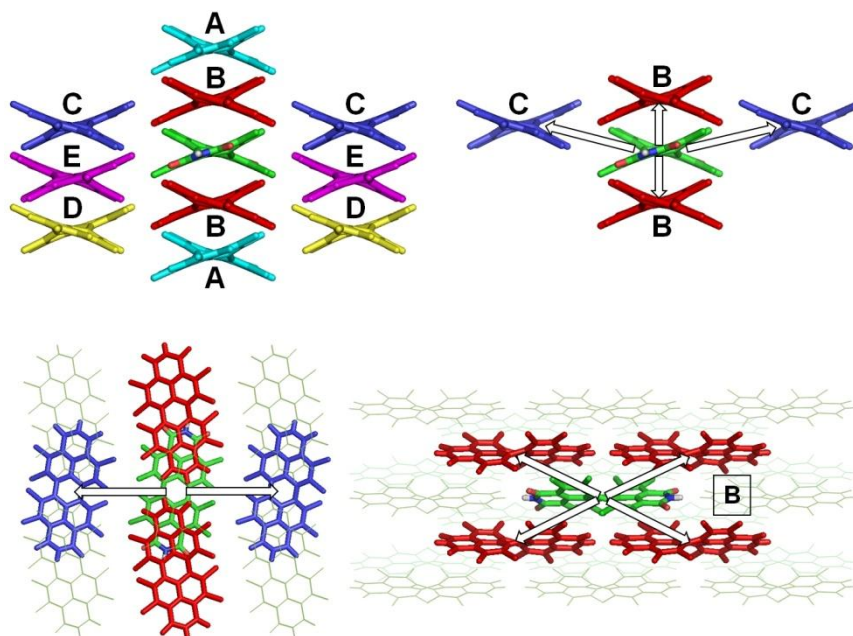


**Figure 6.118** Crystal of **8Cl**: (top, left) the possible *intrawall* (red and cyan molecules) and *interwall* (blue, yellow, and purple molecules) paths (labeled with capital letters) taking as reference the green central molecule. (top, right) Paths included in KMC simulations owing to non-negligible electronic couplings. (bottom, right) Top view of the *intrawall* and *interwall* charge paths and (bottom, right) the *intrawall* path B. Figure adapted from <sup>43</sup>.

The analysis of near neighbor molecules and intermolecular distances between centers of mass (see the radial distribution function in Figure 6.106) of **8Cl** shows two *intrawall* charge transfer paths A and B (distances 7.3585 and 8.1101 Å, respectively) and a number of *interwall* paths, shown with different colors in Figure 6.118. Of the two *intrawall* paths, only B is associated with a remarkable electronic coupling of 327  $cm^{-1}$ , due the close distance (about 3.4 Å) between the planes containing the PBI cores. The distance between PBI cores is instead twice as big for path A, which accounts for its almost negligible electronic coupling (see Table 6.23). Among *interwall* paths, only path C shows a notable value, still considerably smaller than that dominating the *intrawall* path. Therefore, the charge transport is expected to be governed by the *intrawall* propagation and essentially bidimensional along the wall, which is also expected to form the layer of molecules in edge-on configuration forming the OTFT film. The computed charge mobility of **8Cl** is the second highest after **1a** (Table 6.24), as experimentally observed for the group of PBI derivatives considered in this work. The dimer-trapping effect is completely removed in the solid state structure of **8Cl** owing to its slipped brickstone arrangement. The electronic coupling is large and comparable to systems **1a** and **2d**, but the peculiar sequence of available *intrawall* jumps improves the efficiency of charge propagation, compared to **2d**, which results in a larger mobility for the octachloro derivative. Notably, the application of an electric field along the *a* and *b* crystallographic axes (namely, in the plane of one PBI wall, likely corresponding to the layer of edge-on oriented molecules in the film of OTFT devices) confirms the large mobility, with a better efficiency for the field applied along the *a*-axis (see Table 6.24).

Given the relevant role of the *intrawall* electronic coupling B, thermal effects were also investigated. The dynamic evolution of this electronic coupling at 300 K is depicted in Figure 6.119 along with its distribution fitted with a Gaussian function. The standard deviation of the distribution is *ca.* 86  $cm^{-1}$ , about one-fourth of its average value, very similar to the B electronic coupling of **2d**. More interesting, the standard deviation is one-fourth of that computed for the intracolumn path of **1a**, further supporting the evidence that thermal effects modulate remarkably less the charge transfer integrals of core-twisted PBI derivatives compared to planar-core PBI derivatives.

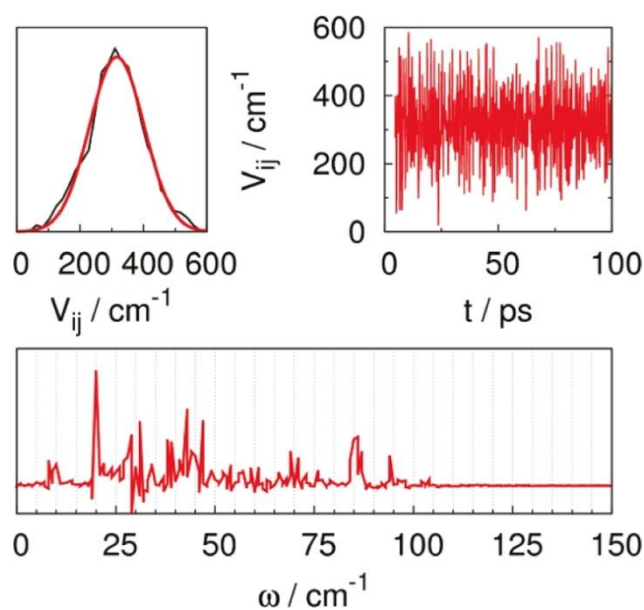


**Figure 6.119** Thermal disorder effects (300 K) on the distribution of the *intrawall* electronic coupling associated with the charge path B of **8Cl**. (top, left) Gaussian fitting of the B3LYP/3-21G\* computed dispersion of the electronic couplings. (top, right) Dispersion of computed values as a function of simulation time. (bottom) Fourier transform of the autocorrelation function of the electronic couplings. Figure adapted from <sup>43</sup>.

The Fourier transform of the autocorrelation function of the computed electronic coupling shows a number of peaks below  $100 \text{ cm}^{-1}$ . Lattice vibrations falling in the correct frequency region involve the opposite sliding of perylene cores belonging to adjacent PBI molecules, similarly to other PBI derivatives (Figure 6.120).

As for system **2d**, the electronic coupling fluctuations are modest, and the hopping event is faster than the fluctuations. Therefore, the thermalized limit could not be applied in the evaluation of charge transfer rate constants. Since thermal fluctuations are modest ( $\langle V_{ij} \rangle^2$  and  $\langle (V_{ij})^2 \rangle$  are similar), the static crystal value of the electronic coupling was employed to evaluate the rate constants collected in Table 6.23.

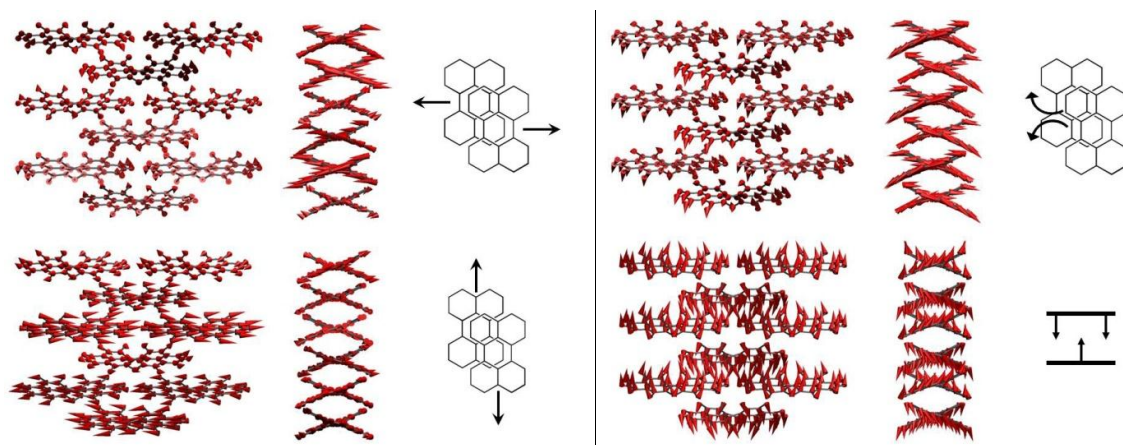


**Figure 6.120** Representative lattice vibrations of **8Cl** modulating the *intrawall* electronic coupling for path B. The frequencies of the lattice vibrations are  $19\text{ cm}^{-1}$  (top, left),  $29\text{ cm}^{-1}$  (bottom, left),  $42\text{ cm}^{-1}$  (top, right) and  $85\text{ cm}^{-1}$  (bottom, right). Figure adapted from <sup>43</sup>.

In summary, we have investigated the electron transport properties of four core-twisted chlorinated PBI derivatives and compared the results with those of the planar-core unsubstituted PBI derivative **1a** displaying a remarkably large mobility.

Quantum-chemical calculations show that chlorination (as well as fluorination or fluoroalkylation) in the bay region enhances the *n*-type character by lowering the LUMO levels and increasing the computed electronic affinities.

Calculations of charge transfer rate constants, according to the non-adiabatic hopping approach, and propagation of the charge carriers within a KMC scheme lead to predicted charge mobilities of **1a**, **2d**, and **8Cl** that reflect the order detected by experimental measurements, a notable result considering the conditions and the limits imposed by the model (perfect crystal structure, diluted charges). This indicates that, for the systems investigated here and displaying the largest mobilities, experimental crystal structures are reliable starting points to study charge transport properties of thin-film devices whose exact morphology is not completely known.

The emphasis of this study is not, however, on absolute values of computed charge mobilities but on the structural motifs determining different charge transport properties and thermal fluctuations of electronic couplings.

In contrast to planar-core PBI derivatives such as **1a**, the solid state structure of core-twisted PBI is generally characterized by the presence of the two enantiomeric forms of the PBI

derivative alternating along  $\pi$ -stacked PBI columns (**2d** and **1b**) or along the slipped brickstone arrangement of **8Cl**. This characteristic generally implies an asymmetry in the charge transfer probability along a given direction, particularly relevant along the *intracolumn* propagation direction since it reduces the charge transport efficiency because of a dimer-trapping (or retardation) effect. We have shown that this effect is strongly operative for the *intracolumn* charge transport channel of **2d**, and we can conclude that system **2d** shows a relatively large mobility owing to the non-negligible contribution of *intercolumn* jumps which allow escape of the charge from trapping along a  $\pi$ -stacked PBI column. The mobility does not reach the values of the parent derivative **1a** because of the larger intramolecular reorganization energy, combined with the presence of the *intracolumn* dimer-trapping effect. Nevertheless, the availability of efficient *intercolumn* paths is fundamental to improve the mobility of columnar core-twisted PBI derivatives. Such a dimer-trapping effect is completely removed in the solid state structure of **8Cl** owing to its slipped brickstone arrangement, and the peculiar sequence of available *intrawall* jumps improves the efficiency of charge propagation which results in a larger mobility compared to **2d**.

The effect of thermal motion on the modulation of electronic couplings has been explored for the planar-core derivative **1a** and for the core-twisted derivatives displaying the largest mobilities (**2d** and **8Cl**). While electronic coupling fluctuations are very large for the planar-core **1a** and influence fundamentally its charge transport, such effects are dramatically reduced for core-twisted chlorinated derivatives although the average amplitude of intermolecular motions is similar for planar-core and core-twisted derivatives. Therefore, the drastic decrease in thermal fluctuations is attributed to a reduced orbital overlap and  $\pi$  stacking efficiency induced by core twisting.

From the Fourier transform of the autocorrelation functions of the electronic couplings, the active lattice vibrations are identified. For all the systems investigated, the most active lattice frequencies are located in the 20-60  $cm^{-1}$  region and generally correspond to the sliding of two adjacent PBI molecules in opposite direction to maximize the change in orbital overlap and  $\pi$ - $\pi$  stacking.

The study reveals that the reduced  $\pi$ - $\pi$  stacking induced by core-twisting influences not only static properties of the molecular material but also dynamical effects that should be considered in the design of future organic semiconductor architectures.

## 6.8 References

- [1] (a) Martin, R. E.; Diederich, F. *Angew. Chem. Int. Ed.* **1999**, *38*, 1350; (b) Gross, M.; Müller, D. C.; Nothofer, H.-G.; Scherf, U.; Neher, D.; Brauchle, C.; Meerholz, K. *Nature* **2000**, *405*, 661; (c) Tour, J. M. *Chem. Rev.* **1996**, *96*, 537; (d) Dutta, T.; Woody, K. B.; Parkin, S. R.; Watson, M. D.; Gierschner, J. *J. Am. Chem. Soc.* **2009**, *131*, 17321; (e) Tsuda, A.; Osuka, A. *Science* **2001**, *293*, 79; (f) Baumgarten, M.; Müller, M.; Bohnen, A.; Müllen, K. *Angew. Chem. Int. Ed.* **1992**, *31*, 448; (g) Wu, J.; Watson, M. D.; Tchegbotareva, N.; Wang, Z.; Müllen, K. *J. Org. Chem.* **2004**, *69*, 8194.
- [2] (a) Heckmann, A.; Lambert, C. *Angew. Chem. Int. Ed.* **2011**, DOI: 10.1002/anie.201100944; (b) Hankache, J.; Wenger, O. S. *Chem. Rev.* **2011**, *111*, 5138.
- [3] Brédas, J.-L.; Beljonne, D.; Coropceanu, V.; Cornil, J. *Chem. Rev.* **2004**, *104*, 4971.
- [4] Robin, M. B.; Day, P. *Adv. Inorg. Chem. Radiochem.* **1967**, *10*, 247.
- [5] (a) Brunshwig, B. S.; Creutz, C. *Chem. Soc. Rev.* **2002**, *31*, 168; (b) Nelsen, S. F. *Chem. Eur. J.* **2000**, *6*, 581; (c) Demadis, K. D.; Hartshorn, C. M.; Meyer, T. J. *Chem. Rev.* **2001**, *101*, 2655; (d) Launay, J.-P.; Coudret, C.; Hortholary, C. *J. Phys. Chem. B* **2007**, *111*, 6788.
- [6] Kaupp, M.; Renz, M.; Parthey, M.; Stolte, M.; Würthner, F.; Lambert, C. *Phys. Chem. Chem. Phys.* **2011**, *13*, 16973-16986.
- [7] (a) Marcus, R. A. *Pure Appl. Chem.* **1997**, *69*, 13; (b) Marcus, R. A.; Sutin, N. *Comments Inorg. Chem.* **1986**, *5*, 119.
- [8] (a) Chen, P.; Meyer, T. J. *Chem. Rev.* **1998**, *98*, 1439; (b) Nelsen, S. F.; Tran, H. Q. *J. Phys. Chem. A* **1999**, *103*, 8139; (c) Brunshwig, B. S.; Ehrenson, S.; Sutin, N. *J. Phys. Chem.* **1986**, *90*, 3657; (d) Nelsen, S. F.; Trieber, D. A.; Ismagilov, R. F.; Teki, Y. *J. Am. Chem. Soc.* **2001**, *123*, 5684.
- [9] (a) Yan, Q.; Zhao, D. *Org. Lett.* **2009**, *11*, 3426; (b) Yuan, Z.; Xiao, Y.; Qian, X. *Chem. Commun.* **2010**, *46*, 2772.
- [10] (a) Hassan, J.; Sévignon, M.; Gozzi, C.; Schulz, E.; Lemaire, M. *Chem. Rev.* **2002**, *102*, 1359; (b) Ma, D.; Cai, Q. *Acc. Chem. Res.* **2008**, *41*, 1450; (c) Ley, S. V.; Thomas, A. W. *Angew. Chem. Int. Ed.* **2003**, *42*, 5400; (d) Beletskaya, I. P.; Cheprakov, A. V. *Coord. Chem. Rev.* **2004**, *248*, 2337; (e) Monnier, F.; Taillefer, M. *Angew. Chem. Int. Ed.* **2009**, *48*, 6954; (f) Li, Y.; Tan, L.;

Wang, Z.; Qian, H.; Shi, Y.; Hu, W. *Org. Lett.* **2008**, *10*, 529-532; (g) Li, Y.; Li, C.; Yue, W.; Jiang, W.; Kopecek, R.; Qu, J.; Wang, Z. *Org. Lett.* **2010**, *12*, 2374.

[11] Qian, H.; Negri, F.; Wang, C.; Wang, Z. *J. Am. Chem. Soc.* **2008**, *130*, 17970-17976.

[12] (a) Qian, H.; Wang, Z.; Yue, W.; Zhu, D. *J. Am. Chem. Soc.* **2007**, *129*, 10664; (b) Shi, Y.; Qian, H.; Li, Y.; Yue, W.; Wang, Z. *Org. Lett.* **2008**, *10*, 2337; (c) Zhen, Y.; Qian, H.; Xiang, J.; Qu, J.; Wang, Z. *Org. Lett.* **2009**, *11*, 3084; (e) Zhen, Y.; Wang, C.; Wang, Z. *Chem. Commun.* **2010**, *46*, 1926; (d) Wu, Y.; Zhen, Y.; Ma, Y.; Zheng, R.; Wang, Z.; Fu, H. *J. Phys. Chem. Lett.* **2010**, *1*, 2499; (e) Wang, H.; Su, H.; Qian, H.; Wang, Z.; Wang, X.; Xia, A. *J. Phys. Chem. A* **2010**, *114*, 9130.

[13] Jiang, W.; Xiao, C.; Hao, L.; Wang, Z.; Ceymann, H.; Lambert, C.; Di Motta, S.; Negri, F. *Chem. Eur. J.* accepted DOI:10.1002/chem.201103954

[14] (a) Hill, D. J.; Mio, M. J.; Prince, R. B.; Hughes, T. S.; Moore, J. S. *Chem. Rev.* **2001**, *101*, 3893; (b) Pu, L. *Chem. Rev.* **1998**, *98*, 2405; (c) Wilson, J. N.; Steffen, W.; Mckenzie, T. G.; Lieser, G.; Oda, M.; Neher, D.; Bunz, U. H. F. *J. Am. Chem. Soc.* **2002**, *124*, 6830; (d) Bringmann, G.; Mortimer, A. J. P.; Keller, P. A.; Gresser, M. J.; Garner, J.; Breuning, M. *Angew. Chem., Int. Ed.* **2005**, *44*, 5384; (e) Jeukens, C. R. L. P. N.; Jonkheijm, P.; Wijnen, F. J. P.; Gielen, J. C.; Christianen, P. C. M.; Schenning, A. P. H. J.; Meijer, E. W.; Maan, J. C. *J. Am. Chem. Soc.* **2005**, *127*, 8280; (f) Hassey, R.; Swain, E. J.; Hammer, N. I.; Venkataraman, D.; Barnes, M. D. *Science* **2006**, *314*, 1437; (g) Nuckolls, C.; Katz, T. J.; Collings, P. J.; Castellanos, L. *J. Am. Chem. Soc.* **1999**, *121*, 79.

[15] (a) Morrison, D. J.; Trefz, T. K.; Piers, W. E.; McDonald, R.; Parvez, M. *J. Org. Chem.* **2005**, *70*, 5309; (b) Lu, J.; Ho, D. M.; Vogelaar, N. J.; Kraml, C. M.; Pascal Jr., R. A. *J. Am. Chem. Soc.* **2004**, *126*, 11168; (c) Buss, V.; Falzewski, S.; Kolster, K. *J. Org. Chem.* **1999**, *64*, 1071.

[16] (a) Wolf, C.; König, W. A.; Roussel, C. *Liebigs Ann.* **1995**, 781; (b) Müllen, K.; Heinz, W.; Klärner, F.-G.; Roth, W. R.; Kindermann, I.; Adamczak, O.; Wette, M.; Lex, J. *Chem. Ber.* **1990**, *123*, 2349; (c) Bott, G.; Field, L. D.; Sternhell, S. *J. Am. Chem. Soc.* **1980**, *102*, 5618.

[17] (a) Osswald, P.; Würthner, F. *J. Am. Chem. Soc.* **2007**, *129*, 14319; (b) Osswald, P.; Leusser, D.; Stalke, D.; Würthner, F. *Angew. Chem., Int. Ed.* **2005**, *44*, 250; (c) Osswald, P.; Reichert, M.; Bringmann, G.; Würthner, F. *J. Org. Chem.* **2007**, *72*, 3403.

- [18] Zhen, Y.; Yue, W.; Li, Y.; Jiang, W.; Di Motta, S.; Di Donato, E.; Negri, F.; Ye, S.; Wang, Z. *Chem. Commun.* **2010**, 46, 6078-6080.
- [19] (a) Rabideau, P. W.; Sygula, A. *Acc. Chem. Res.* **1996**, 29, 235-242. (b) Wu, Y.; Siegel, J. S. *Chem. Rev.* **2006**, 106, 4843-4867. (c) Tsefrikas, V. M.; Scott, L. T. *Chem. Rev.* **2006**, 106, 4868-4884. (d) Kawase, T.; Kurata, H. *Chem. Rev.* **2006**, 106, 5250-5273.
- [20] (a) Scott, L. T.; Boorum, M. M.; McMahon, B. J.; Hagen, S.; Mack, J.; Blank, J.; Wegner, H.; Meijere, A. D. *Science* **2002**, 295, 1500-1503. (b) Bronstein, H. E.; Choi, N.; Scott, L. T. *J. Am. Chem. Soc.* **2002**, 124, 8870-8875.
- [21] (a) Sygula, A.; Rabideau, P. W. *J. Am. Chem. Soc.* **1999**, 121, 7800-7803. (b) Seiders, T. J.; Elliott, E. L.; Grube, G. H.; Siegel, J. S. *J. Am. Chem. Soc.* **1999**, 121, 7804-7813. (c) Sakurai, H.; Daiko, T.; Hirao, T. *Science* **2003**, 301, 1878.
- [22] (a) Bendikov, M.; Wudl, F. *Chem. Rev.* **2004**, 104, 4891-4945. (b) Anthony, J. E. *Chem. Rev.* **2006**, 106, 5028-5048. (c) Wu, Y.; Li, Y.; Gardner, S.; Ong, B. S. *J. Am. Chem. Soc.* **2005**, 127, 614-618.
- [23] (a) Imamura, K.; Takimiya, K.; Aso, Y.; Otsubo, T. *Chem. Commun.* **1999**, 1859-1860. (b) Mascal, M.; Lera, M.; Blake, A. J. *J. Org. Chem.* **2000**, 65, 7253-7255. (c) Mascal, M.; Bertran, J. C. *J. Am. Chem. Soc.* **2005**, 127, 1352-1353.
- [24] Qian, H.; Yue, W.; Zhen, Y.; Di Motta, S.; Di Donato, E.; Negri, F.; Qu, J.; Xu, W.; Zhu, D.; Wang, Z. *J. Org. Chem.* **2009**, 74, 6275-6282.
- [25] Renz, M.; Theilacker, K.; Lambert, C.; Kaupp, M. *J. Am. Chem. Soc.* **2009**, 131, 16292.
- [26] (a) Jacquemin, D.; Wathélet, V.; Perpète, E. A.; Adamo, C. *J. Chem. Theor. Comput.* **2009**, 5, 2420; (b) Santoro, F.; Barone, V.; Improta, R. *J. Comput. Chem.* **2008**, 29, 957.
- [27] Peach, M. J. G.; Benfield, P.; Helgaker, T.; Tozer, D. J. *J. Chem. Phys.* **2008**, 128, 044118-1-8.
- [28] Fazzi, D.; Canesi, E. V.; Negri, F.; Bertarelli, C.; Castiglioni, C. *ChemPhysChem* **2010**, 11, 3685-3695.
- [29] Di Motta, S.; Negri, F.; Fazzi, D.; Castiglioni, C.; Canesi, E. V. *J. Phys. Chem. Lett.* **2010**, 1, 3334-3339.

- [30] (a) Kikuchi, A.; Ito, H.; Abe, J. *J. Phys. Chem. B* **2005**, *109*, 19448; (b) Lahti, P. M.; Ichimura, A. S.; Sanborn, J. A. *J. Phys. Chem. A* **2001**, *105*, 251.
- [31] (a) Liu, W.; Settels, V.; Harbach, P. H. P.; Dreuw, A.; Fink, R. F.; Engels, B. *J. Comp. Chem.* **2011**, *32*, 1971; (b) Zhao, H.; Pfister, J.; Settels, V.; Renz, M.; Kaupp, M.; Dehm, V. C.; Würthner, F.; Fink, R. F.; Engels, B. *J. Am. Chem. Soc.* **2009**, *131*, 15660.
- [32] Qian, H.; Liu, C.; Wang, Z.; Zhu, D. *Chem. Commun.* **2006**, 4587–4589.
- [33] Ackermann, L.; Althammer, A. *Angew. Chem., Int. Ed.* **2007**, *46*, 1627–1629.
- [34] (a) Kosugi, M.; Ogata, T.; Terada, M.; Sano, H.; Migita, T. *Bull. Chem. Soc. Jpn.* **1985**, *58*, 3657–3658. (b) Zhang, X.; Côté, A. P.; Matzger, A. J. *J. Am. Chem. Soc.* **2005**, *127*, 10502–10503.
- [35] (a) Hartwig, J. F. In *Handbook of Organopalladium Chemistry for Organic Synthesis*; Negishi, E. I., de Meijere, A., Eds.; Wiley-Interscience: Weinheim, Germany, **2002**. (b) Jiang, L.; Buchwald, S. L. In *Metal-Catalyzed Cross-Coupling Reactions*, 2nd ed.; de Meijere, A., Diederich, F., Eds.; John Wiley & Sons: Weinheim, Germany, **2004**.
- [36] (a) Haddon, R. C.; Scott, L. T. *Pure Appl. Chem.* **1986**, *58*, 137–142. (b) Haddon, R. C. *J. Am. Chem. Soc.* **1987**, *109*, 1676–1685. (c) Haddon, R. C. *Science* **1993**, *261*, 1545–1550.
- [37] You, C.; Dobrawa, R.; Möller, C. R. S.; Würthner, F. *Top. Curr. Chem.* **2005**, *258*, 39.
- [38] Kasha, M.; Rawls, H. R.; Ashraf El-Bayoumi, M. *Pure Appl. Chem.* **1965**, *11*, 371.
- [39] (a) Hush, N. S. *Coord. Chem. Rev.* **1985**, *64*, 135; (b) Hush, N. S. *Electrochim. Acta* **1968**, *13*, 1005; (c) Nelsen, S. F.; Ismagilov, R. F.; Trieber, D. A. *Science* **1997**, *278*, 846.
- [40] Cisnetti, F.; Ballardini, R.; Credi, A.; Gandolfi, M. T.; Masiero, S.; Negri, F.; Pieraccini, S.; Spada, G. P. *Chem. Eur. J.* **2004**, *10*, 2011.
- [41] Coropceanu, V.; Cornil, J.; da Silva, D. A.; Olivier, Y.; Silbey, R.; Brédas, J.-L. *Chem. Rev.* **2007**, *107*, 926.
- [42] Di Donato, E.; Fornari, R. P.; Di Motta, S.; Li, Y.; Wang, Z.; Negri, F. *J. Phys. Chem. B* **2010**, *114*, 5327.
- [43] Di Motta, S.; Siracusa, M.; Negri, F. *J. Phys. Chem. C* **2011**, *115*, 20754.

- [44] (a) Li, Y.; Wang, Z. *Org. Lett.* **2009**, *11*, 1385–1387. (b) Jiang, W.; Qian, H.; Li, Y.; Wang, Z. *J. Org. Chem.* **2008**, *73*, 7369–7372.
- [45] Li, Y.; Gao, J.; Di Motta, S.; Negri, F.; Wang, Z. *J. Am. Chem. Soc.* **2010**, *132*, 4208–4213.
- [46] (a) Novoselov, K. S.; Geim, A. K.; Morozov, S. V.; Jiang, D.; Zhang, Y.; Dubonos, S. V.; Grigorieva, I. V.; Firsov, A. A. *Science* **2004**, *306*, 666–669. (b) Geim, A. K.; Novoselov, K. S. *Nat. Mater.* **2007**, *6*, 183–191. (c) Li, X.; Wang, X.; Zhang, L.; Lee, S.; Dai, H. *Science* **2008**, *319*, 1229–1232. (d) Wang, X.; Ouyang, Y.; Li, X.; Wang, H.; Guo, J.; Dai, H. *Phys. Rev. Lett.* **2008**, *100*, 206803.
- [47] Han, M. Y.; Özyilmaz, B.; Zhang, Y.; Kim, P. *Phys. Rev. Lett.* **2007**, *98*, 206805.
- [48] (a) Jiao, L.; Zhang, L.; Wang, X.; Diankov, G.; Dai, H. *Nature* **2009**, *458*, 877–880. (b) Kosynkin, D. V.; Higginbotham, A. L.; Sinitskii, A.; Lomeda, J. R.; Dimiev, A.; Price, B. K.; Tour, J. M. *Nature* **2009**, *458*, 872–876.
- [49] Yang, X.; Dou, X.; Rouhanipour, A.; Zhi, L.; Räder, H. J.; Müllen, K. *J. Am. Chem. Soc.* **2008**, *130*, 4216–4217.
- [50] (a) Jankowiak, H. C.; Stuber, J. L.; Berger, R. *J. Chem. Phys.* **2007**, *127*, 234101. (b) Santoro, F.; Imbrota, R.; Lami, A.; Bloino, J.; Barone, V. *J. Chem. Phys.* **2007**, *126*, 084509. (c) Santoro, F.; Lami, A.; Imbrota, R.; Barone, V. *J. Chem. Phys.* **2007**, *126*, 184102. (d) Dierksen, M.; Grimme, S. *J. Chem. Phys.* **2004**, *120*, 3544–3554. (e) Borrelli, R.; Peluso, A. *J. Chem. Phys.* **2003**, *119*, 8437–8448.
- [51] (a) Keszthelyi, T.; Balakrishnan, G.; Wilbrandt, R.; Yee, W. A.; Negri, F. *J. Phys. Chem. A* **2000**, *104*, 9121–9129. (b) Di Donato, E.; Vanzo, D.; Semeraro, M.; Credi, A.; Negri, F. *J. Phys. Chem. A* **2009**, *113*, 6504–6510.
- [52] Di Donato, E.; Tommasini, M.; Fustella, G.; Brambilla, L.; Castiglioni, C.; Zerbi, G.; Simpson, C. D.; Müllen, K.; Negri, F. *Chem. Phys.* **2004**, *301*, 81–93.
- [53] Yue, W.; Gao, J.; Li, Y.; Jiang, W.; Di Motta, S.; Negri, F.; Wang, Z. *J. Am. Chem. Soc.* **2011**, *133*, 18054–18057.
- [54] (a) Kelley, T. W.; Baude, P. F.; Gerlach, C.; Ender, D. E.; Muiyres, D.; Haase, M. A.; Vogel, D. E.; Theiss, S. D. *Chem. Mater.* **2004**, *16*, 4413. (b) Jang, B.-B.; Lee, S. H.; Kafafi, Z. H. *Chem. Mater.* **2006**, *18*, 449. (c) Murphy, A. R.; Fréchet, J. M. J. *Chem. Rev.* **2007**, *107*, 1066.

[55] (a) Anthony, J. E. *Angew. Chem., Int. Ed.* **2008**, *47*, 452. (b) Moon, H.; Zeis, R.; Borkent, E.-J.; Besnard, C.; Lovinger, A. J.; Siegrist, T.; Kloc, C.; Bao, Z. *J. Am. Chem. Soc.* **2004**, *126*, 15322. (c) Bendikov, M.; Wudl, F.; Perepichka, D. F. *Chem. Rev.* **2004**, *104*, 4891.

[56] Chen, Z.; Müller, P.; Swager, T. M. *Org. Lett.* **2006**, *8*, 273.

[57] (a) Usta, H.; Facchetti, A.; Marks, T. J. *Acc. Chem. Res.* **2011**, *44*, 501. (b) Würthner, F.; Stolte, M. *Chem. Commun.* **2011**, *47*, 5109. (c) Katsuta, S.; Tanaka, K.; Maruya, Y.; Mori, S.; Masuo, S.; Okujima, T.; Uno, H.; Nakayama, K.; Yamada, H. *Chem. Commun.* **2011**, *47*, 10112.

[58] (a) Katz, H. E.; Lovinger, A. J.; Johnson, J.; Kloc, C.; Siegrist, T.; Li, W.; Lin, Y.-Y.; Dodabalapur, A. *Nature* **2000**, *404*, 478. (b) Gao, X.; Di, C.; Hu, Y.; Yang, X.; Fan, H.; Zhang, F.; Liu, Y.; Li, H.; Zhu, D. *J. Am. Chem. Soc.* **2010**, *132*, 3697. (c) Gsänger, M.; Oh, J. H.; Könemann, M.; Hoffken, H. W.; Krause, A. M.; Bao, Z.; Würthner, F. *Angew. Chem., Int. Ed.* **2010**, *49*, 740. (d) Schmidt, R.; Oh, J. H.; Sun, Y.; Deppisch, M.; Krause, A. M.; Radacki, K.; Braunschweig, H.; Könemann, M.; Erk, P.; Bao, Z.; Würthner, F. *J. Am. Chem. Soc.* **2009**, *131*, 6215-6228. (e) Guo, X.; Watson, M. D. *Org. Lett.* **2008**, *10*, 5333. (f) Lu, X.; Zhu, W.; Xie, Y.; Li, X.; Gao, Y.; Li, F.; Tian, H. *Chem. Eur. J.* **2010**, *16*, 8355.

[59] CCDC 809110 (3d) contains the supplementary crystallographic data for paper <sup>53</sup>. These data can be obtained free of charge from The Cambridge Crystallographic Data Centre via [http://www.ccdc.cam.ac.uk/data\\_request/cif](http://www.ccdc.cam.ac.uk/data_request/cif). Crystal data for 3d: single crystals suitable for X-ray diffraction were obtained by slowly evaporating a solution of 3d in solution of dichloromethane and methanol at room temperature. C<sub>46</sub>H<sub>44</sub>F<sub>14</sub>N<sub>2</sub>O<sub>4</sub>, M = 954.83, monoclinic space group Cc, a = 27.048(6), b = 14.838(3), c = 11.731(3) Å, α = 90.00°, β = 101.587(3)°, γ = 90.00°. V = 4611.9(18), Z = 4, black crystal.

[60] Odom, S. A.; Parkin, S. R.; Anthony, J. E. *Org. Lett.* **2003**, *5*, 4245.

[61] Thalacker, C.; Röger, C.; Würthner, F. *J. Org. Chem.* **2006**, *71*, 8098.

[62] (a) Chun, D.; Cheng, Y.; Wudl, F. *Angew. Chem., Int. Ed.* **2008**, *47*, 8380. (b) Kaur, I.; Stein, N. N.; Kopeski, R. P.; Miller, G. P. *J. Am. Chem. Soc.* **2009**, *131*, 3424.

[63] (a) Zhang, K.; Huang, K. W.; Li, J. L.; Luo, J.; Chi, C. Y.; Wu, J. S. *Org. Lett.* **2009**, *11*, 4854-4857. (b) Pappenfus, T. M.; Chesterfield, R. J.; Frisbie, C. D.; Mann, K. R.; Casado, J.; Raff, J. D.; Miller, L. L. *J. Am. Chem. Soc.* **2002**, *124*, 4184-4185. (c) Takahashi, T.; Matsuoka, K. I.; Takimiya, K.; Otsubo, T.; Aso, Y. *J. Am. Chem. Soc.* **2005**, *127*, 8928-8929.

- [64] (a) Schmidt-Mende, L.; Fechtenkötter, A.; Müllen, K.; Moons, E.; Friend, R. H.; MacKenzie, J. D. *Science* **2001**, *293*, 1119–1122. (b) Zang, L.; Che, Y. K.; Moore, J. S. *Acc. Chem. Res.* **2008**, *41*, 1596–1608. (c) Ribierre, J. C.; Fujihara, T.; Watanabe, S.; Matsumoto, M.; Muto, T.; Nakao, A.; Aoyama, T. *Adv. Mater.* **2010**, *22*, 1722–1726. (d) Ribierre, J. C.; Watanabe, S.; Matsumoto, M.; Muto, T.; Aoyama, T. *Appl. Phys. Lett.* **2010**, *96*, 083303. (e) Ribierre, J. C.; Watanabe, S.; Matsumoto, M.; Muto, T.; Nakao, A.; Aoyama, T. *Adv. Mater.* **2010**, *22*, 4044–4048.
- [65] (a) Ortiz, R. P.; Casado, J.; Gonzalez, S. R.; Hernandez, V.; Navarrete, J. T. L.; Viruela, P. M.; Orti, E.; Takimiya, K.; Otsubo, T. *Chem. Eur. J.* **2010**, *16*, 470–484. (b) Ortiz, R. P.; Facchetti, A.; Marks, T. J.; Casado, J.; Zgierski, M. Z.; Kozaki, M.; Hernandez, V.; Navarrete, J. T. L. *Adv. Funct. Mater.* **2009**, *19*, 386–394. (c) Ortiz, R. P.; Casado, J.; Hernandez, V.; Navarrete, J. T. L.; Viruela, P. M.; Orti, E.; Takimiya, K.; Otsubo, T. *Angew. Chem., Int. Ed.* **2007**, *46*, 9057–9061.
- [66] Ortiz, R. P.; Casado, J.; Hernandez, V.; Navarrete, J. T. L.; Orti, E.; Viruela, P. M.; Milián, B.; Hotta, S.; Zotti, G.; Zecchin, S.; Vercelli, B. *Adv. Funct. Mater.* **2006**, *16*, 531–536.
- [67] (a) Agostinelli, T.; Caironi, M.; Natali, D.; Sampietro, M.; Dassa, G.; Canesi, E. V.; Bertarelli, C.; Zerbi, G.; Cabanillas-Gonzalez, J.; De Silvestri, S.; Lanzani, G. *J. Appl. Phys.* **2008**, *104*, 114508. (b) Yao, Y.; Liang, Y. Y.; Shrotriya, V.; Xiao, S. Q.; Yu, L. P.; Yang, Y. *Adv. Mater.* **2007**, *19*, 3979–3983.
- [68] (a) Zhang, F. L.; Mammo, W.; Andersson, L. M.; Admassie, S.; Andersson, M. R.; Inganas, O. *Adv. Mater.* **2006**, *18*, 2169–2173. (b) Zimmerman, J. D.; Diev, V. V.; Hanson, K.; Lunt, R. R.; Yu, E. K.; Thompson, M. E.; Forrest, S. R. *Adv. Mater.* **2010**, *22*, 2780–2783.
- [69] Calzado, C. J.; Cabrero, J.; Malrieu, J. P.; Caballol, R. *J. Chem. Phys.* **2002**, *116*, 2728–2747.
- [70] Bonacic-Koutecky, V.; Koutecky, J.; Michl, J. *Angew. Chem., Int. Ed. Engl.* **1987**, *26*, 170–189.
- [71] Paci, I.; Johnson, J. C.; Chen, X. D.; Rana, G.; Popovic, D.; David, D. E.; Nozik, A. J.; Ratner, M. A.; Michl, J. *J. Am. Chem. Soc.* **2006**, *128*, 16546–16553.
- [72] Kolc, J.; Downing, J. W.; Manzara, A. P.; Michl, J. *J. Am. Chem. Soc.* **1976**, *98*, 930–937.
- [73] Zimmerman, P. M.; Zhang, Z.; Musgrave, C. B. *Nature Chem.* **2010**, *2*, 648–652.

- [74] (a) Bendikov, M.; Duong, H. M.; Starkey, K.; Houk, K. N.; Carter, E. A.; Wudl, F. *J. Am. Chem. Soc.* **2004**, *126*, 7416–7417. (b) Kamada, K.; Ohta, K.; Shimizu, A.; Kubo, T.; Kishi, R.; Takahashi, H.; Botek, E.; Champagne, B.; Nakano, M. *J. Phys. Chem. Lett.* **2010**, *1*, 937–940.
- [75] Lanzani, G.; Cerullo, G.; Zavelani-Rossi, M.; De Silvestri, S.; Comoretto, D.; Musso, G.; Dellepiane, G. *Phys. Rev. Lett.* **2001**, *87*, 187402.
- [76] (a) Schwerin, A. F.; Johnson, J. C.; Smith, M. B.; Sreearunothai, P.; Popovic, D.; Cerny, J.; Havlas, Z.; Paci, I.; Akdag, A.; MacLeod, M. K.; Chen, X.; David, D. E.; Ratner, M. A.; Miller, J. R.; Nozik, A. J. *J. Phys. Chem. A* **2010**, *114*, 1457–1473. (b) Muller, A. M.; Avlasevich, Y. S.; Schöller, W. W.; Müllen, K.; Bardeen, C. J. *J. Am. Chem. Soc.* **2007**, *129*, 14240–14250.
- [77] (a) Froelich, W.; Dewey, H. J.; Deger, H.; Dick, B.; Klingensmith, K. A.; Puettmann, W.; Vogel, E.; Hohlneicher, G.; Michl, J. *J. Am. Chem. Soc.* **1983**, *105*, 6211–6220. (b) Schulten, K.; Karplus, M. *Chem. Phys. Lett.* **1972**, *14*, 305–309. (c) Orlandi, G.; Zerbetto, F.; Zgierski, M. Z. *Chem. Rev.* **1991**, *91*, 867–891. (d) Kohler, B. E.; Spangler, C.; Westerfield, C. J. *Chem. Phys.* **1988**, *89*, 5422–5428.
- [78] Hosteny, R. P.; Dunning, J. T. H.; Gilman, R. R.; Pipano, A.; Shavitt, I. *J. Chem. Phys.* **1975**, *62*, 4764–4779.
- [79] (a) Nakano, M.; Kishi, R.; Ohta, S.; Takahashi, H.; Kubo, T.; Kamada, K.; Ohta, K.; Botek, E.; Champagne, B. *Phys. Rev. Lett.* **2007**, *99*, 033001. (b) Konishi, A.; Hirao, Y.; Nakano, M.; Shimizu, A.; Botek, E.; Champagne, B.; Shiomi, D.; Sato, K.; Takui, T.; Matsumoto, K.; Kurata, H.; Kubo, T. *J. Am. Chem. Soc.* **2010**, *132*, 11021–11023.
- [80] Werner, H.-J.; Knowles, P. J. *J. Chem. Phys.* **1985**, *82*, 5053–5063.
- [81] Celani, P.; Werner, H.-J. *J. Chem. Phys.* **2000**, *112*, 5546–5557.
- [82] (a) Zerbetto, F.; Zgierski, M. Z.; Negri, F.; Orlandi, G. *J. Chem. Phys.* **1988**, *89*, 3681–3688. (b) Negri, F.; Zgierski, M. Z. *J. Chem. Phys.* **1994**, *100*, 2571–2587. (c) Negri, F.; Zgierski, M. Z. *J. Chem. Phys.* **2001**, *115*, 1298–1311.
- [83] Werner, H.-J.; Knowles, P. J.; Lindh, R.; Manby, F. R.; Schütz, M.; Celani, P.; Korona, T.; Mitrushenkov, A.; Rauhut, G.; Adler, T. B.; Amos, R. D.; Bernhardsson, A.; Berning, A.; Cooper, D. L.; Deegan, M. J. O.; Dobbyn, A. J.; Eckert, F.; Goll, E.; Hampel, C.; Hetzer, G.; Hrenar, T.; Knizia, G.; Koppl, C.; Liu, Y.; Lloyd, A. W.; Mata, R. A.; May, A. J.; McNicholas, S. J.; Meyer, W.; Mura, M. E.; Nicklass, A.; Palmieri, P.; Pflüger, K.; Pitzer, R.; Reiher, M.;

Schumann, U.; Stoll, H.; Stone, A. J.; Tarroni, R.; Thorsteinsson, T.; Wang, M.; Wolf, A. *MOLPRO*, version 2008.1, *A package of ab initio programs*; University College Cardiff Consultants Limited: Wales, U.K., **2008**; see <http://www.molpro.net>.

[84] Birnbaum, D.; Fichou, D.; Kohler, B. E. *J. Chem. Phys.* **1992**, *96*, 165–169.

[85] Oliva, M. M.; Casado, J.; Navarrete, J. T. L.; Patchkovskii, S.; Goodson, T.; Harpham, M. R.; de Melo, J. S. S.; Amir, E.; Rozen, S. *J. Am. Chem. Soc.* **2010**, *132*, 6231–6242.

[86] Simpson, J. H.; McLaughlin, L.; Smith, D. S.; Christensen, R. L. *J. Chem. Phys.* **1987**, *87*, 3360–3365.

[87] Wang, Y.; Di Motta, S.; Negri, F.; Friedlein, R. *J. Am. Chem. Soc.* **2011**, *133*, 10054–10057.

[88] Käfer, D.; Witte, G. *Phys. Chem. Chem. Phys.* **2005**, *7*, 2850–2853.

[89] (a) Abdou, M. S. A.; Orfino, F. P.; Son, Y.; Holdcroft, S. *J. Am. Chem. Soc.* **1997**, *119*, 4518–4524. (b) Collins, P. G.; Bradley, K.; Ishigami, M.; Zettle, A. *Science* **2000**, *287*, 1801–1804. (c) Meijer, E. J.; Detcheverry, C.; Baesjou, P. J.; van Veenendaal, E.; de Leeuw, D. M.; Klapwijk, T. M. *J. Appl. Phys.* **2003**, *93*, 4831–4835.

[90] Anthopoulos, T. C.; Shafai, T. S. *Appl. Phys. Lett.* **2003**, *82*, 1628–1630.

[91] (a) Mitrofanov, O.; Lang, D. V.; Kloc, C.; Wikberg, J. M.; Siegrist, T.; So, W.-Y.; Sergent, M. A.; Ramirez, A. P. *Phys. Rev. Lett.* **2006**, *97*, 166601. (b) Lu, C.-K.; Meng, H.-F. *Phys. Rev. B* **2007**, *75*, 235206. (c) Tanaka, Y.; Kanai, K.; Ouchi, Y.; Seki, K. *Chem. Phys. Lett.* **2007**, *441*, 63–67. (d) Vollmer, A.; Jurchescu, O. D.; Arfaoui, I.; Salzmann, I.; Palstra, T. T. M.; Rudolf, P.; Niemax, J.; Pflaum, J.; Rabe, J. P.; Koch, N. *Eur. Phys. J. E* **2005**, *17*, 339–343. (e) Song, X.; Wang, L.; Fan, Q.; Wu, Y.; Wang, H.; Liu, C. *Appl. Phys. Lett.* **2010**, *97*, 032106. (f) Najafov, H.; Mastrogiovanni, D.; Garfunkel, E.; Feldman, L. C.; Podzorov, V. *Adv. Mater.* **2011**, *23*, 981–985.

[92] (a) Mitsuhashi, R.; Suzuki, Y.; Yamanari, Y.; Mitamura, H.; Kambe, T.; Ikeda, N.; Okamoto, H.; Fujiwara, A.; Yamaji, M.; Kawasaki, N.; Maniwa, Y.; Kubozono, Y. *Nature* **2010**, *464*, 76–79. (b) Okamoto, H.; Kawasaki, N.; Kaji, Y.; Kubozono, Y.; Fujiwara, A.; Yamaji, M. *J. Am. Chem. Soc.* **2008**, *130*, 10470–10471. (c) Kawasaki, N.; Kubozono, Y.; Okamoto, H.; Fujiwara, A.; Yamaji, M. *Appl. Phys. Lett.* **2009**, *94*, 043310.

- [93] Kuritka, I.; Negri, F.; Brancolini, F.; Suess, C.; Salaneck, W. R.; Friedlein, R. *J. Phys. Chem. B* **2006**, *110*, 19023.
- [94] Zhao, Y.; Truhlar, D. G. *Theor. Chem. Acc.* **2008**, *120*, 215.
- [95] (a) Gao, L.; Deng, Z. T.; Ji, W.; Lin, X.; Cheng, Z. H.; He, X. B.; Shi, D. X.; Gao, H.-J. *Phys. Rev. B* **2006**, *73*, 075424. (b) Craciun, M. F.; Giovannetti, G.; Rogge, S.; Brocks, G.; Morpurgo, A. F.; van den Brink, J. *Phys. Rev. B* **2009**, *79*, 125116.
- [96] Anders, H.; Johan, B.; Sven, S. *Phys. Rev. B* **2006**, *73*, 184114.
- [97] Friedlein, R.; Crispin, X.; Pickholz, M.; Keil, M.; Stafström, S.; Salaneck, W. R. *Chem. Phys. Lett.* **2002**, *354*, 389–391.
- [98] Di, C.; Liu, Y.; Yu, G.; Zhu, D. *Acc. Chem. Res.* **2009**, *42*, 1573–158.
- [99] (a) Granucci, G.; Persico, M. *Chem. Phys. Lett.* **1993**, *205*, 331–336. (b) Weselowski, T. A.; Parisel, O.; Ellinger, Y.; Weber, J. *J. Phys. Chem. A* **1997**, *101*, 7818.
- [100] Graf, U.; Niikura, H.; Hirayama, S. *J. Phys. Chem. A* **1997**, *101*, 1292.
- [101] Di Motta, S.; Di Donato, E.; Negri, F.; Orlandi, G.; Fazzi, D.; Castiglioni, C. *J. Am. Chem. Soc.* **2009**, *131*, 6591–6598.
- [102] (a) Welnic, W.; Wuttig, M. *Mater. Today* **2008**, *11*, 20–27. (b) Ling, Q.-D.; Liaw, D.-J.; Zhu, C.; Chan, D. S.-H.; Kang, E.-T.; Neoh, K.-G. *Prog. Polym. Sci.* **2008**, *33*, 917–978.
- [103] Scott, J. C.; Bozano, L. D. *Adv. Mater.* **2007**, *19*, 1452–1463.
- [104] (a) Mukherjee, B.; Pal, A. *J. Org. Electron.* **2006**, *7*, 249–255. (b) Tondelier, D.; Lmimouni, K.; Vuillaume, D.; Fery, C.; Haas, G. *Appl. Phys. Lett.* **2004**, *85*, 5763–5765.
- [105] Bozano, L. D.; Kean, B. W.; Deline, V. R.; Salem, J. R.; Scott, J. C. *Appl. Phys. Lett.* **2004**, *84*, 607–609.
- [106] Donhauser, Z. J.; Mantooth, B. A.; Kelly, K. F.; Bumm, L. A.; Monnell, J. D.; Stapleton, J. J.; Price, D. W.; Rawlett, A. M.; Allara, D. L.; Tour, J. M.; Weiss, P. S. *Science* **2001**, *292*, 2303–2307.
- [107] (a) Bandyopadhyay, A.; Pal, A. *J. Phys. Chem. B* **2003**, *107*, 2531–2536. (b) Chen, J.; Reed, M. A.; Rawlett, A. M.; Tour, J. M. *Science* **1999**, *286*, 1550–1552.

- [108] (a) Bandyopadhyay, A.; Pal, A. J. *Appl. Phys. Lett.* **2004**, *84*, 999–1001. (b) Solak, A. O.; Ranganathan, S.; Itoh, T.; McCreery, R. L. *Electrochem. Solid State Lett.* **2002**, *5*, E43-E46.
- [109] (a) Rath, A. K.; Pal, A. J. *Org. Electron.* **2008**, *9*, 495–500. (b) Majee, S. K.; Bandyopadhyay, A.; Pal, A. J. *Chem. Phys. Lett.* **2004**, *399*, 284–288. (c) Rath, A. K.; Sahu, S.; Pal, A. J. *Appl. Phys. Lett.* **2006**, *89*, 142110.
- [110] (a) Caironi, M.; Natali, D.; Canesi, E.; Bianco, A.; Bertarelli, C.; Zerbi, G.; Sampietro, M. *Thin Solid Films* **2008**, *516*, 7680–7684. (b) Caironi, M.; Natali, D.; Sampietro, M.; Bertarelli, C.; Bianco, A.; Dundulachi, A.; Canesi, E.; Zerbi, G. *Appl. Phys. Lett.* **2006**, *89*, 243519.
- [111] Fazzi, D.; Castiglioni, C.; Negri, F.; Bertarelli, C.; Famulari, A.; Meille, S. V.; Zerbi, G. *J. Phys. Chem. C* **2008**, *112*, 18628–18637.
- [112] (a) Mukherjee, B.; Batabyal, S. K.; Pal, A. J. *Adv. Mater.* **2007**, *19*, 717–722. (b) Bandyopadhyay, A.; Chowdhury, A.; Pal, A. J. *Opt. Mater.* **2006**, *28*, 1432–1436. (c) Mukherjee, B.; Pal, A. J. *Synth. Met.* **2005**, *155*, 336–339. (d) Mukherjee, B.; Pal, A. J. *Appl. Phys. Lett.* **2004**, *85*, 2116–2118.
- [113] Novembre, C.; Guerin, D.; Lmimouni, K.; Gamrat, C.; Vuillaume, D. *Appl. Phys. Lett.* **2008**, *92*, 103314.
- [114] (a) Koh, S. E.; Risko, C.; da Silva, D. A.; Kwon, O.; Facchetti, A.; Brédas, J.-L.; Marks, T. J.; Ratner, M. A. *Adv. Funct. Mater.* **2008**, *18*, 332–340. (b) Norton, J. E.; Brédas, J.-L. *J. Am. Chem. Soc.* **2008**, *130*, 12377–12384.
- [115] Cheung, D. L.; Troisi, A. *Phys. Chem. Chem. Phys.* **2008**, *10*, 5941–5952.
- [116] Song, Y.; Di, C.; Yang, X.; Li, S.; Xu, W.; Liu, W.; Yang, L.; Shuai, Z.; Zhang, D.; Zhu, D. *J. Am. Chem. Soc.* **2006**, *128*, 15940–15941.
- [117] (a) Mattheus, C. C.; Dros, A. B.; Baas, J.; Meetsma, A.; de Boer, J. L.; Palstra, T. T. M. *Acta Crystallogr., Sect. C* **2001**, *57*, 939–941. (b) Zanotti, G.; Bardi, R.; Del Pra, A. *Acta Crystallogr., Sect. B* **1980**, *36*, 168–171. (c) Ueda, I. *J. Phys. Soc. Jpn.* **1961**, *16*, 1185–1194. (d) Vazquez, C.; Calabrese, J. C.; Dixon, D. A.; Miller, J. S. *J. Org. Chem.* **1993**, *58*, 65–81.
- [118] Allinger, N. L.; Yuh, H. Y.; Lii, J. H. *J. Am. Chem. Soc.* **1989**, *111*, 8551–8566.
- [119] Troisi, A.; Orlandi, G. *J. Phys. Chem. A* **2006**, *110*, 4065–4070.

- [120] Berendsen, H. J. C.; Postma, J. P. M.; van Gusteren, W. F.; Di Nola, A.; Haak, J. R. *J. Chem. Phys.* **1984**, *81*, 3684–3690.
- [121] (a) Troisi, A.; Orlandi, G.; Anthony, J. E. *Chem. Mater.* **2005**, *17*, 5024–5031. (b) Troisi, A. *Adv. Mater.* **2007**, *19*, 2000–2004.
- [122] Schottky, W. *Z. Phys.* **1942**, *118*, 539–592.
- [123] (a) Kahn, A.; Koch, N.; Gao, W. *J. Polym. Sci., Part B: Polym. Phys.* **2003**, *41*, 2529–2548. (b) Gao, W.; Kahn, A. *Org. Electron.* **2002**, *3*, 53–63.
- [124] Pope, M.; Swenberg, C. E. *Electronic Processes in Organic Crystals and Polymers*; Oxford University Press: New York, Oxford, **1999**; p 1328.
- [125] Boesch, S. E.; Grafton, A. K.; Wheeler, R. A. *J. Phys. Chem.* **1996**, *100*, 10083–10087.
- [126] Chen, E. C. M.; Wentworth, W. E. *J. Chem. Phys.* **1975**, *63*, 3183–3191.
- [127] (a) Ishii, H.; Sugiyama, K.; Ito, E.; Seki, K. *Adv. Mater.* **1999**, *11*, 605–625. (b) Vazquez, H.; Flores, F.; Oszwaldowski, R.; Ortega, J.; Perez, R.; Kahn, A. *Appl. Surf. Sci.* **2004**, *234*, 107–112.
- [128] (a) Coropceanu, V.; Andre, J. M.; Malagoli, M.; Brédas, J.-L. *Theor. Chem. Acc.* **2003**, *110*, 59–69. (b) Malagoli, M.; Coropceanu, V.; da Silva, D. A.; Brédas, J.-L. *J. Chem. Phys.* **2004**, *120*, 7490–7496.
- [129] Facchetti, A. *Chem. Mater.* **2011**, *23*, 733–758.
- [130] (a) Jung, B. J.; Tremblay, N. J.; Yeh, M. L.; Katz, H. E. *Chem. Mater.* **2011**, *23*, 568–582. (b) Anthony, J. E.; Facchetti, A.; Heeney, M.; Marder, S. R.; Zhan, X. W. *Adv. Mater.* **2010**, *22*, 3876–3892. (c) Yan, H.; Chen, Z. H.; Zheng, Y.; Newman, C.; Quinn, J. R.; Dotz, F.; Kastler, M.; Facchetti, A. *Nature* **2009**, *457*, 679–U1. (d) Chua, L. L.; Zaumseil, J.; Chang, J. F.; Ou, E. C. W.; Ho, P. K. H.; Sirringhaus, H.; Friend, R. H. *Nature* **2005**, *434*, 194–199.
- [131] Bao, Z.; Lovinger, A. J.; Brown, J. J. *Am. Chem. Soc.* **1998**, *120*, 207–208.
- [132] Handa, S.; Miyazaki, E.; Takimiya, K.; Kunugi, Y. *J. Am. Chem. Soc.* **2007**, *129*, 11684–11685.
- [133] Handa, S.; Miyazaki, E.; Takimiya, K. *Chem. Commun.* **2009**, 3919–3921.

- [134] (a) Oh, J. H.; Suraru, S. L.; Lee, W. Y.; Könemann, M.; Hoffken, H. W.; Roger, C.; Schmidt, R.; Chung, Y. Y.; Chen, W. C.; Würthner, F.; Bao, Z. N. *Adv. Funct. Mater.* **2010**, *20*, 2148–2156. (b) Jung, B. J.; Sun, J.; Lee, T.; Sarjeant, A.; Katz, H. E. *Chem. Mater.* **2009**, *21*, 94–101.
- [135] Horowitz, G.; Kouki, F.; Spearman, P.; Fichou, D.; Nogues, C.; Pan, X.; Garnier, F. *Adv. Mater.* **1996**, *8*, 242–245.
- [136] (a) Schmidt, R.; Ling, M. M.; Oh, J. H.; Winkler, M.; Könemann, M.; Bao, Z. N.; Würthner, F. *Adv. Mater.* **2007**, *19*, 3692–3695. (b) Oh, J. H.; Liu, S.; Bao, Z.; Schmidt, R.; Würthner, F. *Appl. Phys. Lett.* **2007**, *91*, 212107. (c) Ling, M. M.; Erk, P.; Gomez, M.; Könemann, M.; Locklin, J.; Bao, Z. N. *Adv. Mater.* **2007**, *19*, 1123–1127. (d) Gsänger, M.; Oh, J. H.; Könemann, M.; Hoffken, W.; Krause, A. M.; Bao, Z.; Würthner, F. *Angew. Chem., Int. Ed. Engl.* **2010**, *49*, 740–743. (e) Brooks, A. J.; Facchetti, A.; Wasielewski, M. R.; Marks, T. J. *J. Am. Chem. Soc.* **2007**, *129*, 15259–15278.
- [137] (a) Ruiz Delgado, M. C.; Pigg, K. R.; Da Silva Filho, D. A.; Gruhn, N. E.; Sakamoto, Y.; Suzuki, T.; Osuna, R. M.; Casado, J.; Hernandez, V.; Navarrete, J. T. L.; Martinelli, N. G.; Cornil, J.; Sanchez-Carrera, R. S.; Coropceanu, V.; Brédas, J.-L. *J. Am. Chem. Soc.* **2009**, *131*, 1502–1512.
- [138] Tang, M. L.; Oh, J. H.; Reichardt, A. D.; Bao, Z. N. *J. Am. Chem. Soc.* **2009**, *131*, 3733–3740.
- [139] Chen, Z. J.; Debije, M. G.; Debaerdemaeker, T.; Osswald, P.; Würthner, F. *ChemPhysChem* **2004**, *5*, 137–140.
- [140] (a) Marcon, V.; Breiby, D. W.; Pisula, W.; Dahl, J.; Kirkpatrick, J.; Patwardhan, S.; Grozema, F.; Andrienko, D. *J. Am. Chem. Soc.* **2009**, *131*, 11426–11432. (b) Hansen, M. R.; Graf, R.; Sekharan, S.; Sebastiani, D. *J. Am. Chem. Soc.* **2009**, *131*, 5251–5256. (c) Chen, Z. J.; Baumeister, U.; Tschierske, C.; Würthner, F. *Chem. Eur. J.* **2007**, *13*, 450–465. (d) Stehr, V.; Pfister, J.; Fink, R. F.; Engels, B.; Deibel, C. *Phys. Rev. B* **2011**, *83*, 155208. (e) Geng, Y.; Wang, J. P.; Wu, S. X.; Li, H. B.; Yu, F.; Yang, G. C.; Gao, H. Z.; Su, Z. M. *J. Mater. Chem.* **2011**, *21*, 134–143.
- [141] McMahon, D. P.; Troisi, A. *J. Phys. Chem. Lett.* **2010**, *1*, 941–946.
- [142] Würthner, F. *Pure Appl. Chem.* **2006**, *78*, 2341–2349.

- [143] Li, C.; Mishchenko, A.; Li, Z.; Pobelov, I.; Wandlowski, T.; Li, X. Q.; Wurthner, F.; Bagrets, A.; Evers, F. *J. Phys.: Condens. Matter* **2008**, *20*, 374122.
- [144] Martinelli, N. G.; Olivier, Y.; Athanasopoulos, S.; Delgado, M. C. R.; Pigg, K. R.; da Silva, D. A.; Sanchez-Carrera, R. S.; Venuti, E.; Della Valle, R. G.; Brédas, J.-L.; Beljonne, D.; Cornil, J. *ChemPhysChem* **2009**, *10*, 2265–2273.
- [145] (a) Troisi, A.; Nitzan, A.; Ratner, M. A. *J. Chem. Phys.* **2003**, *119*, 5782–5788. (b) Skourtis, S. S.; Balabin, I. A.; Kawatsu, T.; Beratan, D. N. *Proc. Natl. Acad. Sci. U.S.A.* **2005**, *102*, 3552–3557. (c) Troisi, A.; Ratner, M. A.; Zimmt, M. B. *J. Am. Chem. Soc.* **2004**, *126*, 2215–2224.
- [146] (a) Tan, L.; Zhang, L.; Jiang, X.; Yang, X. D.; Wang, L. J.; Wang, Z.; Li, L. Q.; Hu, W. P.; Shuai, Z. G.; Li, L.; Zhu, D. B. *Adv. Funct. Mater.* **2009**, *19*, 272–276. (b) Nan, G. J.; Yang, X. D.; Wang, L. J.; Shuai, Z. G.; Zhao, Y. *Phys. Rev. B* **2009**, *79*, 115203. (c) Yang, X. D.; Wang, L. J.; Wang, C. L.; Long, W.; Shuai, Z. G. *Chem. Mater.* **2008**, *20*, 3205–3211. (d) Martinelli, N. G.; Savini, M.; Muccioli, L.; Olivier, Y.; Castet, F.; Zannoni, C.; Beljonne, D.; Cornil, J. *Adv. Funct. Mater.* **2009**, *19*, 3254–3261. (e) Athanasopoulos, S.; Kirkpatrick, J.; Martinez, D.; Frost, J. M.; Foden, C. M.; Walker, A. B.; Nelson, J. *Nano Lett.* **2007**, *7*, 1785–1788. (f) Olivier, Y.; Lemaire, V.; Brédas, J.-L.; Cornil, J. *J. Phys. Chem. A* **2006**, *110*, 6356–6364. (g) Andrienko, D.; Kirkpatrick, J.; Marcon, V.; Nelson, J.; Kremer, K. *Phys. Status Solidi B* **2008**, *245*, 830–834.
- [147] Deng, W. Q.; Goddard III, W. A. *J. Phys. Chem. B* **2004**, *108*, 8614–8621.
- [148] Troisi, A. *Chem. Soc. Rev.* **2011**, *40*, 2347–2358.
- [149] Würthner, F. *Chem. Commun.* **2004**, 1564–1579.
- [150] (a) Chen, J. H.; Subramanian, S.; Parkin, S. R.; Siegler, M.; Gallup, K.; Haughn, C.; Martin, D. C.; Anthony, J. E. *J. Mater. Chem.* **2008**, *18*, 1961–1969. (b) Park, S. K.; Jackson, T. N.; Anthony, J. E.; Mourey, D. A. *Appl. Phys. Lett.* **2007**, *91*, 063514. (c) Anthony, J. E.; Brooks, J. S.; Eaton, D. L.; Parkin, S. R. *J. Am. Chem. Soc.* **2001**, *123*, 9482–9483.
- [151] Troisi, A. *J. Chem. Phys.* **2011**, *134*, 034702.

## CHAPTER 7 - CONCLUDING REMARKS

In this dissertation, the structural, electronic, optical, and charge transport characteristics of several organic semiconductors have been discussed from a theoretical and computational point of view, with the purpose of better understanding the structure-property relationships governing those phenomena on which new-generation organic technology relies. Particular care has been addressed to the rationalization of optical and charge transport properties in terms of both intra- and intermolecular features. Moreover, a considerable part of this project involved the development of a home-made set of procedures and parts of software code (referred to as the Pandora Suite) required to assist the modeling of charge transport properties in the framework of the non-adiabatic hopping mechanism applied to organic crystalline materials.

Investigations were carried out by means of an integrated computational approach encompassing quantum-chemical calculations, molecular dynamics and kinetic Monte Carlo simulations.

Suitable quantum-chemical methods were employed to obtain an accurate and realistic description of electronic structure and optical properties, along with intra- and intermolecular interactions which govern optoelectronic and charge transport properties of the investigated molecular materials. Most quantum-chemical calculations were based on the used density functional theory, owing to the large dimension of some of the systems investigated. Electronic correlation was introduced also at CASSCF + CASPT2 methods for smaller and more treatable systems. When required, long-range corrected functionals were adopted to adequately deal with charge-transfer character states or non-covalent interactions. In some cases, the vibronic structure associated with electronic spectra was also modeled within the Franck-Condon approximation. Because of the large dimension of most of the systems investigated, basis sets were generally restricted to 3-21G\* and 6-31G\*. The considerable collection of related systems investigated and the very good agreement with experiment have shown that available DFT and TDDFT functionals are reliable and suitable for the description of optical and structural properties of rylene derivatives not only for

neutral systems but also for the optical properties of electrochemically generated charged systems.

Molecular dynamics simulations were performed to evaluate thermally induced disorder effects on the charge transport of the molecular materials, whereas the investigation of the charge transport phenomena occurring in molecular crystals relied also on kinetic Monte Carlo simulations.

The studies presented in this dissertation were carried out within two main fields of interest.

As a first part of my investigations, I have mainly discussed the optical, electronic, and structural properties of several core-extended rylene derivatives, which can be regarded to as model compounds for graphene nanoribbons, along with other organic semiconductors such as tetracene diimides, quinoidal oligothiophenes, and oxygen doped picene for which experimental optoelectronic properties have been determined by research groups that have long-standing collaborations with the research group where my thesis was developed.

My theoretical and computational studies have clarified how different connectivity and derivatizations, such as the inclusion of condensed five-membered aromatic heterocycles, can modulate opto-electronic properties through the modification of the  $\pi$ -conjugation of the compounds. Accordingly, all the reported experimental observations have found a suitable explanation in terms of computed results. Indeed, on the one hand, it has been shown how optical transitions undergo bathochromic or hypsochromic shifts or even give rise to new spectral features. On the other hand, the effect of substituents and core extension on charge transport character has been considered as well. For instance, *n*-type character strengthening has been discussed as a consequence of both  $\pi$ -system extension and functionalization with electron-withdrawing groups such as fluoroalkyl and chlorine substituents.

As an example of device application, the structural characteristics governing the efficiency of resistive molecular memories based on a derivative of benzoquinone have been studied.

As for the second field of interest, a comprehensive study has been carried out to investigate the structural and thermal effects governing charge transport in planar- and twisted-core PBI derivatives. The interplay between intramolecular structure, intermolecular packing and

available charge transport paths has been carefully investigated for a number of PBI derivatives featuring both planar and twisted core. It has been highlighted that core twisting along with the presence of enantiomers in the molecular crystal bear imbalances in charge transfer, such as the so-called dimer-trapping (or retardation effect), that can be extremely detrimental for the charge mobility of the material. On the other hand, the analysis of available charge transfer events occurring within a given packing arrangement has revealed that efficient inter-column charge transport can occur beside the more obvious intra-column charge transport for a number of PBI derivatives. Therefore, a rationalization of charge mobility trends and isotropic or rather anisotropic conduction for fluoroalkylated and chlorinated PBIs has been provided.

Thermally induced disorder effects have also been taken into account. Indeed, as recently shown in literature, the description of hopping patterns can be strongly modulated by thermally induced electronic coupling fluctuations which may open new channels for charge transport. Based on the analysis carried out on PBI derivatives, I have shown that the large thermally induced electronic coupling fluctuations strongly activate the intra-column channel that would be otherwise inaccessible for planar core derivatives. On the other hand, it has been pointed out that twisted-core PBIs, which feature less favorable  $\pi$ - $\pi$  interactions because of the twisted  $\pi$ -system, are less sensitive to such thermal effects than planar-core PBIs.

To summarize, the results reported in this dissertation suggest how a solid computational approach may help to rationalize the structural, electronic, optical, and charge transport properties of organic materials, possibly contributing to the design of new photoactive chromophores as well as high-performance semiconductors. Indeed, issues like photoactivity, *n*-type or *p*-type character, level alignment, electronic coupling effects, and charge mobility, to name a few, can realistically be addressed by means of theoretical and computational methods.